**Universitat Politècnica de València**

Departament d'Enginyeria Hidràulica i Medi Ambient
PhD Program in Water and Environmental Engineering


PhD Thesis

# Remote Sensing and UAVs for the geomorphological and habitat analyses in ephemeral and permanent Mediterranean streams

Presented by:
**Carlos Antonio Puig Mengual**

Supervisors:
**Francisco Martínez Capel**
**Carmelo Conesa García**

Valencia (Spain), June, 2021

*“A mi padre, a mi madre, a mi hermana*

*y a toda mi familia y amigos”*

# Agradecimientos

El desarrollo y finalización de esta tesis doctoral ha sido posible gracias a diferentes personas e instituciones que han hecho posible alcanzar este objetivo.

En primer lugar, agradecer a Universitat Politècnica de València y a todos los profesores que me han formado durante mis años de estudios y que me han convertido en el profesional que soy hoy. Gracias a ellos he podido adquirir habilidades y conocimientos que durante estos años de desarrollo de mi tesis me han ayudado a alcanzar todas las metas marcadas y que en mi futuro camino como investigador me permitirán alcanzar todo aquello que me proponga.

Agradecer también al Instituto de Investigación para la Gestión Integrada de Zonas Costeras (IGIC) del Campus de Gandia la posibilidad de formar parte de él y desarrollar mis investigaciones y trabajos juntamente con los profesionales que lo integran.

También me gustaría agradecer a los profesores Michael McClain y Paolo Paron del Instituto IHE Delft, Institute for Water Education (Países Bajos) por su ayuda y apoyo, por brindarme la posibilidad de trabajar junto a ellos y a un gran grupo de investigadores y profesionales en el proyecto internacional "Habitat Modelling and Fish Habitat Analyses within the Project Rufiji River Basin Environmental Flow Assessment" financiado por Intitute for Water Education IHE Delft UNESCO Foundation y por U.S. Agency for International Development (Gobierno de EE.UU.) En este proyecto pude entrar en contacto con las dinámicas de trabajo multidisciplinares de grandes equipos de investigación para desarrollar mis habilidades en los diferentes flujos de trabajo que se presentaron.

Agradecer también a Francisca Segura y a Carles Sanchis por su ayuda y trabajo conjunto en el proyecto “Natural and anthropogenic changes in Mediterranean river drainage basins: historical impacts on rivers morphology, sedimentary flows and vegetation” financiado por el MINECO (CGL2013-44917-R). En el desarrollo de las tareas asociadas a este proyecto pude adquirir conocimientos necesarios y de gran valor que durante el desarrollo de mi tesis me apoyaron en la consecución de resultados.

Agradecer especialmente y con especial cariño a Amy S. Woodget (Loughborough University, Reino Unido) y a toda su familia por toda la ayuda, apoyo y cariño que me brindaron durante mi estancia en el University College Worcester. Muchas gracias, Amy por tu paciencia, tu profesionalidad y tus valores, contigo pude crecer como investigador y mejorar mi formación, trabajamos duro juntos y esta tesis en buena parte es gracias a ti y a nuestro trabajo conjunto.

Agradecimiento sincero también para Daniele Tonina y al Center for Ecohydraulics Research at the University of Idaho, gracias por apoyar esta tesis doctoral y por el trabajo realizado juntos durante este tiempo. Tu experiencia y profesionalidad han servido para ayudarme a mejorar el trabajo que aquí presento y que seguro seguiremos mejorando y colaborando en futuros proyectos.

Especial agradecimiento para dos profesionales que han estado siempre a mi lado para echarme una mano y apoyarme en todo lo que fuese necesario en mi trabajo del día

a día, Rafael Muñoz Mas y Virginia Garófano Gómez. Muchas gracias por estar ahí siempre y ayudarme a saltar las dificultades que se presentaban y compartir conmigo vuestra experiencia y buen hacer.

Agradecer también a Javier Estornell por el apoyo y dedicación brindado para el desarrollo de esta tesis, y por su ayuda durante estos años para mejorar la calidad de los trabajos generados.

Agradecimiento y reconocimiento a todo el trabajo realizado para llevar a cabo esta tesis a Carmelo Conesa, codirector de esta tesis. Su trabajo y dedicación ha permitido desarrollar esta tesis doctoral, que en buena parte se debe a su impecable dirección y enorme capacidad de trabajo. Gracias a su experiencia y conocimientos he podido mejorar mis capacidades y adquirir nuevas habilidades en mi carrera como investigador. Agradecer también por supuesto a la Universidad de Murcia y la Universidad de Alicante así como al proyecto de investigación "Respuesta morfológica y sistémica al cambio climático en cauces efímeros mediterráneos: dinámica, resiliencia y propuestas de actuación" funded by ERDF/Spanish Ministry of Science, Innovation and Universities—State Research Agency/Project CGL2017-84625-C2-1-R (CCAMICEM); State Program for Research, Development and Innovation Focused on the Challenges of Society, del Ministerio de Economía y Competitividad (MINECO) y EU FEDER (Project TEC2017-85244-C2-1-P) y de la Universidad de Alicante (vigrob-157 and GRE18-05). Agradecer a todos y cada uno de los investigadores y profesionales que han participado en este proyecto y han apoyado el desarrollo de los trabajos que se presentan en esta tesis.

Especial agradecimiento con todo cariño a mi familia, mis seres queridos y amigos que han estado a mi lado todos estos años de trabajo y que finalmente se ha conseguido finalizar y presentar esta tesis doctoral. Gracias a mi familia por todo el apoyo que me han brindado y soporte día tras día para conseguirlo, gracias a mis padres, a mi hermana Silvia, a mis abuelos que siempre estarán junto a mi para apoyarme, a toda mi familia y amigos que han estado siempre a mi lado para ayudarme con lo que les pidiese sin importar las largas jornadas de trabajo de campo o las llamadas a cualquier hora. Gracias a todos ellos por estar ahí y confiar en mí y en mi trabajo.

Y finalmente, el agradecimiento más especial y profundo a Francisco Martínez Capel, Paco, por aguantar todos estos años y confiar en mí y en el trabajo que podíamos desarrollar juntos, por todo su apoyo, conocimientos y valores que me ha inculcado durante todo este tiempo. Una parte de ti está en todos los párrafos anteriores de agradecimientos porque todo eso lo he podido conseguir gracias a ti y a la confianza que has depositado en mí siempre. Gracias también a tu familia, a Esther y Ana, por darme su apoyo y cariño durante estos años. Gracias a los tres por sentir y padecer junto a mí, el resultado obtenido es en gran parte vuestro también.

Agradecer a mi madre, Jovita, por estar a mi lado, apoyarme, darme todo su cariño y cuidarme todos los días, ella me ha dado siempre las fuerzas para seguir trabajando y pelear por conseguir todo lo que proponga, muchas gracias por quererme tanto y cuidarme siempre.

Antes de terminar esta sección de agradecimientos me gustaría dedicar todo este trabajo y dedicación a una persona muy especial para mí, la más importante en mi vida,

la persona que siempre ha estado, está y estará, la persona que confía en mi día y noche, la persona que me ha apoyado siempre y dado todo el cariño y amor posible para darme las fuerzas de seguir adelante y querer siempre alcanzar todo lo posible de la mejor manera. Quiero dedicar este trabajo y éxito, así como siempre lo he hecho y haré a mi padre, Antonio, por ser como eres y porque eres mi referente y la persona en la que quiero verme reflejado siempre. Muchas gracias papá por todo.

Muchas gracias de corazón a todos.

# Acknowledgements

The development and completion of this doctoral thesis have been possible thanks to different people and institutions that have made it possible to achieve this objective.

First of all, I would like to thank Universitat Politècnica de València and all the professors who have trained me during my years of studies and who have made me the professional I am today. Thanks to them I have been able to acquire skills and knowledge that during these years of development of my thesis have helped me to achieve all the goals set and that in my future path as a researcher will allow me to achieve everything that I set out to do.

Also, thank the Research Institute for Integrated Coastal Zone Management (IGIC) of the Gandia Campus for the possibility of being part of it and developing my research and work together with the professionals who make it up.

I would also like to thank professors Michael McClain and Paolo Paron from the IHE Delft Institute, Institute for Water Education (The Netherlands) for their help and support, for giving me the opportunity to work alongside them and a large group of researchers and professionals in the international project "Habitat Modeling and Fish Habitat Analyzes within the Project Rufiji River Basin Environmental Flow Assessment" funded by the Institute for Water Education IHE Delft UNESCO Foundation and the US Agency for International Development (US Government) In this project I was able to get in touch with the multidisciplinary work dynamics of large research teams to develop my skills in the different workflows that were presented.

Also thank Francisca Segura and Carles Sanchis for their help and joint work in the project "Natural and anthropogenic changes in Mediterranean river drainage basins: historical impacts on rivers morphology, sedimentary flows and vegetation" funded by MINECO (CGL2013-44917-R). In the development of the tasks associated with this project, I was able to acquire necessary and valuable knowledge that, during the development of my thesis, supported me in achieving results.

Special thanks to Amy S. Woodget (Loughborough University, UK) and her entire family for all the help, support and love they gave me during my stay at University College Worcester. Thank you very much, Amy, for your patience, your professionalism and your values, with you I was able to grow as a researcher and improve my training, we work hard together and this thesis is largely thanks to you and our joint work.

Sincere thanks also to Daniele Tonina and the Center for Ecohydraulics Research at the University of Idaho, thank you for supporting this doctoral thesis and for the work done together during this time. Your experience and professionalism have served to help me improve the work that I present here and that we will surely continue to improve and collaborate in future projects.

Special thanks to two professionals who have always been by my side to lend me a hand and support me in whatever is necessary for my day-to-day work, Rafael Muñoz Mas and Virginia Garófano Gómez. Thank you very much for always being there and helping me to overcome the difficulties that arose and share with me your experience and good work.

Also thank Javier Estornell for the support and dedication provided for the development of this thesis, and for his help during these years to improve the quality of the work generated.

Thanks and appreciation for all the work done to carry out this thesis to Carmelo Conesa, co-director of this thesis. His work and dedication have allowed the development of this doctoral thesis, which is largely due to his impeccable direction and enormous capacity for work. Thanks to his experience and knowledge, I have been able to improve my skills and acquire new skills in my career as a researcher. Also of course thank the University of Murcia and the University of Alicante as well as the research project "Morphological and systemic response to climate change in ephemeral Mediterranean channels: dynamics, resilience and action proposals" funded by ERDF / Spanish Ministry of Science, Innovation and Universities — State Research Agency / Project CGL2017-84625-C2-1-R (CCAMICEM); State Program for Research, Development and Innovation Focused on the Challenges of Society, of the Ministry of Economy and Competitiveness (MINECO) and EU FEDER (Project TEC2017-85244-C2-1-P) and of the University of Alicante (vigrob-157 and GRE18-05). Thank every one of the researchers and professionals who have participated in this project and have supported the development of the works presented in this thesis.

Special thanks with all affection to my family, my loved ones and friends who have been by my side all these years of work and who have finally been able to finish and present this doctoral thesis. Thanks to my family for all the support they have given me and support day after day to achieve it, thanks to my parents, my sister Silvia, my grandparents who will always be with me to support me, all my family and friends who have He was always by my side to help me with whatever I asked, regardless of the long days of fieldwork or calls at any time. Thanks to all of them for being there and trusting me and my work.

And finally, the most special and profound thanks to Francisco Martínez Capel, Paco, for putting up with all these years and trusting in me and in the work that we could develop together, for all his support, knowledge and values that he has instilled in me during all this time. A part of you is in all the previous paragraphs of thanks because I have been able to achieve all these thanks to you and the trust that you have always placed in me. Thanks also to your family, Esther and Ana, for giving me their support and love during these years. Thank you all three for feeling and suffering with me, the result obtained is largely yours as well.

Thank my mother, Jovita, for being by my side, supporting me, giving me all her love and taking care of me every day, she has always given me the strength to continue working and fight to achieve everything I propose, thank you very much for loving me so much and take care of me always.

Before ending this section of thanks I would like to dedicate all this work and dedication to a very special person for me, the most important in my life, the person who has always been, is and will be, the person who trusts my day and night, the person who has always supported me and given all the affection and love possible to give me the strength to move forward and always want to achieve everything possible in the best way. I want to dedicate this work and success, as I have always done and will do to my father,

Antonio, for being who you are and because you are my reference and the person in whom I always want to see myself reflected. Thank you very much dad for everything.

Thank you all from the bottom of my heart.

# Resumen

Los ecosistemas riparios presentan una gran variabilidad, desde un punto de vista geomorfológico como hidrológico y ecológico, incluyendo las complejas interacciones que la morfología y la vegetación de ribera puede presentar. La vegetación se presenta como un factor físico muy influyente en los sistemas fluviales, con una relación directa en los procesos geomorfológicos que tienen lugar en los corredores fluviales. La detección, monitoreo y evaluación de los procesos que se desarrollan en el espacio ripario son clave a la hora de poder entender las funciones ecológicas y el desarrollo de dichos hábitats, y por tanto para tomar decisiones para su conservación y restauración. Según la distribución de especies y los rasgos de las plantas, las comunidades vegetales y su dinámica presentan distintas características en el ecosistema ripario, a las cuales los métodos de detección y monitoreo deben adaptarse.

Los constantes cambios que sufren estos espacios a lo largo del tiempo se deben en gran parte a procesos físicos relacionados con las dinámicas de erosión y sedimentación, las variaciones de la trayectoria del cauce, variaciones en la distribución de especies y vegetación en el bosque de ribera, etc., pero también se deben al impacto antropogénico, que puede llegar a generar grandes desajustes en la dinámica ecológica de los ecosistemas en cuestión. Debido a las interacciones de diversos procesos y alteraciones antropogénicas, y las complejas dinámicas espacio-temporales, resulta necesario continuar desarrollando metodologías teóricas y prácticas para la monitorización y caracterización de estos ecosistemas.

La teledetección, incluyendo el uso de drones, se presenta como una herramienta muy interesante y óptima para el mapeo y recogida de información en estos espacios naturales. Los beneficios que demuestran las aeronaves no tripuladas –UAV– incluyen las mejoras en la resolución espacial y temporal de los datos capturados, así como la cartografía de áreas extensas en poco tiempo, lo que los convierte en instrumentos clave en tareas de gestión y conservación de los espacios riparios.

La necesidad de estudiar la dinámica geomorfológica que se produce en los cauces fluviales ha sido la principal motivación en los estudios que se presentan en esta tesis doctoral. Los capítulos 2 y 3 se basan en técnicas de captura de datos con láser escáner terrestre (TLS) y en el modelado de los datos obtenidos en vuelos fotogramétricos de UAV. Con ellos se han caracterizado los procesos que tienen lugar en una cierta área de estudio, un cauce efímero del sureste de la Península Ibérica, la Rambla de la Azohía (Murcia). Estos estudios también han permitido comparar el ajuste y precisión de los datos capturados a partir de dos técnicas distintas.

Además, el interés en caracterizar los cauces fluviales con un flujo permanente ha motivado el estudio de la topografía sumergida en un tramo de río, segmentado por tipos de mesohábitat. Así pues, el capítulo 4 presenta un algoritmo y una herramienta de corrección para el efecto de la refracción en un tramo del rio Palancia (Castellón), para llevar a cabo la correcta representación de la morfología del lecho sumergido. A partir de la metodología planteada y el algoritmo desarrollado, es posible minimizar los efectos de distorsión debidos a la presencia del agua, para obtener la reconstrucción tridimensional del lecho a partir de imágenes tomadas con UAV. La construcción del modelo 3D se llevó a cabo mediante la técnica de Structure from Motion.

Finalmente, y como elemento clave en la dinámica de los ecosistemas riparios, el capítulo 5 desarrolla una metodología para clasificar las fases de sucesión de la vegetación del bosque ripario. Dichas fases de sucesión se basan en la metodología del proyecto RIPFLOW, que también está implementada en el modelo dinámico CASiMiR-vegetation. En concreto, el caso de estudio en un tramo del río Serpis (Valencia) ha permitido comparar cinco métodos de clasificación, basados en técnicas de remote sensing y modelación matemática. La posibilidad de integrar herramientas que nos permitan monitorizar los cambios ante eventos de distinta magnitud, en ecosistemas riparios mediterráneos, facilitará el mejor entendimiento de los escenarios presentes y posibilitará la modelización precisa de posibles escenarios futuros, con los que poder prever trayectorias de la dinámica ecológica y proponer medidas que mejoren el estado ecológico y reduzcan la alteración antrópica.

# Abstract

Riparian ecosystems show great variability, from a geomorphological, hydrological and ecological point of view, including the complex interactions that riparian morphology and vegetation can present. Vegetation appears as a very influential physical factor in river systems, with a direct relationship in the geomorphological processes that take place in river corridors. The detection, monitoring and evaluation of the processes that take place in the riparian space are key when it comes to understanding the ecological functions and development of these habitats, and therefore for making decisions for their conservation and restoration. According to the distribution of species and plant traits, plant communities and their dynamics present different characteristics in the riparian ecosystem, to which detection and monitoring methods must be adapted.

The constant changes that these spaces undergo over time are largely due to physical processes related to the dynamics of erosion and sedimentation, variations in the path of the channel, variations in the distribution of species and vegetation in the riparian forest, etc. These processes also are due to the anthropogenic impact, which can generate major imbalances in the ecological dynamics of the ecosystems in question. Due to the interactions of various anthropogenic processes and alterations, and the complex spatio-temporal dynamics, it is necessary to continue developing theoretical and practical methodologies for the monitoring and characterization of these ecosystems.

Remote sensing, including the use of drones, is presented as a very interesting and optimal tool for mapping and collecting information in these natural spaces. The benefits demonstrated by unmanned aircraft –UAV– include improvements in the spatial and temporal resolution of the captured data, as well as the mapping of large areas in a short time, which makes them key instruments in the management and conservation tasks of riparian spaces.

The need to study the geomorphological dynamics that occur in river channels has been the main motivation in the studies presented in this doctoral thesis. Chapters 2 and 3 are based on ground-based laser scanner (TLS) data capture techniques and modelling of UAV photogrammetric flight data. They have characterized the processes that take place in a certain study area, an ephemeral riverbed in the southeast of the Iberian Peninsula, the Rambla de la Azohía (Murcia). These studies have also made it possible to compare the fit and precision of the data captured from two different techniques.

In addition, the interest in characterizing the fluvial channels with a permanent flow has motivated the study of the submerged topography in a stretch of river, segmented by types of mesohabitat. Thus, chapter 4 presents an algorithm and a correction tool for the effect of refraction in a stretch of the Palancia river (Castellón), to carry out the correct representation of the submerged bed morphology. From the proposed methodology and the developed algorithm, it is possible to minimize the distortion effects due to the presence of water, to obtain the three-dimensional reconstruction of the bed from images taken with UAVs. The construction of the 3D model was carried out using the Structure from Motion technique.

Finally, and as a key element in the dynamics of riparian ecosystems, chapter 5 develops a methodology to classify the phases of succession of riparian forest vegetation. These succession phases are based on the RIPFLOW project methodology, which is also

implemented in the dynamic CASiMiR-vegetation model. Specifically, the case study in a section of the Serpis River (Valencia) has made it possible to compare five classification methods, based on remote sensing techniques and mathematical modelling. The possibility of integrating tools that allow us to monitor changes in the face of events of different magnitude, in Mediterranean riparian ecosystems, will facilitate a better understanding of the present scenarios and will allow the precise modelling of possible future scenarios, with which to predict paths of ecological dynamics. and propose measures that improve the ecological status and reduce human disturbance.

# Resum

Els ecosistemes riparis presenten una gran variabilitat, des d'un punt de vista geomorfològic com a hidrològic i ecològic, incloent les complexes interaccions que la morfologia i la vegetació de ribera pot presentar. La vegetació es presenta com un factor físic molt influent en els sistemes fluvials, amb una relació directa en els processos geomorfològics que tenen lloc en els corredors fluvials. La detecció, monitoratge i avaluació dels processos que es desenvolupen en l'espai ripari són clau a l'hora de poder entendre les funcions ecològiques i el desenvolupament d'aquests hàbitats, i per tant per a prendre decisions per a la seua conservació i restauració. Segons la distribució d'espècies i els trets de les plantes, les comunitats vegetals i la seua dinàmica presenten diferents característiques en l'ecosistema ripari, a les quals els mètodes de detecció i monitoratge han d'adaptar-se.

Els constants canvis que pateixen aquests espais al llarg del temps es deuen en gran part a processos físics relacionats amb les dinàmiques d'erosió i sedimentació, les variacions de la trajectòria del llit, variacions en la distribució d'espècies i vegetació en el bosc de ribera, etc., però també es deuen a l'impacte antropogènic, que pot arribar a generar grans desajustaments en la dinàmica ecològica dels ecosistemes en qüestió. A causa de les interaccions de diversos processos i alteracions antropogèniques, i les complexes dinàmiques espaciotemporals, resulta necessari continuar desenvolupant metodologies teòriques i pràctiques per al monitoratge i caracterització d'aquests ecosistemes.

La teledetecció, incloent l'ús de drons, es presenta com una eina molt interessant i òptima per al mapatge i recollida d'informació en aquests espais naturals. Els beneficis que demostren les aeronaus no tripulades –UAV– inclouen les millores en la resolució espacial i temporal de les dades capturades, així com la cartografia d'àrees extenses en poc temps, la qual cosa els converteix en instruments clau en tasques de gestió i conservació dels espais riparis.

La necessitat d'estudiar la dinàmica geomorfològica que es produeix en els llits fluvials ha sigut la principal motivació en els estudis que es presenten en aquesta tesi doctoral. Els capítols 2 i 3 es basen en tècniques de captura de dades amb làser escàner terrestre (TLS) i en el modelatge de les dades obtingudes en vols fotogramètrics de UAV. Amb ells s'han caracteritzat els processos que tenen lloc en una certa àrea d'estudi, un llit efímer del sud-est de la Península Ibèrica, la Rambla de la Azohía (Múrcia). Aquests estudis també han permés comparar l'ajust i precisió de les dades capturades a partir de dues tècniques diferents.

A més, l'interés a caracteritzar els llits fluvials amb un flux permanent ha motivat l'estudi de la topografia submergida en un tram de riu, segmentat per tipus de mesohábitat. Així doncs, el capítol 4 presenta un algorisme i una eina de correcció per a l'efecte de la refracció en un tram del va riure Palància (Castelló), per a dur a terme la correcta representació de la morfologia del llit submergit. A partir de la metodologia plantejada i l'algorisme desenvolupat, és possible minimitzar els efectes de distorsió deguts a la presència de l'aigua, per a obtindre la reconstrucció tridimensional del llit a partir d'imatges preses amb UAV. La construcció del model 3D es va dur a terme mitjançant la tècnica de Structure from Motion.

Finalment, i com a element clau en la dinàmica dels ecosistemes riparis, el capítol 5 desenvolupa una metodologia per a classificar les fases de successió de la vegetació del bosc ripari. Aquestes fases de successió es basen en la metodologia del projecte RIPFLOW, que també està implementada en el model dinàmic CASiMiR-vegetation. En concret, el cas d'estudi en un tram del riu Serpis (València) ha permés comparar cinc mètodes de classificació, basats en tècniques de remote sensing i modelatge matemàtic. La possibilitat d'integrar eines que ens permeten monitorar els canvis davant esdeveniments de diferent magnitud, en ecosistemes riparis mediterranis, facilitarà el millor enteniment dels escenaris presents i possibilitarà la modelització precisa de possibles escenaris futurs, amb els quals poder preveure trajectòries de la dinàmica ecològica i proposar mesures que milloren l'estat ecològic i reduïsquen l'alteració antròpica.

# GENERAL INDEX

# 1. Introduction

The study of biodiversity and the natural environment in any setting and ecosystem is key to understanding the behaviour of the processes that take place in them (Naiman et al., 1993; Pollock et al., 1998; Tockner and Ward, 2001). Knowing how the natural variables behave and monitoring their dynamics and interrelations allow us to define the state of these scenarios reliably and precisely, as well as the possible conditioning factors that may affect them (Dufour et al., 2013; Džubáková et al., 2015).

Riparian ecosystems are considered spaces with a large spatio-temporal variability and biodiversity, where the very active dynamics of ecological processes make it necessary to apply different techniques and methods of modelling (Stella et al., 2013). The possibility to characterize their natural state and quantify the variations and unfolding events allow to understand their behaviour and trends (Greet et al., 2011).

Ephemeral streams are watercourses in arid and semi-arid environments with unstable morphology and high temporal variability of runoff. The episodes of sudden and extreme discharges that are isolated in time alternate with long periods of drought (Conesa-García et al., 2020). These types of currents are particularly sensitive to short-term climatic changes, and human impacts can alter their degree of response, sometimes leading to large morphological adjustments during flash floods (Segura-Beltrán and Sanchis-Ibor, 2013).

The energy flows and the sediment transport in the river networks is not only related with physical aspects of sediment and organic matter storage, but also with chemical and biological aspects that are related to plant species (Viles et al., 2008). The consideration of this dual implication allows the development of geomorphology as an interrelation between physical processes and biological evolutionary processes, incorporated into geomorphology in the last two decades (Corenblit et al., 2007, 2008).

With the study of the river ecosystem dynamics, we can better develop and understand its biogeomorphic approach (Corenblit, 2006; Gurnell and Petts, 2006). Hydrogeomorphic processes, geomorphology, and vegetation communities and distribution show very strong interrelations in river corridors (Steiger et al., 2005; Tabacchi et al., 2005). The continuous mechanical processes of immersion, sediment erosion, transport and deposition, destruction and removal of plants, import and export of new pioneer species due to flow dynamics (Naiman and Décamps, 1997; Tabacchi et al., 1998) drive vegetation successions regressive or progressive (Bendix, 1998). In addition, the distribution of vegetation can strongly interact and affect the flow of water and therefore the transport of sediments (Samani and Kouwen, 2002; Yen, 2002) with which a significant effect is exerted on the river corridors and the margins of the rivers.

The geomorphological characterization of the river channels and the modelling of their dynamics is crucial when it comes to understanding the processes that occur (Hupp and Osterkamp, 1996; Bennett and Simon, 2013; Gregory et al., 1991). And, in addition, the implication that river flow fluctuations has in the riparian vegetation is key to understanding and modelling the development of the plants (Vesipa et al., 2017; Perucca et al., 2007).

In this sense, Mediterranean riparian ecosystems present characteristics and conditions that cause the changes and variability have a strong impact on natural processes development (Stella et al., 2013; Martínez- Fernández et al., 2018). During the year these ecosystems usually present a distinctly cool and wet season followed by a warm and dry season, they are influenced by a sequence of regular and often extreme flooding with strong storms and rainfall and drying periods (Gasith and Resh, 1999). The irregular flows throughout the year are partially related to the meteorological nature of the Mediterranean climate. However, furthermore, anthropic elements of flow sectioning cause alterations in the quantity and quality of the water that flows through the Mediterranean riparian ecosystems (Alba-Tercedor et al., 2002).

The rainy seasons in the Mediterranean climate are very short and with a tendency to torrential and not gradual discharge, which causes a defect in the continuity of the flow. In addition, the continuous presence of elements of channel segmentation for irrigation and transport of water outside of the river, together with the discharge and presence of chemical substances bring on the impoverish of the quantity and quality of the transported water. These facts are presented as risks for the normal development of the riparian ecosystem (Munné and Prat, 2011), thus its monitoring and control is necessary to take care of these ecosystems.

## 1.1 Ephemeral streams

Mediterranean ephemeral streams are particularly sensitive to short-term climatic changes, and the impacts related to human activities may affect the degree of response of them (Conesa-García et al., 2020). Heavy rainfalls can produce large volumes of torrential runoff and therefore an increase in the energy load in the transport of sediments. That is why the morphology of the channel is modified and contributes to the dynamics and changes in the riparian habitats (Latron and Gallart, 2008; Lana-Renault et al., 2007).

The need to monitor the meteorological events and quantify their effects on fluvial forms implies the opportunity of integrating efficient and precise methodologies for the control and study of these processes. The geomorphological dynamics produced in the erosion and sedimentation processes are associated with changes in the trajectory and redistribution of the geological forms present in the channel. To be able to model their behaviour and control the possible adverse effects associated, it is important to develop methodologies that allow their trends to be analysed (González-Hidalgo et al., 2007; García-Ruiz et al., 2013). Geomorphological mapping of river forms and geomorphological units is a useful tool to recognize the evolution, changes and response of ephemeral river adjustments to hydrological events (Ibisate et al., 2021).

Traditionally, these measurement tasks of the study areas have been carried out with topographic instrumentation such as total stations, levels, GPS stations, etc. Employing point-to-point data capture techniques on the ground and complementing the information through photointerpretation of aerial and satellite images (Lee, 2001; Knight et al., 2011). The evolution in measurement systems has made it possible to develop massive information capture instruments with sufficient precision and accuracy to be able to validate the resulting digital models. The emergence of the terrestrial laser scanner (TLS) has allowed us to generate dense point clouds in a short time, collecting detailed information from the measured areas and enabling the generation of true-to-reality digital terrain models in a fast and reliable way (Williams et al., 2011; Heritage and Milan, 2009).

However, the use of these methodologies proposes the survey of areas of reduced extension in each of the field campaigns, and therefore the use of drones is presented as a precise, reliable and very optimal alternative. The use of drones allows us to survey large areas in less time and provides us with a better perspective to analyse the channel behaviour and to carry out this continuous changes and trends monitoring (Wójcik et al., 2019; Flener et al., 2013). In addition, in the case of ephemeral streams, the use of UAVs in the study of the hydromorphological processes is key, due to their intermittent activity and the need for a rapid response to provide with a precise survey.

## 1.2 Permanent streams and riparian forest

The Mediterranean riparian ecosystems are not only constituted by ephemeral and semi-temporary river channels; in many locations we find permanent channels with an intense interaction between the hydrological dynamics, the hydraulic conditions and the riparian and aquatic vegetation. Some variations in the river flow have connections with the development and shaping of riparian vegetation (Rivaes et al., 2013).

The structure of the Mediterranean riparian ecosystem and its lateral and vertical water connections present a direct relation with the distribution of plant communities (Richter et al., 1997). The interrelationship between fluvial geomorphic processes and riparian vegetation dynamics creates topographic diversity, soil moisture gradients, and patches of fluvial disturbance that characterize riparian ecosystems (Merritt et al., 2010).

Traditionally, the study and characterization of the vegetation that develop in the riparian forest has been carried out by means of photointerpretation of aerial images and analysis of multispectral satellite images (Bertoldi et al., 2011; Alexandridis et al., 2008). The constant evolution of technology and sensors has made it possible day by day to improve the spatial resolution of the products obtained, smaller pixel size, improve the temporal resolution of the captured images, allowing continuous monitoring with a shorter time between captures (Huylenbroeck et al., 2020; Kollár et al., 2013).

This evolution of technology has made it possible to improve the analysis and discussion methodologies of the processes at the same time, managing to carry out much more precise characterizations that are faithful to reality. This has made it possible to understand the dynamics that occur in the riparian forest and define techniques and actions that improve the ecological status of these ecosystems and guarantee the correct development and quality of these natural spaces (Rivaes et al., 2013; Akay et al., 2014).

An interesting study on riparian forest dynamics and dynamic modelling was the RIPFLOW Project, whose main objective was the definition of sequences and retrogressions as response to physical parameters in order to simulate the distribution of riparian vegetation over time and space (Garcia-Arias et al., 2011). This model used succession vegetation phases which represent the physiology and phenology evolution in time of the vegetation (Frances, 2009).

Our study has been based on the definition of succession phases for the analysis of the vegetation through remote sensing techniques. Both tools, the RIPFLOW and the CASIMIR-vegetation, based on succession phases, require the development of tools or models that allow automatic classification from remote sensing large areas, applying these works to study areas of greater extension than those used in research projects.

The possibility of classifying the riparian vegetation is considered as a key tool in the study of the riparian habitat (Corbacho et al., 2003) The limitations arisen in this field are largely due to the remote data and the spatial and temporal resolution of such an information. In addition, the ability to provide accurate and reliable information on the characteristics of the land cover is a decisive factor when it comes to understanding the dynamics that develop in these scenarios. In addition to the data, it is necessary to carry out studies and practical cases in different scenarios to understand the potential of existing tools and methodologies and to be able to develop and adapt new techniques.

## 1.3 General characteristics of riparian vegetation in relation to the biogeomorphological succession

The term ecological succession defined by (Clements, 1916) identifies these as plant species that tend to change and their progressive replacement due to the relationships between organisms and the natural space where they are located and develop their life.

Through multiple studies and research in this field, this concept evolved and transformed over the years, adapting to both environmental and physical conditions (Pickett et al., 1989; Tilman, 1990). In general, it is considered that small-scale changes in the environment could cause changes in the trends of the vegetation series and therefore opening the possibility of studying various trends in the successions (Cattelino et al., 1979; Cooper et al., 2003).

Variations in characteristics of the environment such as the topography of the area, the local humidity, the availability, or shortage of nutrients, or in general any type of variation or change over the study area, will affect more or less the autogenic and allogenic drivers developing interactions and modifications in the successional trajectories.

An example of this behaviour is reflected in the scenarios that configure river ecosystems where riparian zones and alluvial plains are defined (Bridge, 2003; Naiman et al., 2005). In these natural spaces, the geomorphology and vegetation tend to support important modifications due to variations in hydrosedimentary dynamics. Due to this behaviour, the types of vegetation present in the area tend to develop adaptation, development and survival strategies in multiple scenarios and space-time scales (Hupp and Osterkamp, 1996; Bornette et al., 2008).

These dynamics and natural processes have motivated various authors such as to deepen and investigate in this area (Corenblit et al., 2009; Corenblit et al., 2007; Gurnell et al., 2016). The definition of phases of the succession of plant species, adapted to the possible hydrogeomorphological and ecological effects, allows us to understand the dynamics that these species are undergoing and to be able to corroborate it with multitemporal field data.

The analysis of the changes in the succession phases from a floristic point of view (Amoros and Wade, 1996) presents certain limitations when it comes to being able to generalize trends and behaviours. Attending to considerations taken based on this

approach, we can observe certain limitations due to local and regional conditions derived from habitat characteristics. For its part, the taxonomy and detailed study of the species does not allow a definitive understanding of the mechanisms of adaptation of the species to the biological processes that they may have undergone.

In the case of riparian environments, there has been a tendency in recent years to monitor and understand the functional changes that vegetation presents and the effects to develop during environmental variations (Aguiar et al., 2018; Stromberg and Merritt, 2016; Garófano-Gómez et al., 2017).

The great variability of species present in most of the riparian ecosystems is difficult to discriminate due to the environmental conditions that develop in these areas, which causes the inclusion and convergence of multiple species with similar traits in equivalent taxa. An example of this process is observed in pioneer riparian plant species that present similar morphological, biomechanical, and life-history attributes, which optimizes their recruitment and establishment (Tabacchi et al., 2019). The recruitment phase consists of the natural regeneration and colonization of plant species in the available spaces within the riparian ecosystem. For its part, the establishment phase is the fixation of these species and their viability to development and growth (Dixon, 2003).

The species that are distributed in different riparian areas may be different, but they occupy a place in a geomorphological and hydrogeomorphological succession phase, such as the recruitment or establishment phase, with similar characteristics. Therefore, it is possible to develop a generic description that serves at the same time for different sites and river basins. Then, a great advantage of the succession phase approach is that we can make an analogy even if the species are different instead of site-specific features. This permits worldwide application and eliminates divergences (e.g. species composition, ecoregion differences) that make generalized application unfeasible in many other models (Rivaes et al., 2014).

A relevant recent study by Tabacchi et al. (2019) has developed the definition of the succession phases based on the characteristic features or traits of the riparian plants. In this work, two phases of the vegetation succession have been defined: the biogeomorphological successional phase (B) and the ecological phase (E). According to the proposed model, the plant communities in phase B are mainly characterized by pioneering herbaceous and woody species capable of resisting floods (resistant strategy) and colonizing flood-disturbed areas (resilient strategy). These communities tend to fix and stabilize sediment loads with variable textures according to the intensity of the process along the successional gradient. The variations produced in this phase of succession are more or less reversible depending on the degree of connection with the hydrogeomorphological alteration.

In the second successional phase (E), the drivers of the community (the main processes) are biotic interactions such as facilitation, tolerance, interspecific competition, or herbivory. This phase with such processes dominates in higher areas with less flooding, and the plant communities are mainly competitive species. In general, only exceptional floods of great magnitude can reverse this phase.

This approach of succession phases has been used in the RIPFLOW model as well as in other studies (Tabacchi et al., 2019; Corenblit et al., 2007; Rivaes et al., 2013),

facilitating the comparison between different countries and characterizing in a generic way the succession phases in the different riparian ecosystems.

The use of succession phases facilitates the analysis of the succession/retrogression of riparian plant communities in different hydrological scenarios. In addition, it facilitates the analyses of results with a large amount of spatio-temporal information that can be very useful in decision-making, and the comparison between different management hypotheses of these ecosystems (Garcia-Arias et al., 2011).

In addition, the succession phase approach allows us the conceptual modelling of life-cycle dynamics and the analysis of how vegetation evolves and takes different paths and scenarios (Corenblit et al., 2007), thus presenting itself as a study and research line with many possibilities and alternatives in its future application.

## 1.4 Objectives and structure of the thesis

This thesis has the general aim of developing methodologies for the characterization and study of the riparian ecosystem, from the geomorphological and ecological perspective, oriented to their practical application in river research and management. In all the case studies, the scenarios to carry out the experimental developments were Mediterranean riparian ecosystems.

This general aim comprised four phases, corresponding to four general objectives, as I explain here:

- The geomorphological characterization of ephemeral rivers and the characterization of their fluvial forms to assess the event-scale sediment budget, using techniques of remote sensing and data collected with terrestrial laser scanner (TLS) and unmanned aerial vehicles (UAVs).

- Spatially-explicit analysis of stream power and transport efficiency in accordance with the areas of erosion and deposition, in multitemporal studies in ephemeral rivers, using TLS and UAV and comparing this two methodologies.

- Development of an algorithm and a tool (coding in C++) to develop 3D models of the submerged morphology in rivers using UAVs techniques, in order to make point-by-point correction of the refraction effect of water. This algorithm allows the extraction of hydraulic characteristics such as depth and river cross sections in permanent rivers under certain conditions.

- Analysis and comparison of mathematical models for the classification of riparian vegetation according to its succession phases in a natural environment, from a multispectral satellite image (QuickBird©). Such classification is relevant to develop dynamic models of riparian vegetation in ample and representative river segments.

To achieve these four objectives, this doctoral thesis is configured in several chapters, and each of them is structured in the format of a scientific article. For each of them, the study area and its characteristics, the methods used, and the results are

explained, to later discuss those results and draw conclusions from the methodology and workflow developed. Here below, a summary of each of the chapters is described.

Chapter 2: Combining Structure from Motion (SfM) photogrammetry and Terrestrial Laser Scanning to Assess Event-Scale Sediment Budgets along a Gravel-Bed Ephemeral Stream. The power of the flow along the river streams is directly related to the rate of energy expenditure associated with that river flow. Being able to calculate this information through reliable and precise topographic data is very important for the correct morphological characterization of the riverbed. In this chapter, we wanted to quantitatively relate the morphological variations in an ephemeral stream of gravel bed, the Rambla de la Azohía, with the gradients of power, critical power and energy, along a series of study sections. For this, high resolution digital terrain models were used, combined with orthophotographs and 3D point clouds in the period 2018-2020. These products were developed from terrestrial laser scanner techniques and UAV flights. With the proposed work, it was possible to estimate the spatial variability of the sediments and evaluate the mobility of the channel riverbed during the study period at different spatial scales. This article was published in **Remote Sensing** 2020, 12, 3624; doi: 10.3390 / rs12213624.

Chapter 3: Stream power and morphological bed changes in an ephemeral channel. The deposition and removal of sediments and the geomorphological dynamics in streams have a direct relationship with the velocity and power of the river flows. Therefore, the stream power causes local spatial variations in the erosion and deposition, and also depends on the quantity and frequency of events over time. This dependence on isolated and discrete events makes their analysis and study complex. This chapter aims to quantitatively analyse the relationship between morphological processes and the stream power in some reference sections in the Rambla de la Azohia in the period 2018-2020. To carry out this study, high resolution digital terrain models were used in combination with aerial images and 3D point clouds. The process of generating these cartographic products was based on two different techniques: terrestrial laser scanning and UAV flights. From the combination of these two technologies, we estimated the spatial variability of the sediments and the mobility of the stream bed as a function of the events that took place in that time period. This article has been accepted for publication in the international journal **Geomorphology**.

Chapter 4: Spatial validation of submerged fluvial topographic models by mesohabitat units. The management of river systems requires to a large extent the characterization and mapping of the morphology of the river bed, in order to analyse the processes and trends that are developed and to be able to design river restoration projects with accurate information. Therefore, to make 3D models of the river bed, it is necessary to consider the effect of water refraction, if remote sensing techniques are to be applied. Traditionally, remote sensing techniques have required a high cost in time and risk for the technicians due to the access and travel along these natural areas. At present, the appearance of detection and determination systems for topobathymetric light and images captured from UAVs are becoming promising and effective topographic methodologies. The use of this type of aircrafts, together with advanced photogrammetric processing techniques, provide with a novel and high-resolution approach to modelling underwater river morphology. This chapter is an extension of this article published in an international congress: DEM generation in a Mediterranean river using structure from motion algorithm on HD video

recorded from a UAV (Palancia River, Spain), International Symposium and Exhibition on Hydro-Environment Sensors and Software (HydroSenSoft 2017), ISBN/ISSN 978-90-824846-2-5. Also this complete article was published by **The International Journal of Remote Sensing** 2020, VOL. 42, NO. 7, 2391-2416; doi: 10.1080 / 01431161.2020.1862433

Chapter 5: Classification of riparian vegetation types based on supervised classification algorithms. A case study in a Serpis River segment (Valencia). The development of methodologies for the classification of riparian vegetation types is very important to model the trends and dynamics that take place in the riparian ecosystem and its evolution throughout the years and in response to hydrological alteration. The main objective of this work was to analyse and compare different classification models and their validity in the automatic classification of vegetation succession phases over a specific study area of the Serpis River (Valencia). This vegetation succession phases were based on those used in the dynamic simulation model RIPFLOW. For this, different methods of classification were used on QuickBird© satellite images, such as minimum distance, maximum likelihood, parallelepiped, Mahalanobis distance, and neural networks in three cases. This chapter is an extension of this article published in an international congress: Caracterización de vegetación riparia aplicando algoritmos de clasificación supervisada. Caso de estudio Río Serpis (Valencia). Pp. 797-804 in RESTAURARIOS, III Congreso Ibérico de Restauración Fluvial. Actas del Congreso. ISBN: 978-84-09-11806-9.

## 1.5 References


Aguiar, F. C., Segurado, P., Martins, M. J., Bejarano, M. D., Nilsson, C., Portela, M. M. and Merritt, D. M., 2018. "The abundance and distribution of guilds of riparian woody plants change in response to land use and flow regulation". Journal of Applied Ecology, 55(5), 2227–2240. https://doi.org/10.1111/1365-2664.13110

Akay, A. E., Sivrikaya, F. and Gulci, S., 2014. "Analyzing Riparian Forest Cover Changes along the Firniz River in the Mediterranean City of Kahramanmaras in Turkey." Environmental Monitoring and Assessment 186 (5): 2741–2747. doi:10.1007/s10661-013-3575-7.

Alba-Tercedor, J., Jaímez-Cuéllar, P., AÍvarez, M., Avileś, J., Bonada, N., Casas, J. and Mellado, A., 2002. "Caracterización Del Estado Ecológico de Ríos Mediterráneos Ibéricos Mediante El Índice IBMWP (Antes BMWP')." Limnetica 21 (3–4): 175–185.

Alexandridis, T. K., Zalidis, G.C. and Silleos, N.G., 2008. "Mapping Irrigated Area in Mediterranean Basins Using Low Cost Satellite Earth Observation." Computers and Electronics in Agriculture 64 (2): 93–103. doi:10.1016/j.compag.2008.04.001.

Amoros, C. and Wade, P. M., 1996. "Ecological successions". In G. E. Petts, & C. Amoros (Eds.), The fluvial hydrosystems (pp. 211–241). London: Chapman & Hall.

Bendix, J., 1998. "Impact of a flood on southern California riparian vegetation". Physical Geography 19, 162–174.

Bennett, S. J. and Simon, A., 2013. "Riparian Vegetation and Fluvial Geomorphology." Riparian Vegetation and Fluvial Geomorphology 14: 277–295. doi:10.1029/WS008.

Bertoldi, W., Drake, N. A. and Gurnell, A. M., 2011. "Interactions between River Flows and Colonizing Vegetation on a Braided River: Exploring Spatial and Temporal Dynamics in Riparian Vegetation Cover Using Satellite Data." Earth Surface Processes and Landforms 36 (11): 1474–1486. doi:10.1002/esp.2166.

Bornette, G., Tabacchi, E., Hupp, C., Puijalon, S. and Rostan, J. C., 2008. "A model of plant strategies in fluvial hydrosystems". Freshwater Biology, 53(8), 1692–1705. https://doi.org/10.1111/j.1365-2427.2008.01994. X

Bridge, J. S., 2003. "Rivers and floodplains: Forms, processes, and sedimentary record." Malden, USA: Blackwell.

Cattelino, P. J., Noble, I. R., Slatyer, R. O. and Kessell, S. R., 1979. "Predicting the multiple pathways of plant succession". Environmental Management, 3(1), 41–50. https://doi.org/10.1007/BF01867067

Clements, F. E., 1916. "Plant succession. An analysis of the development of vegetation". Washington: Carnegie Institution of Washington. https://doi.org/10.5962/bhl.title.56234

Conesa-García, C., Pérez-Cutillas, P., García-Lorenzo, R., Eekhout, J., Gómez-Gutiérrez, A., Millares-Valenzuela, A. and Martínez-Salvador, A., 2020. "Dimensionless Morphological Ratios versus Stream Power Variations at Bankfull Stage in an

Ephemeral Channel." Geomorphology 361. doi:10.1016/j.geomorph.2020.107199.

Cooper, D. J., Andersen, D. C. and Chimner, R. A., 2003. "Multiple pathways for woody plant establishment on floodplains at local to regional scales". Journal of Ecology, 91(2), 182–196. https://doi.org/10.1046/j.1365- 2745.2003.00766.x

Corbacho, C., Sánchez, J.M. and Costillo, E., 2003. "Patterns of Structural Complexity and Human Disturbance of Riparian Vegetation in Agricultural Landscapes of a Mediterranean Area." Agriculture, Ecosystems and Environment 95 (2–3): 495–

Corenblit, D., Steiger, J., Gurnell, A. M., Tabacchi, E. and Roques, L., 2009. "Control of sediment dynamics by vegetation as a key function driving biogeomorphic succession within fluvial corridors." Earth Surface Processes and Landforms, 34(13), 1790–1810. https://doi.org/10.1002/esp.1876

Corenblit, D., Tabacchi, E., Steiger, J. and Gurnell, A. M., 2007. "Reciprocal interactions and adjustments between fluvial landforms and vegetation dynamics in river corridors: A review of complementary approaches". Earth-Science Reviews, 84(1–2), 56–86. https://doi.org/10.1016/j.earscirev.2007.05.004

Corenblit, D., 2006. "Structure et dynamique du paysage fluvial: étudedes rétroactions entre processus hydro-géomorphologiques etdynamique de la végétation du Tech (Pyrénées orientales)".Unpublished Ph.D. Thesis, University Paul Sabatier, ToulouseIII, France

Corenblit, D., Steiger, J., Gurnell, A.M. and Tabacchi, E., 2007. "Darwinian origin of landforms". Earth Surface Processes and Landforms 32: 2070–2073

Corenblit, D., Gurnell, A.M., Steiger, J. and Tabacchi, E., 2008. "Reciprocal adjustments between landforms and living organisms: extended geomorphic evolutionary insights". Catena 73: 261–273

Dixon, M. D., 2003. "Effects of Flow Pattern of Riparian Seedling Recruitment on Sandbars in the Wisconsin River, Wisconsin, USA." Wetlands 23 (1): 125–139. doi:10.1672/0277-5212

Dufour, S., Bernez, I., Betbeder, J., Corgne, S., Hubert-Moy, L., Nabucet, J., Rapinel, S., Sawtschuk, J. and Trollé, C., 2013. "Monitoring Restored Riparian Vegetation: How Can Recent Developments in Remote Sensing Sciences Help?" Knowledge and Management of Aquatic Ecosystems, no. 410: 10. doi:10.1051/kmae/2013068.

Džubáková, K., Molnar, P., Schindler, K. and Trizna, M., 2015. "Monitoring of Riparian Vegetation Response to Flood Disturbances Using Terrestrial Photography." Hydrology and Earth System Sciences 19 (1): 195–208. doi:10.5194/hess-19-195-2015.

Flener, C., Vaaja, M., Jaakkola, A., Krooks, A., Kaartinen, H., Kukko, A., Kasvi, E., Hyyppä, H., Hyyppä, J. and Alho, P., 2013. "Seamless Mapping of River Channels at High Resolution Using Mobile LiDAR and UAV-Photography." Remote Sensing 5 (12): 6382–6407. doi:10.3390/rs5126382.

Francés, F., (2009). "RIPFLOW project description". Second Trans-European Water Research Management Conference, Bridging the Sci-Pol gap. Bruselas (Bélgica).

Garcia-Arias, A., Frances, F., Andrés-Domenech, I., Vallés, F., Garófano-Gómez, V. and

Martinez-Capel, F., 2011. “Modelación Dinámica de La Vegetación de Ribera. Calibración Del Modelo RIPFLOW y Su Aplicación En Escenarios de Regulación de Caudales.”

García-Ruiz, J. M., Nadal-Romero, E., Lana-Renault, N. and Beguería, S., 2013. “Erosion in Mediterranean Landscapes: Changes and Future Challenges.” Geomorphology 198. Elsevier B.V.: 20–36. doi:10.1016/j.geomorph.2013.05.023.

Garófano-Gómez, V., Metz, M., Egger, G., Díaz-Redondo, M., Hortobágyi, B., Geerling, G., Corenblit, D. and Steiger, J., 2017. “Vegetation Succession Processes and Fluvial Dynamics of a Mobile Temperate Riparian Ecosystem: The Lower Allier River (France).” Http://Journals.Openedition.Org/Geomorphologie 23 (vol. 23-n° 3). Groupe français de géomorphologie: 187–202. doi:10.4000/GEOMORPHOLOGIE.11805.

Gasith, A. and Resh, V.H., 1999. “Streams in mediterranean climate regions: Abiotic Influences and Biotic Responses to Predictable Seasonal Events”. Annual Review of Ecological Systems 30: 51–81

González-Hidalgo, J. C., Peña-Monné, J.L. and de Luis, M., 2007. “A Review of Daily Soil Erosion in Western Mediterranean Areas.” Catena 71 (2): 193–199. doi:10.1016/j.catena.2007.03.005.

Greet, J., Webb, J.A. and Cousens R.D., 2011. “The Importance of Seasonal Flow Timing for Riparian Vegetation Dynamics: A Systematic Review Using Causal Criteria Analysis.” Freshwater Biology 56 (7): 1231–1247. doi:10.1111/j.1365-2427.2011.02564.x.

Gregory, S. V., Swanson, F.J., McKee, W.A. and Cummins, K.W., 1991. “An Ecosystem Perspective of Riparian Zones.” BioScience 41 (8): 540–551. doi:10.2307/1311607.

Gurnell, A. M., Corenblit, D., García de Jalón, D., González del Tánago, M., Grabowski, R. C., O'Hare, M. T. and Szewczyk, M., 2016. “A conceptual model of vegetation–hydrogeomorphology interactions within river corridors”. River Research and Applications, 32(2), 142–163. https://doi.org/10.1002/rra.2928

Gurnell, A.M. and Petts, G.E., 2006. “Trees as riparian engineers: theTagliamento River, Italy”. Earth Surface Processes and Landforms31, 1558–1574

Heritage, G. L., and Milan, D.J., 2009. “Terrestrial Laser Scanning of Grain Roughness in a Gravel-Bed River.” Geomorphology 113 (1–2). Elsevier B.V.: 4–11. doi:10.1016/j.geomorph.2009.03.021.

Hupp, C. R. and Osterkamp, W.R., 1996. “Riparian Vegetation and Fluvial Geomorphic Processes.” Geomorphology 14 (4 SPEC. ISS.). Elsevier: 277–295. doi:10.1016/0169-555X(95)00042-4.

Huylenbroeck, L., Laslier, M., Dufour, S., Georges, B., Lejeune, P. and Michez, A., 2020. “Using Remote Sensing to Characterize Riparian Vegetation: A Review of Available Tools and Perspectives for Managers.” Journal of Environmental Management 267 (March). Elsevier Ltd: 110652. doi:10.1016/j.jenvman.2020.110652.

Ibisate, A., Ollero, A., García, J. H., Ortiz Martínez de Lahidalga, J., Sáenz de

Olazagoitia, A., Hermoso, Y., Conesa-García, C. and Gómez-Gutiérrez, A., 2021. "Geomorphological evolution of ephemeral rivers through historical and UAVs images". EGU General Assembly 2021, online, 19–30 Apr 2021, EGU21-6012, https://doi.org/10.5194/egusphere-egu21-6012, 2021.

Knight, J., Mitchell, W.A. and Rose, J., 2011. "Geomorphological Field Mapping. Developments in Earth Surface Processes". Vol. 15. Elsevier B.V. doi:10.1016/B978-0-444-53446-0.00006-9.

Kollár, S., Vekerdy, Z. and Márkus, B., 2013. "Aerial Image Classification for the Mapping of Riparian Vegetation Habitats." Acta Silvatica et Lignaria Hungarica 9 (1): 119–133. doi:10.2478/aslh-2013-0010.

Lana-Renault, N, Latron, J. and Regüés, D., 2007. "Streamflow Response and Water-Table Dynamics in a Sub-Mediterranean Research Catchment (Central Pyrenees)." Journal of Hydrology 347 (3–4): 497–507. doi:10.1016/j.jhydrol.2007.09.037.

Latron, J. and Gallart, F., 2008. "Runoff Generation Processes in a Small Mediterranean Research Catchment (Vallcebre, Eastern Pyrenees)." Journal of Hydrology 358 (3–4): 206–220. doi:10.1016/j.jhydrol.2008.06.014.

Lee, E. M., 2001. "Geomorphological Mapping." Geological Society Special Publication 18 (1). Geological Society of London: 53–56. doi:10.1144/gsl.eng.2001.018.01.08.

Martínez-Fernández, V., Van Oorschot, M., De Smit, J., González del Tánago, M. and Buijse, A.D., 2018. "Modelling Feedbacks between Geomorphological and Riparian Vegetation Responses under Climate Change in a Mediterranean Context." Earth Surface Processes and Landforms 43 (9): 1825–1835. doi:10.1002/esp.4356.

Merritt, D.M., Scott, M.L., Poff, L.N., Auble, G.T. and Lytle, D.A., 2010. "Theory, methods and tools for determining environmental flows for riparian vegetation: riparian vegetation-flow response guilds". Freshwater Biology 55: 206–225. DOI: 10.1111/j.1365-2427.2009.02206.x.

Munné, A. and Prat, N., 2011. "Effects of Mediterranean Climate Annual Variability on Stream Biological Quality Assessment Using Macroinvertebrate Communities." Ecological Indicators 11 (2): 651–662. doi:10.1016/j.ecolind.2010.09.004.

Naiman, R. J., Décamps, H. and McClain, M. E., 2005. "Catchments and the physical template". In Riparia: Ecology, conservation, and management of streamside communities (pp. 19-48).

Naiman, R. J., Décamps, H. and Pollock, M., 1993. "The Role of Riparian Corridors in Maintaining Regional Biodiversity." Ecological Applications 3 (2). Wiley: 209–212. doi:10.2307/1941822.

Naiman, R.J. and Décamps, H., 1997. "The ecology of interfaces, riparian zones". Annual Review of Ecology and Systematics 28, 621–658.

Perucca, E., Camporeale, C. and Ridolfi, L., 2007. "Significance of the Riparian Vegetation Dynamics on Meandering River Morphodynamics." Water Resources Research 43 (3): 1–10. doi:10.1029/2006WR005234.

Pickett, S. T. A., Kolasa, J., Armesto, J. and Colins, S. L., 1989. "The ecological concept

of disturbance and its expression at various hierarchical levels". Oikos, 54, 129–136. https://doi.org/10.2307/3565258

Pollock, M. M., Naiman, R.J. and Hanley, T.A., 1998. "Plant Species Richness in Riparian Wetlands-a Test of Biodiversity Theory." Ecology 79 (1): 94–105. doi:10.1890/0012-9658(1998)079[0094:PSRIRW]2.0.CO;2.

Richter, B.D., Baumgartner, J.V. and Wigington, R., 1997. "How much water does a river need?". Freswater Biology 37: 231–249.

Rivaes, R., Rodríguez-González, P.M., Albuquerque, A., Pinheiro, A.N., Egger, G. and Ferreira, M.T., 2013. "Riparian Vegetation Responses to Altered Flow Regimes Driven by Climate Change in Mediterranean Rivers." Ecohydrology 6 (3): 413–424. doi:10.1002/eco.1287.

Rivaes, R., Rodríguez-González, P. M., Ferreira, M. T., Pinheiro, A. N., Politti, E., Egger, G., García-Arias, A. and Francés, F., 2014. "Modeling the Evolution of Riparian Woodlands Facing Climate Change in Three European Rivers with Contrasting Flow Regimes." Public Library of Science. doi:10.1371/journal.pone.0110200.

Samani, J.M.N. and Kouwen, N., 2002. "Stability and erosion in grassedchannels". Journal of Hydraulic Engineering, vol. 128. AmericanSociety of Civil Engineers, pp. 40–45.

Segura-Beltrán, F. and Sanchis-Ibor, C., 2013. "Assessment of Channel Changes in a Mediterranean Ephemeral Stream since the Early Twentieth Century. The Rambla de Cervera, Eastern Spain." Geomorphology 201. Elsevier B.V.: 199–214. doi:10.1016/j.geomorph.2013.06.021.

Steiger, J., Tabacchi, E., Dufour, S., Corenblit, D. and Peiry, J.L., 2005. "Hydrogeomorphic processes affecting riparian habitat withinalluvial channel-floodplain river systems, a review for thetemperate zone". River Research and Applications 21, 719–737

Stella, J. C., Riddle, J., Piégay, H., Gagnage, M. and Trémélo, M.L., 2013. "Climate and Local Geomorphic Interactions Drive Patterns of Riparian Forest Decline along a Mediterranean Basin River." Geomorphology. doi:10.1016/j.geomorph.2013.01.013.

Stella, J. C., Rodríguez-González, P.M., Dufour, S. and Bendix, J., 2013. "Riparian Vegetation Research in Mediterranean-Climate Regions: Common Patterns, Ecological Processes, and Considerations for Management." Hydrobiologia 719 (1): 291–315. doi:10.1007/s10750-012-1304-9.

Stromberg, J. C. and Merritt, D. M., 2016. "Riparian plant guilds of ephemeral, intermittent and perennial rivers". Freshwater Biology, 61(8), 1259–1275. https://doi.org/10.1111/fwb.12686

Tabacchi, E., Planty-Tabacchi, A.M., Roques, L. and Nadal, E., 2005. "Seed inputs in riparian zones: implications for plant invasion". River Research and Applications 21, 299–313.

Tabacchi, E., Correll, D.L., Hauer, R., Pinay, G., Planty-Tabacchi, A.M. and Wissmar, R.C., 1998. "Development, maintenance and role ofriparian vegetation in the river landscape". Freshwater Biology 40,497–516

Tabacchi, E., González, E., Corenblit, D., Garófano-Gómez, V., Planty-Tabacchi, A. M. and Steiger, J., 2019. “Species Composition and Plant Traits: Characterization of the Biogeomorphological Succession within Contrasting River Corridors.” River Research and Applications 35 (8): 1228–1240. doi:10.1002/rra.3511.

Tilman, D., 1990. “Constraints and tradeoffs: Toward a predictive theory of competition and succession”. Oikos, 58(1), 3–15. https://doi.org/ 10.2307/3565355

Tockner, K. and Ward, J.V., 2001. “Biodiversity along Riparian Corridors.” SIL Proceedings, 1922-2010 27 (7): 3981–3981. doi:10.1080/03680770.1998.11901742.

Vesipa, R., Camporeale, C. and Ridolfi, L., 2017. “Effect of River Flow Fluctuations on Riparian Vegetation Dynamics: Processes and Models.” Advances in Water Resources. doi:10.1016/j.advwatres.2017.09.028.

Viles, H.A., Naylor, L.A., Carter, N.E.A. and Chaput, D., 2008. “Biogeomor- phological disturbance regimes: progress in linking ecological and geomorphological systems”. Earth Surface Processes and Landforms 33: 1419–1435.

Williams, R., Brasington, J., Vericat, D., Hicks, M., Labrosse, F. and Neal, M., 2011. “Monitoring Braided River Change Using Terrestrial Laser Scanning and Optical Bathymetric Mapping”. Developments in Earth Surface Processes. Vol. 15. Elsevier B.V. doi:10.1016/B978-0-444-53446-0.00020-3.

Wójcik, A., Klapa, P., Mitka, B. and Piech, I., 2019. “The Use of TLS and UAV Methods for Measurement of the Repose Angle of Granular Materials in Terrain Conditions.” Measurement: Journal of the International Measurement Confederation. doi:10.1016/j.measurement.2019.07.015.

Yen, B.C., 2002. “Open channel flow resistance”. Journal of Hydraulic Engineering, vol. 128. American Society of Civil Engineers, pp. 20–39.

# 2. Combining SfM photogrammetry and Terrestrial Laser Scanning to assess event-scale sediment budgets along a gravel-bed ephemeral stream


## Abstract

Stream power represents the rate of energy expenditure along a stream flow and can be calculated using topographic data acquired via SfM photogrammetry and Terrestrial Laser Scanning. This study sought to quantitatively relate morphological adjustments in the Azohía Rambla, a gravel-bed ephemeral stream in southeastern Spain, to stream power gradients along different reference channel reaches of 200 to 300 m in length. High-Resolution Digital Terrain Models (HRDTM), combined with ortophotographs and point clouds from 2018, 2019, and 2020, and ground-based surveys, were used to estimate the spatial variability of morphological sediment budgets and to assess channel bed mobility during the study period at different spatial scales: reference channel reaches (RCR), pilot bed survey areas (PBSA), and representative geomorphic units (RGU).The optimized complementary role of the SfM technique and TLS allowed the generation of accurate and reliable HRDTM, upon which 1D hydrodynamic models were calibrated and sediment budgets calculated. The resulting high-resolution maps allowed a spatially-explicit analysis of stream power and transport efficiency in relation to volumes of erosion and deposition in the RCR and PBSA. In addition, net incision or downcutting and vertical sedimentary accretion were monitored for each flood event in relation to bedforms and hydraulic variables. Sediment sources and sinks and bed armoring processes showed different trends according to the critical energy and power gradient, which were verified from field observations.



**Keywords:** SfM Photogrammetry, Terrestrial Laser Scanning, stream power, morphological sediment budget, bedforms, gravel-bed ephemeral channel, southeastern Spain.

## 2.1 Introduction

Ephemeral streams are dry, irregular, and often unpredictable watercourses, particularly sensitive to short-term climatic changes and to human impacts. Consequently, their response can be highly variable, ranging from slight river-bed adjustments (Segura-Beltrán and Sanchis-Ibor, 2013) to overall changes in channel geometry after flash floods (Conesa-García, 1995; Sutfin et al., 2014; Norman et al., 2017). This type of streams is found in large areas around the world, in arid and semi-arid environments, where quite fragile hydromorphological systems often form, subjected to a metastable dynamic equilibrium that strongly depends on the frequency and magnitude of floods. During periods of relatively more frequent and lower magnitude peak flows, surface bed washing and downcutting phenomena can produce secondary channels, lateral erosion, and partial destruction of low bars (Graf, 1988). Infrequent and large floods affect the entire main channel, modifying its global geometry, and create prominent features of aggradation and incision, depending on the bed materials (Conesa, 1995).

Although ephemeral streams tend to maintain similar flow characteristics over long periods of time (Bull and Kirkby, 2002), there are semi-arid Mediterranean areas whose dry and intermittent streams are being subjected to the effects of the current climate change and have begun to show signs of relatively rapid geomorphic adjustment. A clear example of this is the coastal drainage system in southeastern Spain, mainly composed of ephemeral gravel-bed streams (EGBS). These ephemeral channels usually transport a high tractive load from heavily weathered headwater areas and alluvial channel banks, producing an abundant amount of coarse sediment (gravel and pebbles). In general, they are channels with a high width-to-depth ratio, which, except in sections of structural geological control, run through poorly consolidated alluvial formations, showing great dynamism and instability. Their upper reaches dissect steep alluvial fans, giving rise to entrenched and deep channels subjected to downcutting and basal erosion, which cause frequent breaks and collapses of material. In addition, downstream, these EGBS experience channel widening, aggradation and bed armoring (Török et al., 2017). As a result, the streambed often is very permeable, so flood peak discharges decrease sharply downstream due to transmission losses (Goodrich et al., 1997; Shaw and Cooper, 2008). Due to high infiltration rates, incision and transport capacity decrease, while vegetation tends to grow locally on stable bars and subsurface moisture storage increases, promoting positive feedback for instream aggradation (Meritt and Wohl, 2003; Camporeale et al., 2006; Reid and Frostick, 2011). Downstream, alluvium within the channel increases in thickness and smooths the bed slope, creating a channel profile that is straighter than concave, unlike in perennial rivers (Martín-Vide, 1997; Chen et al., 2019).

The scientific literature on spatial morphological variability in EGBS in relation to erosion volumes, deposition, and sediment transport (sediment budget) on a detailed scale is scarce. Recently, high resolution techniques, such as Structure-from-Motion (SfM) photogrammetry and Terrestrial Laser Scanning (TLS), have been tested to evaluate morphological adjustments in ephemeral streams (Brasington et al., 2012; Picco et al., 2013; Calle et al., 2018; Flatley and Rutherfurd, 2018; Galea et al., 2019).

In this paper we propose an approach to assess the event-scale sediment budget along an ephemeral gravel-bed channel, that couples the results of the Structure-from-Motion Multi-View Stereo (SfM-MVS) and TLS techniques. The use of SfM-MVS in a low-altitude unmanned aerial vehicle (UAV) allows the development of orthomosaics and

high-resolution digital elevation models (<5 cm per pixel) (Clapuyt et al., 2016; Marteau et al., 2017). This survey product offers significantly better resolution and much lower processing costs than others generated by traditional imaging platforms, such as satellites or aircraft (Remondino et al., 2011; Shintani and Fonstad, 2017; Legleiter and Harrison, 2019; Tonina et al., 2019). In geomorphological studies, UAV technology has already been applied to monitor fluvial system changes and dynamics (Mosbrucker et al., 2017; Salmela et al., 2020; Rowley et al., 2020). The high temporal resolution offered by UAV allows assessment of the rapid evolution of river ecosystems. The UAV-SfM technique, when compared to traditional photogrammetry and other topographic surveying approaches (e.g., total station and DGPS), has proven to be particularly effective for the detection of channel morphological changes (Cook, 2017; Vázquez-Tarrío et al., 2017; Conesa-García et al., 2019).

Laser scanning is a land surveying technique that accurately measures and collects millions of points in a few minutes, providing geometrical information from a scene by precisely measuring the time-of-flight of laser beams. A laser scanner device can be mounted on moving vehicles, such as UAVs or ground-based vehicles (for TLS). The 3D point cloud (3DPC) datasets obtained from these techniques have usually exploited geometrical features identification and extraction, providing unlimited possibilities in geomorphology and, more specifically, in fluvial geomorphology (Clapuyt et al., 2016; French, 2003; Heritage and Hetherington, 2007; Notebaert et al., 2007).

In order to estimate the morphological sediment budgets in EGBS three analyses were performed using SfM-MVS and TLS, as follows: 1) An analysis of hydraulic variables at the cell scale was performed for the flash floods under study, based on rasterized information from cross-section data and using 1D hydrodynamic modeling and High-resolution Digital Terrain Models (HRDTM); 2) Erosion and deposition values and net sediment budgets were extracted from datasets of SfM and TLS for periods with different numbers and magnitudes of events; 3) The 3DPC datasets were used to calculate a set of statistical parameters, regarding elevation and volume differences after each event in reference channel reaches (RCR), pilot bed survey areas (PBSA), and representative geomorphic units (RGU).

The paper is organized as follows. Section 2 describes the study areas and the field surveys performed. The methodology adopted is outlined in Section 3. The main results are presented and discussed in Section 4, and Section 5 comprises the conclusions.

## 2.2 Study area and field surveys

The SfM and TLS surveys were carried out in the Rambla de la Azohía, located in southeastern Spain (Region of Murcia) (Figure 2.1). The area drained by this ephemeral stream and its tributaries is relatively small (13 $km^2$), to the point that it could be completely covered by a single storm. The climate of the study area presents strong seasonal contrasts, with extreme droughts and monthly ETP values higher than 140 mm in the summer season. These conditions, together with a scarce vegetation cover and very irregular and intense rains, with records above 50 mm/h, often cause large flash floods (Ortega et al., 2014). This watercourse is part of a littoral hydrological system made up of numerous ephemeral gravel-bed channels, draining directly into the Mediterranean Sea. Steep slopes modeled on metamorphic, poorly permeable materials (mainly phyllites, schists, and quartzites), subjected to intense weathering, constitute an important

source of sediments and ensure the supply of coarse particles to the channel when heavy rains occur. As a result of this, the Rambla de la Azohía exhibits a particularly active morphodynamics, ranging from minor bed alterations to large morphological channel changes.

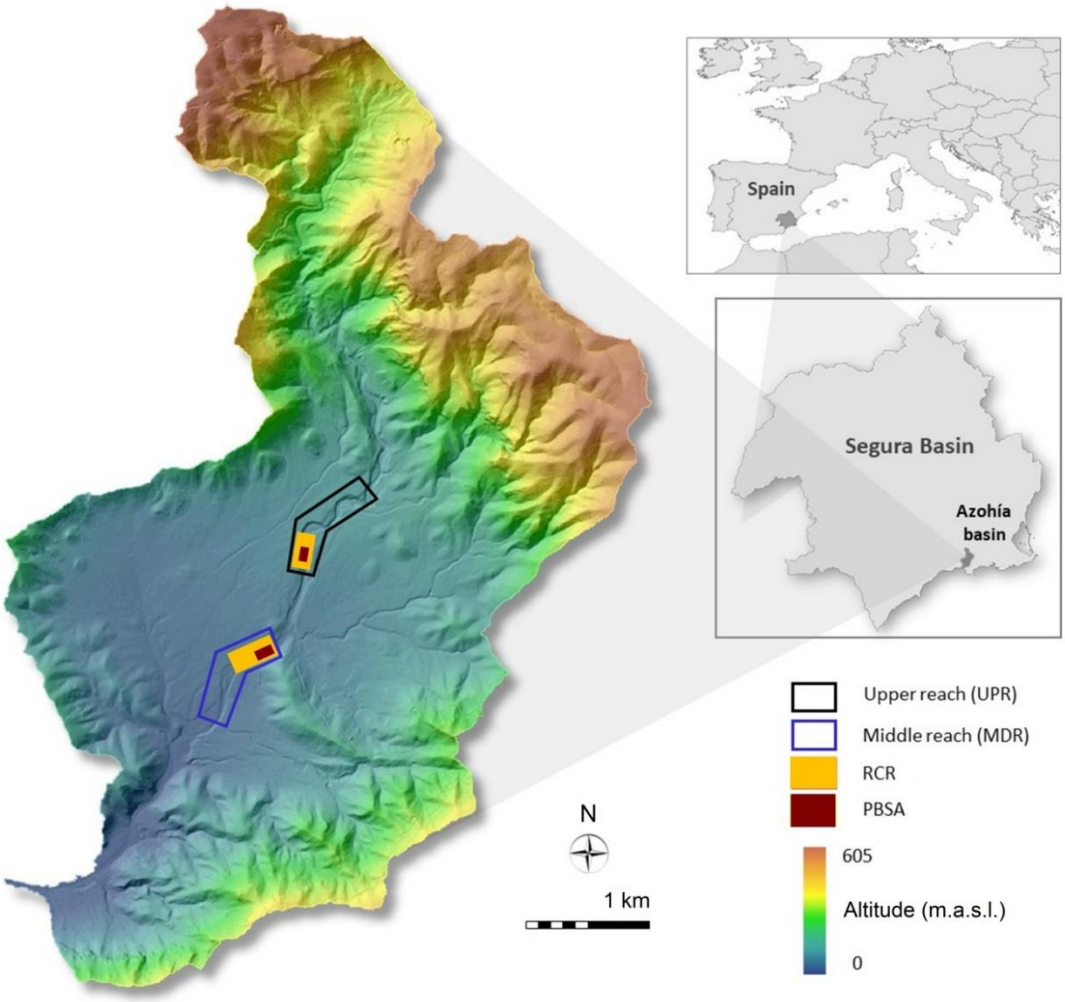


**Figure 2.1.** Study area and location of the different channel stretches monitored by UAV-SfM and TLS during the period September 2018 to January 2020.

The first two flow events of the analysis period (November 18, 2018 and April 19-20, 2019) were monitored by UAV and TLS, covering survey areas with different extensions (Figure 2.1). The UAV-SfM of September 2018 covered a wide area (> 600 m in length) along the upper, middle and lower sections of the study stream, while the TLS only comprised the RCR, upper (UPR) and middle (MDR) shortened reaches (<200 m long), and their respective PBSA within them. After the aforementioned peak flows, a date and common study area were chosen to carry out both SfM-MVS and TLS, in order to obtain the same georeferencing, compare the associated errors, and analyze the possibility of the complementary optimal use in time of both techniques. In fact, the morphological changes produced after the peak flows of September 12-13 and December 2, 2019 were only detected by TLS (Figure 2.2).

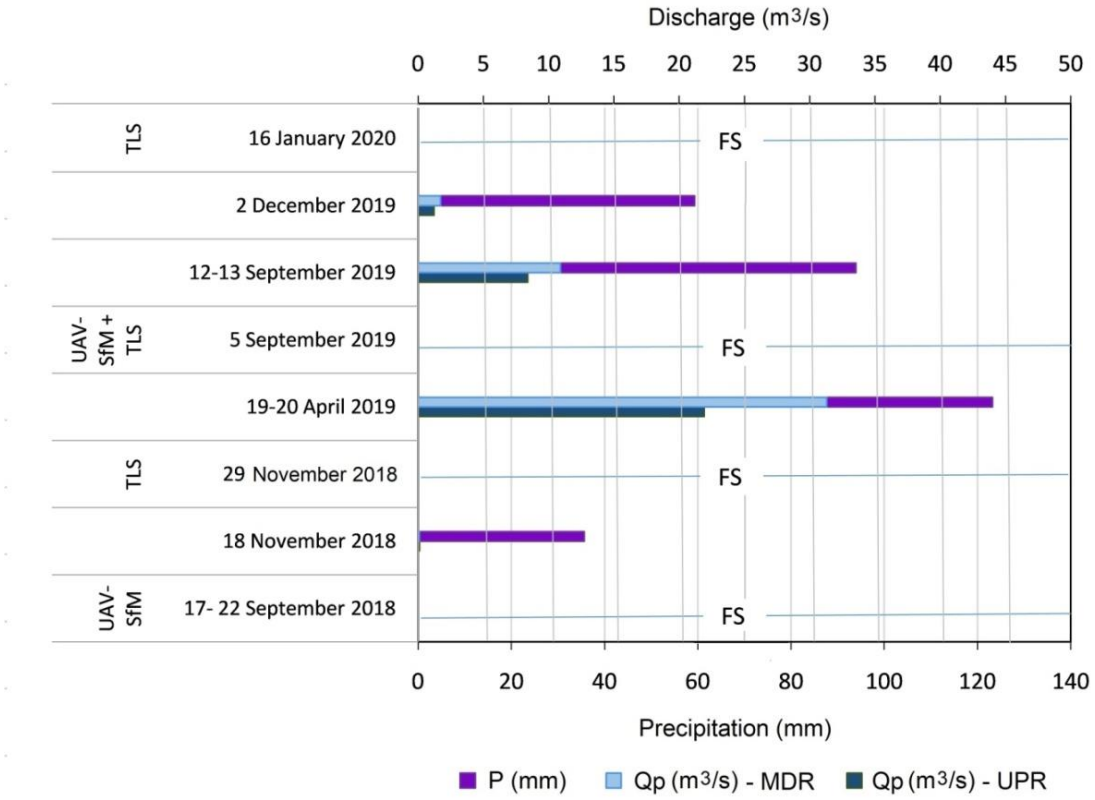


**Figure 2.2.** Chronogram of the flow events and of the field surveys (FS) performed using UAV-SfM and/or TLS techniques.

## 2.3 Materials and Methods

The affected areas, elevation differences, volumes of erosion and deposition, and sediment budgets were obtained for the two RCR (Upper -UPR- and Middle -MDR- stretches), using data derived from UAV-SfM and TLS. To detect changes in bedload budgets at bed level exclusively, an analysis was performed using TLS in pilot survey bed areas (PSBA) with higher point density. The RCRs were delineated using the limits of the water sheet generated by the hydraulic model for each flood event. In addition, the values of the total area of interest ($m^2$) (TAI), total volume difference average ($m^3$) (TVDA), net thickness difference (m) for the area of interest (NTD), and percent imbalance (departure from equilibrium) (PI), among other variables, were provided by both techniques for each of RGU.

### 2.3.1. SfM-MVS photogrammetry

The remote information was collected with a Phantom 4 Pro, with 20 Mpx camera and 1-inch sensor. The photogrammetric parameters of the flights were set before the development of the first field survey and the inspection of the study area, using the software tool DJI GS Pro© with equivalent values for all the surveys; this procedure ensured optimum comparability among the digital elevation models generated at different sites and on different dates. The average flight height was c. 50 m above ground level, resulting in images with a resolution of c. 1-cm.

Standard targets extracted from Agisoft PhotoScan Pro 1.2.2© (Agisoft, Russia) were used as Ground Control Points (GCPs) for georeferencing and analyzing the quality of the reconstructed HRDTM. These targets were randomly distributed throughout each of the stream segments and were surveyed using a Prexiso G5© (Leica, Germany) GPS-RTK instrument. The GPS-RTK instrument was connected to the regional network of GPS GNSS (Network of Reference Stations in the Autonomous Community of Murcia "Meristemum") via mobile signal, to obtain differential corrections in real time. In each survey, c. 66 % of the measured points were subsequently integrated into the model for georeferencing purposes and the remaining 34 % were used as checkpoints for the validation of the HRDTM. Permanent GCPs were also installed, using FENO survey markers in each of the GRS to define common reference points for all surveys and methodologies. All the GPS points were recorded in the WGS84 global reference system.

We selected images with a high level of overlap (80-90%) to ensure successful subsequent image matching (Eisenbeiss and Sauerbier, 2011). These images and the coordinates of the GCPs' were uploaded into structure-from-motion photogrammetry software, Agisoft PhotoScan Pro v.1.2.2© (Agisoft, Russia), and aligned using high precision settings and generic pair preselection to create a sparse point cloud (Puig-Mengual et al. 2017; Puig-Mengual et al. 2021). We optimized the image alignment using the GCPs' data and regenerated the model using the same settings as previously; consequently, the HRDTM, orthophoto, and dense point cloud were exported for further analysis in a global georeferencing system (WGS84).

The DTM of difference (DoD) between the UAVs-collected HRDTM in different field surveys, as well as between the TLS-generated HRDTM, was calculated in ArcGis 10.5 © (ESRI, USA), by subtracting the final topography from the previous topography for the same area (Calle et al. 2018). The same polygon was used for the comparison of the complete RCR, and similarly for the RGU, to maintain the boundaries for change detection, and the HRDTM were created with equal pixel size (0.02 × 0.02 m), starting from a specific point, so that the grid cells were fully coincident. To assess the sediment budgets and morphological bed changes, we used statistics such as the TAI, TVDA, NTD and PI of each of the RGUs. In addition, histograms of the volume and bar graphs were used to represent the trends of elevations.

### 2.3.2. Terrestrial Laser Scanning (TLS)

In this study a terrestrial 3D laser scanner (Leica ScanStation C10 model) was used. This instrument captures the coordinates of points up to 200 m away and the returned energy, and estimates the RBG color using a digital camera. The precision of the instrument is 2 mm. The TLS captures the evenly spaced points when the surface is vertical, but when it is sub-horizontal the scanned points are sparse. Consequently, to scan the bedforms it is necessary to choose elevated positions for the scanner, when possible. Another option is to perform multiple scanning stations and to register them, merging sparse point clouds and reducing the point spacing and the shadow areas.

Several scans were made from different stations placed strategically along the bedforms for detailed geometrical definition using TLS. For each date several scanning stations were made and registered using HDS targets. In addition, the FENO survey markers were also scanned in order to register the TLS point clouds described in the previous section and the SfM datasets. The scan performed on September 5, 2019 was

used as the benchmark for all the TLS scans. On that date, the SfM and TLS data were acquired. The coordinates of the FENO survey markers were extracted from that SfM dataset and the TLS dataset was registered using those coordinates. Consequently, the 2018 and 2020 scans were registered to that benchmark using existing buildings as the reference. The registration was performed using the ICP plugin of CloudCompare and was applied to existing buildings, which were considered as stable areas for the whole study period. Then, the registration was evaluated using the M3C2 plugin of CloudCompare. Both registrations had a mean error of 2 mm.

To study the elevation differences and volume changes, two pilot bed survey areas (PBSA) with higher point density, within the UPR and MDR reference channel reaches, were selected: the upper area (8.55x17.7m$^2$), and the middle area (16.3 x 27.55 m$^2$). The existing vegetation (scrub, bushes, and trees) was removed using the Canupo (CAractérisation de NUages de POints) CloudCompare plugin with specific trainings for both areas (Brodu and Lague, 2012) (Figure 2.3). Then, each area was rasterized using a 5-cm grid and empty areas were interpolated.

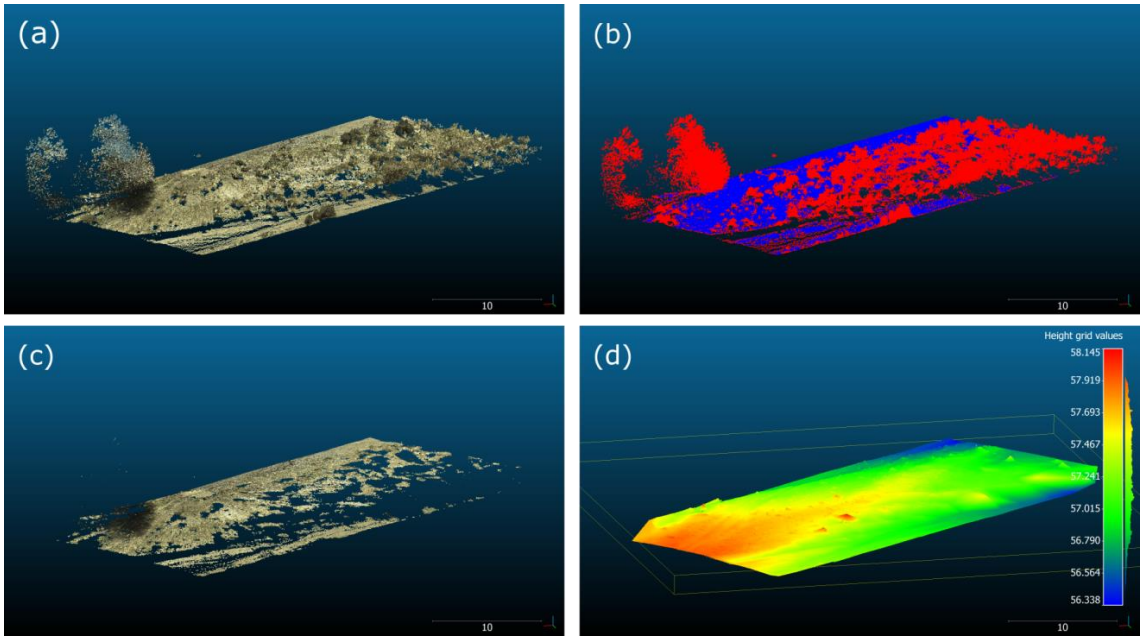


**Figure 2.3.** (**a**) View of the raw 3DPC; (**b**) 3DPC classified by means of the CANUPO plugin of CloudCompare, showing in blue the points classified as ground and in red those classified as vegetation; (**c**) 3DPC after removal of the points classified as vegetation; (**d**) the previous 3DPC rasterized using the rasterization tool of CloudCompare, computing the average height for each 5-cm cell and interpolating the empty cells with the nearest neighbors.

### 2.3.3. Criteria for the selection of reference channel reaches (RCR), pilot bed survey areas (PBSA), and representative geomorphic units (RGU)

Reference upper and middle reaches (Upper and Middle RCR) were chosen depending on the accessibility and the presence of potentially active surface areas. In addition, these stream stretches better represent the variations in the sediment budget and morphological adjustments within the main channel, as opposed to the lower reach, whose

global changes are the product of sediment-laden flood water spills, affecting crevasse splays and a wide active flood bed. In fact, the choice of the Upper and Middle RCR in this EGBS is intended to reflect the clear influence that coarse grain-sizes and bedload, as the dominant transport modality, have on the morphological sediment budget within the channel itself (Zapico et al., 2018). Downstream, along the lower reach to the mouth of this stream, a distributary drainage system exists, which implies that the budget of more complex sediments needs to be evaluated, accounting for mixed sources (hillslopes and secondary channels), for the temporary storage of sediment in bars and alluvial plains (Ali and De Boer, 2003).

The Upper RCR is an entrenched channel stretch that enabled one scanning station at an elevated position. The rest of the scans were performed on the ground close to the bedforms. In the Middle RCR, where bedforms arises and the vegetation cover is scarce, only scanning stations on the ground were performed, reducing the density of the points. The choice of PBSA is intended to detect and quantify precise changes in bed sediment budgets and bed load mobility, while the RGU monitoring allows us to analyse behaviour patterns and spatial variability of forms associated with scouring and deposition areas within the channel.

### 2.3.4 Hydrometeorological and hydraulic data

A rainfall-runoff model was used to simulate runoff on the basis of rainfall events during the budget period. Five pre-simulated runoff events were defined on the basis of the rainfall amount, initial wetness conditions, and initial discharge and were subsequently adjusted according to the real flow heights measured by water pressure sensors. The HEC-HMS 3.5 program (Sharffenberg and Fleming, 2010) was combined with a DTM in grid format and 4 x 4 m cell resolution (NATMUR-08) in order to generate the drainage patterns and catchment limits. Then, in accordance with (Nanía, 2007), we assembled the headwater sub-basins that are homogeneous in texture and roughness and individualized those affected by confluences with important breaks in the bed slope. The main abstraction used was the infiltration curve number (NC) of each sub-basin, following the methodology of the Soil Conservation Service of the US Department of Agriculture (SCS, 1972). The geometries and data tables, referring to the vector lithological layer of the Geological and Mining Institute of Spain (IGME) at a scale of 1: 50,000, and the land use map of the Corine Land Cover (CLC), Level 3 (2012) were combined using GIS to estimate this parameter, according to the different hydrological soil groups and substrate textures. Using the antecedent conditions of dry soil and pluviometric data for intervals of 5 minutes at the Cuesta del Cedacero station, we calculated the dimensionless unit hydrograph of the SCS and its peak unit flow ($q_p$) ($m^3/s$) (Eq. 2.1).

$$q_p = \frac{2.08\,A}{T_p} \tag{2.1}$$

where A is the area of the basin ($km^2$) and Tp the time to peak (h), estimated according to Eq. 2.2.

$$T_p = \frac{D}{2} + t_p \tag{2.2}$$

where D is the duration of the effective rainfall (h) and tp is the lag time, in our case 0.6 times the concentration time of the catchment (Nanía and Gómez Valentín, 2006).

The output data (Figure 2.4) were then transferred to the 1D hydrodynamic model HEC-RAS (USACE, 2016), supported by HRDTM, to obtain the channel profile and cross-sections and hydraulic variables. A total of 212 cross-sections were used, with an average separation of 2.0-3.5 between them in both channel reaches. The theoretical hydrometeorological discharge, estimated for the conditions of a subcritical flow regime, was calibrated using that from the real water height data. Variations in the water level during each flood event were recorded with levelogger sensors and corrected using barometric calibration devices (barologger sensors), located in a station intermediate between the upper and middle reaches. For all the cros- sections, information concerning the flow surface area, hydraulic radius, velocity, shear stress, and stream power was obtained. The power per unit length of stream (Ω) and mean stream power (ω) at peak flood discharge (Qp) were calculated, according to Eq. 2.3 and Eq. 2.4, respectively (Leopold et al., 1964), for each cell i between each pair of cross-sections.

$$\Omega = \gamma Q S_w \tag{2.3}$$

$$\omega = \Omega / w \tag{2.4}$$

Where γ is the specific weight of water ($Nm^{-3}$), Q is the discharge ($m^3/s$), $S_w$ is the water surface slope (m/m), which is used to estimate the energy gradient, w is the water-surface width (m), Ω represents the energy dissipation per unit channel length ($Wm^{-1}$), and ω the energy expenditure per unit bed area ($Wm^{-2}$).

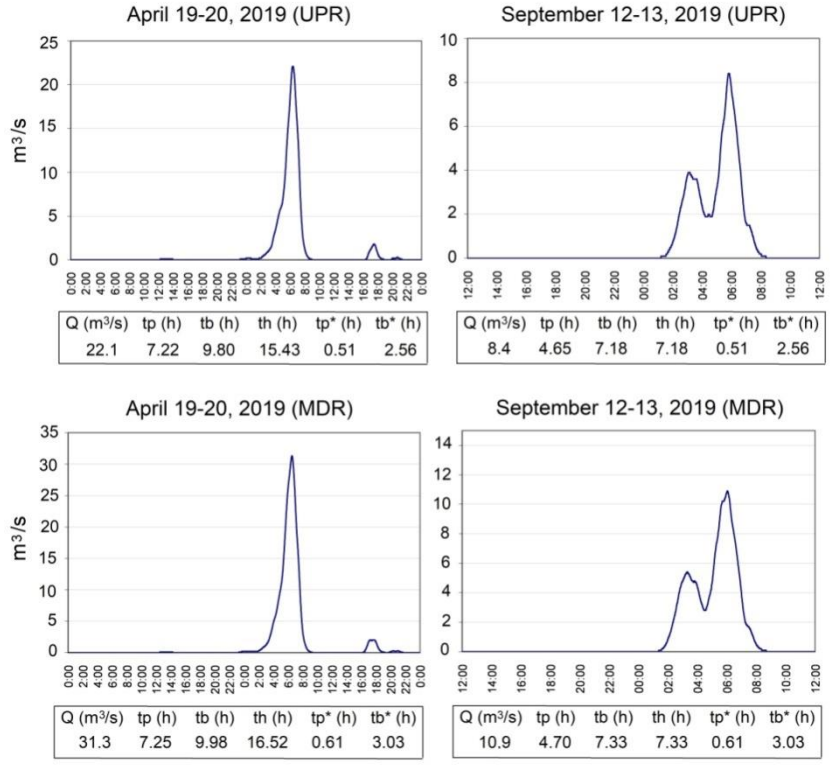


**Figure 2.4.** Hydrographs and associated parameters for the flood events of April 19-20, 2019 and September 12-13, 2019, estimated in intermediate cross-sections of the UPR and MDR stretches. Q = discharge ($m^3/s$); tp = time of peak (h); tb = base time

(h); th = hydrograph duration (h); tp* and tb* = time of peak and base time of the unit hydrograph (h).

The mean stream power gradient ($\partial\omega/\partial s$) was calculated by subtracting ω in cross-sectional cell i from ω in cell i−1 and dividing the difference by the distance between the centroid of each pair of consecutive cells along the channel centerline. In this way, positive $\partial\omega/\partial s$ values indicate downstream increases in ω, while a negative $\partial\omega/\partial s$ indicates that ω is decreasing from one cell to the next (Lea and Legleiter, 2016). The energy expenditure beyond the critical mean stream power ($\omega_c$) and the stream power (ω) / resisting power ($\omega_c$) ratios ($\omega/\omega_c$) were estimated in each cross-sectional cell to determine the spatial variability of the energy available for sediment transport and explain morphological changes during peak flows. The $\omega_c$ was obtained using Eqs. (2.10) and (2.16) from Parker et al. (Parker et al., 2011), which relate $\omega_c$ to slope and grain size. A representative reach pebble count was made in the RCR along transect stretches from one stream bank to the other, while the RGU were sampled by volumetric extraction of bed-material to differentiate surface and subsurface particle-size distributions. The median grain size ($D_{50}$) and 84$^{th}$ percentile ($D_{84}$) were calculated for each transect and set of cross-sections.

### 2.3.5 Sediment budget calculation and detection of RGU adjustments

The sediment budgets in an EBGS accounts for the rates and processes of erosion and bedload transport within the channel, and for the temporary storage of coarse grain-size material in bars and pools along bends and runs. Significant rates of weathering and breakdown of sediment, during transport or storage, are also frequent in semi-arid environments, such as this one (Ali and De Boer, 2003). Variations in bedload transport downstream lead to adjustments in the erosion and deposition volumes, affecting the sediment budget, and vice versa, changes in this budget could condition the amount of material entrained (Wasson, 2002). This premise makes the estimation of sediment budgets a useful and necessary task for the determination of the magnitude of morphological bed changes. An analysis relating event-scale bedload transport to changes in channel morphology is generally difficult, because this requires a detailed topographic survey of the channel immediately before and after each flow event (Kasprak et al., 2015). This consideration is particularly relevant in ephemeral streams, where the channel remains dry most of the time and only carries water in flash floods that last a few hours. Consequently, the monitoring of morphological bed adjustments and the calculation of sediment budgets at the event scale can provide more realistic results than the analysis of long study periods. In our case, a strategy based on the combined use of high definition topographic products was adopted to reveal the geomorphological effects of isolated events or, at most, two events of different magnitudes.

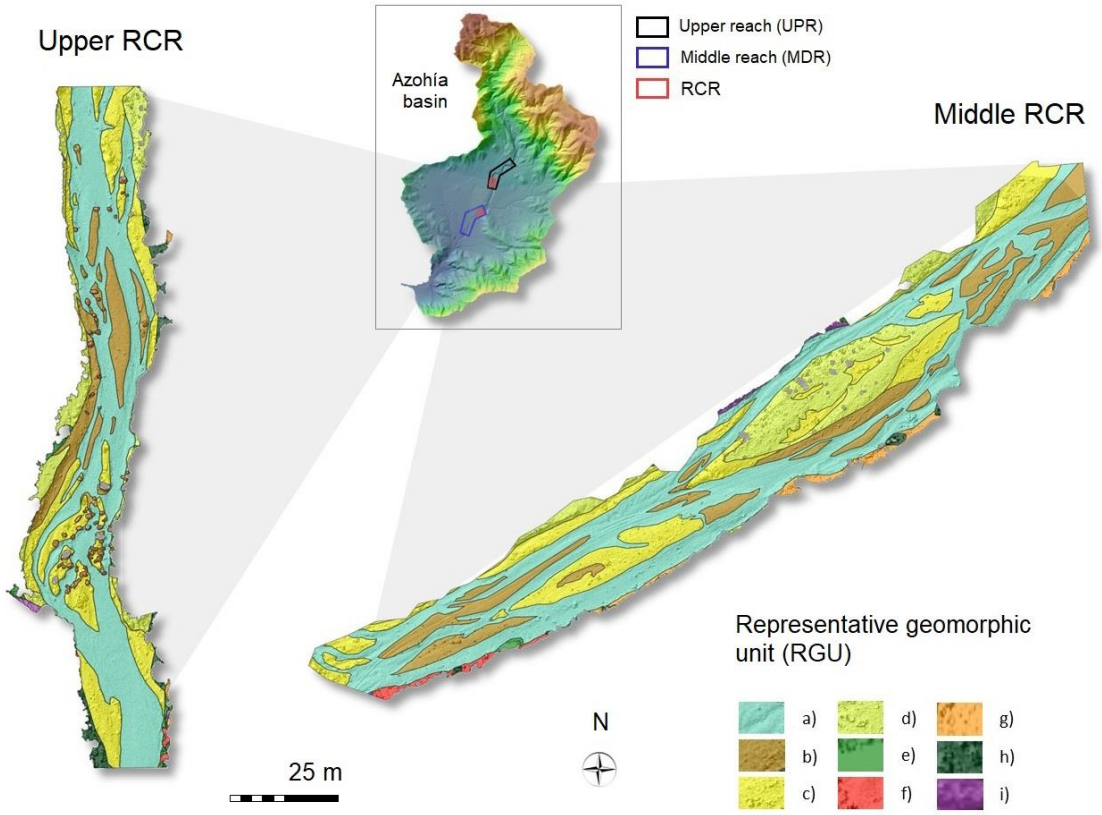


**Figure 2.5.** RGU extracted within the boundaries defining each peak flow in the Upper and Middle RCR: a. Active channel, secondary minor channel inter-bars or run; b. Low, active non-vegetated bar; c. Low, scarcely vegetated bar; d. High, active non-vegetated bar; e. High, scarcely vegetated bar; f. High, vegetated bar; g. Non-vegetated talus or steep bank; h. Non-vegetated steep bank with falling rock blocks; i. Scarcely vegetated talus or steep bank.

High-density 3DPC and HRDTM, generated from SfM-MVS and TLS, were overlain to obtain good accuracy in the sediment budget calculation. At the event level, this evaluation went further, because it allowed us to relate the net bed variations to the characteristics of the hydrograph in question. The errors associated with the use of two surface models to determine volumetric sediment budgets were described and assumed for each comparative survey analysis, according to Brasington et al. (Brasington et al., 2003). The same procedure was applied to detect morphological adjustments attributed to erosion or deposition in the RGU (Figure 2.5), overlaying the 3DPC on the raster image derived from a vector layer that contained the polygons of these geomorphic units within the wetted channel perimeter in each flow event.

## 2.4 Results and discussion

### 2.4.1 Stream power maps

The mean stream power ($\omega$), energy gradient ($\partial\omega/\partial s$), and mean stream power ($\omega$) / resisting power ($\omega_c$) ratio ($\omega/\omega_c$) were estimated discreetly along each of the RCR for the most significant flood events: April 19-20, 2019 and September 12-13, 2019. Figure 2.6

shows the grids of these variables for the UPR and MDR during these events. Theresulting maps were then related to the spatial patterns of sediment budgets in order to explain better the processes that control the morphological channel adjustments.

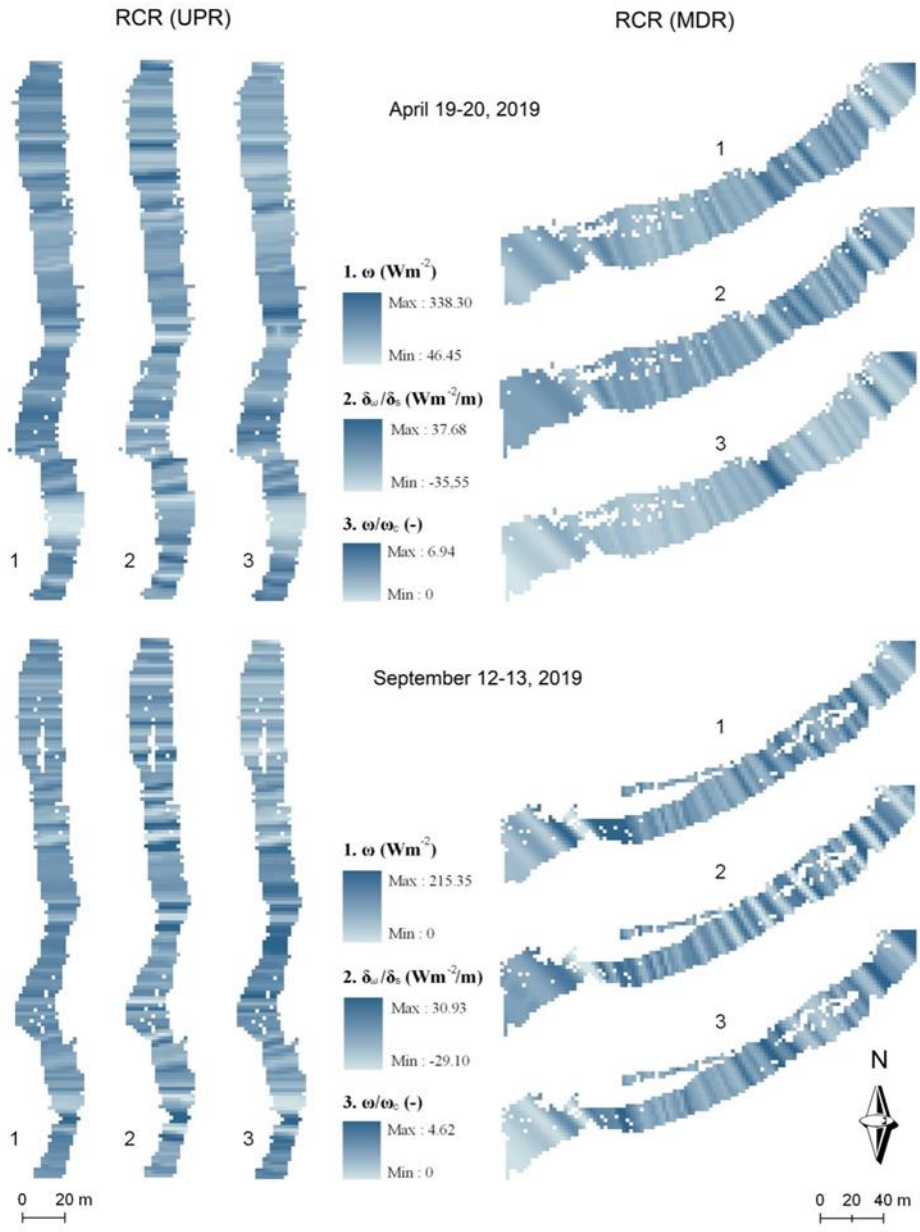


**Figure 2.6.** Values of ω, ∂ω/∂s, and ω/ωc obtained for each cell by spatial interpolation of HEC-RAS data related to equidistant (2.0-3.5 m) cross-sections in the RCR(UPR) and RCR(MDR). Peak floods of 19-20 April, 2019 (upper graph) and 12-13 September, 2019 (lower graph). The maximum color limits encompass the 95% of the data sets.

In the study RCR, the ω during the peak flow of April 19-20, 2019 varied from 0.6 to 371.4 W $m^{-2}$ and the stream power gradient from -40.8 to 51.2 $Wm^{-2}$/m (the upper limits of color displayed in Figure 2.6 for these variables encompass 95% of the data; that is, 338.3 $Wm^{-2}$ and 37.7 $Wm^{-2}$/m, respectively). Note, however, that more than 75% of the set of values of ∂ω/∂s in this event fell within the range 15 to -15 $Wm^{-2}$/m and that the extreme data reflect sharp local changes in ω. As in the case of the flow velocity and

the shear stress, the highest values of ω were concentrated in entrenched channel cross-sections, along straight to slightly sinuous stretches, and locally over steep riffles characterized by high near-bed velocity gradients. This pattern is linked to incision processes in several Mediterranean ephemeral streams (Ortega et al., 2014; Garzón and Alonso, 2002; Hooke, 2006). However, we observed a significantly different behaviour in the gravel beds studied here, where important transitory erosion was often accompanied by extraordinary bedload mobility and high deposition rates, which tended to cause channel aggradation.

The distribution of the $\omega/\omega_c$ ratios was also skewed for both RCR and the flood events, with maximum values very distant from the mean and median. In the events of April and September maximum ratios around 10 and 7 were reached, respectively, in the two reference stretches, with much lower and different medians depending on the section. Specifically, during the peak flood of 19-20 April, 2019, the $\omega/\omega_c$ medians ranged from 2.7 in RCR (UPR) to 1.2 in RCR (MDR).

### 2.4.2 Spatial sediment budgets and morphological changes along RCR and PBSA

#### *2.4.2.1. Sediment budgets in RCR determined from SfM data*

Gravel-bed erosion and aggradation are recurrent geomorphological processes that discretely affect the global evolution of EGBS over time. Changes at the event scale are usually very disparate, in some cases scour and downcutting phenomena predominate, and in others deposition. The present study contributes to a better understanding of the current behaviour of this type of channel and the subsequent trend of its minor adjustments, but it contributes little in relation to possible long-term morphodynamic changes. A good indicator of these adjustments is the sediment budget in the reaches with the highest bedload. In particular, in the RCR analysed here, the bedload experienced important spatial variations at the event scale, significantly affecting the sediment sources (areas of erosion) and sinks (areas of deposition) in the short period of analysis. In the September 2018 - September 2019 stage, lateral erosion from steep alluvial banks, active low bars, partially destroyed coarse bar heads, and finer-grained bar tails provided a large bedload in the downstream direction. As a result, the greatest deposition thicknesses were recorded in the flanks of the longitudinal and medial alluvial bars, in both RCR (see Figure 2.7, drawn up on the basis of SfM-MVS data).

Previous field observations suggest that during low-water stages, as in the event of November 2018, when the top of the bar emerged, vertical accretion of these bars ceases and new secondary channels form, causing small island bars to migrate. The flash flood of April 19-20, 2019 resumed the aggradation process, with very widespread increases in bed height. The SfM statistical data in Table 2.1 show significant cumulative changes in ground surface elevation after the flow events of November 19, 2018 and April 19-20, 2019. An average net thickness difference of around 22 and 21 cm was found in the UPR and MDR, respectively. The sedimentary balance was positive in both RCR, verifying a clear dominance of deposition over erosion. The proximity of both reaches to abundant sources of coarse sediment, mainly due to locally strong connectivity between the channel bed and active alluvial banks, together with a similar bed slope, promoting a notable mobility of the bedload, explains the scarce variation between the RCR in the average sediment budget. The high average deposition rate observed in the MDR (unit TVSL = 0.218 $m^3/m^2$) was not accompanied by equally significant unit volumes of erosion

upstream in the UPR (unit TVSR = 0.128 $m^3/m^2$). This suggests that the sources of sediments include not only the UPR, but also other more entrenched sections close to the headwater area and intermediate sections between the two RCR, where bank breaking and gravel bar removal are especially active processes. In addition, the minor unit net erosion recorded in UPR during this event decreased even more, reaching 0.086 $m^3/m^2$ in MDR (Table 2.1), so the bed cutting could not progress in a downstream direction.

Heterogeneities due to differences in grain-sizes and bedforms may create substantial velocity and shear stress variations across the channel or downstream during a single discharge (Wohl, 2000). This can explain the patchwork of ω values in both reaches (Figure 2.7) and, thus, the spatial changes in sediment budgets displayed in Table 2.1. The UPR registered the highest average unit volume of surface raising and lowering (0.13 and 0.23 $m^3/m^2$, respectively), in line with the highest mean values of ω (72.4 $Wm^{-2}$), but also the highest SD in the net thickness differences and in the $\partial\omega/\partial s$ gradients (16.4 $Wm^{-2}/m$).

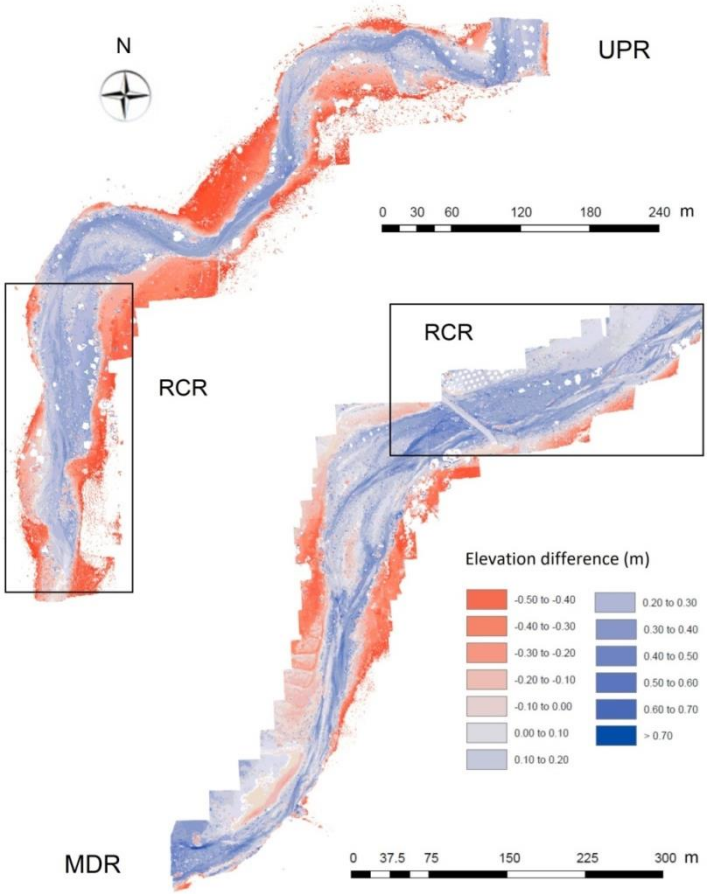


**Figure 2.7.** Surface elevation differences (m) found for the Upper (UPR) and Middle (MDR) RCR, using HRDTM derived from SfM-MVS, for the period September 2018 to September 2019, including the events of November 18, 2018 and April19-20, 2019.

**Table 2.1.** Statistical descriptors relating to the morphological sediment budgets calculated for the overall (OVR) and reference channel reaches (RCR) in the UPR and MDR for the period September 2018 to September 2019 (SfM data).

| Statistical | | TAI | TNVD | | ANTD | | PI | TASL | TASR | UVSL | | UVSR | | SD* |
|---|---|---|---|---|---|---|---|---|---|---|---|---|---|---|
| Channel reach type | | $m^2$ | $m^3$ | % Error | m | % Error | % Value | $m^2$ | $m^2$ | $m^3/m^2$ | % Error | $m^3/m^2$ | % Error | m |
| UPR | OVR | 4657 | 958 | 0.045 | 0.206 | 0.045 | 0.470 | 3728 | 4285 | 0.083 | 0.107 | 0.231 | 0.043 | 0.137 |
| | RCR | 2763 | 614 | 0.044 | 0.222 | 0.044 | 0.486 | 67 | 2695 | 0.128 | 0.069 | 0.231 | 0.043 | 0.118 |
| MDR | OVR | 8720 | 2093 | 0.040 | 0.240 | 0.040 | 0.489 | 234 | 8486 | 0.103 | 0.086 | 0.249 | 0.040 | 0.121 |
| | RCR | 4885 | 1013 | 0.046 | 0.207 | 0.046 | 0.486 | 168 | 4717 | 0.086 | 0.102 | 0.218 | 0.046 | 0.106 |

TAI = Total Area of Interest ($m^2$); TNVD =Total Net Volume Difference ($m^3$); ANTD =Average Net Thickness Difference (m) for the Area of Interest; PI =Percent Imbalance (departure from equilibrium); TASL =Total Area of Surface Lowering ($m^2$); TASR =Total Area of Surface Raising ($m^2$); UVSL = Average Unit Volume of Surface Lowering ($m^3/m^2$); UVSR = Average Unit Volume of Surface Raising ($m^3/m^2$); SD* =Standard Deviation of the Net Thickness Differences (m); UPR = Upper reach; MDR = Middle reach; OVR = Overall channel reach; RCR = Reference channel reach.

### *2.4.2.2. Sediment budget and stream power in PBSA estimated from TLS data*

The results in Table 2.1 (SfM-based results) differ from those obtained using TLS for the same RCR during the period of December 2018 to September 2019, for two reasons. Firstly, there were differences caused by the fact that the UAV-SfM surveys included an event (the peak flow of November 18, 2018) that was not monitored with TLS. Secondly, it is widely accepted that the evaluation of sediment budgets is sensitive to differences in DTM quality and in the process used to suppress vegetation cover, since they inherently incorporate errors into the generated terrain models (Brasington et al., 2003). Although this type of error was considered small in the two RCR, given the high resolution of the DTMs used, this factor cannot be completely discounted in the more vegetated areas.

In addition, the high-density 3D point clouds generated from TLS were applied to pilot bed areas (PBSAs) in order to detect detailed changes in bedload budgets. In Figures 2.8 and 2.9 and Table 2.2, the results obtained during three periods are shown: November 2018 - September 2019, September 2019 - January 2020, and November 2018 - January 2020. The first of these periods offers information on the morphological sediment budgets attributable to the flash flood of April 19-20, 2019; the second includes the peak flows of September 12-13, 2019 and December 2, 2019; and the third covers all three events. In the areas detailed, a positive balance was detected after the first event, with an average unit volume of 21.55 $dm^3/m^2$in PBAS (UPR) and 10.03 $dm^3/m^2$in PBAS (MDR), whereas there was a negative average balance during the second period, when erosion removed 54.12 and 26.25 $dm^3/m^2$, respectively, in these two areas.

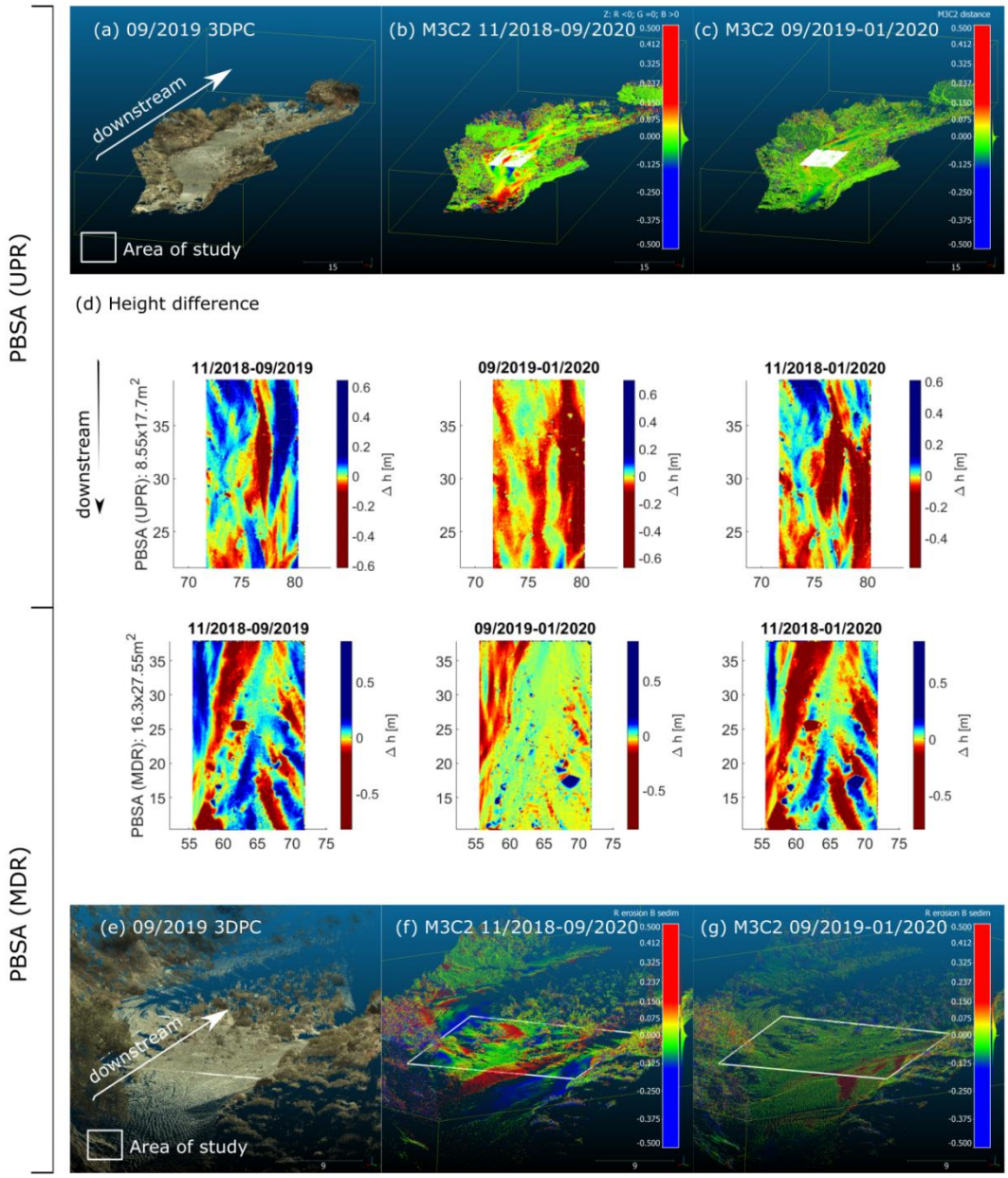


**Figure 2.8. (a)** View of 3DPC captured in 2019; **(b-c)** M3C2 comparison of the 2018-2019 and 2019-2020 3DPCs, respectively; **(d)** height difference between 2018, 2019, and 2020 in the Upper and Middle PBSA; **(e)** view of 3DPC captured in 2019; (f-g) M3C2 comparison of the 2018-2019 and 2019-2020 3DPCs respectively.

**Table 2.2.** Changes in unit volume ($dm^3/m^2$) and total mean volume per budget cell ($dm^3$) obtained for elevation intervals of 10 cm and global height differences (Δe) in each pilot bed survey area (PBSA), based on TLS datasets covering the periods 2018-2019[1], 2019-2020 [2] and 2018-2020[3].

| | Unit volume ($dm^3/m^2$) | | | | | | Total mean volume per budget cell ($dm^3$) | | | | | |
|---|---|---|---|---|---|---|---|---|---|---|---|---|
| | PBSA (UPR) | | | PBSA (MDR) | | | PBSA (UPR) | | | PBSA (MDR) | | |
| Δe (m) | 2018 2019[1] | 2019 2020[2] | 2018 2020[3] | 2018 2019[1] | 2019 2020[2] | 2018 2020[3] | 2018 2019[1] | 2019 2020[2] | 2018 2020[3] | 2018 2019[1] | 2019 2020[2] | 2018 2020[3] |
| -0.5/-0.4 | -0.05 | -0.15 | -0.05 | -3.59 | -0.15 | -3.15 | -1.9 | -5.3 | -2.1 | -312.7 | -10.0 | -243.5 |
| -0.4/-0.3 | 0.00 | -0.21 | -0.02 | -2.46 | -0.02 | -4.65 | 0.0 | -7.4 | -0.6 | -214.1 | -1.3 | -359.1 |
| -0.3/-0.2 | -1.47 | -7.67 | -4.80 | -3.86 | -0.23 | -8.83 | -59.4 | -270.0 | -181.1 | -335.7 | -15.8 | -682.3 |
| -0.2/-0.1 | -6.60 | -22.54 | -22.90 | -16.14 | -9.35 | -19.74 | -266.0 | -793.6 | -865.0 | -1405.4 | -631.2 | -1525.8 |
| -0.1/0 | -11.32 | -26.36 | -19.95 | -11.35 | -23.91 | -14.32 | -456.4 | -928.4 | -753.6 | -987.7 | -1613.6 | -1106.5 |
| ΔV<0 | -19.44 | -56.93 | -47.72 | -37.40 | -33.66 | -50.69 | -783.7 | -2004.7 | -1802.4 | -3255.6 | -2271.9 | -3917.2 |
| 0/0.1 | 21.80 | 2.68 | 11.18 | 18.52 | 3.09 | 15.23 | 878.9 | 94.3 | 422.3 | 1612.5 | 208.7 | 1177.2 |
| 0.1/0.2 | 17.38 | 0.05 | 3.56 | 22.84 | 1.14 | 12.82 | 700.7 | 1.6 | 134.3 | 1988.9 | 76.7 | 991.1 |
| 0.2/0.3 | 1.38 | 0.01 | 0.19 | 4.67 | 0.79 | 2.94 | 55.6 | 0.3 | 7.0 | 406.3 | 53.6 | 227.0 |
| 0.3/0.4 | 0.16 | 0.01 | 0.01 | 0.57 | 0.70 | 1.28 | 6.3 | 0.2 | 0.2 | 49.3 | 46.9 | 99.1 |
| 0.4/0.5 | 0.27 | 0.07 | 0.22 | 0.83 | 1.69 | 2.19 | 10.9 | 2.5 | 8.4 | 72.0 | 114.4 | 169.1 |
| ΔV>0 | 40.99 | 2.82 | 15.16 | 47.43 | 7.41 | 34.46 | 1652.4 | 98.9 | 572.2 | 4129.0 | 500.3 | 2663.5 |
| ΔV | 21.55 | -54.12 | -32.58 | 10.03 | -26.25 | -16.23 | 868.7 | -1905.8 | -1230.2 | 873.4 | -1771.6 | -1253.7 |

Note: Specifically, these periods are as follows: [1] November 2018 to September 2019, [2] September 2019 to January 2020, and [3] November 2018 to January 2020.

The analysis of budgets expressed in unit volume for 10 cm elevation intervals show that the largest volumetric variations implied morphological adjustments, ranging between -0.2 and + 0.2 m in bed elevation (Table 2.2). Within these intervals, the greatest unit volume of deposition (41.3 $dm^3/m^2$) corresponded to PBSA (MDR) after the April 2019 event, and the greatest erosion volume (48.9 $dm^3/m^2$) to PBSA (UPR) after the two minor events of the period September 2019 to January 2020. These data are consistent with those displayed for both cases in the normalized histograms of elevation differences (Figure 2.9), where the interval from 0 to +0.2 m had a cumulative frequency greater than 60% and that from 0 to -0. 2 m exceeded 70%.

Likewise, the variations and signs of the mean energy gradient faithfully reflected the different patterns observed in the bedload budgets of each PBSA. Assuming that $\partial\omega/\partial s$ represents the clearest expression of sediment change in the nearest cell downstream, we can hypothesize that this hydraulic variable had a strong influence on the net erosion or deposition, and on the total mean bedload volume per unit area. However, while the net deposition pattern expected with a higher positive $\partial\omega/\partial s$ did occur, the same did not happen with the net erosion pattern, since the most negative $\partial\omega/\partial s$ registered in PBSA (UPR), during the flood peak on April 19, 2019, finally translated into a unit net volume of downcutting lower than the one accumulated by the minor events of September 2019 and January 2020. The larger flow event in April generated

significantly higher mean $\partial\omega/\partial s$ values than the minor peak flow in September, with a negative sign in PBSA (UPR) and a positive one in PBSA (MDR), which resulted in a decrease from -3.8 to -0.4 $Wm^{-2}/m$ for the first case and from 1.9 to 1.6 $Wm^{-2}/m$ for the second. This suggests that in the major event a much larger bed load was mobilized and replaced than in the minor event, and that during the latter the energy expenditure was used for scouring and there was not enough surplus ($\omega/\omega_c$ = 1.6,vs 2.6 in the April flood) to drag and deposit the material transported from upstream.

**Figure 2.9.** Normalized histograms of the elevation differences shown in Figure 2.8 for the Upper and Middle PBSA, comparing the 2018, 2019, and 2020 3DPCs.

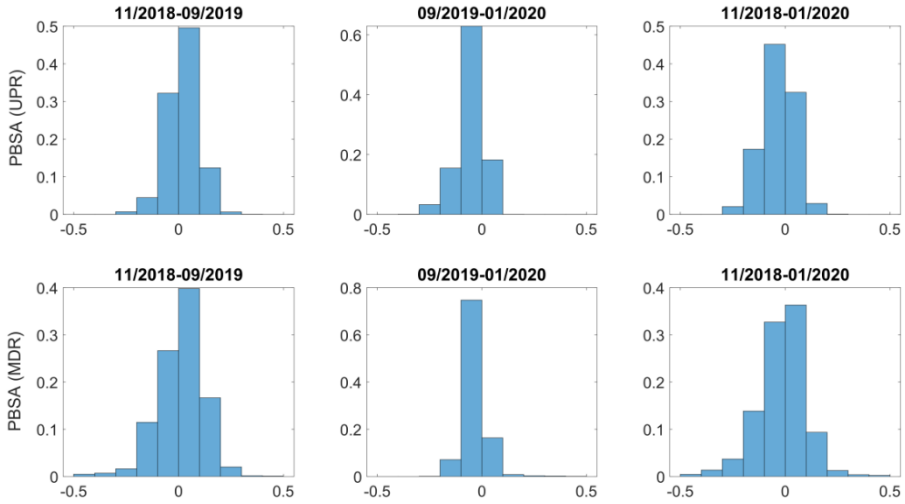


**Table 2.3.** Basic statistical data for the stream power variables estimated for the events of April 19, 2019 and September 12, 2019 in the Upper and Middle PBSA.

| | PBSA (UPR) | | | | | | | PBSA (MDR) | | | | | | |
|---|---|---|---|---|---|---|---|---|---|---|---|---|---|---|
| | $\omega$ | $\partial\omega/\partial s$ | | | $\omega/\omega_c$ | | | $\omega$ | $\partial\omega/\partial s$ | | | $\omega/\omega_c$ | | |
| | (W $m^{-2}$) | ($Wm^{-2}/m$) | | | (-) | | | (W $m^{-2}$) | ($Wm^{-2}/m$) | | | (-) | | |
| Flash flood | Mean | Max | Min | Mean | Max | Min | Mean | Mean | Max | Min | Mean | Max | Min | Mean |
| 19/04/2019 | 163.4 | +8.9 | -28.8 | -3.8 | 3.8 | 1.5 | 2.6 | 145.8 | +34.1 | -26.3 | 2.8 | 2.8 | 0.5 | 1.9 |
| 12/09/2019 | 99.4 | +23.4 | -15.2 | -0.4 | 2.9 | 0.5 | 1.75 | 87.9 | +14.2 | -13.2 | 1.2 | 2.4 | 0.5 | 1.6 |

Such results seem to corroborate the hypothesis that in this EGBS the events of greater magnitude ($Qp \geq 30$ $m^3/s$) produce vertical sedimentary accretion on the bed, exceeding even the critical stress of the coarsest particles (gravel and pebbles) in PBSA (UPR) (mean $\omega / \omega_c > 2$) and thus moving a large bedload downstream. In contrast, more moderate peak flow rates ($Qp \leq 10$ $m^3/s$) were only able to exert a surface washing action, selective transport, and local scouring. In both cases, all the events analysed tended to reinforce and arm the bed, as seen in situ, making it more resistant to erosion in future floods.

*2.4.2.3 Morphological bed adjustments observed in RCR from TLS data*

The detailed topographic survey performed for each channel reach prior to and following a bedload-transporting flow event made it possible to detect precise changes in channel morphology in relation to event scale bedload fluxes. Such an approach was highly recommended by Kasprak et al. (Kasprak et al., 2015), when an HRDTM is available, and by Singer and Michaelides (Singer and Michaelides, 2014) for the case of ephemeral channels, where topography appears to remain unchanged. In Figure 2.10 are shown the morphological changes observed along the channel center line of both RCR using TLS datasets. From this, different patterns of spatial variability were inferred, depending on the reference site, the magnitude of the flood, and the textural and topographic characteristics immediately prior to the occurrence of each event.

In the Upper RCR the major morphological bed changes corresponded to two types of channel narrowing: at the exit of a meander and that due to structural control in less sinuous reaches. In the first case, the forms of excavation and vertical accretion reflected a marked bed alteration just 15 m in length, the incision prevailing in the largest event and the deposition in the least torrential (Figure 2.10c in UPR). In the second case, downstream narrowing, the major event caused significant variations in the topography of the bed, creating new active bars that later, in the event of September 2019, were partially or totally destroyed. These morphological adjustments must have been caused by high stream power values concentrated in short distances -as already suggested by Conesa-García et al. (Conesa-García et al., 2020) for entrenched channel cross-sections- along stretches with sudden changes in bed roughness. This pattern has been found to be linked to channel degradation in semi-arid ephemeral streams (e.g., (Ortega et al., 2014; Hooke, 2006)).

However, we observed significantly different behaviour in the gravel beds studied here, where important transitory erosion was often followed by considerable replenishment of coarse-grained sediments, finally producing bed aggradation. The rest of the stretch showed slight changes in the inter-bends or runs transition zones and significant homogeneous variation in the final part, where progressive erosion downstream caused by the flash flood of April 2019 was partially offset by aggradation processes during the following minor event.

The Middle RCR presents two spatial patterns of geomorphic change: one of them around an extensive central bar (65 m long), characterized by important variations of different sign, depending on whether it is the anterior sector, the bar itself, or the posterior area in a downstream direction. At the back of the bar head, an incision of 0 to -0.5 m was observed, while the head and platform of the bar experienced vertical accretion in both events, and the tail suffered a lowering in height of up to -0.3 m. The minor event in September introduced hardly any variations in this reach except in the final part of the platform, which was lowered by around -0.4 m (Figure 2.10c in MDR). The second pattern, represented in the rest of the RCR, arises from a certain bed stability, only interrupted by slight alternative adjustments of incision and vertical accretion, resulting in net elevation differences between +0.2 and -0.2 m.

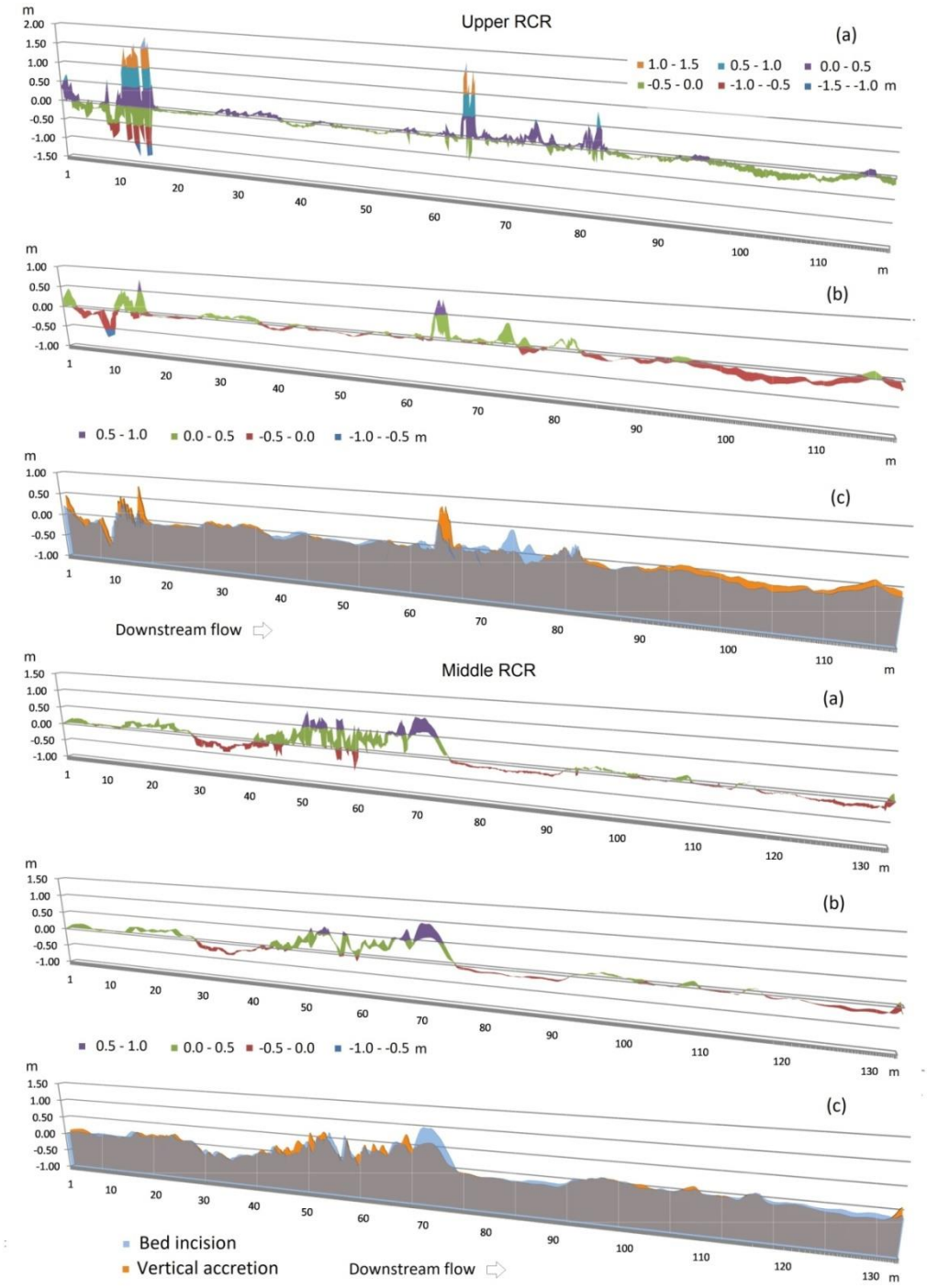


**Figure 2.10.** Thickness of the bed elevation differences caused by the flow peak of September 2019 in relation to those attributed to the flood of April 2019, using gross data with a 10-cm interval **(a)** and moving averages of band 9 **(b)** along the channel center line. The type **(c)** profiles represent the incision and aggradation sites for both peak flows with a band 9 smoothing. The profiles are based on TLS datasets.

### 2.4.3 Sediment budgets for different RGU in relation to stream power data and field surveys

In Table 2.4 are shown standard variables commonly used in sediment budgeting (sediment area and volume) for each representative geomorphic unit (RGU) and RCR, derived from SfM and TLS data, concerning the peak flows produced during their respective field surveys. As mentioned above, the SfM monitoring periods included one more event than those of the TLS; therefore, despite offering fairly similar surface area data for each RGU, they provided different volume data and errors.

Although the time interval considered (September 2018 to September 2019) is relatively short, and only covers one or two events, depending on the type of survey performed, the fact that almost all RGUs registered a positive total average balance in favor of deposition is striking (Table 2.4 and Figure 2.11). Only the inter-bar active bed in the Upper RCR scored a slightly negative budget, according to the TLS data, after the flash flood of April 19-20, 2019. This, added to the fact that the difference in average total thickness (ATTD) or the average unit volume difference (UVDA) for each RGU was always lower with TLS than with SfM, undoubtedly shows that the November 2018 peak flow, although lower than that of April 2019, also contributed to the deposition.

In summary, it can be considered that almost all the bed forms experienced over-sedimentation and, therefore, vertical accretion. The maximum accumulation produced after both events (0.18 to 0.23 $m^3/m^2$) took place on the active bed zones and on the scarcely vegetated gravel bars, which behaved as somewhat unstable forms (Table 2.4 and Figure 2.11). Even the main active bed in run stretches within the middle reach rose. The positive sediment budget in lateral tali and high bars could be misleading (ATTD around 0.20 m), but, nevertheless, corresponds to local collapses of material caused by basal undermining in high detrital banks (Figure 2.12.1 and 2.12.2) and lateral accretion by the adjoining of finer sediments (sand and gravel) in alternate and central bars (Figure 2.12.4). However, this contribution was not sufficient to explain the large imbalance between the average volume of sediment returned to the channel through bank collapse (equivalent to 11% of the total flux) and the net volume of sand and gravel deposited on the bars (66% of the total budget).

Consequently, most of the bedload mobilized and deposited in both stream stretches could come from upper sediment sources, associated with intense downcutting processes in deep gullies that dissect the apical zone of thick alluvial fans. López-Bermúdez et al. (López-Bermúdez et al., 2005), Harvey (Harvey, 2011) and Aguilar et al. (Aguilar et al., 2020) found similar results when studying steep alluvial fans dissected by gullies in semi-arid and arid environments. Simultaneously, low-order gravel bed tributaries at the headwaters currently develop high geomorphic activity, leading to considerable variations in downstream sediment yield, which is consistent with the pattern described by Lisle et al. (Lisle et al., 2000) and Yuill et al. (Yuill et al., 2010) for this type of EGBS.

**Table 2.4.** Descriptors used to evaluate sediment budgets (sediment area and volume), and the associated errors, for RGUs within each of the RCR, in periods overlapped by the initial SfM and TLS surveys between September 2018 and September 2019.

| | | | TAI | TVDA | | ATTD | | PI |
|---|---|---|---|---|---|---|---|---|
| **RCR** | **Method** | **RGU** | **$m^2$** | **$m^3$** | **% Error** | **m** | **% Error** | **%** |
| **UPR** | **SfM** | **Active inter-bar bed (a)** | **1367** | **318.2** | **0.043** | **0.233** | **0.043** | **0.50** |
| | | **Active non-vegetated bar (b)** | **321** | **73.4** | **0.043** | **0.228** | **0.043** | **0.50** |
| | | **Low, scarcely vegetated bar (c)** | **629** | **140.9** | **0.043** | **0.224** | **0.043** | **0.48** |
| | | **High, scarcely vegetated bar (e)** | **233** | **41.8** | **0.051** | **0.179** | **0.051** | **0.44** |
| | | **Vegetated talus or bank (j)** | **62** | **12.7** | **0.043** | **0.205** | **0.043** | **0.45** |
| | **TLS** | **Active inter-bar bed (a)** | **1371** | **-32.7** | **-0.287** | **-0.024** | **-0.287** | **-0.14** |
| | | **Active non-vegetated bar (b)** | **322** | **4.5** | **0.455** | **0.014** | **0.455** | **0.11** |
| | | **Low, scarcely vegetated bar (c)** | **647** | **35.3** | **0.121** | **0.055** | **0.121** | **0.19** |
| | | **High, scarcely vegetated bar (e)** | **235** | **11.9** | **0.134** | **0.051** | **0.134** | **0.16** |
| | | **Vegetated talus or bank (j)** | **65** | **10.7** | **0.044** | **0.165** | **0.044** | **0.35** |
| **MDR** | **SfM** | **Active inter-bar bed (a)** | **2270** | **497.4** | **0.045** | **0.219** | **0.045** | **0.49** |
| | | **Active non-vegetated bar (b)** | **790** | **141.7** | **0.052** | **0.179** | **0.052** | **0.48** |
| | | **Low, scarcely vegetated bar (c)** | **925** | **188.1** | **0.046** | **0.203** | **0.046** | **0.47** |
| | | **High, scarcely vegetated bar (e)** | **670** | **136.1** | **0.048** | **0.203** | **0.048** | **0.49** |
| | | **Scarcely vegetated talus (i)** | **97** | **20.0** | **0.048** | **0.207** | **0.048** | **0.49** |
| | **TLS** | **Active inter-bar bed (a)** | **2254** | **163.0** | **0.096** | **0.072** | **0.096** | **0.22** |
| | | **Active non-vegetated bar (b)** | **778** | **26.0** | **0.200** | **0.033** | **0.200** | **0.14** |
| | | **Low, scarcely vegetated bar (c)** | **919** | **105.2** | **0.063** | **0.114** | **0.063** | **0.29** |
| | | **High, scarcely vegetated bar (e)** | **669** | **100.7** | **0.050** | **0.150** | **0.050** | **0.33** |
| | | **Scarcely vegetated talus (i)** | **103** | **3.2** | **0.203** | **0.032** | **0.203** | **0.07** |

TAI = Total area of interest ($m^2$); TVDA = Total volume difference average ($m^3$); ATTD = Average total thickness difference (m) for Area of Interest; PI = Percent Imbalance (departure from equilibrium).

By comparing the sediment budgets obtained sing TLS after the flash flood of April 2019 with the stream power indicators referring to this event (see Figure 2.6), we observed that the $\omega/\omega_c$ ratio exerted a greater influence than $\partial\omega/\partial s$ on the incision and vertical accretion processes, depending on the predominant type of RGU in each set of cells. Specifically, in sites with dominant changing RGU - such as active channel interbars or runs (a), low, active non-vegetated bars (b) and low, scarcely vegetated bars (c) - strong relationships were found between the ATTD and the $\omega/\omega_c$ ratio ($r^2 \approx 0.89$ in both channel reaches). The relationship of ATTD with $\partial\omega/\partial s$ was also statistically significant, but not as strong as that with the average relative excess energy ($r^2 = 0.83$ and 0.66 in UPR and MDR respectively, p-Value < 0.05 for the 95%confidence interval). In any case, a different behaviour could be intuited in the most unstable bars of each of the RCR in relation to the ratios $\partial\omega/\partial s$ and $\omega/\omega_c$ estimated for each channel stretch. In the Upper RCR cell sets, where these RGU predominated, average values of $\partial\omega/\partial s$ and $\omega/\omega_c$ of -4.4 $Wm^{-2}/m$ and 2.3, respectively, were found, which led to a slight lowering in the active bed (ATTD = -0.024 m) and an average surface raising of only 5 cm in longitudinal non-vegetated bars (Figure 2.12.4). In contrast, smaller values of $\partial\omega/\partial s$ and $\omega/\omega_c$ (-1.6 $Wm^{-2}/m$ and 1.5, respectively) at the front and head of a mid-channel bar (central island), crossing the Middle RCR, caused a thicker deposit (ATTD of 11 to 15 cm) and greater morphological adjustments (Figure 2.12.5).

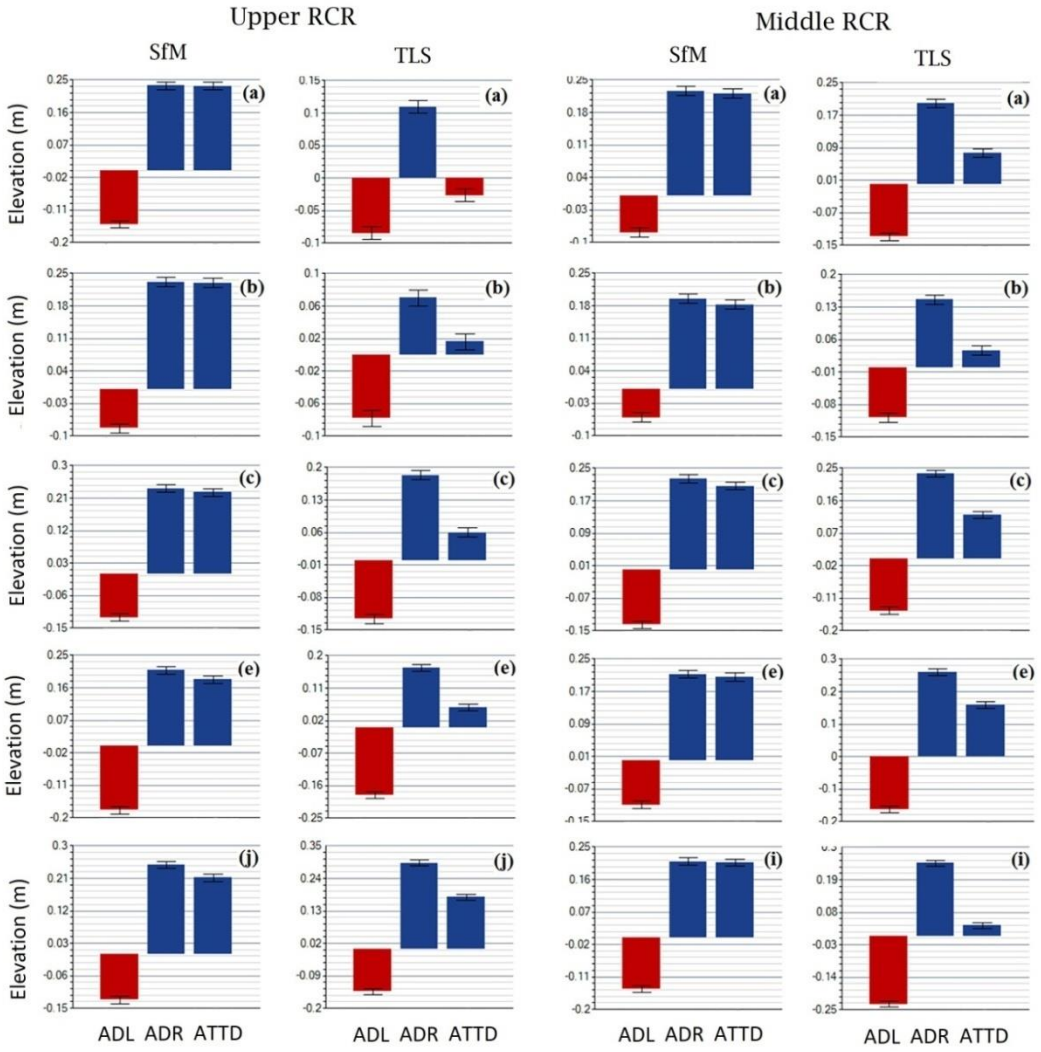

**Figure 2.11.** Average depth of lowering (ADL) and raising (ADR) and average total thickness difference (ATTD) obtained from SfM-MVS and TLS for the GRUs in the Upper and Middle RCR, after the peak flow of April 19-20, 2019. Letters refer to the RGU according to the legend in figure 2.5.

Field observations immediately after this event showed that such sediment budgets were accompanied by a relocation of the bed material and changes in bed texture. Along all the Upper RCR, riffles proved to be the most stable bedforms and preserved the coarsest particles. Also, a large amount of gravel was deposited on runs or pool exit-point bars in bed stretches, in agreement with the results obtained by Thompson et al. (Thompson et al., 1996) and Wohl (Wohl, 2000) in steep bed-gravel streams. In the ascending part of the hydrograph, the steepened water-surface gradients over alternate bars and runs in the Upper RCR must have promoted bed dissection and removal of finer particles, which were then stored in pools downstream. This geomorphic process was described by Lisle and Hilton (Lisle and Hilton, 1999) when studying the fine bed material in pools of natural gravel-bed channels.

**Figure 2.12.** Local material collapses in composite detrital banks after basal undermining caused by the flash flood of April 2019 **(1 and 2)**; entrainment and surface washing of non-cohesive basal bank deposits during the peak flow of September 2019 **(3)**; after the larger event, greater morphological adjustments occurred: lateral accretion of central longitudinal bars in the Upper RCR **(4)**, vertical accretion at the head of a central bar and slight incision on the thalweg bed in MDR **(5)**, a strong net deposition between the upper and Middle RCR (see the levelogger plate that was deeply buried) **(6)**, and high transitory erosion in the main active channel (see a clear example in the Upper RCR) **(7)**.

Downstream, in the Middle RSR new deposits at the head of the mid-bar referred to earlier contributed to raising its surface, mainly with sand and fine gravel (Figure 2.12.5). The somital platform of the central bar was not totally submerged and acted as a roughness element that must have locally increased the vertical velocity of the flow on the flanks, in turn driving the lateral vortex cells, with the consequent start or reactivation of entrainment of the less coarse particles. As the flow cells enlarged and moved locally, incision occurred in secondary active channels around the bar, increasing the bedload pulses downstream.

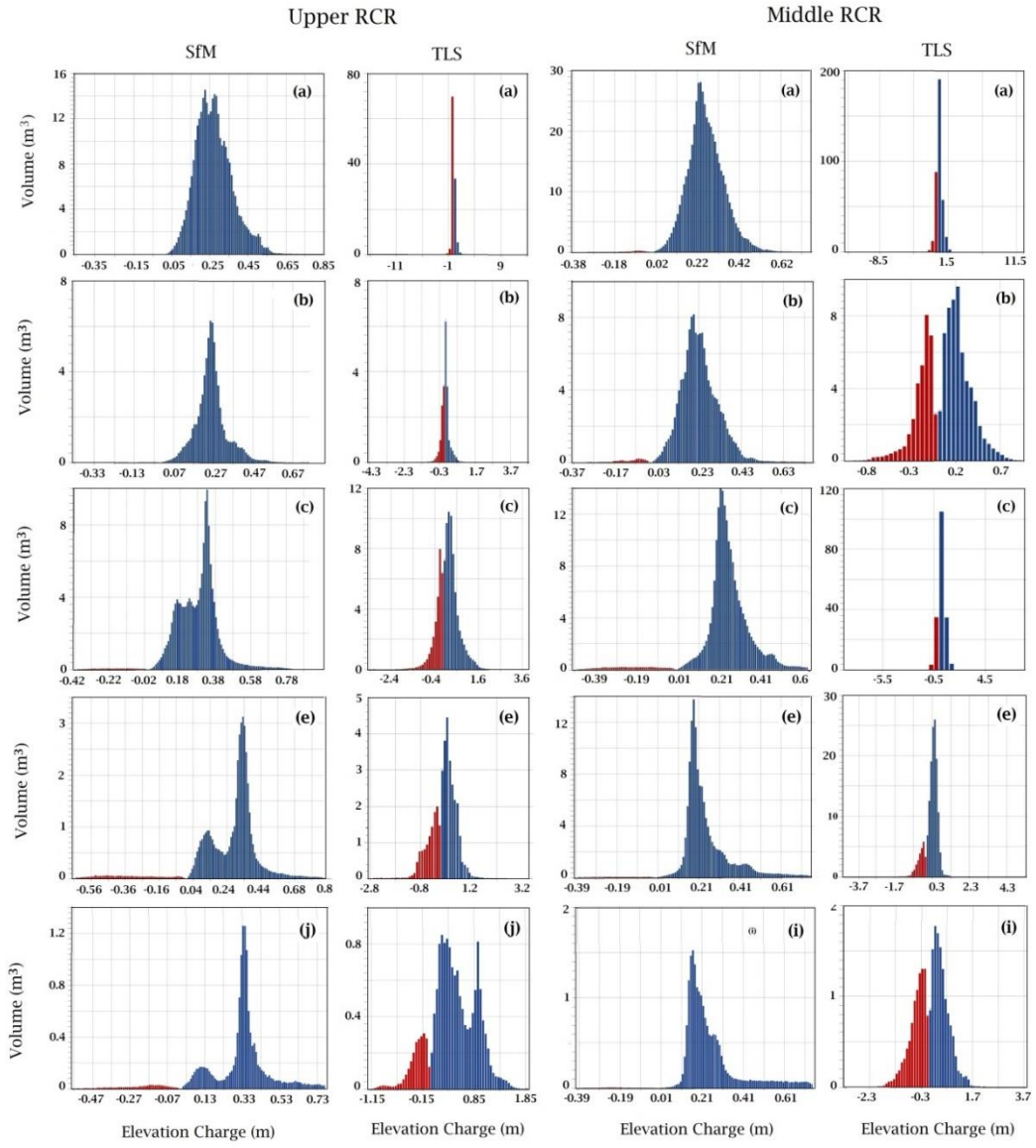

**Figure 2.13.** Differences in absolute net volumes versus variations in elevation (lowering and raising) of the bed surface detected with SfM and TLS for each GRU in the Upper and Middle RCR, after the peak flow of April 19-20, 2019. Letters refer to the RGU according to the legend in figure 2.5.

A similar contrast is provided by the comparison of the differences in absolute net volumes with the corresponding variations in elevation (negative or positive) detected with SfM and TLS. The total net deposition volumes were considerably higher than the erosion in all RGUs and in both RCR, according to the SfM data. Among these bedforms, within the Upper RCR, the active bed registered the highest absolute volume increase (12 to 14 $m^3$), associated with bed raising of 0.2 to 0.3 m (Figure 2.13). Active bars and unstable scarcely vegetated low bars also experienced a significant increase in volume, but with different ranges of heights. The largest net deposition volumes (from 4 to 8 $m^3$) meant increases in height from 0.15 to 0.30 m in the first case (leptokurtic distribution), and from 0.1 to 0.4 m in the second (dominant mesokurtic distribution). The high, sparsely vegetated bars and vegetated tali only exhibited occasional variations that had little impact on the overall channel adjustments. The Middle RCR showed a somewhat different pattern, characterized by Gaussian distributions and a single mode in most RGUs. Here, the active bed once again scored by far the highest volume charge, with maximums of 30 to 37 $m^3$ accompanied by the same bed rises (0.20 to 0.35 m) as in the Upper RCR. The rest of the bedforms received, with respect to the upstream reference reach, a greater sedimentary contribution, that did not translate into substantial morphological changes since the accretion height hardly varied. The reason for this could be the greater wetted channel width and the presence of transverse and central bars in the Middle RCR, compared to the relative channel narrowness and development of longitudinal bars in the upper reach.

The TLS results for the April event provided quite different patterns, with single-mode leptokurtic distributions in the most unstable bed forms: in a, b and c of the Upper RCR and in a and c of the Middle RCR. The only exception was in the behavior of the active bars without vegetation, whose distribution showed two pointed curves in the central part, representing modes of erosion (ADL of -0.1 to -0.2 m) and deposition (ADR of 0.20 to 0.35 m), respectively. This was probably due to unequal morphological adjustments, after transitory erosion occurred in both cases. Field observations verified lower rates of transitory erosion (only 5 cm for this event) in this morphosedimentary unit than in the active bed itself, where depths of 20 to 25 cm were reached (Figure 2.12.7). In the rest of the RGUs, the net volumes of deposition exceeded those of erosion.

On a local scale, it is worth noting the bimodal distribution observed in the scarcely vegetated banks or tali, especially in the Middle RCR, where the maximum volume of erosion supposed an average lowering of the bed surface of around 5 cm and that of deposition an average raising of 7 cm.

Consequently, all the patterns of spatial variability in the sediment budgets, described with SfM and TLS data, showed a clear tendency to increase bedload and granular bed armouring. The supplies of gravel in both RCR exceeded the volume of scour, causing an increasing alluvium that tends to make it more and more difficult to lower the bed surface by downcutting, increases the hydraulic resistance of the bed materials, and redirects the energy expenditure towards the banks. The result is a gradual widening of the channel

and an increase in the width-to-depth ratio, particularly significant in sites of the middle and lower reaches, not subject to geological constrictions.

## 2.5 Conclusions

An excess or deficit of sediment in a sediment budget implies different responses of the channel morphology and bed forms. In the case of EGBS, where the morphological adjustments are the product of complex flow dynamics at the event scale, the approach proposed here, based on the integrated use of UAV-SfM and TLS, has allowed this budget assessment to be satisfactorily addressed. Also, such an approach means economic savings and optimization of monitoring resources, through the synchronized application of both techniques, and the use of one or the other, depending on the magnitude of the event and the type of geomorphic change (overall channel adjustments or changes in bedforms). The SfM-MVS proved to be an appropriate technique for estimating sediment budgets in longer stream stretches, such as RCR over 100 m in length, while TLS provided excellent results for the determination of changes in bedload budgets at more detailed spatial scales (PBSA and RGU). Different complex morphodynamic processes, including total scouring-and-bedload transport and transitory erosion, that must have taken place simultaneously during each flood, could not be directly quantified.

Nevertheless, the sediment budgets expressed in terms of net bed elevations and volumes were calculated with high accuracy for the wetted channel perimeter and the RGU during the monitored peak flows. This information was very useful, especially when coupled with in situ observations made after each event and the stream power parameters, obtained from the calibrated 1D hydrodynamic model. The results from the study sites provided detailed information on the bed loading budgets, location of sediment sources and sinks, and changes in bedforms, but also contributed to a better knowledge of the current morphodynamic trend of this type of EGBS in semi-arid Mediterranean coastal areas. With the support of field research, several hypotheses were verified, the most significant of which relates the magnitude of the events with the geomorphic process and morphological adjustments: specifically, we found that large floods tend to produce vertical sedimentary accretion ($0.20 < ADR < 0.35$ m for a peak flow of 31 $m^3/s$ on April 20, 2019), after having mobilized a large amount of bedload upstream, due to high stream power gradients and excess energy ($-15 < \partial\omega/\partial s < 15$ $Wm^{-2}/m$; $\omega/\omega_c > 2$ for the same event). By contrast, more moderate peak flows ($\leq 10$ $m^3/s$) were only capable of exerting surface washing, selective transport, and local scouring, mainly affecting active low bars.

The lowest net thickness of deposition detected by SfM and TLS in the upper stretch ($ATTD < 0.06$ m) often masked an extraordinary mobility of the gravel deposits, crossing riffles and inter-bar runs, which could only be proved by measuring transitory erosion in the field (0.20 to 0.25 m at the Upper RCR). Regardless of the magnitude of the monitored events, bed armouring was identified in situ, which tends to make the bed more resistant to erosion in future floods. If an increase in the frequency of flash floods due to climate change is confirmed in southeastern Spain, it is foreseeable that in the short and medium term the trend of bed aggradation will continue in these ephemeral gravel streams, fed by the increasing inputs of coarse particles from the slopes, thus promoting lateral erosion and widening the channel, as has already occurred in more arid environments.

**Notation**

| | |
|---|---|
| $D_{50}$ | median grain size (m) |
| $D_{84}$ | particle size corresponding to the 84% of the sample weight (m) |
| $\partial\omega/\partial s$ | mean stream power gradient [$Wm^{-2}/m$] |
| $\gamma$ | specific weight of water ($N/m^3$), |
| i | cell ati cross-section |
| $\Omega$ | cross-sectional stream power [$W\ m^{-1}$] |
| $\omega$ | mean stream power [$Wm^{-2}$] |
| $\omega_c$ | critical mean stream power [$W\ m^{-2}$] |
| $\omega/\omega_c$ | |
| $q_p$ | peak unit flow ($m^3/s$) |
| $r^2$ | determination coefficient |
| $S_w$ | water surface slope [m m−1] |
| tb | base time (h) |
| tb* | base time of the unit hydrograph (h) |
| th | hydrograph duration (h) |
| tp | time of peak (h) |
| tp* | time of peak of the unit hydrograph (h) |
| w | water-surface width (m) |
| ADL | Average depth of lowering |
| ADR | Average depth of raising |
| ANTD | Average Net Thickness Difference (m) for the Area of Interest |
| ATTD | Average total thickness difference (m) for Area of Interest |
| 3DPC | 3D point cloud |
| EGBS | Ephemeral gravel bed stream |
| GCPs | Ground Control Points |
| GNSS | Global Navigation Satellite System |
| HRDTM | High-resolution Digital Terrain Models |
| MDR | Middle reach |
| MVS | Multi-View Stereo |
| OVR | Overall channel reach |
| PBSA | Pilot bed survey area |
| PI | Percent Imbalance (departure from equilibrium) |
| RCR | Reference channel reach |
| RGU | Representative geomorphic unit |
| RPAS | Remotely Piloted Air Systems |
| SfM | Structure from Motion |
| TAI | Total area of interest ($m^2$) |
| TASL | Total Area of Surface Lowering ($m^2$) |
| TASR | Total Area of Surface Raising ($m^2$) |
| TLS | Terrestrial Laser Scanner |
| TNVD | Total Net Volume Difference ($m^3$) |
| TVDA | Total volume difference average ($m^3$) |
| UAV | Unmanned aerial vehicles |
| UPR | Upper reach |
| UVSL | Average Unit Volume of Surface Lowering ($m^3$/m2) |
| UVSR | Average Unit Volume of Surface Raising ($m^3$/m2) |
| SD* | Standard Deviation of the Net Thickness Differences (m) |

## 2.6 References


Aguilar, G., Cabré, A., Fredes, V. and Villela, B., 2020. Erosion after an extreme storm event in an arid fluvial system of the southern Atacama Desert: an assessment of the magnitude, return time, and conditioning factors of erosion and debris flow generation. Nat. Hazards Earth Syst. Sci. 20, 1247–1265.

Ali, K.F.and De Boer, D.H., 2003. Construction of sediment budgets in large-scale drainage basins: the case of the upper Indus River. In Proceedings of the : Erosion Prediction in Ungauged Basins: Integrating Methods and Techniques (Proceedings of symposium HS01 held during IUGG2003 at Sapporo. July 2003); IAI-IS Publ: Sapporo; pp. 206–215.

Brasington, J., Langham, J. and Rumsby, B., 2003. Methodological sensitivity of morphometric estimates of coarse fluvial sediment transport. Geomorphology, 53, 299–316.

Brasington, J., Vericat, D. and Rychkov, I., 2012. Modeling river bed morphology, roughness, and surface sedimentology using high resolution terrestrial laser scanning. Water Resour. Res. 48.

Brodu, N. and Lague, D., 2012. 3D terrestrial lidar data classification of complex natural scenes using a multi-scale dimensionality criterion: Applications in geomorphology. ISPRS J. Photogramm. Remote Sens., 68, 121–134.

Bull, L.J. and Kirkby, M.J., 2002. Dryland rivers characteristics and concepts. In Dryland Rivers: Hydrology and Geomorphology of Semi-arid Channels; Bull, L.J., Kirkby, M.J., Eds.; John Wiley & Sons: Chichester, UK; pp. 3–15.

Calle, M., Alho, P. and Benito, G., 2018. Monitoring ephemeral river changes during floods with SfM photogrammetry. J. Iber. Geol. 44, 355–373.

Camporeale, C., Perona, P. and Ridolfi, L., 2006. Hydrological and geomorphological significance of riparian vegetation in drylands. In Dryland Ecohydrology; D'Odorico, P., Porporato, A., Eds.; Springer Verlag: Dordrecht, The Netherlands; pp. 161–179.

Chen, S.A., Michaelides, K., Grieve, S.W.D. and Singer, M.B., 2019. Aridity is expressed in river topography globally. Nature, 573, 573–577.

Clapuyt, F., Vanacker, V. and Van Oost, K., 2016. Reproducibility of UAV-based earth topography reconstructions based on Structure-from-Motion algorithms. Geomorphology, 260, 4–15.

CloudCompare [GPL software] http://cloudcompare.org/.

Conesa-Garcia, C., 1995. Torrential flow frequency and morphological adjustments of ephemeral channels in southeast Spain. In River Geomorphology; Hickin, E.J., Ed.; John Wiley & Sons: Chichester (UK); pp. 169–192.

Conesa-García, C., Pérez-Cutillas, P., García-Lorenzo, R., Eekhout, J., Gómez-Gutiérrez, Á., Millares-Valenzuela, A. and Martínez-Salvador, A., 2020. Dimensionless morphological ratios versus stream power variations at bankfull stage in an ephemeral channel. Geomorphology, 361, 19.

Conesa-García, C., Pérez-Cutillas, P., García-Lorenzo, R., Gómez-Gutiérrez, Á. Eekhout,

J., Ibisate, A., Ollero, A. and Horacio, J. 2019. Mapping spatial patterns of dimensionless ratios along an ephemeral channel using SfM photogrammetry. Geophys. Res. Abstr. 21 EGU2019.

Cook, K.L., 2017. An evaluation of the effectiveness of low-cost UAVs and structure from motion for geomorphic change detection. Geomorphology, 278, 195–208.

Eisenbeiss, H. and Sauerbier, M., 2011. Investigation of UAV systems and flight modes for photogrammetric applications. Photogramm. Rec, 26, 400–421.

Flatley, A. and Rutherfurd, I., 2018. Using Structure from Motion (SfM) to capture high resolution geomorphic units within small ephemeral channels. In Proceedings of the 20th EGU General Assembly, EGU2018; Austria; Vol. 20, p. 10896.

French, J.R., 2003. Airborne LiDAR in support of geomorphological and hydraulic modelling. Earth Surf. Process. Landforms, 28, 321–335.

Galea, A.B., Sadler, J.P., Hannah, D.M., Datry, T. and Dugdale, S.J., 2019. Mediterranean intermittent rivers and ephemeral streams: Challenges in monitoring complexity. Ecohydrology, 12.

Garzón, G. and Alonso, A., 2002. Comparison of the flood response of a braided and a meandering river, conditioned by anthropogenic and climatic changes. In Flood and megaflood processes and deposits: Recent and ancient examples; Martini, I.P., Baker, V.R., Garzón, G., Eds.; Blackwell Publishing Ltd: Oxford; p. 320 ISBN 978-1-444-30430-5.

Goodrich, D.C., Lane, L.J., Shillito, R.M., Miller, S.N., Syed, K.H. and Woolhiser, D.A., 1997. Linearity of basin response as a function of scale in a semiarid watershed. Water Resour. Res. 33, 2951–2965.

Graf, W.L. 1998. Fluvial Processes in Dryland Rivers; Springer-Verlag, Ed.; Berlin.

Harvey, A., 2011. Dryland Alluvial Fans. In Arid Zone Geomorphology: Process, Form and change in Drylands; John Wiley & Sons, Ltd: Chichester, UK; pp. 333–371.

Heritage, G.L. and Hetherington, D., 2007. Towards a protocol for laser scanning in fluvial geomorphology. Earth Surf. Process. Landforms, 32, 66–74.

Hooke, J.M. 2006. Human impacts on fluvial systems in the Mediterranean region. Geomorphology, 79, 311–335.

Kasprak, A., Wheaton, J.M., Ashmore, P.E., Hensleigh, J.W. and Peirce, S. 2015. The relationship between particle travel distance and channel morphology: Results from physical models of braided rivers. J. Geophys. Res. Earth Surf., 120, 55–74.

Lea, D.M. and Legleiter, C.J., 2016. Mapping spatial patterns of stream power and channel change along a gravel-bed river in northern Yellowstone. Geomorphology, 252, 66–79.

Legleiter, C.J. and Harrison, L.R. 2019. Remote Sensing of River Bathymetry: Evaluating a Range of Sensors, Platforms, and Algorithms on the Upper Sacramento River, California, USA. Water Resour. Res.2019, 55, 2142–2169.

Leopold, L.B., Wolman, M.G. and Miller, J.P., 1964. Fluvial Processes in Geomorphology; Dover Publications, Inc.: New York.

Lisle, T.E. and Hilton, S., 1999. Fine bed material in pools of natural gravel bed channels. Water Resour. Res., 35, 1291–1304.

Lisle, T.E., Nelson, J.M., Pitlick, J., Madej, M.A.and Barkett, B.L., 2000. Variability of bed mobility in natural, gravel-bed channels and adjustments to sediment load at local and reach scales. Water Resour. Res., 36, 3743–3755.

López-Bermúdez, F., Boix-Fayos, C., Solé-Benet, A., Albaladejo, J., Barberá, G.G., Del Barrio, G., Castillo, V., Garcia, J., Lázaro, R. and Martínez-Mena, M.D.2005.. Landscapes and desertification in south-east Spain. overview and field sites. In Proceedings of the Sixth International Conference on Geomorphology. Field Trip Guide - A5; Zaragoza, p. 40.

Marteau, B., Vericat, D., Gibbins, C., Batalla, R.J. and Green, D.R., 2017. Application of Structure-from-Motion photogrammetry to river restoration. In Proceedings of the Earth Surface Processes and Landforms; John Wiley and Sons Ltd., Vol. 42, pp. 503–515.

Martín-Vide, J.P., 1997. Ingeniería Fluvial; Edicions UPC, Universitat Politècnica de Catalunya: Barcelona; ISBN 9788498801569.

Merritt, D.M. and Wohl, E.E., 2003. Downstream hydraulic geometry and channel adjustment during a flood along an ephemeral, arid-region drainage. Geomorphology, 52, 165–180.

Mosbrucker, A.R., Major, J.J., Spicer, K.R. and Pitlick, J., 2017. Camera system considerations for geomorphic applications of SfM photogrammetry. Earth Surf. Process. Landforms, 42, 969–986.

Nanía, L.S., 2007. Manual Básico de HEC-HMS 3.0.0 y HEC-GeoHMS 1.1; Granada.

Nanía, L.S. and Gómez Valentín, M., 2006. Ingeniería Hidrológica; Grupo Editorial Universitario. Granada, Ed.; ISBN 84-8491-636-7.

Norman, L.M., Sankey, J.B., Dean, D., Caster, J., Delong, S., Delong, W. and Pelletier, J.D., 2017. Quantifying geomorphic change at ephemeral stream restoration sites using a coupled-model approach. Geomorphology, 283, 1–16.

Notebaert, B., Verstraeten, G., Govers, G. and Poesen, J., 2009. Qualitative and quantitative applications of LiDAR imagery in fluvial geomorphology. Earth Surf. Process. Landforms, 34, 217–231.

Ortega, J.A., Razola, L. and Garzón, G., 2014. Recent human impacts and change in dynamics and morphology of ephemeral rivers. Nat. Hazards Earth Syst. Sci., 14, 713–730.

Parker, C., Clifford, N.J. and Thorne, C.R., 2011. Understanding the influence of slope on the threshold of coarse grain motion: Revisiting critical stream power. Geomorphology, 126, 51–65.

Picco, L., Mao, L., Cavalli, M., Buzzi, E., Rainato, R. and Lenzi, M.A., 2013. Evaluating short-term morphological changes in a gravel-bed braided river using terrestrial laser scanner. Geomorphology, 201, 323–334.

Proyecto NATMUR-08 Catálogo de Geoservicios de Medio Natural, Vuelo fotogramétrico digital y levantamiento LIDAR de la Región de Murcia. Available

online: http://www.murcianatural.carm.es/natmur08/ (accessed on Sep 2, 2018).

Puig-Mengual, C., Woodget, A.S., Muñoz-Mas, R. and Martinez-Capel, F., 2021. Spatial validation of submerged fluvial topographic models by mesohabitat units. International Journal of Remote Sensing, 42, 2391-2416.

Puig-Mengual, C., Martínez-Capel, F., Woodget, A.S. and Muñoz-Mas, R., 2017. DEM generation in a Mediterranean river using Structure From Motion algorithm on HD video recorded from a UAV (Palancia River, Spain). In Proceedings of the Proceedings of HydroSenSoft, International Symposium and Exhibition on Hydro-Environment Sensors and Software; Madrid, Spain.

Reid, I. and Frostick, L.E., 2011. Channel form, flows and sediments of endogenous ephemeral rivers in deserts. In Arid Zone Geomorphology: Process, Form and Change in Drylands; Thomas, D.S.G., Ed.; Chichester, UK; pp. 301–332.

Remondino, F., Barazzetti, L., Nex, F., Scaioni, M. and Sarazzi, D., 2011. UAV photogrammetry for mapping and 3d modeling–current status and future perspectives. ISPRS - Int. Arch. Photogramm. Remote Sens. Spat. Inf. Sci., 38, 25–31.

Rowley, T., Ursic, M., Konsoer, K., Langendon, E., Mutschler, M., Sampey, J and Pocwiardowski, P., 2020. Comparison of terrestrial lidar, SfM, and MBES resolution and accuracy for geomorphic analyses in physical systems that experience subaerial and subaqueous conditions. Geomorphology, 355, 107056.

Salmela, J., Kasvi, E., Vaaja, M.T., Kaartinen, H., Kukko, A., Jaakkola, A. and Alho, P., 2020. Morphological changes and riffle-pool dynamics related to flow in a meandering river channel based on a 5-year monitoring period using close-range remote sensing. Geomorphology, 352, 106982.

Scharffenberg, W.A. and Fleming, M.J., 2010. Hydrologic Modelling System HEC-HMS. User`s Manual. Version 3.5.; US Army Corps of Engineers, Ed.; Davis, California.

SCS (Soil Conservation Service) National Engineering Handbook; Section 4. U.S. Department of Agriculture Washington D.C., Ed.; 1972;

Segura-Beltrán, F. and Sanchis-Ibor, C., 2013. Assessment of channel changes in a Mediterranean ephemeral stream since the early twentieth century. The Rambla de Cervera, eastern Spain. Geomorphology, 201, 199–214.

Shaw, J.R. and Cooper, D.J., 2008. Linkages among watersheds, stream reaches, and riparian vegetation in dryland ephemeral stream networks. J. Hydrol., 350, 68–82.

Shintani, C. and Fonstad, M.A., 2017. Comparing remote-sensing techniques collecting bathymetric data from a gravel-bed river. Int. J. Remote Sens., 38, 2883–2902.

Singer, M.B. and Michaelides, K., 2014. How is topographic simplicity maintained in ephemeral dryland channels? Geology, 42, 1091–1094.

Sutfin, N.A., Shaw, J., Wohl, E.E. and Cooper, D., 2014. A geomorphic classification of ephemeral channels in a mountainous, arid region, southwestern Arizona, USA. Geomorphology, 221, 164–175.

Thompson, D.M., Wohl, E.E. and Jarrett, R.D., 1996. A revised velocity-reversal and

sediment-sorting model for a high-gradient, pool-riffle stream. Phys. Geogr., 17, 142–156.

Tonina, D., McKean, J.A., Benjankar, R.M., Wright, C.W., Goode, J.R., Chen, Q., Reeder, W.J., Carmichael, R.A. and Edmondson, M.R., 2019. Mapping river bathymetries: Evaluating topobathymetric LiDAR survey. Earth Surf. Process. Landforms2019, 44, 507–520.

Török, G., Baranya, S. and Rüther, N., 2017. 3D CFD Modeling of Local Scouring, Bed Armoring and Sediment Deposition. Water, 9, 56.

USACE (US Army Corps of Engineers) HEC-RAS, Rivers Analysis System. Hydraulic Reference Manual, version 5.0; Hydrologic Engineering Center, USA: Davis, California, 2016.

Vázquez-Tarrío, D., Borgniet, L., Liébault, F. and Recking, A., 2017. Using UAS optical imagery and SfM photogrammetry to characterize the surface grain size of gravel bars in a braided river (Vénéon River, French Alps). Geomorphology, 285, 94–105.

Wasson, R.J., 2002. Sediment budgets, dynamics, and variability: new approaches and techniques. In Proceedings of the The Structure, Function and Management Implications of Fluvial Sedimentary Systems; IAHS Publ: Alice Springs, Australia.

Wohl, E., 2000. Mountain Rivers. Water Resources Monograph 14; Uniom, A.G., Ed.; Washington DC, USA.

Yuill, B., Nichols, M. and Yager, E., 2010. Coarse bed material patch evolution in low-order, ephemeral channels. Catena, 81, 126–136.

Zapico, I., Laronne, J.B., Lucía, A. and Martín-Duque, J.F.,2018. Morpho-textural implications to bedload flux and texture in the sand-gravel ephemeral Poveda Gully. Geomorphology, 322, 53–65.

# 3. Changes in stream power and morphological adjustments at the event-scale and high spatial resolution along an ephemeral gravel-bed channel


## Abstract

Sediment budgets and morphological channel adjustments are closely related to changes in stream power. In ephemeral channels, whose geomorphic response depends on the magnitude and frequency of discrete hydrological events isolated in time, such relationships are often difficult to establish. This study sought to quantitatively relate morphological adjustments to stream power along different reference channel reaches for the period 2018-2020 in the Azohía Rambla, a Mediterranean gravel-bed ephemeral stream in southeastern Spain. Very high resolution digital terrain models (VHRDTM), combined with ortophotographs and 3D point clouds, generated via SfM photogrammetry and terrestrial laser scanning (TLS) for pre- and post-event stages, together with ground-based surveys were used to estimate the spatial variability of morphological sediment budgets and to assess channel bed mobility and changes in net sediment flux during the study period in two spatial scenarios: reference channel reaches (RCRs) and pilot bed survey areas (PBSAs).The hydraulic variables (flow velocity, Froude number, shear stress, mean stream power and energy gradient, among other) were estimated using a 1D hydrodynamic model calibrated with field information. The high resolution maps allowed a spatially-explicit analysis of stream power and transport efficiency in accordance with the areas of erosion and deposition in each RCR. The incision and bed armoring processes showed different trends according to the stream power ($\omega$), cumulative excess energy ($\varepsilon_c$), and relative bed stability (RBS). The greatest morphological adjustments at the event scale coincided with $\omega$ values above 300 $Wm^{-2}$, $\varepsilon_c$ higher than 3 MJ, and RBS below 0.5. The relationships between the mean stream power gradient at peak flood discharges and the changes in bed elevation verified the bed aggradation (an average surface raising of 0.17 to 0.22 m for $\delta\omega/\delta s$ of -6.2 to -14.5 $Wm^{-2}/m$) during the major flood and bed scour (average surface lowering of 0.16 to 0.19 m for $\delta\omega/\delta s$ of 5.8 to 10.6 $Wm^{-2}/m$)in the moderated events at the bankfull and sub-bankfull stages.



**Keywords:** Stream power, morphological sediment budget, bedforms, SfM photogrammetry, terrestrial laser scanning, gravel-bed ephemeral channel, Southeastern Spain.

## 3.1 Introduction

Bed permeability and transmission losses, transport of mixed grain size materials, and especially the episodic and sudden nature of runoff events, are factors that make it quite difficult to get flow rates and assess morphodynamics in ephemeral gravel channels. In these streams sediment budgets and morphological channel adjustments depend on runoff, which is mainly controlled by the type of rainfall and the environmental conditions of the watershed area and the channel itself (Rojan et al., 2020). Particularly in arid and semiarid basins, they are settings for extreme morphological dynamics, associated with irregular and torrential peak flows, capable of reaching very high stream power values and sediment loads. The geomorphic response of these dry streams varies according to the magnitude and frequency of the flow events, which are especially sensitive to short-term climatic changes and human impacts (Segura-Beltrán and Sanchis-Ibor, 2013; Conesa-García et al., 2020a). The nature and impact of this response depend on the entity of each event, since larger and more energetic discharges mobilize and deposit a greater bed load, and minor events promote scouring and down-cutting phenomena (Pryor et al., 2014; Lotsari et al., 2018). The consequent effects vary from local bedform disturbances in low-flow stages to overall channel adjustments after flash floods (Conesa-García et al., 1995; Benito et al., 2011; Norman et al., 2017).

Evaluation of the magnitude of geomorphic changes in ephemeral gravel-bed streams (EGBSs) is difficult because of the lack of gauging records, the permeability of the bed, abrupt variations in bedload, and their highly changeable hydromorphological dynamics. This explains why the literature on EGBSs is relatively scarce and requires more effort on empirical analysis and morphodynamic modeling (Bizzi and Lerner, 2015, Lotsari et al., 2018). In particular, the spatial and temporal morphological variability in EGBSs, as a function of variations in stream power, has been little studied (Levick et al., 2008; Ortega et al., 2014). Sutfin et al. (2014) proposed a non-metric multidimensional scale ordering, based on geometric and hydraulic variables: width-to-depth ratio (W/D), stream gradient (S), stream power ($\Omega$), and shear stress ($\tau$). Other authors related morphological adjustments in EGBSs to systematic changes in the mean stream power ($\omega$) / resisting power ($\omega_c$) ratio ($\omega/\omega_c$) (Bull, 1997), and hence in the transport efficiency, associated with the mean stream power gradient ($\partial\omega/\partial s$) and excess energy (Conesa-García et al., 2020b). Nor are there many studies aimed at evaluating these morphological changes in relation to erosion volumes, deposition, and sediment transport (sediment budgets) on a detailed scale. The multi-temporal application of very high resolution digital terrain models (VHRDTM) (pixel size <5 cm), generated using Structure-from-Motion Multi-View Stereo (SfM-MVS) from low-altitude unmanned aerial vehicles (UAV), has recently demonstrated its proficiency in the monitoring of submerged physical habitats of perennial and temporary streams (Woodget et al., 2019; Rowley et al., 2020; Salmela et al., 2020; Puig-Mengual et al., 2021) and morphological adjustments in dry channels (Calle et al., 2018; Flatley and Rutherfurd, 2018; Galea et al., 2019; Conesa-García et al., 2020a,b). Furthermore, this ability also extends to the detailed analysis of stream bed grain size and bedforms (Woodget and Austrums 2017; Vázquez-Tarrío et al., 2017) as well as rapid geomorphic changes, which affect the fluvial ecosystem dynamics (Rusnák et al., 2018). In addition, the 3D point clouds (3DPC) and VHR DTM, produced using terrestrial laser scanning (TLS), with a pixel size lower than 3 cm, offers higher performance to detect spatial differences in surface bed texture caused by specific events (Notebaert et al., 2009; Conesa-García et al., 2020a).

In this paper we propose an approach to assess, at the event scale, the relationships between sediment fluxes and stream power along an ephemeral gravel-bed channel, combining VHRDTM, provided by SfM-MVS and TLS, and a 1D hydrodynamic model calibrated using field information. Specifically, there were two primary objectives: (1) to detect spatio-temporal patterns of sediment budgets and morphological adjustments along stream reaches with high bedload, and (2) to evaluate the relationships between changes in stream power and variations in erosion and deposition rates. These objectives were achieved in three steps: 1) the 3DPC datasets were used to test significant changes in height and volume after each event in reference channel reaches (RCRs) and pilot bed survey areas (PBSAs); 2) the results of hydraulic modeling during flash floods, including flow competence and bed stability indices, were analyzed at the cell scale; 3) erosion values, deposition, and net sediment flux were averaged for each budget cell from datasets of SfM and TLS; 4) the resulting maps of stream power, total volume difference average, and net thickness difference were combined to determine spatial relationships between these variables for each event. The work related to the first objective was focused on defining the spatial patterns of bed elevation changes, and associated processes of erosion and deposition, attributable to the magnitude of the flood or the combination of events.

To test the second objective different hypotheses were examined:

(1) Spatial changes in ω values do not have a direct relationship with variations in bed stability associated with variable critical bed-shear stress and moving bed forms.
(2) The ω thresholds usually related to morphological changes in perennial gravel streams may differ from those required in unstable, ephemeral gravel-bed channels.
(3) The variability patterns of ω reflect the fluctuations in the flow velocity, shear stress, and Froude number.
(4) Greater changes in bed elevation and net sediment flux are mainly due to larger positive and negative values of the mean stream power gradient ($\partial\omega/\partial s$) and the ω/ωc ratio.
(5) Sites with the greatest ω/ωc ratios will have the highest values of cumulative excess energy per unit bed area ($\varepsilon_c$) and total sediment flux (T), which will promote bed scouring and vertical accretion processes. Conversely, locations where $\omega_c$equals or surpasses ωwill show the lowest $\varepsilon_c$ and T, and the most stable bedforms.

## 3.2 Study area and environmental setting

This research was carried out in the Azohía Rambla, an EGBS draining a small coastal mountainous basin (13 $km^2$) in southeastern Spain (Region of Murcia) (Figure 3.1). The study site is located in the Internal Zones of the eastern Betic Cordillera, so it takes part in the geological characteristics of its three major complexes (Nevado-Filábride, Alpujárride, and Maláguide) (Egeler and Simon, 1969). The present-day contacts of these complexes are extensional detachments and low-angle normal faults. Metamorphic, poorly permeable materials (mainly phyllites, schists, and quartzites), of Permian and Triassic age, mainly appear in the headwater areas, while Quaternary detrital sediment and Miocene marls predominate in the alluvial fans and marginal zones of the valley bottom, respectively.

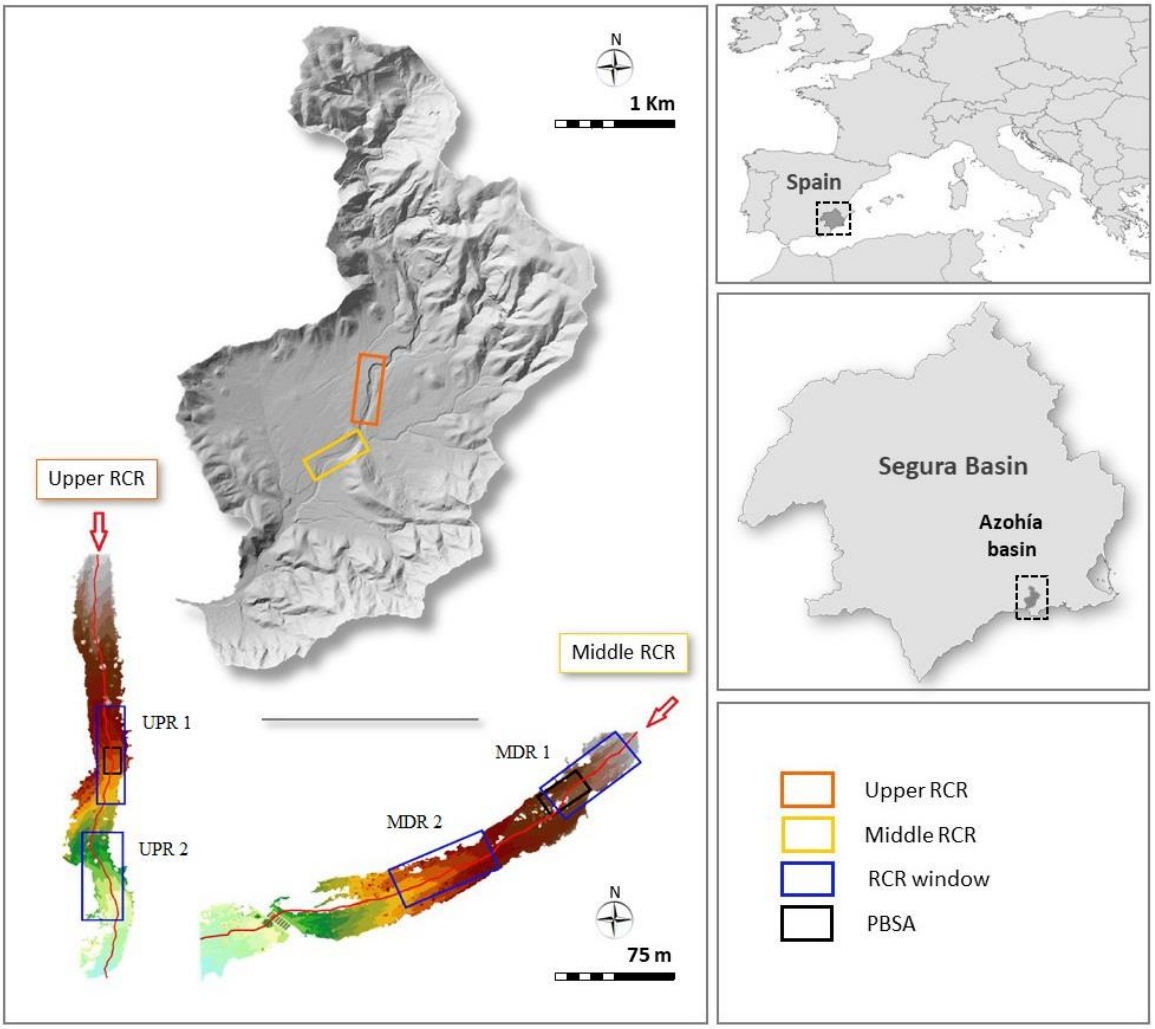


**Figure 3.1**. Location of the study area (Azohía Rambla basin) in southeastern Spain, and indication of the monitored channel reaches (upper and middle RCRs and their respective PBSAs).

Semiarid environmental conditions (precipitation of 310 mm/year, with a maximum 30-minute rainfall intensity above 50 mm $h^{-1}$, extreme droughts, and very high monthly potential evapotranspiration values (> 140 mm in the summer months) play a relevant role here in weathering and erosion processes. Added to this is scarce vegetation cover and steep slopes, which often lead to large flash floods and intense fluvial geomorphic activity. A dense network of steep gullies in the headwaters area and detrital channel banks act as highly productive sources of sediment, especially coarse material (gravel and pebbles). As a result, the Rambla de la Azohía exhibits an active morphodynamics (rapid changes in bedform type and channel geometry). Two RCRs (the upper and middle RCR), of 160 m in length, were chosen based on the accessibility and type of geomorphic adjustment. These stream stretches better represent the changes in stream power and their relationships with the variations in net sediment fluxes and bedforms. In contrast, in the lower reach, global changes are the product of sediment-laden floodwater spills, affecting crevasse splays and a wide, active flood bed, making it difficult to apply this approach (Ali and De Boer, 2003).

## 3.3 Materials and methods

VHRDTM derived from UAV-SfM, Global Navigation Satellite System (GNSS) data, and TLS were used to determine sediment budgets and changes in bed elevation in pre- and post-event stages and to establish the topographic base before each flash flood. In both RCRs, erosion and deposition areas and volumes were obtained at the pixel level for each event, while at the cell scale morphological sediment budgets and net sediment fluxes were averaged. The hydraulic datasets were obtained from the application of a 1D hydrodynamic model fed by theoretical hydrographs, previously calibrated and validated with direct water measurements during the runoff, made using pressure sensors. Using a GIS to integrate all this information, spatial sediment budgets and stream power values were mapped and their relationships were calculated under different balances (negative or positive) between $\omega$ and $\omega_c$ for each pair of consecutive cells. Seven significant rainfall events (>35 mm/day) occurred in the analysis period (September 18, 2018 to January 9, 2021), but only three of them generated peak discharges capable of causing perceptible geomorphic effects: a larger one, characterised by a bank overtopping discharge (flash flood of 19–20 April 2019), and two other moderate peak discharges at bankfull and sub-bankfull stages, the peak flow of 24 March 2020, and 12 September 2019, respectively (Table 3.1).

**Table 3.1.** Dates of occurrence of flow events and field surveys using UAV-SfM and/or TLS techniques, with indication of rainfall data and peak discharges for each channel reach.

| Event/ Field Survey | Date | P (mm) | Rainfall Duration (h) | I1h (mm $h^{-1}$) | I30' (mm $h^{-1}$) | Qp ($m^3$ $s^{-1}$) | | |
|---|---|---|---|---|---|---|---|---|
| | | | | | | UPR | MDR | LWR |
| UAV-SfM | 18 September, 2018 | | | | | | | |
| Peakflow | 18 November, 2018 | 35.6 | 9.3 | 17.6 | 32.4 | 0.1 | 0.1 | 0.2 |
| TLS | 29 November, 2018 | | | | | | | |
| Peakflow | 19-20 April, 2019 | 123.2 | 21.2 | 37.3 | 46.0 | 21.9 | 31.3 | 46.1 |
| UAV-SfM/TLS | 5 September, 2019 | | | | | | | |
| Peakflow | 12 September, 2019 | 93.9 | 16.9 | 20.2 | 26.4 | 8.4 | 10.9 | 15.1 |
| Peakflow | 2 December, 2019 | 59.3 | 20.3 | 9.8 | 17.8 | 1.2 | 1.7 | 2.9 |
| TLS | 16 January, 2020 | | | | | | | |
| PeakFlow | 20 January, 2020 | 66.3 | 20.8 | 10.6 | 12.8 | 2.7 | 3.6 | 5 |
| Peakflow | 23-24 March, 2020 | 119.3 | 34.2 | 22.9 | 28.8 | 11,6 | 15,4 | 20,8 |
| UAV-SfM/TLS | 26 July, 2020 | | | | | | | |
| Peakflow | 9 January, 2021 | 41.0 | 34.0 | 2.7 | - | 0.3 | 0.4 | 0.8 |

P = precipitation (mm); Qp = peak discharge ($m^3$ $s^{-1}$); I1h = rainfall intensity (mm $h^{-1}$); I30' = maximum 30-minute rainfall intensity (mm $h^{-1}$); UPR = upper channel reach; MDR = middle reach; and LWR = lower reach.

Specifically, five follow-up stages resulted from the combination of the two techniques. Two of them were covered by SfM data: 1) September 2018 to September 2019, including the events of November 18, 2018 and April 19-20, 2019, and 2) September 2019 to July 2020, during which four moderate or low peak flows occurred. The other three survey periods were defined from the TLS surveys: 3) December 2018 to September 2019, including only the flash flood from April 19 to 20, 2019, 4) September 2019 to January 2020, in which the flood of September 12-13, 2019, was the key event, and 5) January 2020 to July 2020, which monitored the peak flow on March 24, 2020. Changes in morphological sediment budgets were quantified for all stages using channel-

bed pixels extracted from the two types of VHR MDT. However, relationships between stream power variables and changes in bed elevation and bedload sediment mass balance at the event scale could only be analyzed with the pre and post-event TLS surveys.

### 3.3.1. Changes in ground elevation and sediment budgets derived from VHR MDT datasets

Changes in bed elevation, areas and volumes of erosion and deposition, and sediment fluxes (net -ΔV- and total -T- flux) were calculated for both RCRs (upper -UPR- and middle -MDR- stretches) using VHR MDT and high-density 3DPC, generated from the SfM-MVS and TLS surveys. In particular, average difference in total volume, net thickness difference, total area of surface lowering and raising, and percent imbalance (departure from equilibrium), among other variables, were provided by both techniques for the two RCRs. Comparison of each pair of successive high resolution images at the pixel level (2-3 cm pixel size) yielded very good accuracy in the calculation of sediment budgets based on the monitored events. The errors associated with these estimates were described and assumed for each comparative survey analysis, according to Brasington et al. (2003). The areas with the highest density 3DPC (PSBAs) were used to monitor modifications of the detail in the bedforms.

#### *3.3.1.1. SfM-MVS photogrammetry*

The selected channel stretches and adjacent areas were surveyed using a Phantom 4 Pro, with a 20-Mp camera and 1-inch sensor, at an average flight height of 50 m, in order to gain very high resolution aerial images (≈ 1-2 cm resolution). The flight track and common parameters were pre-programmed for the software tool DJI GS Pro© for all the surveys. Ground Control Points (GCPs) and Check Points (CPs) were established in the field, using coded targets printed from Agisoft PhotoScan Pro 1.2.2 © software (Agisoft, Russia). In each of the surveys, approximately 66 % of the measured points corresponded to GCPs, for geo-referencing purposes, and the remainder corresponded to CPs for the validation of the VHRDTM (Conesa et al., 2020a; Puig-Mengual et al., 2021). The topographic survey of the coded marks was carried out by a GPS-RTK Prexiso G5 © station (Leica, Germany), connected via a mobile signal to the regional network of differential corrections, GPS GNSS (Network of Reference Stations in the Region of Murcia "Meristemum"). Among these points, some were permanently marked with FENO survey markers. All field support points were measured in the WGS84 global reference system.

In order to ensure the correct definition of homologous points between images, consistent overlaps of 80 to 90% were applied (Seifert et al., 2019). The captured images, the GCPs, and the CPs were used in the Agisoft PhotoScan Pro v.1.2.2© (Agisoft, Russia) structure-from-motion photogrammetry software, which allowed the generation of point clouds, a continuous textured mesh, VHR DTM (pixel size 0.02 m), and an orthomosaic (Conesa et al., 2020a; Puig-Mengual et al., 2021). These final products were geo-referenced in a global system (WGS84) for further analysis. The digital elevation model of the topographic difference (DoD) between the UAVs-collected VHR DTM in different field surveys, as well as between the TLS-generated VHR DTM, was developed in ArcGis 10.5© (ESRI, USA), by subtraction of the final topography from the previous one for the same area (Wheaton et al., 2010). The extraction mask for the water sheet at different peak flows in each RCR was applied to all the DoDs, thus enabling the precise

comparison of the morphological channel changes and sediment budgets associated with each event.

*3.3.1.2. Terrestrial Laser Scanning (TLS)*

A Leica ScanStation C10 model terrestrial 3D laser scanner was used to get a high resolution sediment budget. This scanner captures point cloud geometrical information at a velocity of 50,000 points per second at a distance of up to 300 m, with a precision of 2 mm. This information was combined with high resolution and high quality 2D RGB true color camera information. Multiple overlapped scans were performed from different benchmarks intentionally selected along the channel bed to cover the total area of interest for a detailed geometrical definition. The output 3D point clouds (3DPC) were then registered, using HDS targets from the dataset of September 5th, 2019 as the master 3DPC for all the TLS scans. On this date a field survey was jointly carried out with SfM-MVS, using FENO survey marks as the common reference for both techniques, TLS and UAV-derived 3DPC. The scans performed in November 2018, January 2020, and June 2020 were registered at that benchmark, with a mean error of 2 mm, using the iterative closest point (ICP) plugin of CloudCompare software and some stable nearby buildings as reference points. Then, the differences in elevation and the volume changes after each flow event were calculated for both pilot bed survey areas (PBSAs), one within the upper RCR (8.55 x 17.7 m) and the second in the middle RCR (16.3 x 27.55 m). The vegetation, mainly composed of scrubs and shrubs, was removed using the CANUPO CloudCompare plugin (Brodu and Lague, 2012; Girardeau-Montaut, 2020; Lague et al., 2013). Subsequently, the 3DPC data captured for the different dates were rasterized, resulting in a 5-cm grid, and were interpolated for those pixels in which no TLS information was available. Figure 3.2 shows the steps taken to reach the rasterized 3D point cloud, once the vegetation cover had been removed.

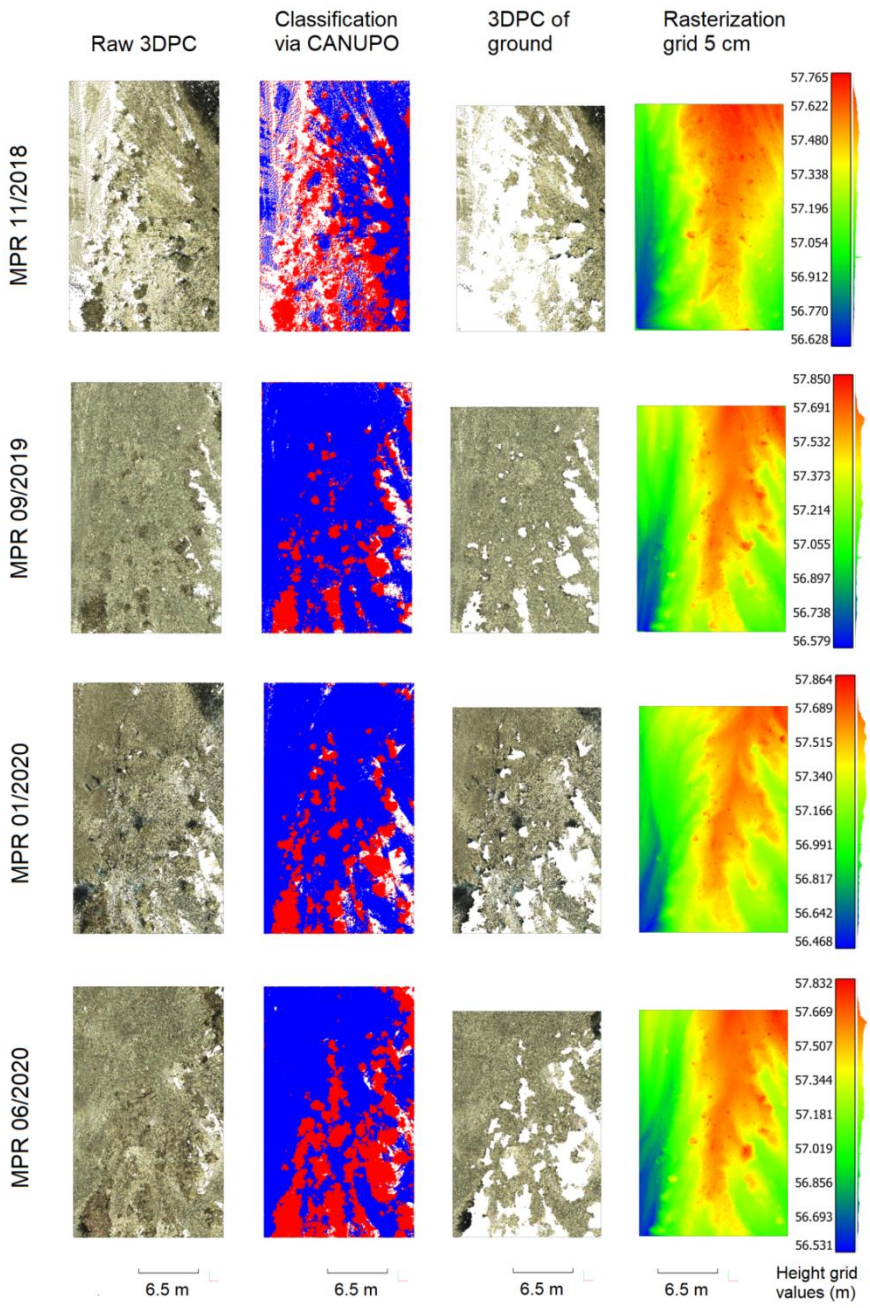


**Figure 3.2.** Rasterization process for the MPR presented as a grid. Each row corresponds to a scan and the labels show the respective dates. The first column shows the raw 3DPC, the second the classification using CANUPO (Lague et al., 2013), the third the extraction of the ground points, and the fourth the rasterized 3DPC.

*3.3.1.3. Morphological sediment budgets at the cell scale*

Areas of erosion and deposition were quantified by comparing each pair of successive VHR DTM and high-density 3DPC generated from SfM-MVS and TLS surveys, respectively. The resulting bed elevation change maps were used to determine sediment budgets within a series of 212 budget cells with a lateral extent defined by the union of the water sheet polygons for each flood event and a downstream length of 2.5-3.0 m. Average bed elevation differences were calculated for each budget cell from all the pixel values in that cell. Net sediment fluxes ($\Delta V$) were given for each budget cell

and for the entire 160 m upper and middle RCRs by expressing negative (bed scouring) or positive (vertical accretion) differences in bed elevation, while total sediment flux (T) was calculated as the sum of gross erosion (E) and gross deposition (D).

### 3.3.2. Rainfall-runoff method and hydraulic modeling

Hydrographs were estimated using a rainfall-runoff model, at the beginning of each RCR, for the flood events that occurred during the analysis period (2018-2021). Field indicators, such as evidence of high-water marks (HWM), and water levels measured by pressure sensors (Levelogger Edge LT and Baralogger Edge) were used to test and calibrate the hydrograph data for each event. The most common HWM found were vegetation debris, which may be close to the water level during peak flow. In addition, pressure level sensors (PLS) were placed between both RCRs. The barometric compensation was automatically performed, so the delay to compensate for the fluctuations in atmospheric pressure recorded by the levelogger was minimal, leading to accurate water level data. The SCS dimensionless unit hydrograph (SCS, 1972) was calculated for the soil moisture conditions before rainfall-produced floods and from hyetograph data for intervals of 5 minutes at the Cuesta del Cedacero station. By combining the HEC-HMS 3.5 program, the HEC-GeoHMS 1.1 of ArcView 3.x, and a DTM with a grid resolution of 4 × 4 m (Project Natmur, 2008), we generated the drainage networks and watersheet areas. As the main hydrological abstraction, the infiltration curve number (NC) of each sub-basin was used. Maps were drawn up in a GIS environment to define soil types, vegetation, and slopes, using the lithological layer in vector format from the Geological and Mining Institute of Spain (IGME) (1:50,000), soil mapping of the LUCDEME project (1:100,000), Corine Land Cover maps (CLC2012), and 1:5,000 orthophotographs.

The peak discharge data were then transferred to the 1D hydrodynamic model HEC-RAS (USACE, 2016), supported by VHR DTM, in order to get the flow cross-sections, channel profiles, water sheet limits, and hydraulic variable datasets. A total of 100 cross-sections were drawn in the upper RCR and 112 in the middle RCR, with an average separation of 2.0-3.5 m between them, for subcritical flow regimes. The results obtained in the calibration and validation events were evaluated using the Nash-Sutcliffe efficiency (NS) and percent bias (PBIAS). The respective values of NS and PBIAS were 0.86 and 7.81% in the calibration period and 0.81 and -4.1% in the validation events.

### 3.3.3. Mapping spatial changes in stream power during peak discharges

The peak discharges used to calculate stream power along the RCRs included a major flash flood (19-20 April, 2019) and two moderate flow events (12-13 September, 2019 and 24 March, 2020), all having different geomorphic impacts. For each cross-sectional flow area, information was obtained about the hydraulic radius (R), velocity (υ), Froude number (Fr), shear stress (τ), and stream power. Power per unit length of stream (Ω) and mean stream power (ω) at peak flood discharge ($Q_p$) were calculated according to Eqs. 3.1 and 3.2, respectively (Leopold et al., 1964).

$$\Omega = \gamma Q S_w \quad (3.1)$$

$$\omega = \Omega / w \quad (3.2)$$

where γ is the specific weight of water ($Nm^{-3}$), Q is peak discharge ($m^3/s$), $S_w$ is the water surface slope (m/m), which is used to estimate the energy gradient, and w is the water-surface width (m). Ω represents the energy dissipation per unit channel length and ω the energy expenditure per unit bed area. The width, average depth, and maximum water depth for each cross-section and its corresponding raster cell were acquired from the cross-sectional polygons of flow. The stream power values extracted by cross-section were averaged by budget cell level (i.e. ω) to compare with the sediment budgets at the same scale (Figure 3.3). For this purpose, a spatial interpolation of the values obtained in the consecutive cross-section pairs (Conesa García et al., 2020b) was performed, resulting in raster maps with cells of similar size to those got for the calculation of sediment budget.

The mean stream power gradient ($\partial\omega/\partial s$) was calculated by subtracting ω in cross-sectional cell i from the average ω in cells i−1 to i-3 and dividing the difference by the distance between the centroids of the extreme cells in each set of consecutive four budget cells along the channel centerline. This distance was normally around 10 m, as each cell is 2.5-3.0 m long. Positive and negative $\partial\omega/\partial s$ values show downstream increases and decreases in ω, respectively (Lea and Legleiter, 2016).The parentheses refer to the location of a given cell (for example, ω in cell i would be expressed as ω (i)).

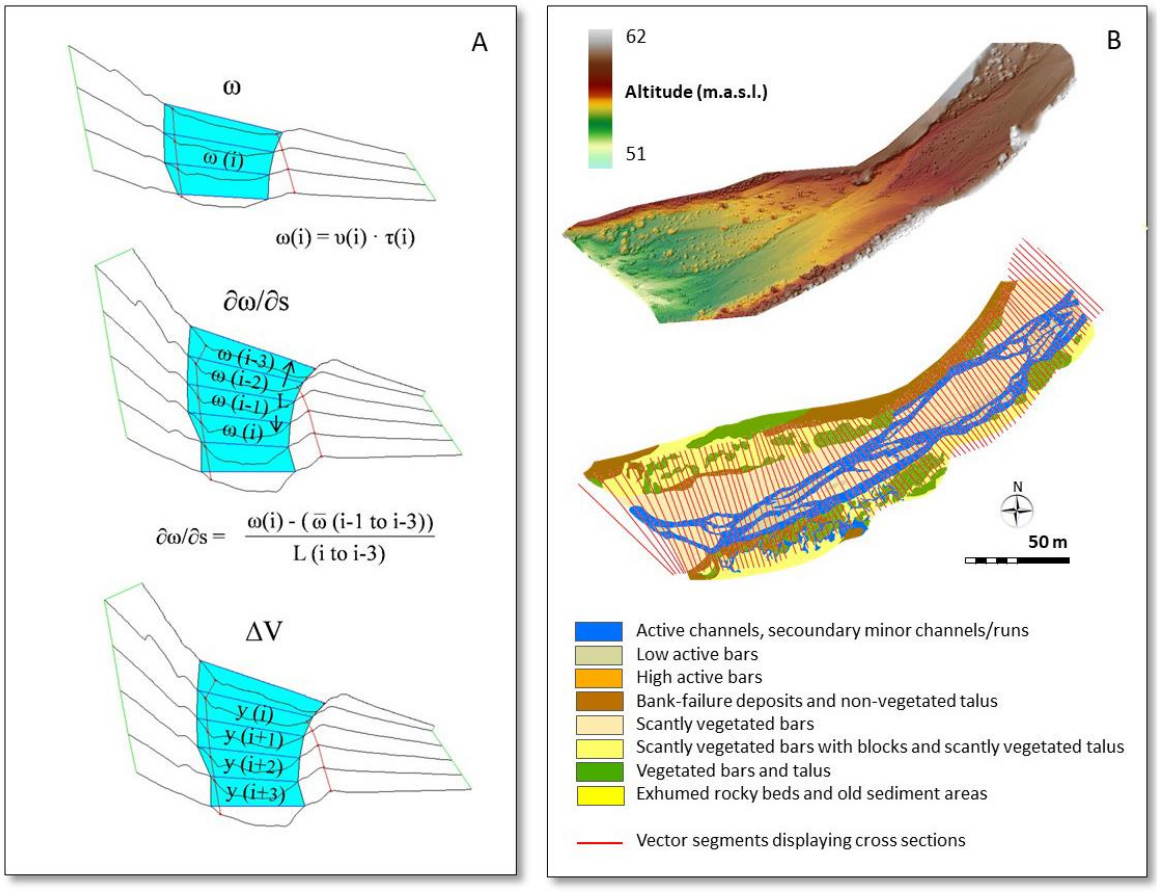


**Figure 3.3.** (A) Diagram of budget cells showing how ω, $\partial\omega/\partial s$ and ΔV were estimated. (B) VH DTM (at the top), and raster layer (at the bottom) showing bedforms within the peak flow limits; red vector segments display cross-sections for which $BFS_{pf}$ was calculated.

The energy expended beyond the critical mean stream power ($\omega_c$) and the $\omega/\omega_c$ ratio in each cross-sectional cell were also estimated to assess the spatial distribution of

energy available for sediment transport and morphological bed changes during peak flows. The excess energy per unit bed area (ε) expended above $\omega_c$ in these stages was determined by calculating ω from each peak discharge ($Q_{pf}$) and comparing the values to $\omega_c$ obtained using Eqs. (3.10) and (3.16) from Parker et al. (2011), which calculate $\omega_c$ as a function of slope and grain size. The bed slope was extracted from the VHR DTM described above. Volumetric grain-size sampling was performed for representative cross-sections in each RCR, differentiating the armored surface layer and the subsurface material. The median grain size ($D_{50}$) and the 84$^{th}$ percentile ($D_{84}$) were calculated for both layers in different bedforms within each cross-section. For the events in which ω was greater than $\omega_c$, the difference between ω and $\omega_c$ was multiplied by the number of seconds that elapsed while the maximum flow lasted, in order to get the excess energy accumulated per unit area of the bed ($\varepsilon_c$), in joules. Finally, the $\varepsilon_c$ values were related to ΔV and total flux (T).

### 3.3.4 Relative bed stability indices and transport efficiency

The transport efficiency in this EGBS was tested by combining two substrate stability indices: 1) the "Relative Bed Stability" (RBS), and 2) the "Bed-form Stability" (BFS). We adopted the RBS index from Olsen et al. (1997), defined as the ratio between the critical bed shear stress required to mobilize the $D_{84}$ size particle ($\tau_{c84}$) and the shear stress reached in each flow peak ($\tau_0$) (Eq. 3.3).

$$\mathrm{RBS} = \tau_{c84}/\tau_0 \quad (3.3)$$

$$\tau_{c84} = \tau_c^*(\rho_s - \rho)gD_{84} \quad (3.4)$$

where $\rho_s$ and ρ represent the sediment and water densities, respectively, g is the acceleration due to gravity, and $\tau_c^*$ is the critical value of the dimensionless Shields parameter. Finally, the shear stress for the discharge peak in each flow event was estimated as:

$$\tau_0 = \rho g R S \quad (3.5)$$

where R is the hydraulic radius and S is the water surface slope. If RBS is greater than 1, the bed is presumed to be fully mobilized only for peak discharges larger than that considered and the channel bed is relatively stable under such conditions. Conversely, if RBS is less than 1, the bed is mobilized at the sub-peak flow stage and the bed is presumed to be unstable, the transport efficiency increasing as the index approaches 0.
The BFS index, described by Conesa-García et al. (2020b), defines the relative stability of the bed forms according to the particle grain-sizes, vegetation cover, and height on the bed; for peak flow events($BFS_{pf}$), it was calculated using Eq. 3.6.

$$\mathrm{BFS}_{\mathrm{pf\,(i)}} = \left[\left(\sum \mathrm{vr}_{\mathrm{bgu(i)}} \cdot \mathrm{w}_{\mathrm{bgu\,(i)}}\right)/\mathrm{W}_{\mathrm{pf\,(i)}}\right]/\mathrm{n}_{\mathrm{bgu\,(i)}} \quad (3.6)$$

where $vr_{bgu}$ is the value assigned to each type of bed geomorphic unit ($bgu$), depending on its resistance to erosion observed in recent torrential flows, $w_{bgu}$ is the width of each $bgu$ in a channel cross-section, $W_{fp}$ is the flow width, and $n_{bgu}$ is the number of $bgu$. In our case, the maximum $n_{bgu}$ = 8, with the corresponding values of $vr_{bgu}$, as follows (from samller to larger resistance): 1. Active channels, secondary minor channels/runs, pools,

and gully beds; 2. Low active bars; 3. High active bars; 4. Bank-failure deposits and non-vegetated talus; 5. Scantly vegetated bars; 6. Scantly vegetated bars with blocks and scantly vegetated talus; 7. Vegetated bars and talus; 8. Exhumed rocky beds (substrate outcrops) and old sediment areas (rock blocks and cohesive bars) (Figure 3.3). Such classes were extracted from the $bgu$ affected by each peak flow. This index varies between 0 and 1, and the value of 0.5 is a threshold that discriminates in relative terms between stable ($BFS_{pf} > 0.5$) and unstable bed forms.

3.3.5. Relationships of stream power with sediment budget and bed stability

Values of the volumes of erosion (EV) and deposition (DV), net volume fluxes (ΔV), and elevation differences (Δe) averaged for each budget cell i, from high resolution data of UAV-SfM and TLS, were got along the two RCRs and for the time intervals under study.

The mean stream power gradients at cell i for the budget cells meeting thecriteria in Table 3.2 were compared to the E and D values at the same cell and to the ΔV volumes at cells i through i + 3 downstream.

Cross-correlation between $\partial\omega/\partial s$ and the net sediment flux at cell i + j was used as described by Lea and Legleiter (2016) to assess the spatial relationship between changes in stream power and transfers of sediment downstream. According to these criteria, it is assumed that only budget cells with ω greater than $\omega_c$ can experience sediment transport at the peak flow stage, the bedload being negligible in cells with a ω/ωc ratio lower than 1. We included in the cross-correlation analysis four conditions, which are described in Table 3.2, and we discarded those that implied the premise of $\omega_c$ being greater than ω.

**Table 3.2.** Cases considered for the comparison of $\partial\omega/\partial s(i)$ and $\varepsilon_c(i)$ with ΔV(i+j) and T(i+j) in each flood event and the hypothesized geomorphic trend in budget cell i or downstream budget cells i+j, according to Lea and Legleiter (2016).

| Case | Description | Hypothesizedgeomorphictrend | % UPR | % MDR |
|---|---|---|---|---|
| 1: ω(i) > ω(i − 1) >ωc | ω increases downstream and exceeds ωc for both budget cells | Erosion | 46.2 | 23.3 |
| 2: ω(i) >ωc> ω(i − 1) | ω increases downstream and exceeds ωc in cell i | Minorerosion | 0.0 | 11.7 |
| 3: ω(i − 1)> ω(i) >ωc | ω decreases downstream but exceeds ωc for both budget cells | Minordeposition | 52.3 | 55.0 |
| 4: ω(i − 1) >ωc> ω(i) | ω decreases downstream and falls below ωc in cell i | Deposition | 1.5 | 10.0 |

The percentages refer to the frequency of each case in the upper and middle RCRs for the flow peak of 19-20 April, 2019.

Hypotheses (1) and (2) were tested by using scatter plots to relate $\partial\omega/\partial s(i)$ to E(i), D(i), and ΔV(i + 1 to 3). By interpreting these scatter plots, the effect of the downstream spatial lag on the relationship between $\partial\omega/\partial s$ and sediment flux was evaluated. Furthermore, the excess accumulated energy per unit area of the bed, εc (i), was plotted against the total accumulated flux (T) to examine hypothesis (3), that there is a positive correlation between these two variables.

### 3.3.6. Assessment of bed elevation profiles using channel central and lateral lines

To assess changes in bed elevation a comparison of the longitudinal and transverse channel profiles was performed throughout the two RCRs and PBSAs. Specifically, three longitudinal profiles derived from SfM data and four from TLS surveys during the November 2018 to July 2020 period were compared. Perpendicular to these profiles, three transverse profiles were delineated for each survey date: one central and two at the end of both RCRs and PBSAs. We first obtained the channel centerline (CL) from the flow sheet boundary lines, using the method described by Golly and Turowski (2017). In order to define patterns of lateral bed change regarding the central channel axis, two lateral lines (one separated from the centerline by 3 m in the upper RCR and one separated by 1.5 m in the middle RCR) were drawn: one to the right (RL) and another to the left (LL). From the centerlines and lateral lines, their bed elevation difference values (Δe) were extracted after each of the main study events (April 19, 2019, September 12, 2019, and March 24, 2020). To eliminate the effect of the surface roughness of gravel and pebbles, the pixel values were averaged in 20-cm length intervals. The relationships of Δe CL with Δe RL and Δe LL were plotted. In addition, scatter plots comparing the differences in Δe RL and Δe LL with respect to Δe CL according to downstream distance were displayed for the bed sites with higher density of points and less distortion in the elevation values. The elevation variation patterns thus detected will reflect differential changes in bedload transport and channel bed morphology (e.g. the downstream cross-sectional balance between erosion and deposition) (Kasprak et al., 2015). This is particularly relevant in ephemeral channels, where bed elevation often appears to remain unchanged after a bedload-transporting flow event (Singer and Michaelides, 2014).

## 3.4 Results and discussion

### 3.4.1. Morphological sediment budgets at very high spatial resolution

The DoDs derived from each successive VHR DTM pair made it possible to evaluate very precisely the changes in bed elevation and sediment budget caused by a single isolated flash flood or two or more events of different magnitude. Specifically, in the RCRs studied here, the SfM-MVS data showed very different sediment budget patterns, associated with the magnitude of the monitored events. During the first stage (September 2018–September 2019) the upper RCR functioned as a sink for coarse sediments due to high instantaneous bedload fluxes at the peak flows on November 18, 2018 and April 19-20, 2019, while the middle RCR experienced channel deepening and bar accretion. As a result, the greatest deposition thickness was found in pre-existing alluvial bars (Figure 3.4). In the second period (September 5, 2019 to July 26, 2020), during which two moderate events and two others of very low flow occurred, superficial bed washing and scouring predominated, causing a general surface lowering.

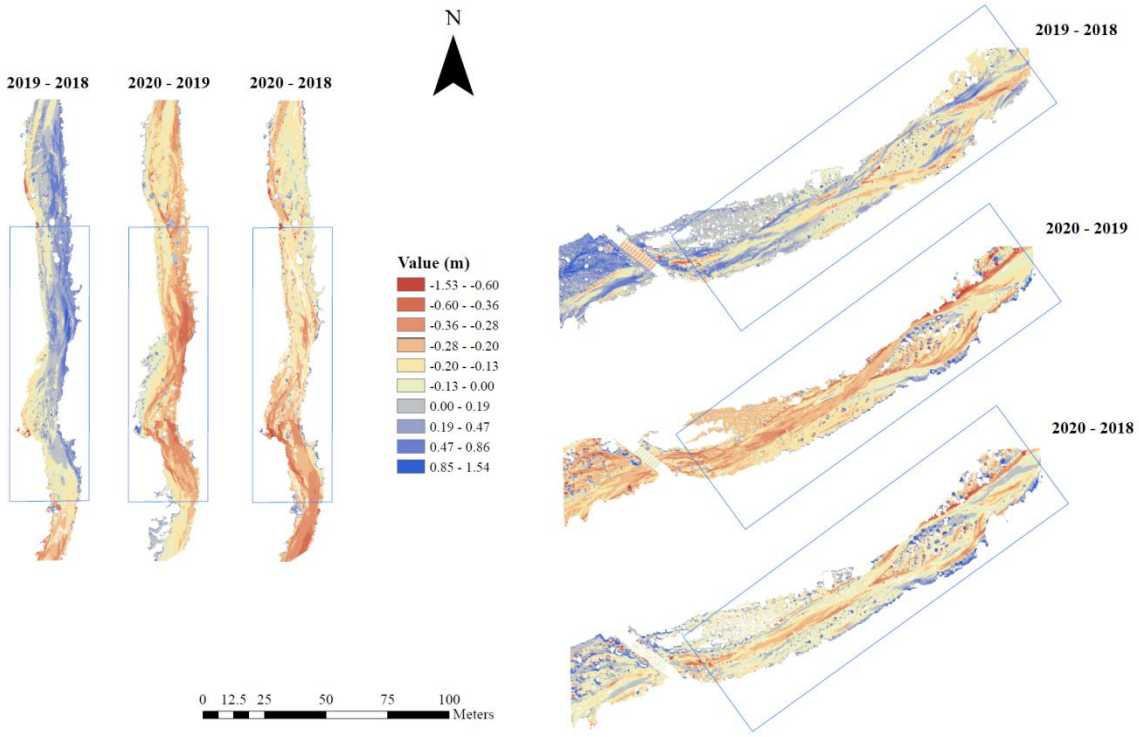


**Figure 3.4.** DEMs of difference (DoDs) for the upper and middle RCRs, using VHR DTM derived from SfM-MVS, for the periods from September 18, 2018 to September 5, 2019, from September 5, 2019 to July 26, 2020, and the two consecutive periods together (2018-2020).

Table 3.3 shows significant cumulative changes in ground surface elevation for both periods. For the upper and middle reaches, the average net thickness differences were, respectively, +22 and +21 cm in the first stage and -19 and -16 cm in the second. The DoDs of these two periods revealed a higher average deposition rate in the middle reach (UVSR = 0.218 $m^3$ $m^{-2}$ and 0.317 $m^3$ $m^{-2}$, respectively) than that of the upstream erosion (UVSL = 0.128 $m^3$ $m^{-2}$ and 0.229 $m^3$ $m^{-2}$, respectively). This suggests that the sources of sediments included not only the upper RCR but also gullies close to the headwater area and intermediate channel sections between the two RCRs, where bank breaking and gravel bar removal are especially active processes (Conesa et al., 2020a). Regarding the Total Net Volume Difference of both DoDs, the increase in net deposition was 2.26 % for the upper RCR and 31.13 % for the middle RCR.

The TLS data provided further information on changes in source-to-sink sediment transfer at the event scale. In particular, morphological sediment budgets in the RCRs and PBSAs were calculated using DoDs for the studied peak events. The PBSAs offered the best results, as they were defined by higher density 3-D point clouds (Figure 3.5).

**Table 3.3.** Statistical descriptors relating to the morphological sediment budgets calculated for the overall channel reach (OVR) and reference channel reaches (RCRs) in the UPR and MDR for the period September 2018 to July 2020 (SfM data).

| Statistic | | TAI | TNVD | | ANTD | | PI | TASL | TASR | UVSL | | UVSR | | SD * |
|---|---|---|---|---|---|---|---|---|---|---|---|---|---|---|
| Channel Reach Type | | $m^2$ | $m^3$ | % Error | m | % Error | % Value | $m^2$ | $m^2$ | $m^3\ m^{-2}$ | % Error | $m^3\ m^{-2}$ | % Error | m |
| Period September 2018 to September 2019 | | | | | | | | | | | | | | |
| UPR | OVR | 4657 | 958 | 0.044 | 0.206 | 0.044 | 0.470 | 372 | 4285 | 0.083 | 0.107 | 0.231 | 0.043 | 0.137 |
| | RCR | 2763 | 613 | 0.044 | 0.222 | 0.044 | 0.486 | 67 | 2695 | 0.128 | 0.070 | 0.231 | 0.043 | 0.118 |
| MDR | OVR | 8720 | 2092 | 0.040 | 0.240 | 0.040 | 0.489 | 234 | 8486 | 0.103 | 0.086 | 0.249 | 0.040 | 0.121 |
| | RCR | 4885 | 1013 | 0.046 | 0.207 | 0.046 | 0.486 | 168 | 4717 | 0.086 | 0.102 | 0.218 | 0.046 | 0.106 |
| Period September 2019 to July 2020 | | | | | | | | | | | | | | |
| UPR | OVR | 4887 | -830 | -0.053 | -0.170 | -0.053 | -0.400 | 4430 | 457 | 0.211 | 0.047 | 0.225 | 0.042 | 0.171 |
| | RCR | 2976 | -575 | -0.048 | -0.193 | -0.048 | -0.420 | 2744 | 232 | 0.229 | 0.043 | 0.237 | 0.040 | 0.162 |
| MDR | OVR | 7795 | -1318 | -0.051 | -0.169 | -0.051 | -0.331 | 6728 | 1068 | 0.246 | 0.040 | 0.314 | 0.031 | 0.256 |
| | RCR | 4707 | -742 | -0.055 | -0.158 | -0.055 | -0.319 | 4044 | 663 | 0.235 | 0.042 | 0.317 | 0.030 | 0.243 |
| Period September 2018 to July 2020 | | | | | | | | | | | | | | |
| UPR | OVR | 4614 | 93 | 0.074 | 0.020 | 0.070 | 0.091 | 2193 | 2421 | 0.095 | 0.068 | 0.125 | 0.066 | 0.185 |
| | RCR | 2750 | 13 | 0.072 | 0.010 | 0.071 | 0.024 | 1466 | 1284 | 0.087 | 0.066 | 0.110 | 0.067 | 0.173 |
| MDR | OVR | 8553 | 637 | 0.090 | 0.074 | 0.090 | 0.219 | 3365 | 5188 | 0.121 | 0.076 | 0.201 | 0.047 | 0.273 |
| | RCR | 4805 | 231 | 0.072 | 0.048 | 0.071 | 0.152 | 2142 | 2663 | 0.124 | 0.076 | 0.186 | 0.051 | 0.252 |

TAI = Total Area of Interest ($m^2$); TNVD =Total Net Volume Difference ($m^3$); ANTD =Average Net Thickness Difference (m) for the Area of Interest; PI =Percent Imbalance (departure from equilibrium); TASL =Total Area of Surface Lowering ($m^2$); TASR =Total Area of Surface Raising ($m^2$); UVSL = Average Unit Volume of Surface Lowering ($m^3\ m^{-2}$); UVSR = Average Unit Volume of Surface Raising ($m^3\ m^{-2}$); SD* =Standard Deviation of the Net Thickness Differences (m); UPR = Upper reach; MDR = Middle reach; OVR = Overall channel reach; RCR = Reference channel reach.

In these areas, the major event produced a positive generalized sediment budget, with an average unit volume of 21.55 $dm^3\ m^{-2}$ in the upper PBAS and 10.03 $dm^3\ m^{-2}$ in the middle PBAS. The two moderate flow events had different behavior patterns: the bankfull discharge caused the highest incision rates in the upper PBAS, with an average unit lowering volume above 90 $dm^3\ m^{-2}$, and the largest deposition in the middle PBAS, where the average unit volume of surface raising was 51.9 $dm^3\ m^{-2}$. By contrast, at the sub-bankfull stage more moderate vertical erosion and bed lowering predominated along both channel stretches.

The analysis of budgets expressed in unit volume for 10-cm elevation intervals shows that the more extensive morphological adjustments coincided with the largest volumetric variations, the bed elevation ranging between −0.2 and +0.2 m (Table 3.4). Within these intervals, the greatest unit volumes of deposition (86.1$dm^3\ m^{-2}$) and erosion (83.2 $dm^3\ m^{-2}$) were recorded in the middle and upper PBSA, respectively, during the bankfull discharge of March 2020.

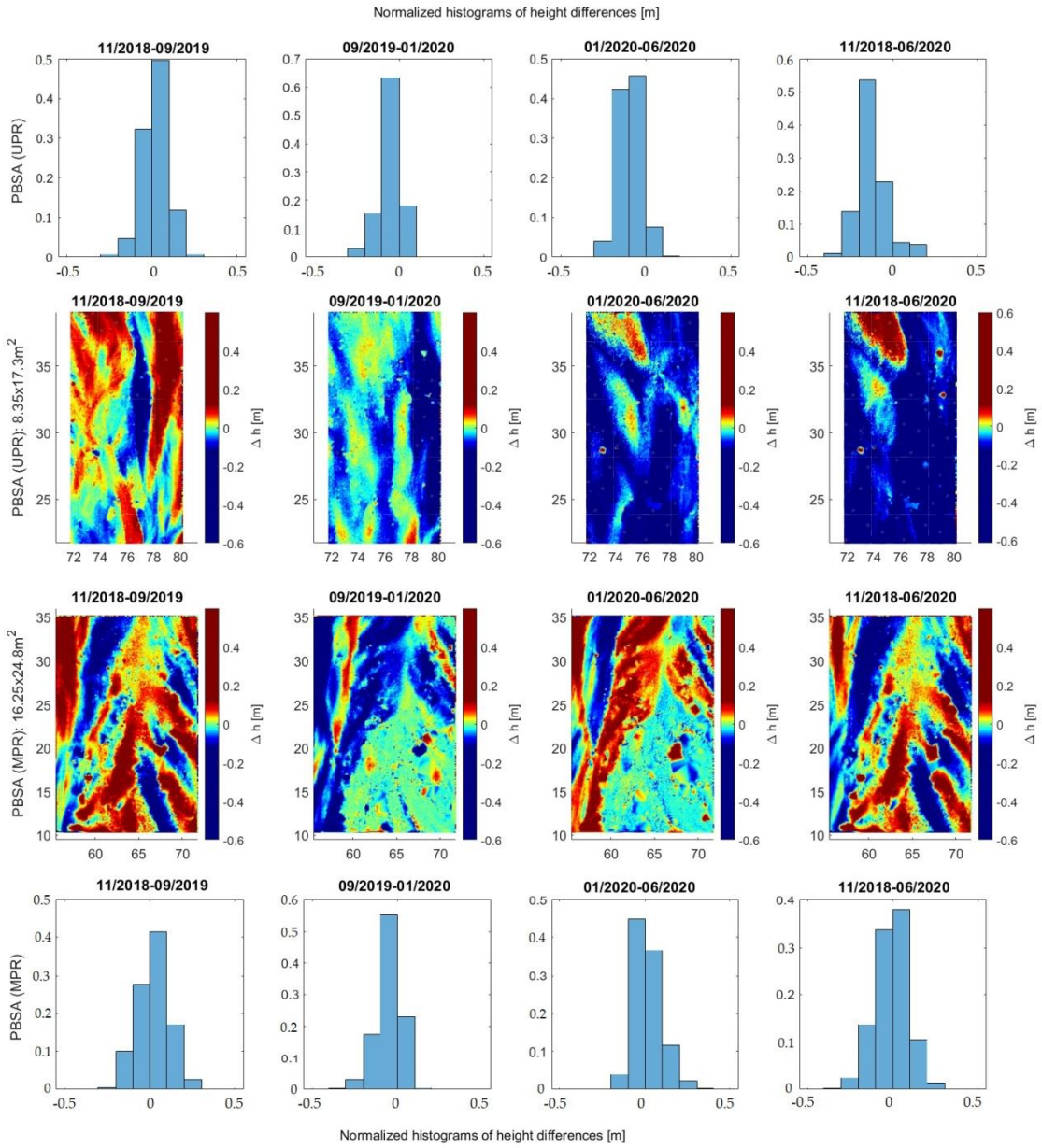


**Figure 3.5.** DEMs of difference (DoDs) and normalized histograms of the height differences for the upper and middle PBSAs, comparing the 2018, 2019, and 2020 3DPCs, based on the TLS survey. They display the sediment budget primarily attributable to the peak flow events of (a) 19-20 April, 2019, (b) 12 September, 2019, (c) 24 March, 2020, and (d) the whole analysis period (November 2018 to July 2020).

These results suggest that effective discharge for bed load transport occurs at higher water stages and greater recurrence intervals than bankfull discharge, which is consistent with the cases studied by Emmett et al. (2001) and Gomez et al. (2007). In both RCRs the channel width is constrained by the stability of the bank material and its resistance to erosion during flows at or near the bankfull stage, which also scour the bed. In addition, constraints on the mobility of bed material, due to channel armoring processes, mean that a higher peak discharge is required to transport the greatest amount of bedload. The budgets at the cell level reflected the same erosion-deposition patterns and relationships between channel reaches as at the pixel resolution.

Table 3.4 also provides the total mean volumes per budget cell for the two PBSAs in each time interval. For the entire analysis period, erosion exceeded deposition, resulting in a final positive net sediment flux. From the net sediment flux volumes in each budget cell, the height of scour and fill were obtained for the three survey stages and the two RCRs (Figure 3.6).

**Table 3.4.** Changes in unit volume ($dm^3\ m^{-2}$) and total mean volume per budget cell ($dm^3$), got for elevation intervals of 10 cm, and global height differences (Δe) in each pilot bed survey area (PBSA), based on TLS datasets covering the periods November 2018 to September 2019[1], September 2019 to January 2020[2], and January 2020 to July 2020[3].

| | Unit volume ($dm^3m^{-2}$) | | | | | | Total mean volume per budget cell ($dm^3$) | | | | | |
|---|---|---|---|---|---|---|---|---|---|---|---|---|
| | PBSA (UPR) | | | PBSA (MDR) | | | PBSA (UPR) | | | PBSA (MDR) | | |
| Δe (m) | 2018 2019[1] | 2019 2020[2] | 2020 2020[3] | 2018 2019[1] | 2019 2020[2] | 2020 2020[3] | 2018 2019[1] | 2019 2020[2] | 2020 2020[3] | 2018 2019[1] | 2019 2020[2] | 2020 2020[3] |
| -0.5/-0.4 | -0.05 | -0.15 | -0.64 | -3.59 | -0.15 | -0.39 | -1.9 | -5.3 | -10.4 | -312.7 | -10.0 | -10.5 |
| -0.4/-0.3 | 0.00 | -0.21 | -0.17 | -2.46 | -0.02 | -0.13 | 0.0 | -7.4 | -57.3 | -214.1 | -1.3 | -3.5 |
| -0.3/-0.2 | -1.47 | -7.67 | -8.76 | -3.86 | -0.23 | -0.10 | -59.4 | -270.0 | -507.5 | -335.7 | -15.8 | -2.8 |
| -0.2/-0.1 | -6.60 | -22.54 | -56.53 | -16.14 | -9.35 | -14.65 | -266.0 | -793.6 | -1281.7 | -1405.4 | -631.2 | -398.5 |
| -0.1/0 | -11.32 | -26.36 | -26.69 | -11.35 | -23.91 | -36.49 | -456.4 | -928.4 | -222.6 | -987.7 | -1613.6 | -992.4 |
| ΔV<0 | -19.44 | -56.93 | -92.79 | -37.40 | -33.66 | -51.76 | -783.7 | -2004.7 | -2079.5 | -3255.6 | -2271.9 | -1407.7 |
| 0/0.1 | 21.80 | 2.68 | 2.30 | 18.52 | 3.09 | 43.04 | 878.9 | 94.3 | 31.7 | 1612.5 | 208.7 | 1170.6 |
| 0.1/0.2 | 17.38 | 0.05 | 0.28 | 22.84 | 1.14 | 43.12 | 700.7 | 1.6 | 78.0 | 1988.9 | 76.7 | 1172.9 |
| 0.2/0.3 | 1.38 | 0.01 | 0.02 | 4.67 | 0.79 | 13.31 | 55.6 | 0.3 | 4.5 | 406.3 | 53.6 | 362.0 |
| 0.3/0.4 | 0.16 | 0.01 | 0.01 | 0.57 | 0.70 | 2.52 | 6.3 | 0.2 | 0.1 | 49.3 | 46.9 | 68.6 |
| 0.4/0.5 | 0.27 | 0.07 | 0.08 | 0.83 | 1.69 | 1.66 | 10.9 | 2.5 | 0.6 | 72.0 | 114.4 | 45.1 |
| ΔV>0 | 40.99 | 2.82 | 2.69 | 47.43 | 7.41 | 103.65 | 1652.4 | 98.9 | 115.0 | 4129.0 | 500.3 | 2819.2 |
| ΔV | 21.55 | -54.12 | -90.10 | 10.03 | -26.25 | 51.89 | 868.7 | -1905.8 | -1964.6 | 873.4 | -1771.6 | 1411.5 |

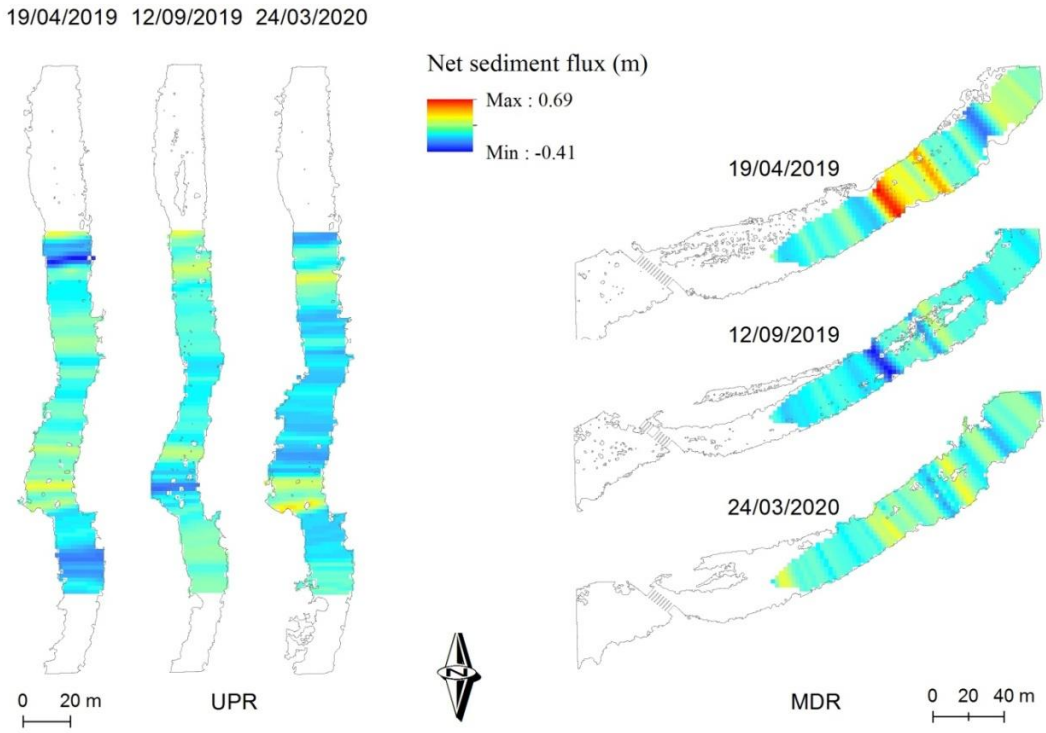


**Figure 3.6**. Normalized net sediment flux for each budget cell in the three peak flows analyzed along the two reference channel reaches (RCR).

3.4.2. Changes in the bed elevation profiles determined using VHR DTM

Variations in the longitudinal and cross-sectional bed elevation profiles make up an indicator of changes in flow velocity and competence, which condition erosion and deposition. Considering the LiDAR-derived bed elevation change along the channel centerline between 2018 and 2020, a substantial variation was observed along both RCRs during the survey periods (Figure 3.7). From November 2018 to September 2019 net deposition predominated, increasing the bed height by between +0.12 and + 0.33 m, especially in the middle RCR. In the following period (September 2019 to January 2020) the pattern of change differed between the two channel stretches, erosion dominating in the upper RCR and the spatial variability of sediment budgets in the middle RCR. In the latter, the sub-bankfull discharge of 12 September, 2019 caused scouring upstream and vertical accretion downstream, without affecting the raised zone of an intermediate high bar, which remained almost completely submerged. Finally, the longitudinal profile of July 2020, due mainly to the bankfull peak flow of 24 March 2020, reflected a general lowering, so that the initial bed surface profile was largely recovered. These changes suggest that, overall, there was more bed aggradation during the flash flood event and more erosion when the events of moderate magnitude occurred. For the analysis period a quasi-equilibrium is observed for the bed profile in the more entrenched upper RCR, since the mean elevation of the active bed did not experience significant temporal variations.

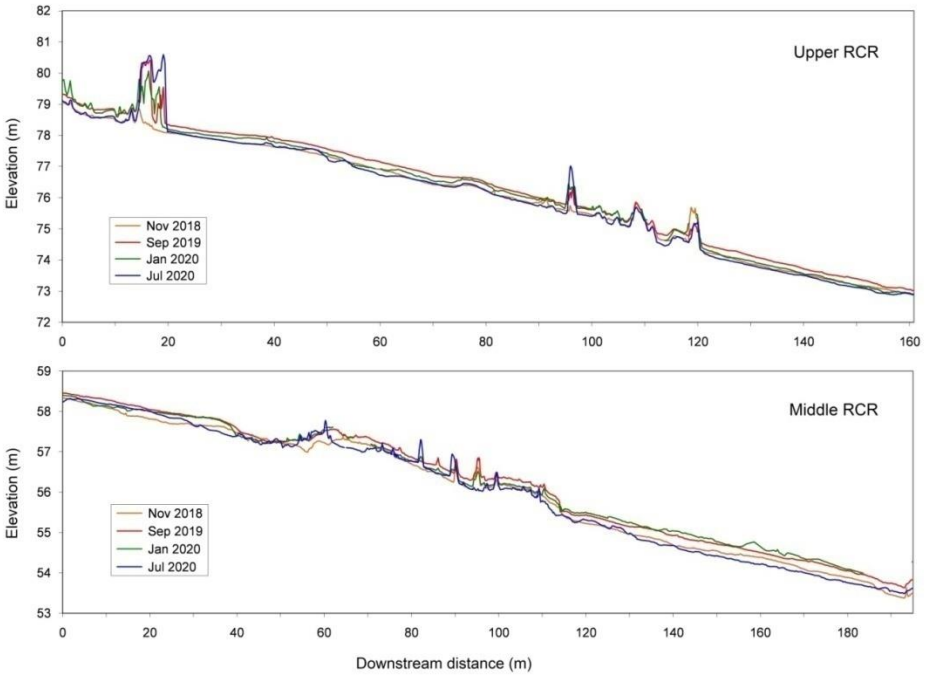


**Figure 3.7.** Longitudinal bed elevation profiles extracted from TLS datasets for each monitoring survey and RCR.

The shapes of the initial (2018) and final (2020) thalweg profiles are relatively similar here, except in certain locations of bedforms: the formation of a new longitudinal bar and the destruction of another, pre-existing one led to a bed raising and lowering, respectively. In contrast, the middle RCR underwent a relatively greater variation in bed elevation as a result of spatial differences in grain size and its pre-existing topography, conditioned by a high and stable central bar that acted as an obstacle to the flow at high water stages. Similar effects have been described by other authors for this type of channel,

during recent monitoring periods (Norman et al., 2017). The rectilinear form of both series of profiles is interrupted only by local ruptures associated with transverse bars that produce short-distance variations in the stream power. Similar to the findings of Pitlick and Cress (2002), these are not strongly influenced by transitions in reach type (alluvial to quasi-alluvial) or by junctions with tributaries.

The spatial variation downstream of the differences in transverse changes in bed elevation for each event and section is depicted in Figures 3.8 and 3.9. Specifically, the scatter plots in Fig. 3.8 show the spatial patterns of the relationships between the changes in the bed height of the center line (CL) and the changes to the left along lateral lines 3 m (CLL) and 6 m (LL) from the CL and to the right, also at 3 m (CLR) and at 6 m (RL). Ten patterns of lateral net sediment fluxes were found, with a marked differentiation between the upper and middle reaches. During the April 2019 event, with respect to the CL, in the upper RCR, the erosion rates and deposition were similar on the left and the deposition decreased towards the right bank. In this stretch an equilibrium between erosion and deposition in the CL seemed to break slightly in favor of erosion, which was more prevalent on both lateral bed sides. By contrast, the morphological adjustments in the middle RCR showed more marked differences between the CL and the lateral bed extremes. In the major flood, aggradation processes were dominant in the entire transversal bed, being more evident towards the banks than in the center of the channel. At sub-bankfull discharge, the balance between erosion and deposition close to the CL gave way to a relative increase in sedimentation in the lateral zones, while under bankfull conditions, represented by the March 2020 event, deposition predominated in the CL and downcutting in the LL.

The profiles in Figure 3.9 display the difference in behavior between the CL and the lateral bed zones for each peak flow, according to the distance downstream. This was defined by calculating the differences in bed height (Δe) of RL and LL relative to the Δe CL.

For the larger flood event, the difference profile of the CL showed greater similarity to that of the right part than to that of the left, although downstream the Δe RL values tended to homogenize with those of the rest of the bed within a general process of bed aggradation. In the middle RCR the values of Δe LL (0.25 to 0.40 m), higher than the positive differences of Δe CL (ranging from 0 to 0.22 m), suggest erosion rates for this event on the left lateral bed ranging from 0.18 to 0.25 m, coinciding with the greatest deposition in a transverse medial bar. The rest of the section registered more deposition in the lateral zones than in the central zone, as can be inferred from the position of the LL and RL difference profiles below CL when they adopt negative values. The September 2019 event involved a more uniform bed downgrading in the upper RCR than in the middle RCR. Along the upper reach, the LC change profile remained almost entirely below 0 m with Δe values generally lower than those of LL and RL, which denotes greater erosion in the areas closest to the banks. Downstream, in the middle RCR the left margin had a geomorphic activity similar to that of the central part, while the area near the right margin acted alternately as a site of scour and vertical accretion.

There was a noticeable dispersion in the bed elevation balances at the beginning of RCR-MDR 2; this may represent interpolation errors caused by low TLS point density and inconsistent spatial geometry between the surveys in this portion of the survey area.

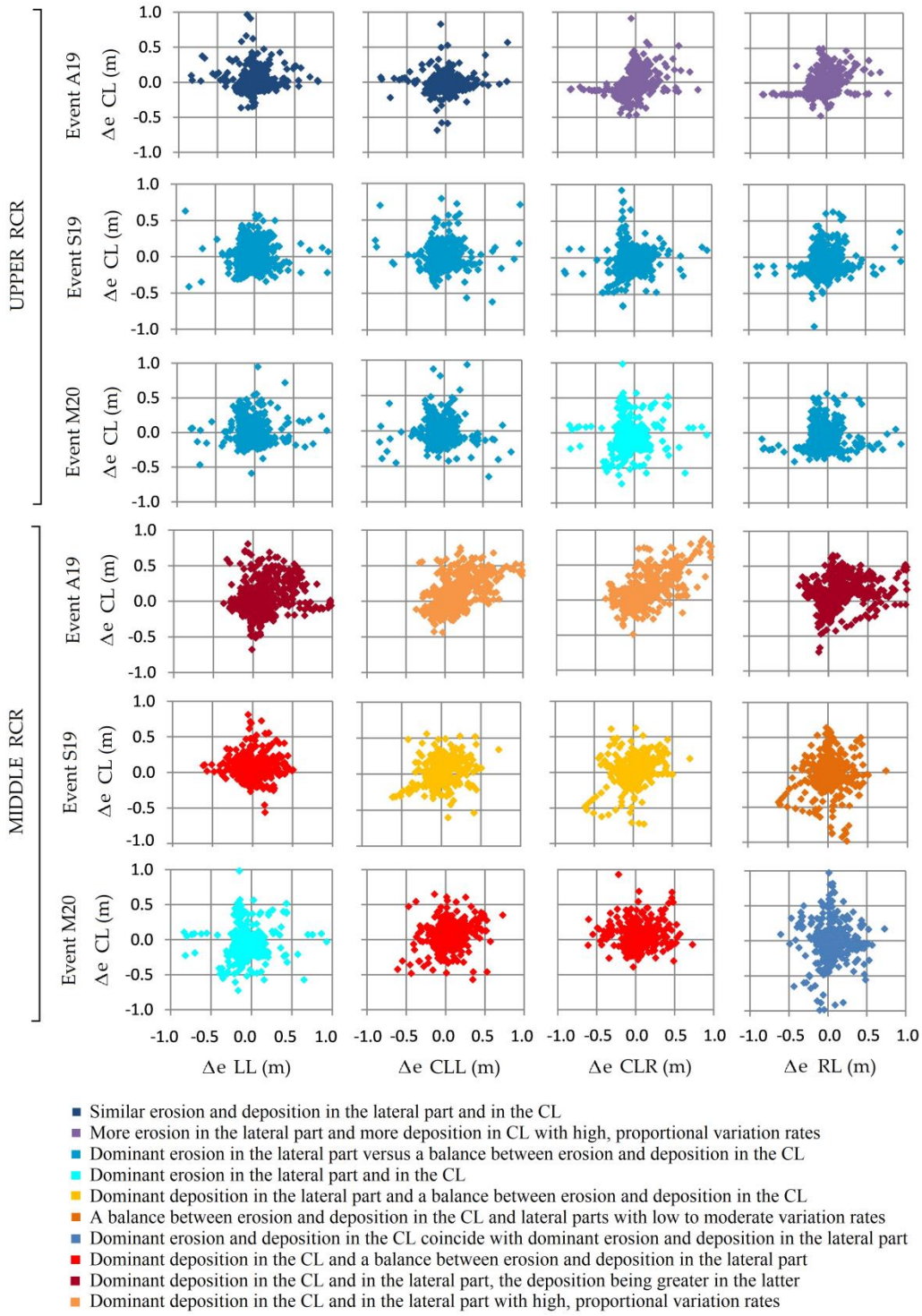


**Figure 3.8.** Relationships between Δe CL and bed elevation differences in lateral channel lines with a separation distance of 3 and 6 m on the right (Δe CLR; Δe RL) and left (Δe CLL; Δe LL) sides. Events of 19-20 April, 2019, 12 September, 2019, and 24 March, 2020.

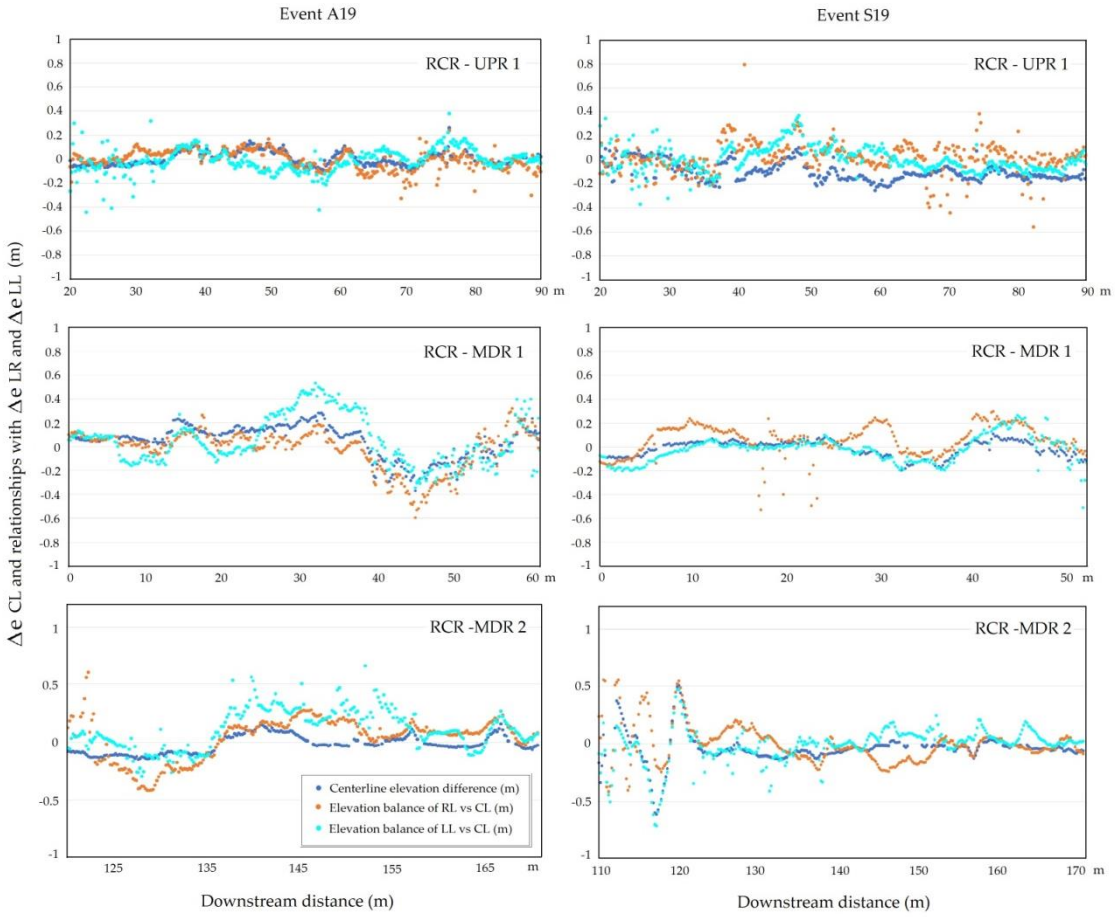


**Figure 3.9.** Scatter plots comparing the differences in Δe RL and Δe LL with respect to Δe CL, versus the downstream distance in the upper and middle RCRs (UPR and MDR respectively). Peak flow events of 19-20 April, 2019 (Event A19) on the left and 12 September, 2019 (Event S19) on the right.

The longitudinal and cross-sectional channel profiles got for the PBSAs (Figure 3.10) show, in great detail, the changes produced at the geoform level. The A'-A to F-F' profiles show the partial disaggregation of a longitudinal central bar and the lowering of the main active channel during the analysis period in the upper RCR.

It is worth noting the contrast between the uniform lowering that the profile of July 2020 exhibits with respect to the initial profile at the head of the bar (D-D') and the inversion of the zones of bed accretion and scour downstream (F-F'). Field surveys confirmed that the central part of the bar (2-4 m in E-E'), composed of the coarsest material (gravel and pebbles) and with an imbricated and massive structure, was the most stable site.

The PBSA in the middle reach encompasses the transition zone to the medial bar head, with crude horizontal bedding and small-scale gravel cross-strata. As the RCR-scale longitudinal profiles have already reflected, the bed surface along the talweg rose during April 2019, fell slightly in September 2019, and recovered its initial profile after the March 2020 bank flow (G'-G). Considering the entire period, a slight net deposition of 0.1 to 0.2 m (J-J') (K-K') in the zone of entry to the bar platform and a decrease of 0.05 to 0.23 m (L-L') in the bar supra-platform deposits were observed.

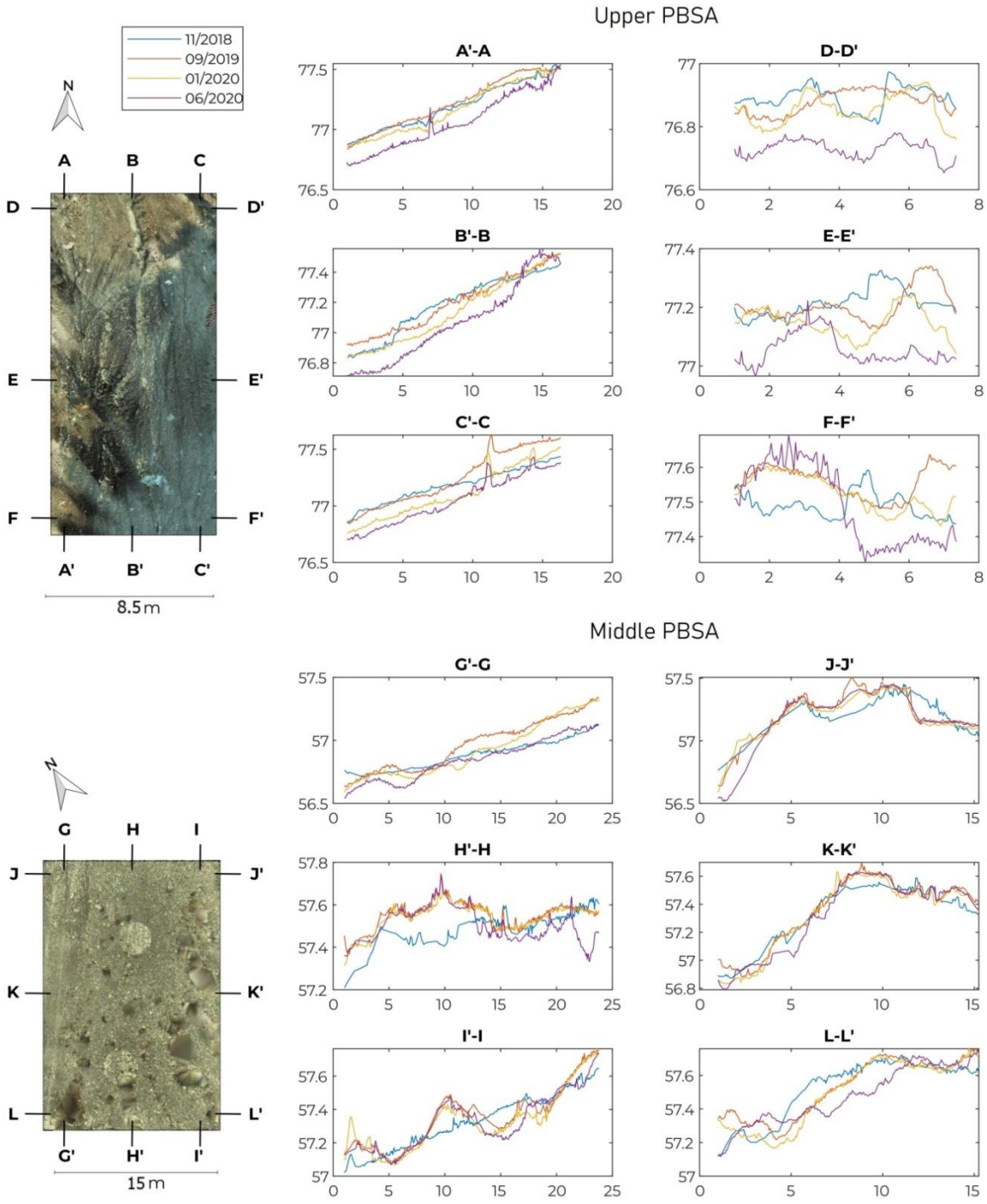


**Figure 3.10.** Longitudinal and cross-sectional channel profiles, extracted from TLS datasets, for each peak flow and monitoring bed survey area (upper and middle PBSAs).

### 3.4.3. Stream power maps and relationships

Hydraulic variables related to stream power (including $\upsilon$, $\tau_0$, $\tau_c$, $\omega$, $\partial\omega/\partial s$, and $\varepsilon$) were estimated continuously along each study RCR for the three main peak flows. Table 3.5 shows some statistical descriptors for them and Fig. 3.11 displays the grids of the $\omega$ and $\varepsilon$ ($\omega$-$\omega_c$). The resultant maps allowed us to infer variations in their values that were then related to the spatial patterns of sediment budgets in order to explain better the processes that control the morphological channel adjustments. The flow velocity ranged

from 1.10 m $s^{-1}$, in sections with greater roughness, dominated by pools, blocks, and scrubs, to 2.65 m $s^{-1}$, at riffle sites. Specifically, the greatest increases in flow velocity occurred in the steepest and narrowest stretches composed of cohesive materials. This is consistent with the view that an entrenched channel tends to remain narrower in bedrock than in gravel bed at similar flow stages (Finnegan et al., 2005).

A more effective indicator for the calculation of the sediment carrying capacity is the relationship between the boundary shear stress ($\tau_0$) and the critical shear stress ($\tau_c$). The spatial variability of both parameters was highly significant in the analyzed reaches, where alternating changes in the bed roughness caused appreciable turbulence and velocity fluctuations. Heterogeneities due to variations in grain sizes and bedforms may create substantial velocity and shear stress variations across the channel or downstream during a single discharge (Wohl, 2000). Consequently, the maps exhibit, in both reaches, a wide patchwork of $\tau_0$ values, ranging from 1.2 to 160 N $m^{-2}$, and somewhat less variability in $\tau_c$ (23.1 to 79 N $m^{-2}$). These ranges were practically maintained downstream, although the variability among sections regarding shear stress was lower in MDR than in UPR. The $\tau_0/\tau_c$ ratio also varied from one stretch to another, so that its average value was considerably higher in the upper reach (2.4), compared to that in MDR (1.6). In accordance with this, the shear stress was more than double the critical shear stress in UPR, which implies a high bed-load capacity and channel degradation. Downstream, incision in the middle reach was likely, but morphological adjustments associated with high rates of sediment entrainment and mobility remained.

**Table 3.5.** Statistical descriptors for hydraulic variables related to stream power during the peak flows of 19 April, 2019 (A19), 12 September, 2019 (S19), and 24 March, 2020 (M20) in the upper and middle RCRs. The values are extracted from the set of cells (i) in each RCR.

| | SV | υ | | | $\tau_0$ | | | ω | | | δω/δs | | | ε | | |
|---|---|---|---|---|---|---|---|---|---|---|---|---|---|---|---|---|
| | | A19 | S19 | M20 | A19 | S19 | M20 | A19 | S19 | M20 | A19 | S19 | M20 | A19 | S19 | M20 |
| Upper RCR | mean | 2.16 | 1.66 | 1.83 | 96.5 | 70.2 | 78.4 | 212.9 | 119.1 | 146.2 | -0.6 | -0.1 | -0.5 | 157.3 | 59.6 | 85.1 |
| | min | 1.34 | 1.12 | 1.10 | 34.2 | 28.1 | 31.8 | 46.5 | 32.2 | 35.4 | -14.5 | -8.3 | -10.7 | -72.9 | -89.2 | -119.5 |
| | max | 2.65 | 2.10 | 2.30 | 160.3 | 103.8 | 118.8 | 371.4 | 209.5 | 245.2 | 14.9 | 10.6 | 5.8 | 333.4 | 166.1 | 189.2 |
| | error | 0.03 | 0.02 | 0.02 | 2.21 | 1.44 | 1.66 | 6.25 | 3.29 | 3.93 | 0.80 | 0.55 | 0.35 | 7.69 | 4.42 | 5.00 |
| | σ | 0.29 | 0.21 | 0.23 | 24.7 | 16.1 | 18.6 | 69.9 | 36.8 | 43.9 | 6.3 | 4.3 | 3.3 | 86.0 | 49.4 | 55.9 |
| | K | 0.53 | -0.11 | 0.72 | -0.12 | -0.21 | 0.00 | -0.37 | -0.36 | -0.03 | 1.01 | 1.26 | 0.06 | 0.29 | 0.15 | 1.11 |
| | Sk | -0.73 | -0.54 | -0.80 | 0.43 | -0.48 | -0.53 | -0.44 | -0.34 | -0.58 | 0.58 | 0.57 | 0.56 | -0.84 | -0.68 | -1.03 |
| Middle RCR | mean | 1.95 | 1.50 | 1.55 | 84.7 | 59.8 | 69.9 | 170.8 | 93.8 | 113.6 | -0.6 | -0.4 | 0.0 | 102.8 | 22.6 | 31.0 |
| | min | 0.50 | 0.37 | 0.28 | 1.2 | 0.73 | 0.39 | 0.59 | 0.27 | 0.11 | -14.1 | -6.2 | -8.0 | -98.8 | -176.5 | -136.2 |
| | max | 2.38 | 1.95 | 2.05 | 146.1 | 110.6 | 125.6 | 344.3 | 215.9 | 253.9 | 15.8 | 6.8 | 7.2 | 306.6 | 149.3 | 167.9 |
| | error | 0.03 | 0.03 | 0.03 | 2.55 | 1.89 | 2.20 | 6.56 | 3.98 | 4.88 | 0.73 | 0.37 | 0.31 | 9.49 | 6.00 | 6.19 |
| | σ | 0.29 | 0.25 | 0.28 | 25.2 | 18.6 | 21.7 | 64.7 | 39.2 | 48.0 | 6.0 | 3.0 | 2.7 | 92.5 | 58.5 | 60.4 |
| | K | 8.56 | 6.50 | 5.73 | 1.55 | 1.63 | 1.26 | 0.53 | 0.93 | 0.28 | 0.37 | -0.08 | 0.50 | 0.47 | 0.93 | 0.16 |
| | Sk | -2.12 | -1.69 | -1.37 | -0.32 | 0.03 | -0.26 | 0.26 | 0.67 | 0.47 | 0.57 | 0.57 | 0.56 | 0.42 | -0.45 | 0.07 |

υ = flow velocity (m $s^{-1}$); $\tau_0$ = shear stress (N $m^{-2}$); ω = mean stream power (W $m^{-2}$/m); δω/δs = mean stream power gradient (W $m^{-2}$/m);ε = excess energy (W $m^{-2}$/m).

Since ω(i) results from the multiplication of υ by $\tau_0$ for a given cell i, the spatial pattern of ω shows a large variability, because of fluctuations of both variables. Particularly, the ω values had an excellent power function fit with υ and $\tau_0$ ($r^2$ = 0.91 and 0.98, respectively). The mean stream power also showed an excellent fit with the Froude number ($r^2$ = 0.84) and the energy slope ($r^2$ = 0.87) when using the same function type,

but its relationship with the hydraulic radius was worse ($r^2$ = 0.45 for a polynomial regression).

In the RCRs studied, the mean stream power during the peak flow of 19-20 April 2019 varied from 0.6 to 371.4 W $m^{-2}$, the excess energy from 333.4 to -98.8 W $m^{-2}$ (Table 3.5, Figure 3.11), and the stream power gradient from -14.5 to 15.8$Wm^{-2}$/m (Fig. 3.12) (the upper limits of color displayed in Figs. 3.11 and 3.12 for such variables encompass 95% of the data).

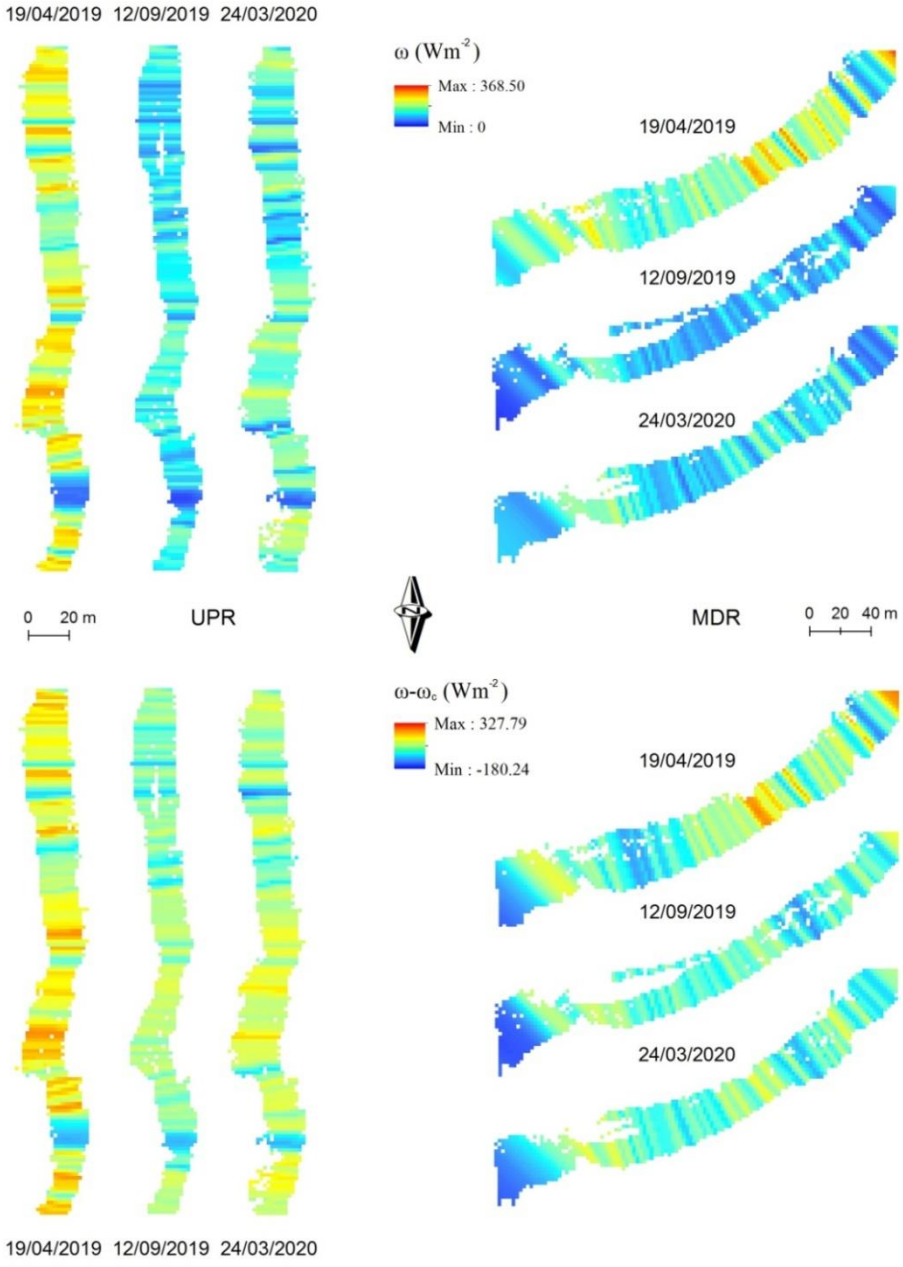


**Figure 3.11.** Values of$\omega$, $\partial\omega/\partial s$, and $\omega/\omega_c$ calculated by cell using spatial interpolation of Hec-RAS data at equidistant (2.0-3.5 m) cross-sections, estimated for the three peak flows in the upper and middle RCRs (UPR and MDR respectively). The maximum color limits encompass 95% of the datasets.

Note, however, that over 75% of the $\partial\omega/\partial s$ values fell within the range 6 to -6 $Wm^{-2}/m$ and that the extreme data reflect local abrupt changes in $\omega$.

As for the flow velocity and the shear stress, the highest values of mean stream power were concentrated in entrenched channel cross-sections, along straight to sinuous stretches, and locally over steep riffles characterized by high near-bed velocity gradients.

This pattern is linked to incision processes in several Mediterranean ephemeral streams (e.g., Garzón and Alonso, 2002, Hooke, 2006, Ortega et al., 2014). However, we observed a significantly unconventional behavior in the gravel beds studied here, where an important transitory erosion was often followed by extraordinary mobility of the bed materials, which caused channel aggradation in the more important events.

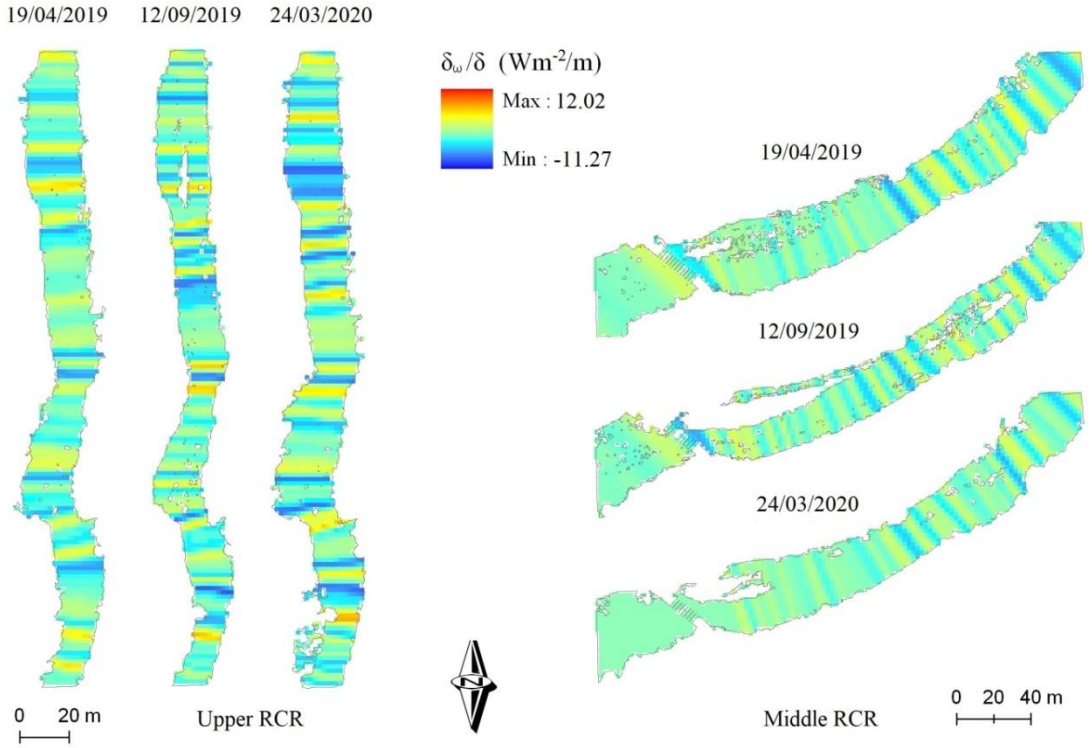


**Figure 3.12.** Values of $\partial\omega/\partial s$ calculated by cell using spatial interpolation of Hec-RAS data related to equidistant (2.0-3.5 m) cross-sections in the upper and middle RCRs, for the peak flood of 19-20 April 2019. The maximum color limits represent 95% of the datasets.

The distribution of the $\omega/\omega_c$ ratios was also skewed for both RCRs and the distinct flood events, with maximum values very distant from the mean and median. In the April and September events maximum ratios around 10 and 7, respectively, were reached in the two reference stretches, with much lower and different medians depending on the reach. Specifically, during the peak flood of 19-20 April 2019, the $\omega/\omega_c$ median was 2.7 in UPR and 1.2 in MDR.

Furthermore, we have verified that the pattern described by other authors for gravel-bed ephemeral streams with a more heterogeneous channel geometry and planform is not fully reproduced here. Conesa-García et al. (2020b) found higher energy balance values in less entrenched and less incised cross-sections transitioning to channel

widening. By contrast, along the straight and slightly sinuous stretches analyzed here the most significant energy balances occurred locally in the more entrenched sections with a low to moderate width-to-depth ratio and high transport capacity. It should be considered that in such gravel-bed streams the grain roughness may become more influential than the changes in bed slope with regard to variations in $\omega_c$ (Rickenman, 2011; Camenen et al., 2012; Conesa-García et al., 2020b).

The spatial variability of ω was contrasted with that of other significant hydraulic variables ($\tau_0$, R, Fr, and $\partial\omega/\partial s$) in a downstream direction along the entirety of the stretches under analysis. Figure 3.13 depicts these comparisons for the flood of April 2019, considering all the cross-sections included in the complete stream reaches and the RCRs. As described above, variations of ω in both RCRs closely followed the pattern of variability observed in the shear stress and Fr distributions. The only nuance was found in the frequency with which Fr reached the value 1 in both stretches, depending on the mean stream power registered. The ω *versus* Fr relationship enabled us to establish, in our case, the value 200 W $m^{-2}$ as the threshold above which the limit defining the subcritical regime is exceeded. This condition occurred in more than 50% of the cross-sections along the UPR, but it was barely reached in the MDR. On the other hand, ω maintained a poorer spatial relationship with the hydraulic radius (R), which was often due to a greater influence of the slope and bed roughness on the stream power. This was particularly evident in the UPR, outside and within the RCR monitored using UAV-SfM and TLS, where increases in ω coincided with decreases in R, and *vice versa*.

The relationship between ω and $\partial\omega/\partial s$ revealed downstream changes in the energy gradient as a function of the mean stream power generated in each budget cell. In the case of the April 2019 event, the highest values of $\partial\omega/\partial s$ were often preceded by high values of ω (above 300 W $m^{-2}$), while the $\partial\omega/\partial s$ close to zero or with a negative sign occurred along sections with low-to-moderate mean stream power ($\omega < 200$ W $m^{-2}$). Except for the final part of the middle reach, where road-crossing drainage culverts locally disturbed the flow, the fluctuations in $\partial\omega/\partial s$ were less pronounced and lower in the MDR than in the UPR.

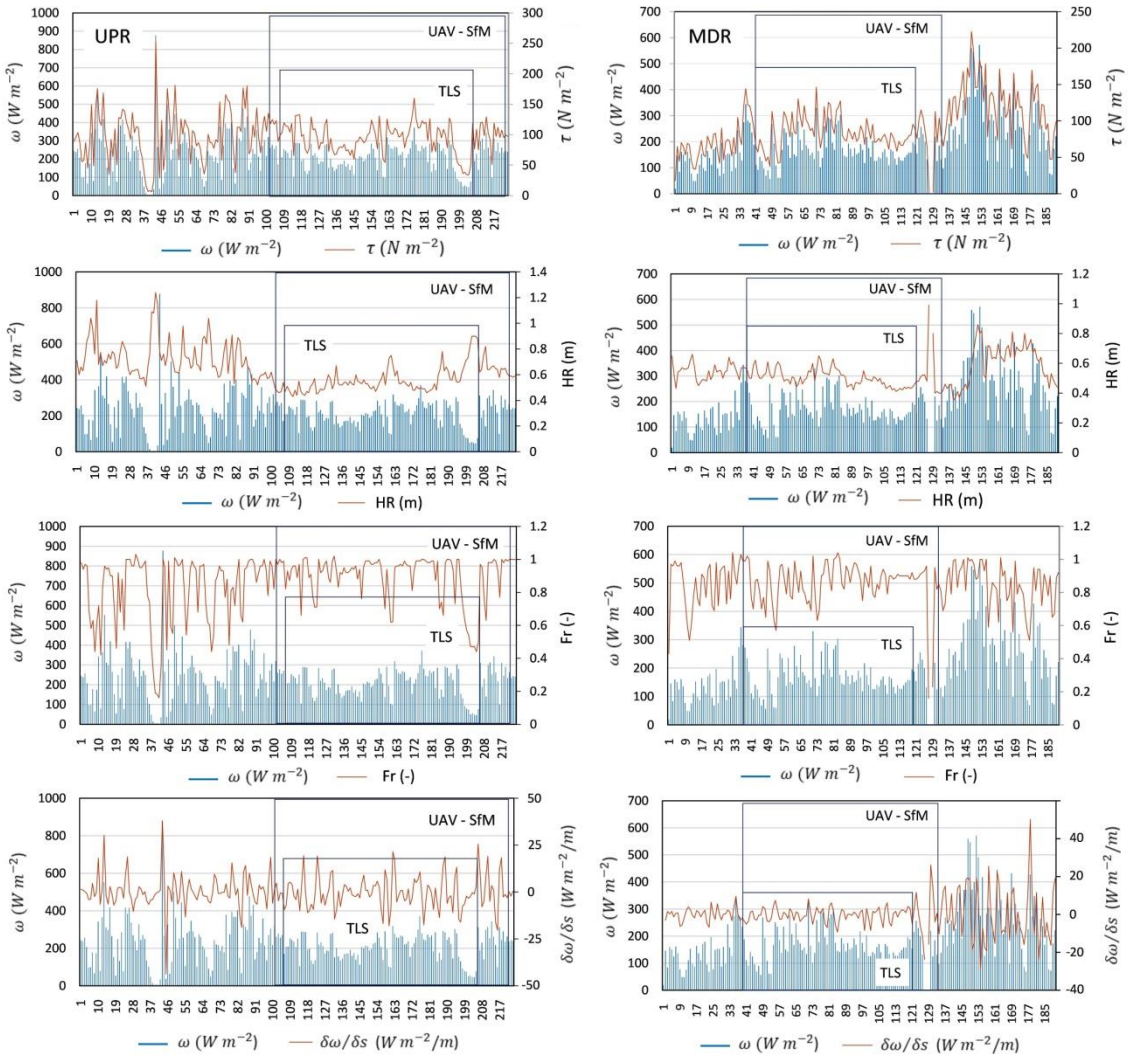


**Figure 3.13.** Spatial variability in the relationships of ω with $\tau_0$, R, Fr, and $\partial\omega/\partial s$ along the UPR (223 equidistant cross-sections, 2.0-3.5 m apart) and the MDR (191 cross-sections), including their respective RCR covered by UAV-SfM and TLS. Peak flood of 19-20 April 2019.

### 3.4.4. Stream power variations versus changes in bed stability

Transport and high incision efficiency often occur when the limiting shear stress and stream power exceed the resistance of the bed materials to be mobilized (Lague, 2014). The bed stability indices used here follow this criterion, but in armored bed channels such as ours the heterogeneity of mixed-grain-size material- including sand, gravel, and pebbles- implies non-unimodal distributions that have an important influence on the initial bedload motion and complicate the bedload transport-rate estimations (Almedeij, 2002).In addition, transport-capacity-based assessments in this type of gravel-bed stream produce results that are sometimes not very consistent with the observed net sediment fluxes, due to discrepancies attributed to non-uniform grain sizes, bed surface armoring, and bedform variability (Buffington and Montgomery, 1997; Hassan et al., 2008; Lisle and Church, 2002).

In the RCRs of this study, high bed armoring and a coarsening-upward trend in most bed deposits led to a relationship between the stability of the armored surface layer and sub-surface detrital layer with the topographic changes observed using VHR DTM. Specifically, relationships between the RBS index attributable to each of these layers and the differences in net bed elevation provided by these spatial models (Δe (SfM-TLS)) after the April flood event were obtained, with the following results:

$$\Delta e\ (SfM\text{-}TLS) = 0.167 \ln(RBSsup) + 0.409 \qquad R^2 = 0.715 \qquad (3.7)$$

$$\Delta e\ (MfS\text{-}TLS) = 0.122 \ln(RBSsub) + 0.506 \qquad R^2 = 0.637 \qquad (3.8)$$

Using regression equations with a logarithmic function, the best fit was achieved for the materials that make up the surface armored layer. This conclusion together with the recommendation to use $D_{84}$ for the bed stability calculations in these cases (Martín-Vide, 2007) led to the adoption of both criteria to estimate RBS. By comparing the map of stream power (Figure 3.7) with the spatial distribution of bedforms and bed stability indices, we explored whether the stream power thresholds set by other authors (e.g. Magilligan, 1992; Stacey and Rutherfurd, 2007) to evaluate transport efficiency classes in non-ephemeral, gravel-bed streams are valid for this GBES type. Concerning the stream power thresholds, these authors proposed 35 $Wm^{-2}$ for riverbed erosion and 300 $Wm^{-2}$ for overall morphological channel changes. In our case, and as already evidenced by Conesa-García et al. (2020b) in the upper Mula stream, a high spatial heterogeneity of bed forms and sediment grain sizes was observed, leading to stability changes over relatively short distances, which locally affected the stream power required for sediment entrainment.

The threshold of 35 $Wm^{-2}$ did not coincide with that of bed instability in many of the cross-sections studied here (Fig. 3.14), and in other cases it did not coincide with the removal threshold, established from negative values of Δe when TLS was used. The ω thresholds to initiate particle movement in unstable bed sections (RBS<1) ranged between 35 and 43.7 $Wm^{-2}$ for the minor peak flow. In the April flood event these thresholds were exceeded in almost all cases because of the greater flow energy generated. In addition, a minimum of 46.5 $Wm^{-2}$in the upper RCR and of 66.4 $Wm^{-2}$ in the middle RCR was required to cause bed incision along the stretches monitored by TLS. Both events exhibited a very efficient transport capacity, with $\tau$ exceeding $\tau_c$ in more than 95% and 86% of the cross-sections in the upper and middle reaches, respectively (Table 3.6).

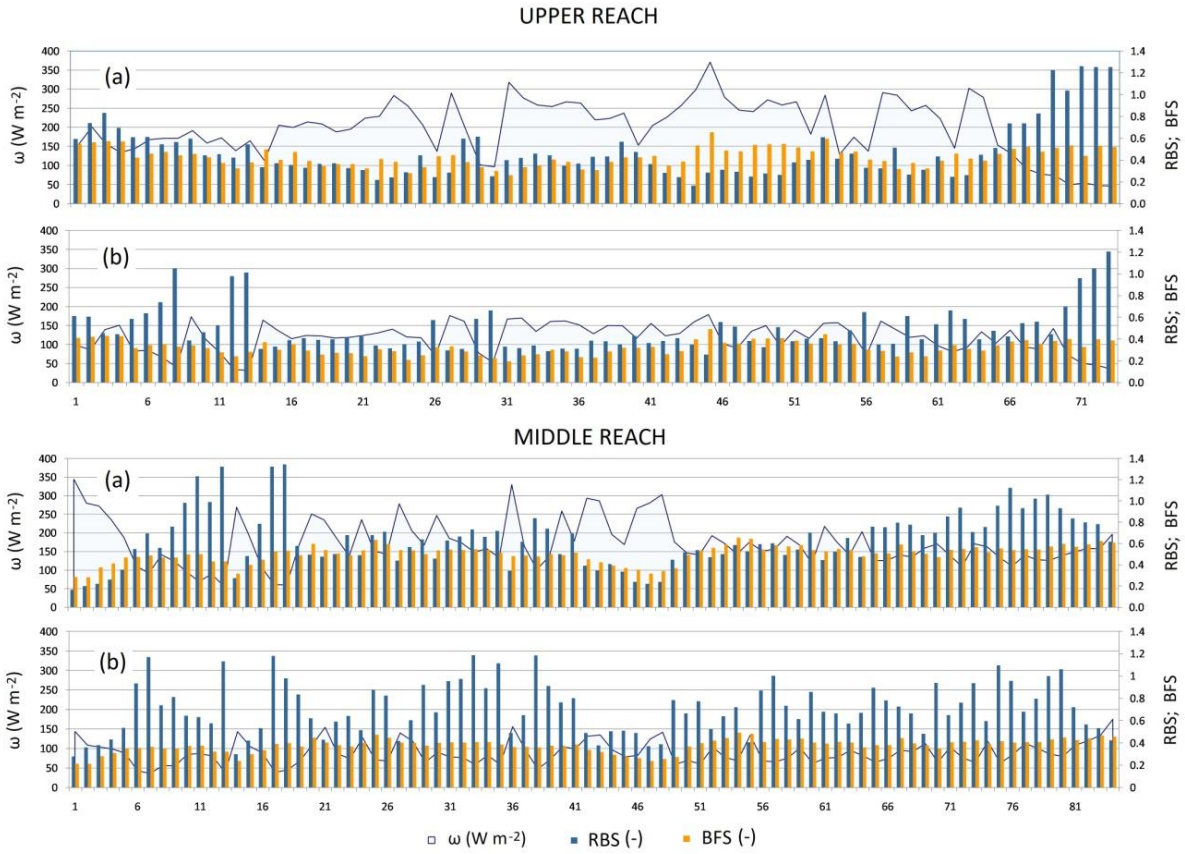


**Figure 3.14.** Mean stream power (ω) versus the Relative Bed Stability (RBS) and Bed Form Stability (BFS) indices estimated in cross-sections along the upper and middle RCRs, in a downstream direction. Flow peaks of 19-20 April 2019 (a) and 12-13 September 2019 (b).

Although the results found for RBS>1cannot be considered statistically significant, the difference in the mean ω between the stable and unstable RCR beds was quite relevant, with the event magnitude being as influential on the sediment transport as the bed grain size. This contrast was somewhat similar in both stretches, which contradicts a progressive decrease in downstream flow competence. The ω needed for transport to start varied only slightly from section to section, so, according to the relationships between the driving forces and sediment loading, particle size and bedforms became two crucial factors in the assessment of morphological bed alterations.

The interval of ω commonly associated with moderate to significant morphological changes in non-ephemeral gravel-bed streams (35-300 W $m^{-2}$) showed different patterns here in terms of magnitude and frequency. The unstable bed sections supported a substantially higher average energy in the upper RCR than in the middle RCR. In particular, most of the ω values along the upper RCR (72nd percentile) on 19-20 April 2019 were in the 150-300 $Wm^{-2}$ interval, scoring a mean of 211.2 $Wm^{-2}$, while in the middle RCR the 72nd percentile dropped to 45% and the mean to160.5 $Wm^{-2}$. For a peak discharge of 21.9 $m^3/s$, the upper reach stream showed a higher transport capacity than the middle stretch (31.3 $m^3/s$) to trigger bed degradation processes (e.g. bed scouring and downcutting). Active bed forms predominated upstream, while erosion-resistant bed

forms and aggradation gravel layers had a greater presence downstream in the middle stream reach.

**Table 3.6.** Statistical descriptors got for ω from different ranges of bed stability indices (RBS and BFS), using the stream power thresholds proposed by Magilligan (1992) and Stacey and Rutherfurd (2007) for the evaluation of flow competence in relation to morphological change in perennial, gravel-bed streams.

| | | Peak flow of 19-20 April 2019 | | | | | | | | Peak flow of 12-13 September 2019 | | | | | | | |
|---|---|---|---|---|---|---|---|---|---|---|---|---|---|---|---|---|---|
| Upper RCR | RG | ω for RBS < 1 | | | | ω for RBS > 1 | | | | ω for RBS < 1 | | | | ω for RBS>1 | | | |
| | I(ω) | <35 | 35-150 | 150-300 | >300 | <35 | 35-150 | 150-300 | >300 | <35 | 35-150 | 150-300 | >300 | <35 | 35-150 | 150-300 | >300 |
| | Ncs | 0 | 22 | 90 | 9 | 0 | 4 | 0 | 0 | 1 | 89 | 29 | 0.0 | 1 | 5 | 0 | 0 |
| | % T | 0.0 | 17.6 | 72.0 | 7.2 | 0.0 | 3.2 | 0.0 | 0.0 | 0.8 | 71.2 | 23.2 | 0.0 | 0.8 | 4.0 | 0.0 | 0.0 |
| | % Ac | | 96.8 | | | | 3.2 | | | | 95.2 | | | | 4.8 | | |
| | % I(ω) | - | 18.2 | 74.4 | 7.4 | - | 100 | - | - | 0.8 | 74.8 | 24.4 | - | 6.7 | 83.3 | - | - |
| | Min | - | 74.3 | 152.4 | 302.8 | - | 47.7 | - | - | 34.8. | 51.2 | 150.3 | - | 32.2. | 36.1 | - | - |
| | Med | - | 123.7 | 230.9 | 321.8 | - | 49.8 | - | - | 34.8 | 110.3 | 164.2 | - | 32.2 | 47.7 | - | - |
| | Max | - | 270.9 | 299.0 | 371.4 | - | 54.8 | - | - | 34.8 | 144.5 | 209.5 | - | 32.2 | 61.7 | - | - |
| | σ | - | 41.2 | 41.5 | 22.1 | - | 3.6 | - | - | 0.0 | 25.4 | 13.3 | - | 0.0 | 10.1 | - | - |
| Middle RCR | RG | ω for RBS < 1 | | | | ω for RBS > 1 | | | | ω for RBS < 1 | | | | ω for 1 > RBS | | | |
| | I(ω) | <35 | 35-150 | 150-300 | >300 | <35 | 35-150 | 150-300 | >300 | <35 | 35-150 | 150-300 | >300 | <35 | 35-150 | 150-300 | >300 |
| | Ncs | 3 | 29 | 54 | 3 | 0 | 9 | 0 | 0 | 3 | 74 | 8 | 0 | 0 | 13 | 0 | 0 |
| | % T | 3.1 | 29.6 | 55.0 | 3.1 | 0.0 | 9.2 | 0.0 | 0.0 | 3.1 | 75.5 | 8.1 | 0.0 | 0.0 | 13.3 | 0.0 | 0.0 |
| | % Ac | | 90.8 | | | | 9.2 | | | | 86.7 | | | | 13.3 | | |
| | % I(ω) | 3.6 | 34.1 | 63.6 | 3.6 | - | 100 | - | - | 3.5 | 87.1 | 9.4 | - | - | 100 | - | - |
| | Min | 0.6 | 91.8 | 151.2 | 303.1 | - | 57.1 | - | - | 0.2 | 43.7 | 150.1 | - | - | 36.8 | - | - |
| | Med | 0.9 | 130.2 | 203.4 | 325.8 | - | 92.2 | - | - | 0.3 | 93.4 | 177.9 | - | - | 58.8 | - | - |
| | Max | 1.2 | 149.6 | 293.4 | 344.3 | - | 128.1 | - | - | 0.3 | 149.7 | 215.9 | - | - | 86.1 | - | - |
| | σ | 0.4 | 16.0 | 42.3 | 21.0 | - | 30.9 | - | - | 0.0 | 26.3 | 24.19 | - | - | 17.0 | - | - |

I(IR) = IR interval; RG = RBS range for which ω (mean stream power) values are calculated; I(ω) = ω interval; Ncs = Number of cross-sections with ω value included in each I(ω); % T = percentage of the number of cases in each ω interval regarding the total number of cases in the entire channel reach; % Ac = accumulative percentage of %T; % I(ω)= percentage of cases in each ω interval regarding the total number of cases in each RBS range. Min, Med, and σ = minimum, median, and standard deviation values of ω for each I(ω) within each RBS range.

This is reflected in the third quartile of the BFS values (Q3 between 0.2 and 0.4 in the upper RCR and between 0.4 and 0.6 in the middle RCR, considering the wetted perimeter during the largest runoff) (Figure 3.14). Regarding the frequency of the ω values within this range, the percentage was slightly higher (89.6%) in the upstream reach than downstream (84.6%). However, ω values above a new sub-threshold around 150 $Wm^{-2}$ were found to cause high mobilization of surface gravels and active alluvial bars. The most entrenched and steepest stretches involved a higher percentage of cases above this limit than those with less embedding and bed slope. In fact, the % ω for the 150-300 $Wm^{-2}$ interval increased from 17.6% in the upper RCR to 29.6% downstream (Table 3.6). By contrast, values from 35 to 150 $Wm^{-2}$ were associated with the removal of bank-failure deposits and moderate changes in active low bars. The greatest morphological adjustments, related to ω values above 300 $Wm^{-2}$, were more frequent along the upper channel reach, where phenomena of lateral erosion and intense reactivation of high, scarcely-vegetated bars occurred. In all of these situations, gravel-bed armoring was reinforced by new inputs of coarse sediments. With the lower peak flows, such as the September 12-13, 2019 event, selective transport dominated, as gravel and sand were mobilized, but not pebbles.

Table 3.7 lists the relationships of Δe with ∂ω/∂s, ε, and RBS in the flash flood of April 2019, based on SfM-MVS and TLS datasets. A relatively close relationship of Δe with excess energy and bed stability was achieved using SfM data, which provided the best fit ($r^2$ of 0.56 to 0.60 for Δe versus ε, and around 0.65 for Δe versus RBS). However, the TLS technique gave good results, with some statistical significance, only when associating Δe with RBS, mainly along the upper reach ($r^2$ = 0.61, p-value <0.05).

The higher correlation established with RBS reflects the strong influence that flow competence exerted, through the selective transport of inhomogeneous granular material (such as sand, gravel, and pebbles), on the bed stability. The excess energy expenditure implies a more moderate fit with the morphological variations at the cell level, a better result being foreseeable when a certain consecutive number of budget cells are considered downstream.

**Table 3.7.** Regression equations defining the relationships of Δe with ∂ω/∂s, ε, and Relative Bed Stability (RBS) at the scale of cell i in the flash flood of April 2019. Datasets of SfM-MVS and TLS extracted for the upper (UPR) and middle (MDR) reaches. Significance level (p-value) < 0.05.

| RCR | Δe vs HV | Method | Num. cells | Equation | $r^2$ |
|---|---|---|---|---|---|
| UPR | Δe vs ∂ω/∂s | SfM | 73 | --- | 0.001 |
| | | TLS | 73 | --- | 0.000 |
| MD | Δe vs ∂ω/∂s | SfM | 72 | --- | 0.020 |
| | | TLS | 72 | --- | 0.003 |
| UPR | Δe vs ε | SfM | 50 | Δe (SfM) = 0.0004 ε + 0.179 | 0.597 |
| | | TLS | 42 | Δe (TLS) = 0.0005 ε - 0.097 | 0.453 |
| MDR | Δe vs ε | SfM | 38 | Δe (SfM) = -0.0002 ε + 0.221 | 0.564 |
| | | TLS | 46 | Δe (TLS) = -0.001 ε + 0.053 | 0.521 |
| UPR | Δe vs RBS | SfM | 50 | Δe (SfM) = -0.135 RBS + 0.296 | 0.639 |
| | | TLS | 42 | Δe (TLS) = -0.218 RBS + 0.078 | 0.606 |
| MDR | Δe vs RBS | SfM | 44 | Δe (SfM) = 0.137 8RBS + 0.132 | 0.648 |
| | | TLS | 40 | Δe (TLS)= 0.321 RBS - 0.198 | 0.520 |

### 3.4.5 Sediment budgets and fluxes versus stream power

The point clouds in Figure 3.15 show the D and E values for the peak flows of April 2019, September 2019, and March 2020 for each cell i, in relation to the mean stream power gradient (∂ω/∂s). Positive and negative values depict surface lowering and raising, respectively. *In situ* field observations made after these events corroborated the morphological adjustments in both directions, with the concurrent deposition and erosion on a metric and centimeter scale. Assuming ∂ω/∂s in a given cell leads to the strongest expression of sediment change in the nearest cell downstream from it, scatter plots relating ∂ω/∂s(i) to ΔV(i+1 to i+3) were also used to explain the influence of the energy gradient on the net flux variations immediately downstream (Figure 3.16).

In all cases, the effect of the four hypothesized geomorphic trends described in Table 3.1 was discriminated at the cell scale. Several patterns of variation were found in this type of relationship, depending on the section in question, the predominant geomorphic process, and the event magnitude: 1) For the three events, regardless of the

peak flow reached, the pattern differed greatly between the two stretches, in relation to the premises established for the balance ω - $\omega_c$ in each pair of neighboring cells.

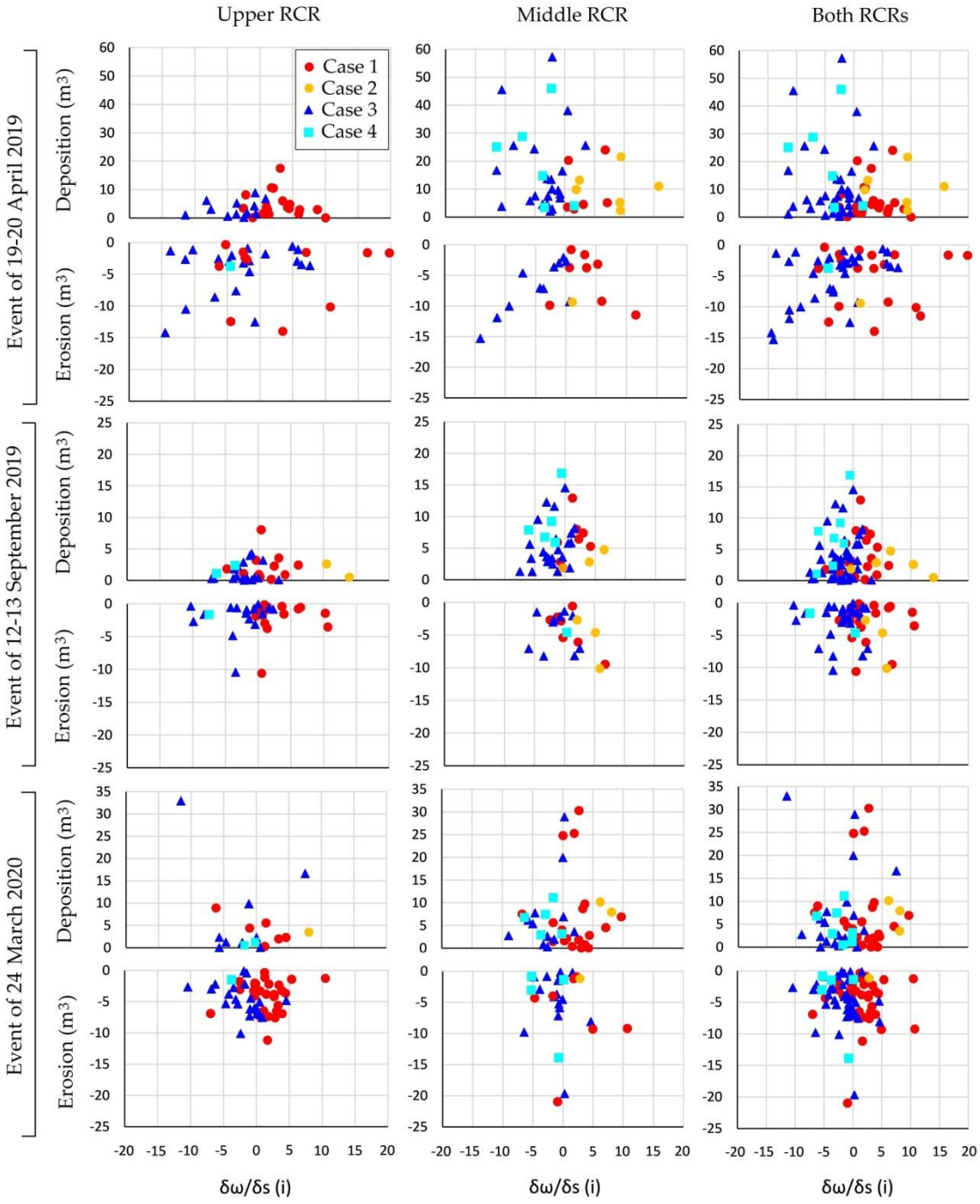


**Figure 3.15.** Plots of ∂ω/∂s(i) versus E(i+ 1) and D(i + 1) for the three peak flows studied along the upper and middle RCRs and the set of both RCRs. Each symbol represents one of the four conditions listed in Table 3.2.

Among the upper RCR relationships practically only cases 1 and 3 were present, while in the middle RCR all cases were represented. 2) During the event of greatest magnitude, the upper section experienced greater net erosion than the middle section, especially in the cells, where ω increased downstream and exceeded $\omega_c$ for both budget cells (case 1), coinciding with ∂ω/∂s values having a positive sign. Also, there were quite a few cross-sections with excess energy despite a decrease in ω downstream (case 3),

resulting in minor deposition that was unable to compensate for transitory erosion. A similar response was found by Conesa-García and García-Lorenzo (2009) in EGBSs draining metamorphic terrains. Consequently, during this type of event the upper reach acts as an important source of sediment for downstream reaches.

Regarding deposition, it was slightly higher in the middle stretch than in the upper section, but the distribution pattern in relation to the energy gradient and the type of case differed considerably between the two channel reaches.

Along the upper RCR the values of D were highest where $\partial\omega/\partial s$ approached zero, and they gradually decreased as the $\partial\omega/\partial s$ values became more positive, which bears some resemblance to the trend described by Lea and Legleiter (2016) for non-ephemeral gravel streams. In contrast, this behavior did not occur in the middle RCR, whose scatter diagram shows a large dispersion of values in all cases. Despite this, the cases representing a minor deposition over a significant accretion dominated here, it being relatively rare that$\omega$ decreased downstream and fell below $\omega_c$ in cell i (case 4) (Figure 3.15). As a result, the middle RCR frequently acted as a sink for material eroded from the closest upstream reach. This is consistent with the results obtained at a large scale by Wilcock and Crowe (2003) and Török et al. (2017), using flume experiments of mixed-size bed sediment, according to which eroded particles tend to be deposited immediately after the erosion zone. There was a lack of a strong and consistent relationship between negative $\partial\omega/\partial s$ values and net deposition in both stretches and all the events. In contrast, the net erosion volumes were always associated with positive values of $\partial\omega/\partial s$ for case 1 at the different flow stages in the reference upper reach but only at the flood discharge in the middle stretch. Energy gradients below 0 produced scour in case 3, when $\omega$ exceeded $\omega_c$ despite decreasing downstream.

Scatter plots relating lags in $\Delta V$ to $\partial\omega/\partial s$ show a limited relationship between these variables at any lag distance between 0 and 3 budget cells (2.5-3.5 m/cell), regardless of the RCR affected. Although the dispersion was high in all cases, we can distinguish two slightly different patterns, according to the RCR. In the upper RCR the net sediment flux, represented in numerous cells by case 3, was more variable as the lag distance increased, passing the 3$^{rd}$ quartile of values from an initial range of +5 to -10 $m^3$ in cells i to + 10 to -15$m^3$ in cells i+3.The opposite occurred with the cells depicting case 1, since the starting cells (i) had more dispersed $\Delta V$ values in a wide range of $\partial\omega/\partial s$, and the most distant budget cells (i+3) showed a concentration of flux volumes of both signs between -5 and +10 $m^3$ for $-5 < \partial\omega/\partial s < 10$ W $m^{-2}$/m.

The spatial variation pattern of $\Delta V$ in relation to $\partial\omega/\partial s$ found for the reference MDR was characterized by a lack of change with the immediate lag distance (i+2) (Figure 3.16). At most, only a few budget cells i that met the condition in case 4 showed variation in short downstream paths. For cell i+1, all the net flux values, corresponding to this class of cases, were positive and variable (0 to 45 $m^3$), most occurring within a relatively narrow negative $\partial\omega/\partial s$ range (between 2 and 7 W $m^{-2}$/m).

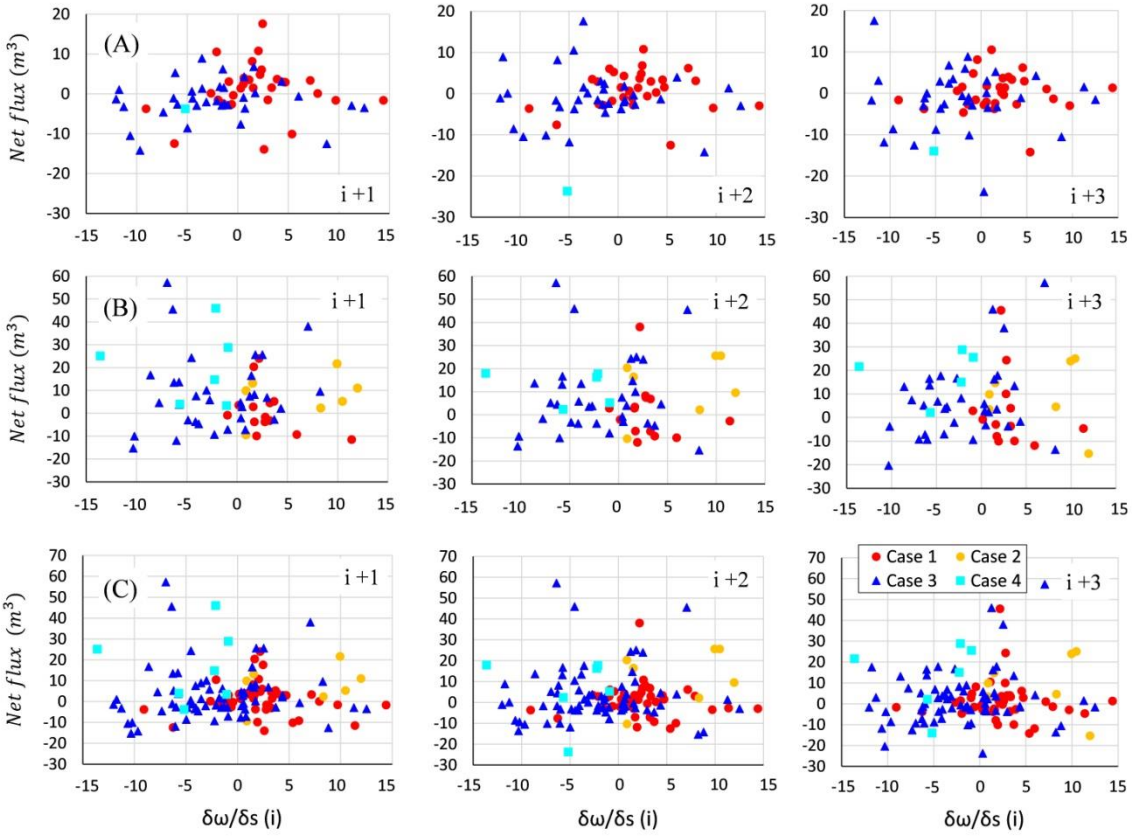


**Figure 3.16.** Plots of $\partial\omega/\partial s(i)$ (W $m^{-2}$/m) versus $\Delta V$ (i+1 to i+3) ($m^3$) for the upper (A) and middle (B) reaches and the sum of both channel stretches (C) for the flood of April 2019. These values represent the net sediment fluxes observed for downstream average lags of 3 m (i + 1) to 9 m (i + 3). Each symbol represents one of the four conditions highlighted in Table 3.2.

The response immediately downstream (cell i+2) translated into a concentration of $\Delta V$ (0 to 20 $m^3$) for the same range of energy gradient, part of that variability being recovered in the next cell. In addition, isolated lags in high net fluxes belonging to case 3 were marginally significant, the influence of $\partial\omega/\partial s$ declining as the distance increased. These results are not significantly consistent, since the association of $\Delta V$ with negative values of $\partial\omega/\partial s$ in cases 1 and 2 and with positive values of $\partial\omega/\partial s$ in cases 3 and 4 suggests that $\partial\omega/\partial s$ was not strongly related to E and D, which agrees with what was shown by Lea and Legleiter (2016).

Regarding the total net flux, $\partial\omega/\partial s$ (i) maintained the same variation pattern with T as with $\Delta V$ (i+1), having a positive sign in the cells encompassed by cases 1 and 2, and a negative sign in those belonging to cases 3 and 4 (Figure 3.17). Normally, we would expect greater values of $\partial\omega/\partial s$ and $\varepsilon_c$ to be associated with a larger total flux.

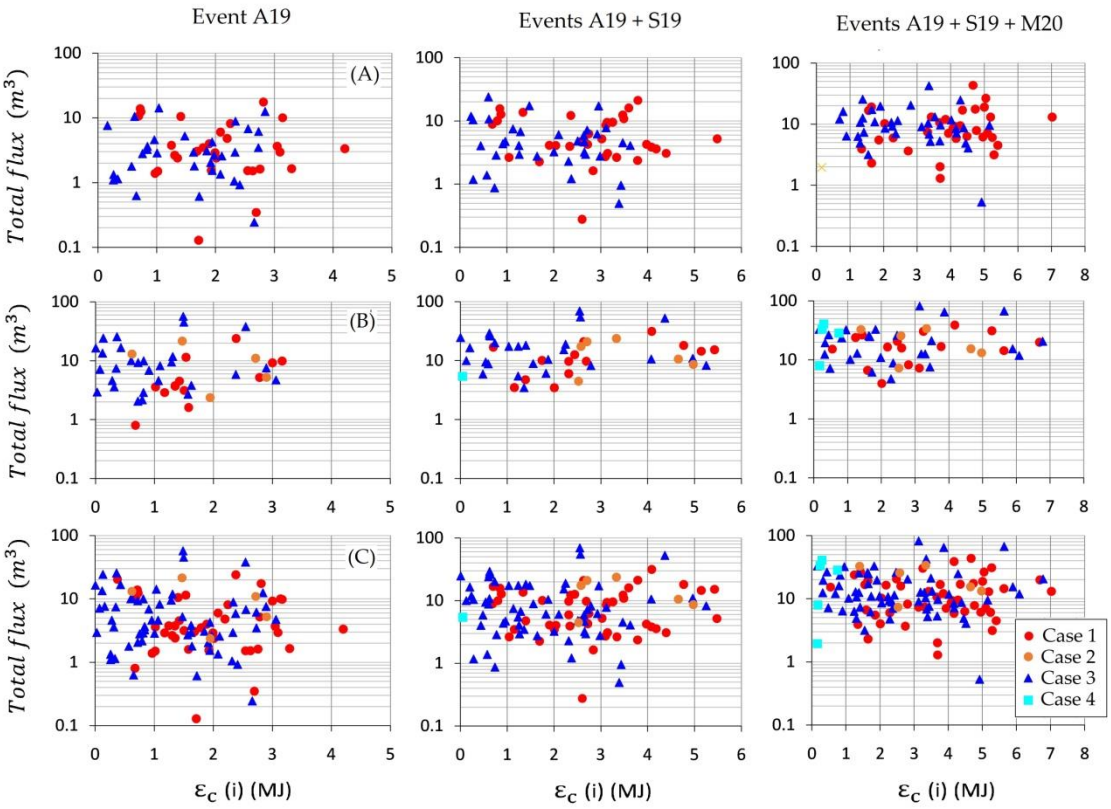


**Figure 3.17.** Plots of T (i + 1) versus $\varepsilon_c$ (i) in MJ - for the event of April 2019, the events of April and September, 2019, and all three events analyzed - along the upper (A) and middle (B) reaches and both channel stretches (C). Each symbol represents one of the four conditions listed in Table 3.3.

However, a high dispersion of these values was a common feature for each channel stretch and study case, as a result of discontinuous changes in bedload and channel morphology. The scattered and skewed distributions of both hydraulic variables could be related to non-homogeneous bed forms or changes in granular texture. Conesa-García et al. (2020b) associated this lack of relationship in another complex gravel-bed dry channel (upper Mula stream, in Southeastern Spain) with the presence of blocks from the bank breaks, pools-riffle sequences, and local transitions from alluvium to substrate outcrop and *vice versa*. Note that the ephemeral stream studied here is characterized by mixed-size bed materials, predominantly gravel, and highly mobile alluvial bars, mostly active bars without vegetation or that are not very stable, that constantly change shape and extension. Especially in the upper reach, isolated groups of blocks deposited by recent collapses or exhumed ancient boulders disturb the flow regime and alter the total sediment flux over short distances. Zapico et al. (2018) analyzed this type of relationship in a steep, sand-gravel ephemeral channel and found, by contrast, a clear relationship between the variation in bedload flux, texture, and total bedload yield (measured directly in the field) and changes in channel shape and bed texture (derived from topographic surveys using SfM and TLS).

The RBS showed a greater mix of dispersed cases regarding the total sediment yield, perhaps due to a different bed response that released various particle sizes at contrasting critical stresses, versus spatial variations in the mean stream power. As other

authors (e.g. Billi, 2011) have verified for ephemeral channels during flash flood events, the bedload here made up most of the total sediment flux. Consequently, variations in the amount and thickness of gravel available for entrainment could lead to fluctuations in the downstream bedload and hence in T values.

In Figure 3.16, $\varepsilon_c(i)$ was plotted against T(i) to examine the hypothesis that these two variables could be correlated. All these scatter plots display point clouds, which represent the relationships between these variables for the flood of April 2019, and the two following minor events, for which ε(i) values were added in chronological order. The condition $\omega(i) > \omega(i-1) > \omega_c$ (case 1), which represents an erosional trend, occurs at an $\varepsilon_c$ value above 0.2 MJ in the upper RCR and above 0.1 MJ in the middle RCR. Below these thresholds the cumulative excess energy per unit bed area ($\varepsilon_c$) over the flow peak time is insufficient to cause scour, although the movement of the bed material load is negligible. Up to an $\varepsilon_c$ value of approximately 1 MJ, budget cells prone to deposition predominated, whereas from this threshold onwards the number of cells with a tendency to suffer erosion increased.

The largest flood, in April 2019, generated a high total net flux, fluctuating between 0.2 and 20 $m^3$ per cell in the upper reach and between 0.8 and 50 $m^3$ per cell in the middle section, associated with $\varepsilon_c$ values of 0.1 to 3.3 MJ. The event of September 2019 had little impact on the T values. On the other hand, the additional consideration of the bankfull event of March 2020 meant an increase of 1 and 2 MJ in the upper and middle stretches, respectively, and a maximum increase in T of 20 $m^3$/cell. Along both reaches, in the entire analysis period, a mean T of 12 $m^3$/cell was mobilized for a mean $\varepsilon_c$ of around 3 MJ. The scarcest movement of bed material corresponded to the budget cells belonging to case 4, with the lowest $\varepsilon_c$, and the highest T values to cells 1 and 3, with $\varepsilon_c$ values ranging from 3 to 6 MJ. However, the total accumulated flux was quite considerable in relation to the basin size and the peak flow generated, especially in the middle section, where 1.5 MJ was enough for T(i) to reach 50 $m^3$. As has been shown in previous studies (Reid and Laronne, 1995), the bed load flux produced in this type of dry stream during torrential flows often exceeds the maximum order of magnitude measured at similar levels of stream power in perennial counterparts.

An ANOVA and the Tukey HSD test were performed to determine if the behavior of each of the four cases of erosion, deposition, and net sediment flux differed among the peak flow events and between the RCRs (Table 3.8).

The results show that there were no significant differences among the means of the four cases for each of the groups identified as variables referring to sediment budgets, which contrasts with the hypothesized conditions from Table 3.2. By contrast, the cases of the $\partial\omega/\partial s$ group generally reflected a significant relationship, with rejection of the null hypothesis of equality of variances and, therefore, important differences between the cases. Considering the entire period, a closer relationship was found for the cases of deposition in the upper RCR and for the cases of erosion in the middle RCR (Table 3.9).

**Table 3.8.** ANOVA and Tukey range test P-values for the evaluation of whether the means among the four cases described in Table 3.2 are significantly different for the sediment budget variables in each peak flow and RCR (asterisks represent significant differences, $p < 0.05$).

| | | 19-20 April, 2019 | | | | 12 September, 2019 | | | | 24 March, 2020 | | | |
|---|---|---|---|---|---|---|---|---|---|---|---|---|---|
| | | E | D | ΔV | δω/δs | E | D | ΔV | δω/δs | E | D | ΔV | δω/δs |
| Upper RCR | ANOVA | 0.95 | 0.40 | 0.14 | 0.01* | 0.93 | 0.90 | 0.78 | 0.01* | 0.41 | 0.74 | 0.54 | 0.01* |
| | 1 vs. 2 | - | - | - | - | - | 0.99 | 0.81 | 0.01* | - | 1.00 | 0.75 | 0.54 |
| | 1 vs. 3 | 0.96 | 0.40 | 0.143 | 0.01* | 0.94 | 0.87 | 1.00 | 0.01* | 0.76 | 0.87 | 0.75 | 0.15 |
| | 1 vs. 4 | 0.97 | - | 0.68 | 0.42 | 0.99 | 1.00 | 0.95 | 0.01* | 0.54 | 0.97 | 0.87 | 0.01* |
| | 2 vs. 3 | - | - | - | - | - | 0.99 | 0.80 | 0.01* | - | 0.97 | 0.88 | 0.25 |
| | 2 vs. 4 | - | - | - | - | - | 1.00 | 0.98 | 0.01* | - | 0.99 | 0.97 | 0.03* |
| | 3 vs. 4 | 0.99 | - | 0.93 | 0.98 | 0.98 | 0.99 | 0.95 | 0.32 | 0.43 | 0.77 | 0.99 | 0.13 |
| Middle RCR | ANOVA | 0.73 | 0.44 | 0.07 | 0.01* | 0.88 | 0.83 | 0.14 | 0.01* | 0.73 | 0.98 | 0.63 | 0.01* |
| | 1 vs. 2 | 0.71 | 1.00 | 0.77 | 0.26 | 0.87 | 0.67 | 0.79 | 0.15 | 0.77 | 0.99 | 0.98 | 0.47 |
| | 1 vs. 3 | 0.94 | 0.99 | 0.43 | 0.01* | 1.00 | 0.99 | 0.95 | 0.01* | 0.85 | 1.00 | 0.68 | 0.01* |
| | 1 vs. 4 | - | 0.50 | 0.04* | 0.01* | 0.99 | 0.22 | 0.26 | 0.04* | 0.92 | 0.99 | 0.95 | 0.08 |
| | 2 vs. 3 | 0.79 | 0.99 | 1.00 | 0.01* | 0.88 | 0.66 | 0.50 | 0.01* | 0.92 | 0.99 | 0.81 | 0.03* |
| | 2 vs. 4 | - | 0.54 | 0.41 | 0.01* | 0.99 | 0.73 | 0.10 | 0.01* | 0.94 | 0.98 | 0.91 | 0.04* |
| | 3 vs. 4 | - | 0.48 | 0.26 | 0.99 | 1.00 | 0.13 | 0.37 | 0.98 | 1.00 | 0.99 | 0.99 | 0.99 |

**Table 3.9.** ANOVA and Tukey range test P-values for the evaluation of whether the means among the four cases described in Table 3.2 are significantly different for the sediment budget variables in the entire analysis period and both RCRs (asterisks indicate significant differences, $p < 0.05$).

| | 29 November 2018 to 26 July 2020 | | | | | | | |
|---|---|---|---|---|---|---|---|---|
| | Upper RCR | | | | Middle RCR | | | |
| | E | D | ΔV | δω/δs | E | D | ΔV | δω/δs |
| ANOVA | 0.62 | 0.80 | 0.74 | 0.01* | 0.98 | 0.30 | 0.21 | 0.01* |
| 1 vs. 2 | - | 0.96 | 0.78 | 0.01* | 1.00 | 0.99 | 0.96 | 0.01* |
| 1 vs. 3 | 0.83 | 0.99 | 0.98 | 0.01* | 0.99 | 0.93 | 0.83 | 0.01* |
| 1 vs. 4 | 0.78 | 0.80 | 0.99 | 0.01* | 0.98 | 0.23 | 0.15 | 0.01* |
| 2 vs. 3 | - | 0.98 | 0.72 | 0.01* | 0.99 | 0.99 | 1.00 | 0.01* |
| 2 vs. 4 | - | 0.99 | 0.91 | 0.01* | 0.99 | 0.59 | 0.61 | 0.01* |
| 3 vs. 4 | 0.66 | 0.84 | 0.98 | 0.33 | 0.99 | 0.39 | 0.34 | 1.00 |

## 3.5 Conclusions

It is known that the morphodynamics in ephemeral streams are subject to non-continuous geomorphic activity associated with hydrological events of different magnitudes, discrete in time. Understanding the morphological adjustments derived from such events in ephemeral gravel-bed channels is often complex, due to the influence of variations in the bedload on the location of sediment sources and sinks within the channel, bed armoring, and changes in bedforms. In such cases, the applicability limits of the existing sediment transport formulas still constrain the accuracy of the numerical modeling, making it advisable to adopt a sediment budget approach. In this case study an excess or deficit of sediment at the event scale implied short-term changes in the bed elevation depending on the peak flow. Such changes were satisfactorily evaluated through

the combined use of SfM-MVS and TLS, according to the spatial scale and geomorphic scenario. The SfM-MVS technique turned out to be suitable for quantifying sediment budgets in RCRs more than 100 m in length, while TLS provided excellent results for the assessment of changes in bedforms at more detailed spatial scales (e.g. PBSAs). In addition, the VHR DTM generated from the combination of both techniques increased the accuracy of the 1-D hydrodynamic model previously calibrated with field data. The ground-based LiDAR-derived bed elevation change depicted the common trend towards a dynamic equilibrium in the upper RCR and a more variable behavior in the middle section, where sediment transport of more variable bedload composition occurred — both in time and space —. The scatter plots relating $\partial \omega / \partial s$ (i) to $\Delta e(i)$ and $\Delta V(i)$ along the middle RCR showed the sparsest distributions and reflected the smallest lag effect (i+n), which also extended to the morphological response.

Hypotheses concerning the relationships between spatial patterns of stream power and changes in bed elevation and sediment fluxes were tested for different conditions of flow competence. The spatial variation pattern of $\Delta V$ with $\partial\omega/\partial s$ was not significantly consistent, since the association of $\Delta V$ with negative values of $\partial\omega/\partial s$ in cases 1 and 2 and with positive values of $\partial\omega/\partial s$ in cases 3 and 4 suggests that $\partial\omega/\partial s$ was not strongly related to erosion and deposition rates. However, a different geomorphic response was found in relation to three discharge thresholds. The largest events, with overtopping flows above 30 $m^3 s^{-1}$, showed the highest values of stream power ($\omega > 300$ $Wm^{-2}$) and great spatial variability in both the mean power gradient ($\sigma > 6$ $Wm^{-2}/m$) and the excess energy ($\sigma > 80$ $Wm^{-2}$). These peak flows mobilized a vast amount of bedload, causing notable transitory erosion and leading to overall vertical accretion. By contrast, $\omega$ values from 35 to 150 $Wm^{-2}$were associated with the removal of bank-failure deposits and moderate changes in active low bars. Bed aggradation especially dominated in the lateral zones, due to bank breakage and displacement of medial gravel bars.

Contrarily, moderate peak flows, at the bankfull and sub-bankfull stages, mainly produced surface washing, selective transport, and scour processes. The effective discharge for bed load transport occurred at stages higher than bankfull discharge. If, as is to be expected in southeastern Spain, climate change implies - in the short and medium term - an increase in the frequency of large events to the detriment of low-water discharges, it is most likely that ephemeral gravel-bed streams will undergo processes more typical of arid regions, such as bed degradation, armoring, lateral erosion, and channel widening. In conclusion, this study provides a useful approach to analyze, at the event scale and very spatial resolution, relationships between stream power variations and morphological bed changes in a typically Mediterranean ephemeral gravel-bed stream. Furthermore, the results, also based on changes in bed stability and sediment fluxes, are applicable to protection and restoration plans in a wide range of ephemeral Mediterranean channels, whose recent dynamics reflects the effects of climate change.

**Notation**

| | |
|---|---|
| bgu | bed geomorphic unit [-] |
| $D_{50}$ | median grain size (m) |
| $D_{84}$ | particle size corresponding to the 84% ofthe sample weight (m) |
| g | acceleration of gravity [m $s^{-2}$] |
| i | cell ati cross-section |
| j | cell lag at j cross-section |
| R | hydraulic radius [m] |
| RBS | relative bed stability index [-] |
| BFS | bedform stability index [-] |
| $r^2$ | determination coefficient [-] |
| $S_w$ | water surface slope [m $m^{-1}$] |
| D | gross deposition ($m^3$) |
| E | gross erosion ($m^3$) |
| Fr | Froude number [-] |
| PBSA | pilot bed survey area |
| $Q_{pf}$ | Peak flow discharge ($m^3$ $s^{-1}$) |
| RCR | reference channel reach |
| T | total sediment flux ($m^3$) |
| $\Delta V$ | net sediment flux ($m^3$) |
| $\partial\omega/\partial s$ | mean stream power gradient [$Wm^{-2}$/m] |
| $\varepsilon_{(i)}$ | excess energy per unit bed area over $\omega_c$ at cell i [W $m^{-2}$] |
| $\varepsilon_c$ | cumulative excess energy per unit bed area (MJ) |
| $\gamma$ | specific weight of water (N $m^{-3}$), |
| $\Omega$ | cross-sectional stream power [W $m^{-1}$] |
| $\omega$ | mean stream power [W $m^{-2}$] |
| $\omega_c$ | critical mean stream power [W $m^{-2}$] |
| $\omega/\omega_c$ | mean stream power ($\omega$) / resisting power ($\omega_c$) ratio [-] |
| $\rho$ | density of water [kg $m^{-3}$] |
| $\rho_s$ | density of sediment [kg $m^{-3}$] |
| $\upsilon$ | flow velocity (m $s^{-1}$) |
| $\tau$ | shear stress (N $m^{-2}$) |
| $\tau_{bf}$ | shear stress at bankfull flow (N $m^{-2}$) |
| $\tau_{c84}$ | critical shear stress required to mobilize $D_{84}$-size particles (N $m^{-2}$) |
| $\tau_c^*$ | critical values of the dimensionless Shields parameter [-] |

## 3.6 References


Ali, K.F. and De Boer, D.H., 2003. Construction of sediment budgets in large-scale drainage basins: The case of the upper Indus River. In Proceedings of the Erosion Prediction in Ungauged Basins: Integrating Methods and Techniques, Montpellier, France, 8–9.

Almedeij, J.H., 2002. Bedload transport in gravel-bed streams under a wide range of Shields stresses. Doctoral Thesis, Virginia Polytechnic Institute and State University, Virginia.

Benito, G., Thorndycraft, V.R., Rico, M.T., Sanchez-Moya, Y., Sopena, A., Botero, B.A., Machado, M.J., Davis, M. and Pérez-González, A., 2011. Hydrological response of a dryland ephemeral river to southern African climatic variability during the last millennium. Quat. Res. 75(3), 471–483.

Billi, P., 2011. Flash flood sediment transport in a steep sand-bed ephemeral stream. Int. J. Sediment Res. 26(2), 193–209.

Bizzi, S. and Lerner, D.N., 2015. The use of stream power as an indicator of channel sensitivity to erosion and deposition processes. River Res. Appl. 31(1), 16–27.

Brasington, J., Langham, J. and Rumsby, B., 2003. Methodological sensitivity of morphometric estimates of coarse fluvial sediment transport. Geomorphology 53(3), 299–316.

Brodu, N. and Lague, D., 2012. 3D terrestrial lidar data classification of complex natural scenes using a multi-scale dimensionality criterion: Applications in geomorphology. ISPRS J. Photogramm. Remote Sens. 68, 121–134.

Buffington J.M. and Montgomery D.R., 1997. A systematic analysis of eight decades of incipient motion studies, with special reference to gravel-bedded rivers. Water Resour. Res. 33(8), 1993–2029.

Bull, W.B., 1997. Discontinuous ephemeral streams: Geomorphology 19, 227–276.

Calle, M., Alho, P. and Benito, G., 2018. Monitoring ephemeral river changes during floods with SfM photogrammetry. J. Iber. Geol. 44(3), 355–373.

Camenen, B., Jaballah M., Geay T., Belleudy P., Laronne J.B. and Laskowski J.P., 2012. Tentative measurements of bedload transport in an energetic alpine gravel bed river. In Munoz, M. (Ed.), River Flow, Taylor & Francis Group, London, pp. 379–386

Conesa-Garcia, C., 1995. Torrential flow frequency and morphological adjustments of ephemeral channels in southeast Spain. In Hickin, E.J. (Ed), River Geomorphology, John Wiley & Sons, Chichester, UK, pp. 169–192.

Conesa-García, C. and García-Lorenzo, R., 2009. Effectiveness of check dams in the control of general transitory bed scouring in semiarid catchment areas (South-East Spain). Water Environ. Res. 23(1), 1–4.

Conesa-García, C., Pérez-Cutillas, P., García-Lorenzo, R., Eekhout, J., Gómez-Gutiérrez, A., Millares-Valenzuela, A. and Martínez-Salvador, A., 2020b. Dimensionless morphological ratios versus stream power variations at bankfull stage in an

ephemeral channel. Geomorphology 361.

Conesa-García, C., Puig-Mengual, C., Riquelme, A., Tomás, T., Martínez-Capel, F., García-Lorenzo, R., Pastor, J.L., Pérez-Cutillas, P. and Cano-Gonzalez, M., 2020a. Combining SfM photogrammetry and terrestrial laser scanning to assess event-scale sediment budgets along a gravel-bed ephemeral stream. Remote Sens. 12(21), 3624.

Egeler, C.G. and Simon, O.J., 1969. Orogenic evolution of the Betic Zone (Betic Cordilleras, Spain), with emphasis on the nappe structures. Geologie en Mijnbouw 48, 296–305.

Emmett, W.W. and Wolman, M.G., 2001. Effective discharge and gravel-bed rivers. Earth Surf. Process. Landf. 26(13), 1369–1380.

Finnegan, N.J., Roe, G., Montgomery, D.R. and Hallet, B., 2005. Controls on the channel width of rivers: Implications for modeling fluvial incision of bedrock. Geology 33, 229–232.

Flatley, A. and Rutherfurd, I., 2018. Using Structure from Motion (SfM) to capture high resolution geomorphic units within small ephemeral channels. 20th EGU General Assembly, EGU2018, Proceedings from the conference held 4-13 April, Vienna, Austria, p.10896.

Galea, A.B., Sadler, J.P., Hannah, D.M., Datry, T. and Dugdale, S.J., 2019. Mediterranean intermittent rivers and ephemeral streams: Challenges in monitoring complexity. Ecohydrology 12(8), e2149.

Garzón, G. and Alonso, A., 2002. Comparison of the flood response of a braided and a meandering river, conditioned by anthropogenic and climatic changes. In Martini, I.P., Baker, V.R., Garzón, G. (Eds.), Flood and Megaflood Processes and Deposits: Recent and Ancient Examples. Blackwell Publishing Ltd., Oxford, UK, pp. 233–249.

Girardeau-Montaut D., 2020. CloudCompare – 3D Point Cloud and Mesh Processing Software (Version 2.11.3). GPL Software. 2020. Open Source Project. http://www.cloudcompare.org/ (accessed 5 May 2021).

Golly, A. and Turowski, J.M., 2017. Deriving principle channel metrics from bank and long-profile geometry with the R-package cmgo. Earth Surf. Dynam. 5, 557–570.

Gomez, B., Coleman, S.E., Sy, V.W.K. and Kent, M., 2007. Channel change, bankfull and effective discharges on a vertically accreting, meandering, gravel-bed river. Earth Surf. Process. Landf. 32(5), 770–785.

Hassan, M.A., Gottesfeld, A.S., Montgomery, D.R., Tunnicliffe, J.F., Clarke, G.K.C., Wynn, G., Jones-Cox, H., Poirier, R., MacIsaac, E., Herunter, H. and Macdonald, S.J., 2008. Salmon-driven bed load transport and bed morphology in mountain streams. Geophys. Res. Lett. 35, L04405.

Hooke, J.M., 2006. Human impacts on fluvial systems in the Mediterranean region. Geomorphology 79, 311–335.

Kasprak, A., Wheaton, J.M., Ashmore, P.E., Hensleigh, J.W. and Peirce, S., 2015. The relationship between particle travel distance and channel morphology: Results from physical models of braided rivers. J. Geophys. Res. Earth Surf. 120, 55–74.

Lague, D., 2014. The stream power river incision model: evidence, theory and beyond. Earth Surf. Process. Landf. 39: 38–61.

Lague, D., Brodu, N. and Leroux, J.J., 2013. Accurate 3D comparison of complex topography with terrestrial laser scanner: Application to the Rangitikei canyon (NZ). ISPRS J. Photogramm. Remote Sens. 82, 1026.

Lea, D.M. and Legleiter, C.J., 2016. Mapping spatial patterns of stream power and channel change along a gravel-bed river in northern Yellowstone. Geomorphology 252, 66–79.

Leopold, L.B., Wolman, M.G. and Miller, J.P., 1964. Fluvial Processes in Geomorphology; Dover Publications, New York.

Levick, L.R., Goodrich, D.C., Mariano Hernandez, M., Pima, J.F., Semmens, D.J., Stromberg, J., Tluczek, M., Leidy, R.A., Scianni, M., Guertin, D.Ph. and Kepner, W.G., 2008. The Ecological and Hydrological Significance of Ephemeral and Intermittent Streams in the Arid and Semi-Arid American Southwest. U.S. Environmental Protection Agency, Office of Research and Development, Washington.

Lisle, T.E. and Church, M., 2002. Sediment transport-storage relations for degrading, gravel bed channels. Water Resour. Res. 38(11), 1219.

Lotsari, E.S., Calle, M., Benito, G., Kukko, A., Kaartinen, H., Hyyppä, J., Hyyppä, H. and Alho, P., 2018. Topographical change caused by moderate and small floods in a gravel bed ephemeral river – a depth-averaged morphodynamic simulation approach. Earth Surf. Dynam. 6, 163–185.

Magilligan, F.J., 1992. Thresholds and the spatial variability of flood power during extreme floods, Geomorphology 5, 373–390.

Martín-Vide, J.P., 2007. Ingeniería Fluvial. Aspectos técnicos y medioambientales. International Centre for Numerical Methods in Engineering (CIMNE), Universitat Politècnica de Catalunya, Barcelona.

Norman, L.M., Sankey, J.B. Dean, D., Caster, J., De Long, S., De Long, W. and Pelletier, J.D., 2017. Quantifying geomorphic change at ephemeral stream restoration sites using a coupled-model approach. Geomorphology 283, 1–16.

Notebaert, B., Verstraeten, G., Govers, G. and Poesen, J., 2009. Qualitative and quantitative applications of LiDAR imagery in fluvial geomorphology. Earth Surf. Process. Landf. 34, 217–231.

Olsen, D.S., Whitaker, A.C. and Potts, D.F., 1997. Assessing Stream Channel Stability Thresholds Using Flow Competence Estimates at Bankfull Stage. J. Am. Water Resour. Assoc. 33, 1197–1207.

Ortega, J.A., Razola, L. and Garzón, G., 2014. Recent human impacts and change in dynamics and morphology of ephemeral rivers. Nat. Hazards Earth Syst. Sci. 14(3), 713–730.

Parker, C., Clifford, N.J. and Thorne, C.R., 2011. Understanding the influence of slope on the threshold of coarse grain motion: Revisiting critical stream power. Geomorphology 126, 51–65.

Pitlick, J., Cress, R., 2002. Downstream changes in the channel geometry of a large gravel bed river. Water Resour. Res. 38(10), 34-1–34-11.

Proyecto NATMUR., 2008. Catálogo de Geoservicios de Medio Natural, Vuelofotogramétrico Digital y levantamiento LIDAR de la Región de Murcia. http://www.murcianatural.carm.es/natmur08/ (accessed 5 May 2021).

Pryor, B.S., Lisle, T., Montoya, D.S. and Hilton, S., 2014. Transport and storage of bed material in a gravel bed channel during episodes of aggradation and degradation: a field and flume study. Earth Surf. Process. Landf. 36, 2028–2041.

Puig-Mengual, C.A., Woodget, A.S., Muñoz-Mas, R. and Martínez-Capel, F., 2021. Spatial validation of submerged fluvial topographic models by mesohabitat units. Int. J. Remote Sens. 42(7), 2391–2416.

Reid, I., Laronne, J.B., 1995. Bedload sediment transport in an ephemeral stream and a comparison with seasonal and perennial counterparts. Water Resour. Res. 31, 773–781.

Rickenmann, D., 2011. Alluvial steep channels: Flow resistance, bedload transport prediction and transition to debris flows. In Church, M., Biron, P., Roy, A. (Eds.), Gravel Bed Rivers: Processes, Tools, Environment. John Wiley & Sons, Chichester, pp. 386–397.

Rojan, E., Dłużewski, M. and Krzemień, K., 2020. Sediment budget of high mountain stream channels in an arid zone (High Atlas mountains, Morocco). Catena 190, 104530.

Rowley, T., Ursic, M., Konsoer, K., Langendon, E., Mutschler, M., Sampey, J. and Pocwiardowski, P., 2020. Comparison of terrestrial lidar, SfM, and MBES resolution and accuracy for geomorphic analyses in physical systems that experience subaerial and subaqueous conditions. Geomorphology 355, 107056.

Rusnák, M., Sládek, J., Kidová, A. and Lehotský, M., 2018. Template for High-Resolution River Landscape Mapping Using UAV Technology. Measurement: Journal of the International Measurement Confederation 115, 139–151.

Salmela, J., Kasvi, E., Vaaja, M. T., Kaartinen, H., Kukko, A., Jaakkola, A. and Alho, P., 2020. Morphological changes and riffle-pool dynamics related to flow in a meandering river channel based on a 5-year monitoring period using close-range remote sensing. Geomorphology 352, 106982.

SCS (Soil Conservation Service), 1972. National Engineering Handbook, Section 4. U.S. Department of Agriculture, Washington, D.C. https://directives.sc.egov.usda.gov/OpenNonWebContent.aspx?content=18393.wba (accessed 5 May 2021).

Segura-Beltrán, F. and Sanchis-Ibor, C., 2013. Assessment of channel changes in a Mediterranean ephemeral stream since the early twentieth century. The Rambla de Cervera, eastern Spain. Geomorphology 201, 199–214.

Seifert, E., Seifert, S., Vogt, H., Drew, D., Van Aardt, J., Kunneke, A. and Seifer, T., 2019. Influence of drone altitude, image overlap, and optical sensor resolution on multi-view reconstruction of forest images. Remote Sens. 11(10), 1252.

Singer, M.B. and Michaelides, K., 2014. How is topographic simplicity maintained in

ephemeral dryland channels?. Geology 42(12): 1091–1094.

Stacey, M. and Rutherfurd, I., 2007. Testing specific stream power thresholds of channel stability with GIS, 5th Annual Australian Stream Management Conference, Albury, pp. 384–389.

Sutfin, N.A., Shaw, J., Wohl, E.E. and Cooper, D., 2014. A geomorphic classification of ephemeral channels in a mountainous, arid region, southwestern Arizona, USA. Geomorphology 221, 164–75.

Török, G.T., Baranya, S. and Rüther, N., 2017. 3D CFD Modeling of Local Scouring, Bed Armoring and Sediment Deposition. Water 9(1), 56.

USACE (US Army Corps of Engineers), 2016. HEC-RAS, Rivers Analysis System. Hydraulic Reference Manual, Version 5.0; Hydrologic Engineering Center: Davis, California.

Vázquez-Tarrío, D., Borgniet, L., Liébault, F. and Recking, A., 2017. Using UAS Optical Imagery and SfM Photogrammetry to Characterize the Surface Grain Size of Gravel Bars in a Braided River (Vénéon River, French Alps). Geomorphology 285, 94–105.

Wheaton, J.M., Brasington, J., Darby, S.E. and Sear, D.A., 2010. Accounting for uncertainty in DEMs from repeat topographic surveys: improved sediment budgets. Earth Surf. Process. Landf. 35(2), 136–156.

Wilcock, P.R. and Crowe, J.C., 2003. Surface-based transport model for mixed-size sediment. J. Hydraul. Eng. 129, 120–128.

Wohl, E., 2000. Mountain Rivers. American Geophysical Union, Washington, DC.

Woodget, A.S. and Austrums, R., 2017. Subaerial Gravel Size Measurement Using Topographic Data Derived from a UAV-SfM Approach. Earth Surf. Process. Landf. 42(9), 1434–1443.

Woodget, A.S., Dietrich, J.T. and Wilson, R.T., 2019. Quantifying below-water fluvial geomorphic change: the implications of refraction correction, water surface elevations, and spatially variable error. Remote Sens. 11(20), 2415.

Zapico, I., Laronne, J.B., Lucía, A. and Martín-Duque, J.F., 2018. Morpho-textural implications to bedload flux and texture in the sand-gravel ephemeral Poveda Gully. Geomorphology 322, 53–65.

# 4. Spatial validation of submerged fluvial topographic models by mesohabitat units


## Abstract

Mapping the streambed morphology is crucial for understanding fluvial forms and processes, for advancing both our knowledge and best management practice of riverine systems. It is often done by wading streams but recently topobathymetric Light Detection and Ranging (LiDAR) and imagery captured from airborne platforms are becoming promising and effective surveying methodologies. The recent use of remotely piloted aerial systems (RPAS) combined with structure-from-motion (SfM) photogrammetric processing provides a novel, high-resolution approach to modelling fluvial morphology. Nevertheless, a complicating factor of such data acquisition in fluvial settings is linked to water bodies, whose presence introduces errors and distortions because of light reflection and refraction at the air–water interface. Although proof-of-concept research has shown it is possible to reduce the effects of refraction in certain settings (e.g., clear waters, unbroken surfaces), corresponding validation methods remain limited to point-based assessments of error, these being typically limited to accessible parts of the channel. Here, we provide the first high-resolution, spatially-continuous validation of a stream reach bathymetry surveyed with SfM and corrected with an advanced refraction method. This method required only the camera co-ordinates and is available as open source, coded in C++. We used RPAS imagery from a regulated reach of the Palancia River, Spain, where a diversion structure fully dewatered the reach and let us obtain the entire streambed topography, which we used as spatially-continuous control topography to compare the bathymetry surveyed from imagery during normal flow conditions. We compared this method with the small angle refraction correction (SARC), which has less data requirements, and analysed the error distribution across habitat types (i.e., pools and riffles). These results showed that our approach had smaller errors than SARC in both habitat types, especially in the riffle. By analysing the relationship between error and channel roughness obtained from our dry-bed model, we found that the greatest errors arise in the peripheral zones of the water surface and in its areas where streambed roughness generates more turbulence. Quantitative validation confirmed the reliability of our method as a relatively low-cost tool for the modelling and management of geomorphology and habitat within small- to medium-sized streams.



**Keywords:** bathymetry, photogrammetry, refraction correction, structure-from-motion (SfM), remotely piloted aerial systems (RPAS)

## 4.1 Introduction

Remotely piloted aerial systems (RPAS) technology, along with its associated data processing and analytical methods, are gaining importance in the scientific community and are now applied in a variety of land-use management and geoscience settings (Pajares, 2015; Gallagher and Lawrence, 2016; Eltner et al., 2016). Utilizing low-altitude RPAS, it is now possible to take successive images and process them using structure-from-motion (SfM) photogrammetry, to derive image and topographic products which have an unprecedented high spatial (< 10 centimetres per pixel) and temporal resolution (as permitted by weather and lighting conditions). Compared with products derived from other imaging platforms, such as satellites or aircraft (Legleiter et al., 2019; Tonina et al., 2019), this resolution is considerably better and the procurement costs are also much lower (Remondino et al., 2011; Shintani and Fonstad 2017). For streams, RPAS technology can be applied to monitor riverine system changes and dynamics. A case in point is where the high temporal resolution offered by RPAS enables an assessment of the rapid evolution of river ecosystems (Polat and Uysal, 2015; Lane et al., 2010; Carbonneau et al., 2012; Rusnák et al., 2018).

Unlike traditional photogrammetry and other topographic surveying approaches (e.g., total station and Differential Global Positioning System - DGPS), this RPAS-SfM technique allows us to characterize and model river fluvial morphology in a way that is neither too expensive nor time consuming (Eisenbeiss and Sauerbier, 2011; Westoby et al., 2012; Fonstad et al., 2013). Moreover, it provides a method for obtaining high resolution, spatially continuous topographic models (Marcus, 2012). Because the type of data obtained in a given field campaign depends on the type of sensor or camera mounted on the RPAS, this approach is highly versatile (Haala et al., 2012). The evolution and development of RPAS technology's applications are accelerating in different fields of riverine ecology; for instance, the information provided by RPAS-SfM surveys allows for the analysis of physical river characteristics, such as river morphology (Woodget et al., 2017; Woodget and Austrums, 2017), including river bed grain size (Woodget et al., 2015; Woodget and Austrums, 2017; Vázquez-Tarrío et al., 2017) and erosion/sedimentation rates processes (Calle et al., 2018; Alfonso-Torreño et al., 2019), as well as general hydromorphology (Rivas Casado et al., 2017; Woodget et al., 2016; Woodget et al., 2019; Dietrich, 2017).

The use of Digital Elevation Models (DEMs) generated using SfM (Clapuyt et al., 2016; Westoby et al., 2012), georeferenced using ground control points (GCPs) (Micheletti et al., 2015; Calle et al., 2018), has become commonplace in geomorphology studies. These models permit the analysis of fluvial behaviour and its associated impacts on sedimentary dynamics of river systems and the evolution of riparian vegetation (Vargas-Luna et al., 2015; Belmar et al., 2013; Coveney and Roberts, 2017). Recent applications of RPAS include the study, quantification and modelling of vegetation (Berni et al., 2009; Avtar et al., 2020; van Iersel et al., 2018), which can serve as a decision tool for the maintenance and conservation of riparian habitats (Muñoz-Mas et al., 2017). Furthermore, the remote monitoring of aquatic macrophytes (Biggs et al., 2018) has emerged as a new challenge in the field of ecohydraulics.

For submerged riverine environments, a fundamental problem when extracting morphological information is the refraction of light that occurs at the air–water interface (Wackrow et al., 2015). Snell's Law is the physical theory that explains this phenomenon

which causes the channel bed to appear at a higher elevation than it really is; thus, its effect must be accounted for, to obtain accurate DEMs and subsequent products. This is a common problem also for topo-bathymetric Light Detection and Ranging (LiDAR), which uses green wavelength light. Topo-bathymetric LiDAR (Bailly et al., 2010; Feurer et al., 2008; Kinzel et al., 2013; Tonina et al., 2019) enables the direct acquisition of dense point clouds in submerged environments (Pan et al., 2015; Mandlburger et al., 2015). It has proven useful in those areas where the depth and dimensions of the river accommodate its use, but its coarse spatial resolution (at the meter scale), lack of reliability in areas with abrupt topographical changes (Tonina et al., 2019) and its high cost preclude it as a viable and effective tool for reach scale applications (tens channel width or few kilometres) or in small streams (approximately channel width less than 7 m) (Kinzel et al. 2013; McKean et al., 2009; Nouwakpo et al., 2016).

In recent years, two key methods have emerged to correct the refraction of RPAS-SfM generated topographic data, which has led to improved estimates of water depth and submerged elevation in small streams (Woodget et al., 2015; Dietrich, 2017). Woodget et al. (2015) proposed a method based on a constant correction that could be applied to an entire stream reach, using SfM-generated DEMs, without considering either point-to-point characteristics or the relative position of the RPAS at the time of image capture. This method generates an estimated water surface position and uses its difference from the underlying DEM to approximate water depths. The constant correction of depth under refraction effects is then applied, as derived from Snell's Law and the refractive index of clear water.

Dietrich (2017) proposed a more complex method, which considers the RPAS's relative position for each image, thereby yielding a three-dimensional (3D) model; the corrected elevations of the streambed were obtained by applying trigonometric principles to obtain the beams projected for each point. In practical terms, this method relies on an algorithm, for which the parameters correspond to the angles of rotation on each axis, type of image, focal length, and sensor type. Dietrich (Dietrich, 2017) also reported a relationship between the highest positive errors and streambed areas with higher roughness. Both Woodget et al. (2015) and Dietrich (2017) validated their refraction-corrected models using point-based elevation measures acquired using a Global Positioning System - Real-time kinematic (GPS-RTK) station and thus they were restricted to wadeable and accessible parts of the stream. Accordingly, neither validation was performed on the entire streambed modelled and thus may not be wholly representative of the site. This drawback limits further investigation into the factors affecting error distributions in refraction-corrected models.

In this article, we introduce and implement a procedure to generate a refraction-corrected model of submerged topography in a regulated stream reach, to address three critical objectives:

i. To provide the first validation of a refraction-corrected submerged fluvial topographic model *in situ*, using a digital elevation dataset of stream topography, obtained when the stream reach was completely dry. This allowed us to compare the DEMs of the same streambed mapped during a wet and a dry period, with resolution of 15 millimetres per pixel. With this, we can assess the pattern of error distribution in a way not previously possible by point-based error evaluations. We can also compare our

outputs with those from the widely applied method of Woodget et al. (2015).

ii. To analyse the elevation error patterns within two mesohabitat types of the stream differing in their hydromorphologic characteristics (namely, pools versus riffles). This constitutes a spatially-continuous validation of the DEM within each of the two mesohabitat types (i.e., all pixels of each model were evaluated). Doing this will assist other researchers develop a more realistic appreciation of the strength of this approach in different types/areas of streams and rivers characterised by different habitat types.

iii. To develop a refraction-correction method available as an open-source software tool in C++ (code included in this article as supplemental material).

## 4.2 Methods

### 4.2.1 Study site

We studied a reach of the Palancia River, located in the province of Castellò (Eastern Iberian Peninsula), Spain, that was 74 metres long with an irregular and intermittent flow regime throughout the year due to water diversion for irrigation. We selected this site because of its variability in morphology (e.g., grain size range: 10 to 500 millimetres) and flow characteristics. The stream reach has an average depth of 30 centimetres and a width of 10 metres. Specifically, as Figure 4.1 shows, we visually identified mesohabitat units characterised by different hydromorphological patterns (Alcaraz-Hernández et al., 2011); three mesohabitat types were observed in the study area: pool, rapid, and riffle. We selected the two largest areas for further analysis by mesohabitat type, namely pool and riffle. One represents a habitat of relatively greater hydraulic depth and lower mean velocity (pool) and the other represents a shallow habitat with higher velocity (riffle). The central segment of the stream's reach we classified as rapid, due to its characteristics and behaviour. In this area, the study and validation of the applied refraction correction method was not carried out because the presence of rough white waters in this area made it impossible to generate a reliable model for the water surface and the streambed. We surveyed the stream channel during a wet period (16 May 2016), when some stream flow was present, and during dry channel conditions (24 June 2016), when water was being extracted into nearby irrigation channels. The stream had low base flows with no storms between these two dates, hence any alteration of the streambed morphology was negligible or minimal. Accordingly, we considered the DEM obtained during dry streambed conditions as the ground truth, with which to validate our refraction-corrected elevation models of the submerged streambed.

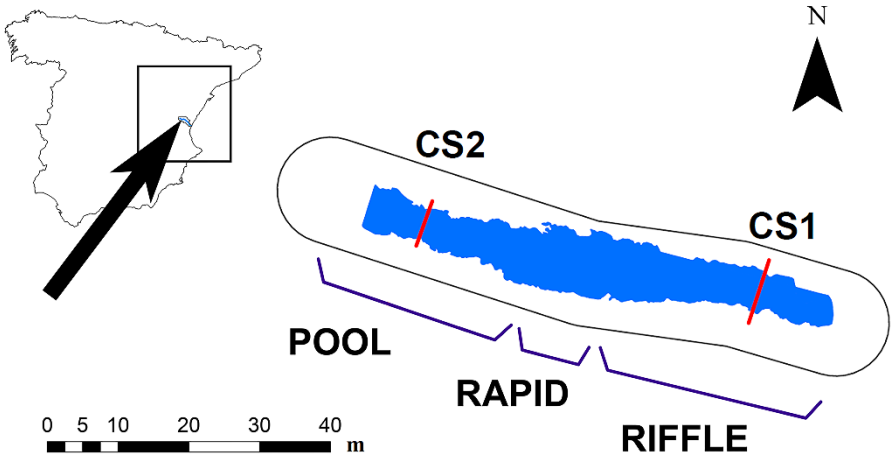


**Figure 4.1.** Location of the Jucar River Basin District (Eastern Spain), and study area (water surface) with different mesohabitat types in the Palancia River, where the two cross-sections were used for comparison in detail (CS1, CS2).

4.2.2 Data acquisition

To obtain aerial imagery of our study site, we used a GoPro Hero 2© (GoPro, USA) High Definition (HD) camera mounted on a DJI Phantom 1© (DJI, China) RPAS. We first extracted images (1920 × 1080 pixels size) from a video recorded along the whole stream reach, and then selected the most representative frames to use as still images, with ca. 750 images used in each campaign. We adopted this approach because we lacked access to the real time image feed from the RPAS or an autopilot system at the time of survey. Therefore, by collecting video we ensured that sufficient imagery was obtained for the whole site to ensure 80% to 90% overlap between images. The GoPro camera was selected because its video output has a high stability and high resolution (1080p resolution), which is essential for a camera on an airborne platform that vibrates because of rotors and variable atmospheric conditions. The average flight height was 10 metres above the stream channel and the camera was set to a zenith angle of 20°. Recent GoPro© camera models (HERO5 Black and newer) can record Global Positioning System (GPS) positional information of the camera at the time of capture. In both campaigns the images were taken around noon, to minimise differences in the incidence of natural light between surveys; the total flight time on both occasions was similar, at ca. 30 minutes.

Before both aerial surveys, we established a network of ground control points (GCPs) around the site and surveyed their positions using a Prexiso G5© (Leica, Germany) GPS-RTK instrument. These GCPs were distributed throughout the stream reach, and unique standard markings from the software tool Agisoft PhotoScan Pro 1.2.2© (Agisoft, Russia) were used to identify them in the images. The GCPs were randomly distributed in three dimensions, following common practice (Martínez-Carricondo et al., 2018).

The GPS-RTK instrument was linked to the regional network of Global Positioning System/Global Navigation Satellite System (GPS/GNSS) (Network of Reference Stations in Valencia "ERVA"), via mobile signalling, to obtain differential corrections by Network Transport RTCM Internet Protocol (NTRIP) of the coordinates

in real time. Each GCP position was recorded in the WGS84 reference system, having an accuracy of 1 centimetre in both planimetry and altimetry. In each campaign, 70% of the measured points were used for georeferencing and scaling purposes; the remaining 30% were used to quantify the accuracy of the derived topography. During the first flight campaign (wet period), we surveyed 74 metres of the stream length and used 31 ground control points (GCPs) and 14 check points (CPs). During the second survey (dry period), we covered the same reach and used a smaller number of GCPs (29) and CPs (12) (Figure 4.2). The latter's slightly lower sampling effort (fewer GCPs) was justified since it would not affect the accuracy of the georeferencing model (Tonkin and Midgley 2016).

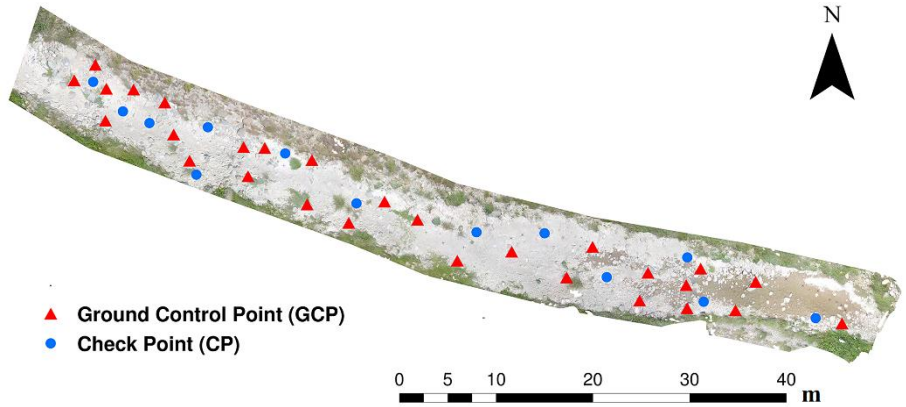


**Figure 4.2**. Spatial location of the Ground Control Points (GCPs) and checkpoints on the stream channel for the field campaign with dry channel (Dry phase).

### 4.2.3 Image and Data Processing

In both surveys (wet and dry), we selected a series of still frames from the video footage. Specifically, we only selected images having a high level of overlap (80% to 90%) to ensure that the image matching was successful and robust (Eisenbeiss and Sauerbier, 2011). For the first survey, during wet channel conditions, we selected those images with the least distortion, and which gave a clear view of the water's edge, as this is a key parameter for correcting the effects of refraction. For the second campaign, during dry channel conditions, we instead selected those images giving a clear view of the channel bed, to obtain a real ground model for validation purposes. In the surveys, we divided the video into individual image frames with a time interval of 1 second, among which the most representative frames of our area of interest, and of the highest quality, were selected. Any frames that were unfocused, redundant or showed sun reflection were discarded. Figure 4.3 shows the DEM built in the Agisoft PhotoScan Pro program.

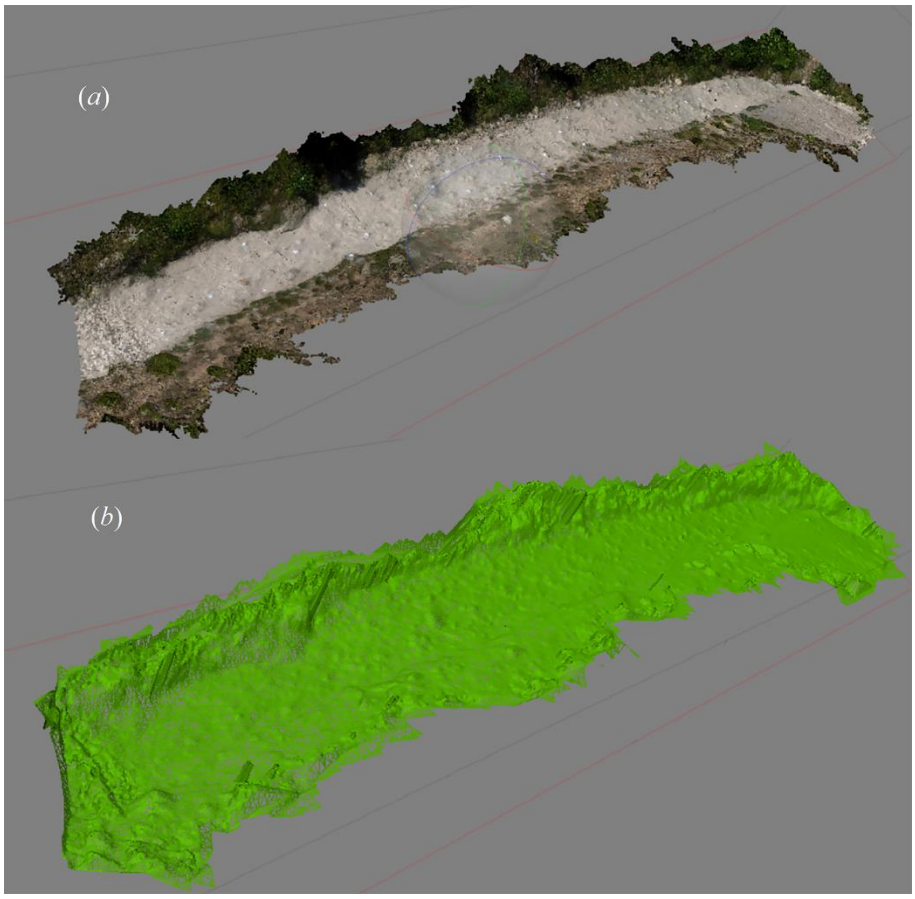


**Figure 4.3**. (a) Digital surface model with texture of the study area at dry phase, from which the models for the two mesohabitats units where extracted. (b) Digital surface model without texture of the study area at dry phase. Both generated by Agisoft PhotoScan Pro© and showed on an isometric view.

The selected images were uploaded into structure-from-motion photogrammetry software, namely Agisoft PhotoScan Pro v.1.2.2© (Agisoft, Russia). The workflow comprised several key steps: image import, image alignment, geometry building, texture building, georeferencing, optimization of image alignment, and re-building of scene geometry and texture (Woodget et al., 2015). The images were aligned using high accuracy settings and generic pair preselection, to create a sparse point cloud. Next, we densified the point cloud using the "Build Dense Cloud" setting, and created a surface mesh, which was then textured using the original input images. To georeference the model, we located each GCP and assigned their respective coordinates recorded in the field survey. Finally, we optimised the image alignment using the GCP reference data and regenerated the model using the same settings, before exporting the DEM, orthophoto, and dense point cloud for further analysis (Figure 4.4).

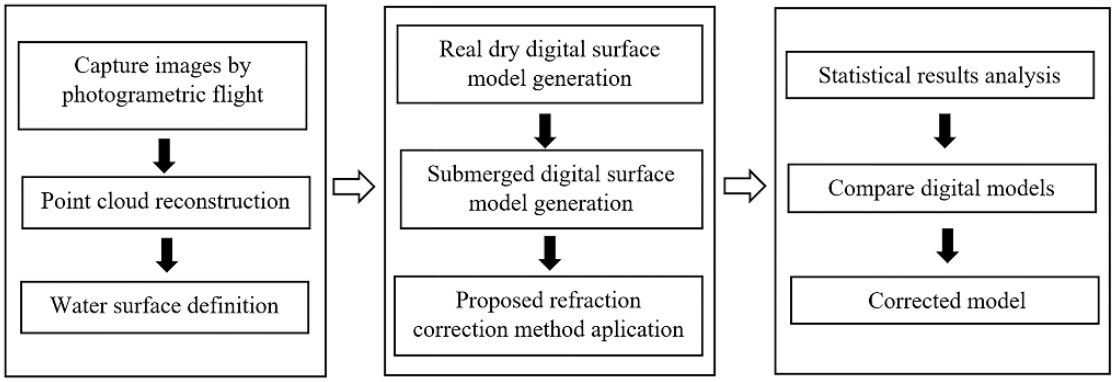


**Figure 4.4.** Workflow of the photogrammetric process.

### 4.2.4 Refraction correction

The presence of water causes a distortion when defining the correct depth and morphology of the fluvial streambed when relying solely on photogrammetric methods (Westaway et al., 2001). This results in elevation models typically overestimating the true elevation of the channel bed. The correction method we developed and describe here is based on coordinates that describe the position of the RPAS at the point at which each image (frame) is actually captured. We used these positions to apply a geometric correction to the light beam as it is refracted at the water–air interface, as detailed below. This methodology is similar to that developed by Dietrich (2017). Yet Dietrich's algorithm requires knowing different parameters of the camera, namely those of its exterior orientation (pitch, roll, and yaw) and internally (focal length and sensor size). By contrast, our algorithm only requires data of the camera's position when each image was taken.

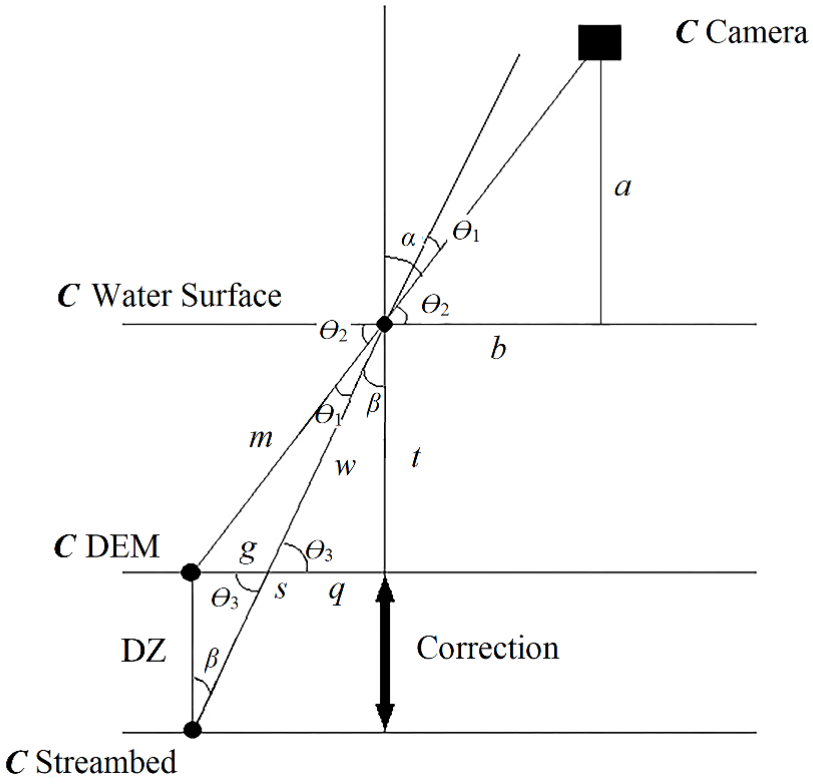

**Figure 4.5.** Geometric representation of the elements involved in the correction of the refraction effect. Where (C) represents the coordinates of each point at each surface, and the vertical distance (DZ) between each DEM point and his counterpart of the streambed represents the value of the refraction correction.

Figure 4.5 shows the geometric elements we used to generate the mathematical equations and to resolve the refraction effect problem, to better estimate the true elevation of the streambed. The "***C*** Camera" position refers to the camera's 3D coordinates at the moment when each image was captured; the "***C*** DEM" position represents the 3D coordinates of each point within the dense cloud, before applying any refraction correction; this point cloud was obtained from the SfM reconstruction by PhotoScan with the whole RPAS imagery at the wet period. The "***C*** Water Surface" position corresponds to the point at which the light beam crosses the water–air interface, for each point on the channel bed observed by the camera. This continuous water surface was generated via interpolation of the 3D coordinates of 190 points measured by the GPS-RTK station (recorded approximately every 1 metre) along the streambanks during the wet campaign. Thus, this continuous water surface and the points defined by the visual rays between the camera and the points of the SfM DEM (***C*** DEM) are defined before the algorithm starts. The "***C*** Streambed" position represents the corrected 3D coordinates of each point that contributes to defining the stream's morphology. The geometric configuration lets us compute the value of the *Z*-coordinate difference between the SfM DEM (***C*** in Figure 4.5) and the streambed position in the same vertical (***C*** Streambed), i.e. DZ. This procedure, as it is explained in detail below, enables us to correct for any elevation overestimation of the submerged topography. Table 4.1 includes the symbols and descriptions of the variables used in all the calculations.

**Table 4.1**. Descriptions of the variables in Figure 4.5 and throughout the text and equations.

| Variable | Description |
|---|---|
| ***C*** Camera | Three dimensional coordinates of RPAS camera |
| ***C*** Water Surface | Three dimensional coordinates of water surface point cloud |
| ***C*** DEM | Three dimensional coordinates of initial digital elevation model (SfM DEM) |
| ***C*** Streambed | Three dimensional corrected coordinates of submerged point cloud |
| ***B*** DEM | Two dimensional coordinates of initial digital elevation model (SfM DEM) |
| $n$ | Refracting index according to Snell's law |
| $\Theta_1$ | Deviation angle due to water effect |
| $\Theta_2$ | Complementary angle of $\alpha$ |
| $\Theta_3$ | $\beta + 90°$ it is the supplementary angle |
| $\alpha$ | Angle of incidence |
| $a$ | Vertical distance between camera and each point of water surface |
| $b$ | Horizontal distance between camera and each point of water surface |
| $\beta$ | Angle of refraction |
| $m$ | Distance between ***C*** Water Surface and ***C*** DEM on the straight line |
| $w$ | Distance with $\Theta_1$ angle deviation from each water surface point to the SfM DEM |
| $t$ | Vertical distance from each water surface point to the SfM DEM surface (***C*** DEM) |
| $g$ | Horizontal distance between each DEM point and the footprint of $w$ ray |
| $s$ | Horizontal distance between each ***C*** DEM and the footprint of $t$ (vertical) ray |
| $q$ | Difference distance between $s$ and $g$ |
| DZ | Elevation correction of the water refraction effect |

The first step was the calculation of the horizontal and vertical distance values from the camera to each of the points of the water surface within the camera's Instantaneous Field Of View (IFOV). Those distances are calculated from the camera's 3D coordinates and the water surface points obtained as described above (see Figure 4.5). For each camera's position, we define the vertical straight line, and the line between the camera's position and each of the points of the water surface (visual ray). Then, the distances are calculated, being the vertical distance the difference in elevation (*Z* coordinate) between the camera and the intersection of the vertical line with the water surface, and the horizontal distance the Euclidean distance between their planimetric coordinates. To do this, the external and internal orientation parameters of the camera at each position were obtained from the SfM reconstruction software (PhotoScan®); then, we define each camera's IFOV, based on the approximate ground coordinates of the four image's footprints.

The second step was the calculation of the angles between the rays as depicted in Figure 4.5. The angle $\Theta_2$ is the tangent of the triangle where a and b are known, and α is the complementary angle. Then, applying Snell's law, the $\beta$ angle is derived from the $\alpha$. These angles are based on the physical principles of Snell's Law, where the passage of the light from one medium to another of different density can be defined by a refractive index (*n*). In our case, Snell's Law was defined according to the Equation (4.1), where $n_{air} = 1$, and $n_{water} = 1.34$, as follows:

$$n_{air} \times \sin \alpha = n_{water} \times \sin \beta \qquad (4.1)$$

As depicted in Figure 4.5, for each point, there is an initial geometric environment before the ray enters the water, and a second geometric environment once the ray is in the water. Thus, to solve the corrected DZ value, we must take the aforementioned angular values and the coordinates of the DEM generated via SfM (***C*** DEM). The following equations (Equation (4.2) to Equation (4.4)) were applied to develop the trigonometrical environment. The angles in Figure 4.5 ($\alpha, \beta$) define the position and orientation of each of the projected rays in the equations, for correcting the position of each point (***C*** DEM); $\Theta_3$ is then calculated to allow the calculation of the correction, DZ. Table 4.1 provides the variables' description;

$$\alpha = 90° - \Theta_2 \qquad (4.2)$$

$$\Theta_1 = \alpha - \beta \qquad (4.3)$$

$$\Theta_3 = 90° - \beta \qquad (4.4)$$

In the third step, these angular values are applied in trigonometrical equations to solve the corrected *Z* coordinate for each "***B*** DEM", getting the "***C*** Streambed". Those trigonometrical equations use several parameters which represent distances depicted in Figure 4.5 and defined in Table 4.1 (*t, w, m, g, q, s,* DZ) (Equation (4.5) to Equation (4.10)):

$$t^2 + s^2 = m^2 \qquad (4.5)$$

$$t = w \times \cos \beta \qquad (4.6)$$

$$w^2 = t^2 + q^2 \qquad (4.7)$$

$$g = s - q \qquad (4.8)$$

$$g = (\mathrm{DZ}) \times \tan \beta \qquad (4.9)$$

The last step is to calculate the $Z$ coordinate of the Streambed with Equation (4.10);

$$Z_{\mathrm{Streambed}} = Z_{\mathrm{DEM}} - (\mathrm{DZ}) \qquad (4.10)$$

Where $Z_{\mathrm{DEM}}$ is the elevation or $Z$ coordinate of each point of the SfM DEM. To implement this correction, we used the point cloud generated from RPAS imagery of the stream reach acquired during its wet period. We computed light rays' angles by projecting a line from each point of this cloud with the RPAS coordinates when the corresponding image had been acquired. We then defined the position of the water's surface from the orthoimagery and extracted this as a 3D-surface in a point cloud form.

By knowing the camera's position (***C*** camera), the generated position of the channel bed (***C*** DEM), the position of the water surface (***C*** water surface), and the refractive index of clear water, we could compute the position of a refraction-corrected channel bed (***C*** streambed) for each point in the cloud. Each point of the water surface point cloud and its corresponding DEM point were solved individually by the algorithm processes for all the stream bed. We have identified which points were defined by each camera position attending to the IFOV and the external and internal camera parameters. The point cloud was then rasterized to create a refraction-corrected DEM. This generated DEM has a pixel size of 15 millimetres, this being the minimum possible pixel size obtained from the point cloud generated in the photogrammetric process. Table 4.2 provides the error statistics for both the wet and dry surveys; note that each pixel is defined by a point in the cloud. Finally, the performance of the method is quantified by comparing the topography between the wet and the dry survey, with the latter being considered the true topography. We coded the algorithm in C++ Programming Language and Software (Dennis Ritchie and Bell Laboratories 1972), taking advantage of different math functions implemented in its C++ libraries (distributed in the Supplementary Material). Due to the time needed to calculate all the equations involved, we opted to divide the reach into five distinct sections; this process, while not strictly necessary, did save some time as we could test the algorithm's results while the other blocks were processed, and it guarded against potential data loss due to blackouts. Afterwards, we merged all the corrected values to obtain the continuous digital model with the corrected stream depth.

**Table 4.2.** Statistical descriptors of the errors (m) in the two DEMs generated; wet campaign (top), dry campaign (bottom).

| Statistical descriptor | $\Delta X$ (m) | $\Delta Y$ (m) | $\Delta Z$ (m) |
|---|---|---|---|
| Mean | 0.011 | 0.023 | 0.022 |
| Standard deviation | 0.013 | 0.023 | 0.031 |
| Average | 0.005 | 0.034 | 0.011 |
| RMSE | 0.013 | 0.083 | 0.027 |
| P25 | -0.007 | 0.024 | -0.004 |
| P75 | 0.021 | 0.042 | 0.017 |
| Statistical descriptor | $\Delta X$ (m) | $\Delta Y$ (m) | $\Delta Z$ (m) |
| Mean | 0.037 | 0.022 | 0.044 |
| Standard deviation | 0.041 | 0.032 | 0.046 |
| Average | 0.014 | -0.014 | 0.026 |
| RMSE | 0.054 | 0.050 | 0.096 |
| P25 | -0.034 | -0.039 | -0.001 |
| P75 | 0.050 | 0.004 | 0.067 |

### 4.2.5 Validation

To assess the quality of our refraction-corrected model, we relied on three methods: (a) comparing it to the model of the dry streambed, which we consider to represent the true morphology of the stream; (b) comparing it to the results of another method proposed by Woodget et al. (2015) (hereon: small angle refraction correction, or SARC), and; (c) assessing the spatial distribution of point cloud roughness. These methods try to independently define the accuracy and variability of our proposed method. Given the relevance of substrate size (i.e. channel bed roughness) for turbulence, and thus for potential sun reflection and the quality of the images and subsequent DEMs, the spatial distribution of roughness was considered a relevant factor worth evaluating in the comparison. Dietrich (2017) had already established the relation between the error of a digital model and sediment size of the stream. Furthermore, assessing streambed roughness has important consequences for further calculations of hydraulic modelling in streams, such as the inundation area for a given discharge, simulated depth, shear stress, and bed mobility (Brasington et al., 2012; Dietrich, 2017).

In this work, the proposed method was compared with the SARC method which only accounts for changes in light velocity but not in change in light direction—we wanted to understand the behaviour and errors in these two opposite approaches. Furthermore, in the Discussion section of this paper, these obtained values are compared and interpreted in the context of values supplied by other correction methods, including the refraction correction based on a similar methodology to ours (i.e. Dietrich, 2017), albeit generated for different study areas and datasets under differing validation process.

For validation methods (a) and (b), we compared our refraction-corrected DEM with the DEM of (a) the dry streambed and (b) the channel bed derived with the SARC

method, by computing the difference between DEMs using the raster calculator tool within ArcGIS© and statistically analysing these differences. We also generated a dataset composed of random points, distributed throughout the stream reach; this was done to compare with similar point to raster analysis done in previous works (Govedarica et al., 2018; Koci et al., 2017) and typically done when the full DEM as reference is not available. We extracted the DEM elevations for each point in this dataset from all three models (dry bed, our method, SARC method), for further statistical comparisons and to carry out linear regression. Additionally, we compared the relative positions of the water surface and DEM bed morphologies using two channel cross-sections (positions defined in Figure 4.1, in pool and riffle). With such a comparison, differences among the three models of this stream reach can be visualised (Grabowski et al., 2014). We extracted the elevation values along these cross-sections for all models, to analyse the data through linear regression. The outputs of the linear regressions were discussed using measures of goodness-of-fit ($R^2$), based on the Kolmogorov-Smirnov test and the kurtosis *z*-value. In making these comparisons, however, we ignored elements that could have emerged from the stream water surface (e.g., rocks, boulders, vegetation), which if found were first removed from the analysis (with the masking tool in ArcGis©).

For method (c), we analysed the relationship between the point cloud roughness and DEM elevation error. For this, elevation error was defined as the difference between our refraction corrected DEM and the DEM of the dry streambed. In this way, our analysis aimed at exploring how the morphology and irregularities of the sediments that define the stream can influence the correct definition of the DEM result (Brasington et al., 2012; Dietrich, 2017). Point cloud roughness was computed for the location of 850 randomly distributed points; it is defined as the standard deviation (SD) of elevation within 25 centimetres kernels (Vázquez-Tarrío et al., 2017) and obtained by the ArcGIS© Kernel Function (Zucchini, 2003). The roughness values for each point were then plotted against the error values computed under the validation method (a), using the model of the dry streambed (i.e., the true DEM). This comparison was also made for the correction method proposed in this work versus that of the Woodget's–SACR-method.

## 4.3 Results

A visual assessment indicated the presence of different mesohabitat types in the study site with contrasting physical characteristics. However, it was impossible to evaluate the rapid zone of our stream reach (central segment, Figure 4.1) using any refraction correction methods, due to its turbulent water surface and suspended sediments, neither of which could be accounted for in modelling underwater morphology. Average depth within the pool was 48 centimetres, dropping to 25 centimetres in the riffle. Variations in surface velocity were also evident between the habitat types. The lengths of the pool and riffle respectively were 34 metres and 31 metres.

Our refraction correction algorithm was designed and run on an Intel Core i7 with 16Gb of RAM and a Nvdia Gforce 8Gb graphic card. The time needed to fully develop the entire stretch of the stream was ca. 45 hours (i.e., for 800 m × 800 m of stream habitats in total, approximating the blue area in Figure 4.1). The computing time can vary depending on the density of the input point cloud. The refraction correction process works on a point–to-point in generating these individual corrections.

4.3.1 Performance of our method: methods (a) and (b)

Figure 4.6 shows the spatial pattern of the elevation differences between our method and the model of the dry streambed (top row) computed using the whole rasters. The highest errors are evident in peripheral areas and near emergent rocks of the stream reach.

Table 4.3 provides the statistical differences between all three models of the channel bed (dry, our method, SARC method). These values were estimated as the difference between the computed DEMs and the DEM of the dry campaign. Here, we highlight that in our method the mean error is lower in comparison to the SARC method; accordingly, the maximum error was slightly reduced (8%). Furthermore, in the pool, the reduction of the mean error was 9%. By contrast, the standard deviation of the errors was smaller for SARC method. The difference between the SARC and dry stream channel indicates a large influence of mesohabitat type in the error assessment, because the average error was 40% higher in the pool (36 millimetres) with respect to the riffle.

**Table 4.3.** Statistical summary of the raster differences of the three digital elevation models (DEM) in the study site of the Palancia River by mesohabitat type, i.e., pool and riffle, and all together (emerging rocks were discarded). That is, the proposed method, the small angle refraction correction method-SARC (Woodget et al. 2015) and the dry streambed (true DEM).

| | Difference; Proposed Method vs. Dry streambed | | | Difference; SARC Method vs. Dry streambed | | |
|---|---|---|---|---|---|---|
| Statistical descriptor | Pool | Riffle | Pool+Riffle combined | Pool | Riffle | Pool+Riffle combined |
| Mean Error (m) | 0.119 | 0.066 | 0.074 | 0.145 | 0.114 | 0.125 |
| Standard Deviation (m) | 0.125 | 0.086 | 0.133 | 0.103 | 0.085 | 0.096 |
| Minimum (m) | -1.744 | -1.682 | -1.744 | -1.462 | -1.532 | -1.532 |
| Maximum (m) | 0.765 | 0.753 | 0.765 | 0.771 | 0.810 | 0.810 |

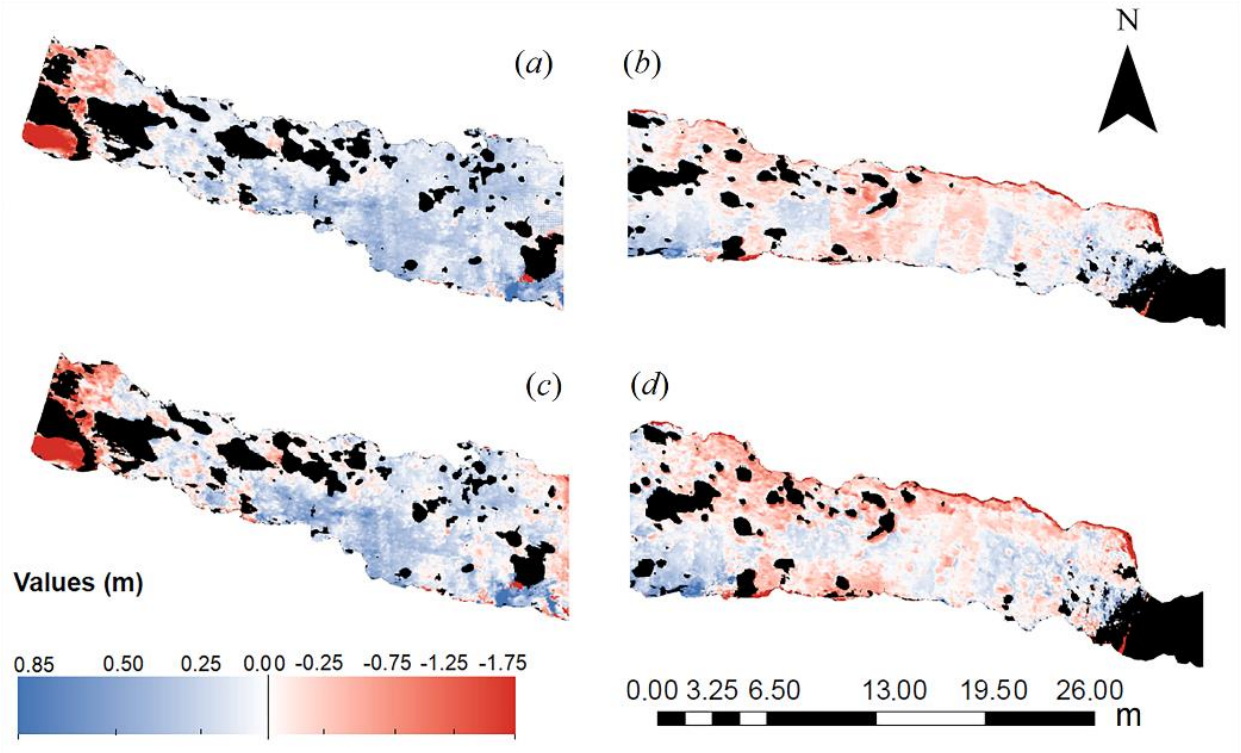


**Figure 4.6.** Raster difference between the proposed method and DEM of the dry streambed (top), (a) Proposed method (pool), (b) Proposed method (riffle). Raster difference between small angle refraction correction - SARC method and DEM of the dry streambed (bottom), (c) SARC method (pool). (d) SARC method (riffle).

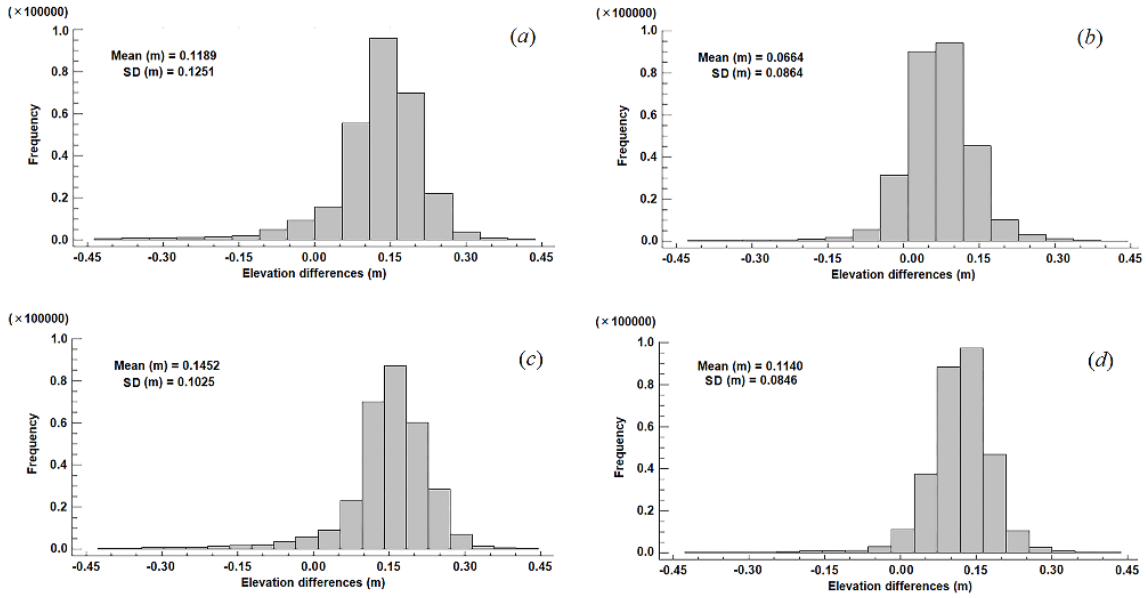


**Figure 4.7.** Frequency histogram of the raster difference between the proposed method and DEM of the dry streambed (Top), (a) Proposed method (pool), (b) Proposed method (riffle). Frequency histogram of the raster difference between small angle refraction correction - SARC method and DEM of the dry streambed (bottom), (c) SARC method

(pool). (d) SARC method (riffle). In all histograms the mean and standard deviation (SD) of the error distribution (m) are displayed.

Frequency histograms generated for the analysed rasters allows us to better understand the behaviour of the refraction corrections applied to our stream reach (Figure 4.7), separated by mesohabitat type (pool versus riffle). The comparison of the two methods with the dry DEM showed a positive skew of the error distribution, which indicates a small systematic error in the corrected elevation models. In Figure 4.8, we present the data from two cross-sections (positions defined in Figure 4.1), so as to observe the different models from a transverse viewpoint. We see that the vertical distances between the digital model corrected by the SARC method and the dry streambed are consistently higher than our proposed method. Thus, our proposed method is more accurate and better at representing the true morphology of the channel bed. We also note that differences between our model and the dry streambed were consistently smaller in the pool ((*b*), Figure 4.8) than riffle habitat ((*a*), Figure 4.8).

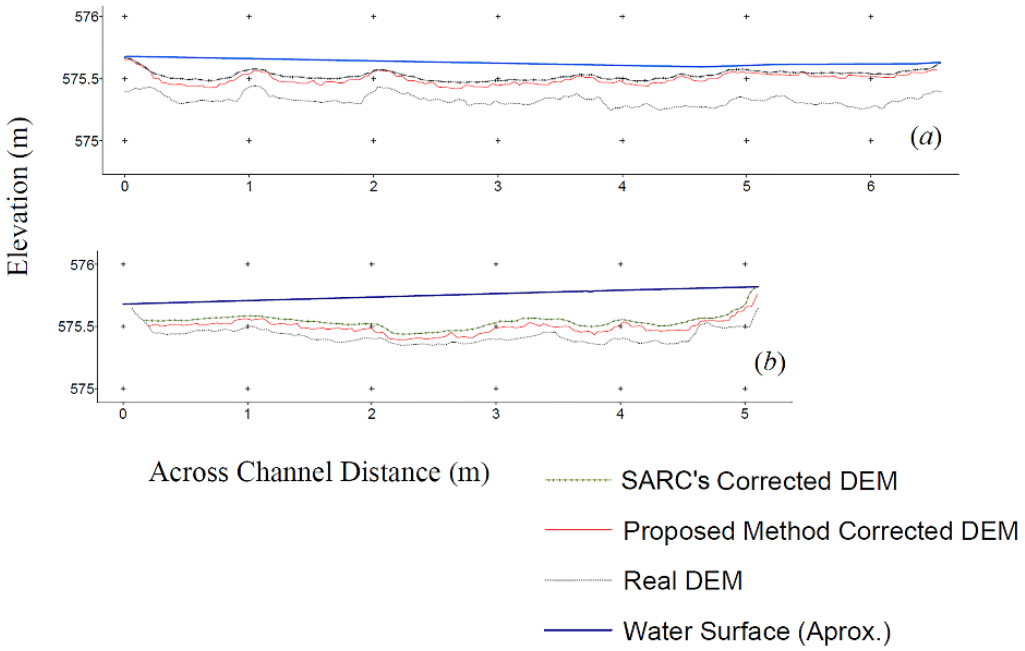


**Figure 4.8.** Comparison of each of the two models with the real DEM in two cross sections of the stream channel at different mesohabitat type, (a) riffle and (b) pool. SARC refers to the small angle refraction correction method.

Figure 4.9 compares the elevation data from our method and the dry-bed DEM, acquired from a series of randomly selected points ($N$ = 850). We found a strong correlation between the submerged terrain elevation obtained by our method and the true DEM, as indicated by the robust linear trend (slope of 0.92), with the coefficient of determination $R^2$ = 0.85. Furthermore, Figures 4.6, 4.7, and 4.9 collectively show that our method generated a trend in modelling that overestimated elevation, to a different extent depending on whether the pool or riffle habitat was analysed. This suggests that the method has reduced but not eliminated the effects of refraction.

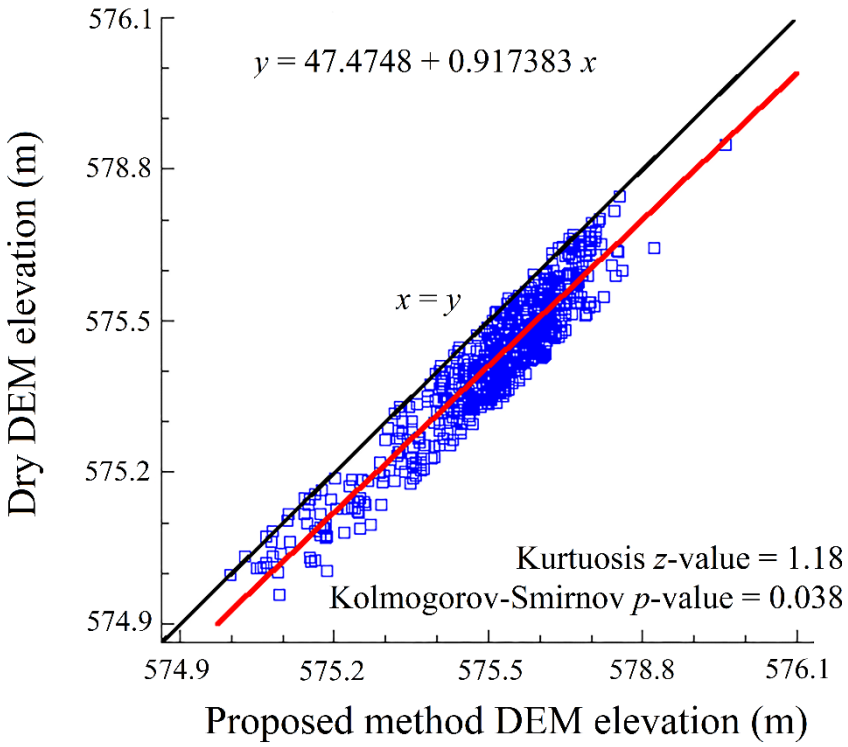


**Figure 4.9.** Correlation between elevations calculated with our method of refraction correction and elevations measured on the dry stream channel.

### 4.3.2 Comparison with point cloud roughness: method (c)

The spatial representation of elevation error revealed the largest errors occurring at the edges of the 3D model (Figure 4.6). In addition, some errors arose in areas of the stream reach where emerging elements were not totally removed (e.g., boulders, vegetation), thus producing some distortion. A comparison of DEM accuracy and morphology roughness values of the stream reach is provided in Figure 4.10 and 4.12. Furthermore, in Figure 4.11 the roughness values are presented in the form of histograms, allowing us to better understand the behaviour of both models.

Finally, bivariate scatterplots (Figure 4.12) showed the relationship between elevation error as a function of roughness for the 850 checking points validated in the previous sections, for the two methods of refraction correction.

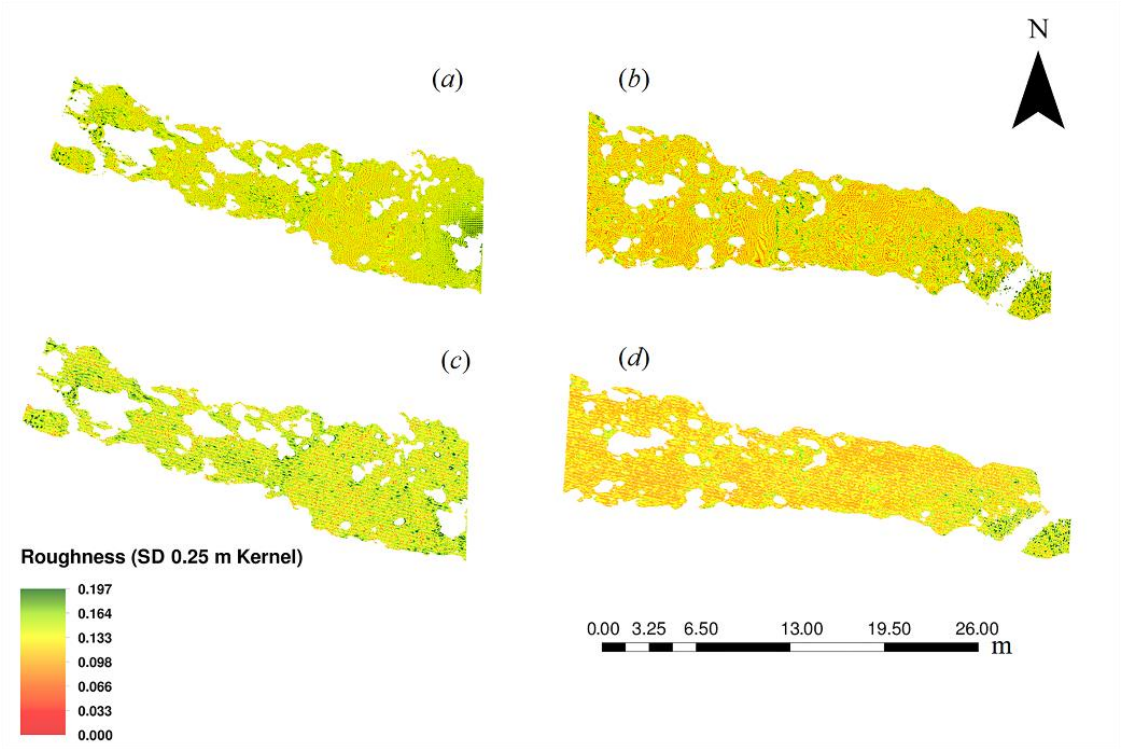


**Figure 4.10.** Representation of elevation error after proposed correction method with respect to the roughness model with standard deviation (SD) of 25 centimetres kernel (Top), (a) Proposed method (pool), (b) Proposed method (riffle). Representation of the elevation error based on the small angle refraction correction method –SARC by Woodget (Woodget et al. 2015), with respect to the roughness model with standard deviation (SD) of 25 centimetres kernel (Bottom), (c) SARC method (pool), (d) SARC method (riffle).

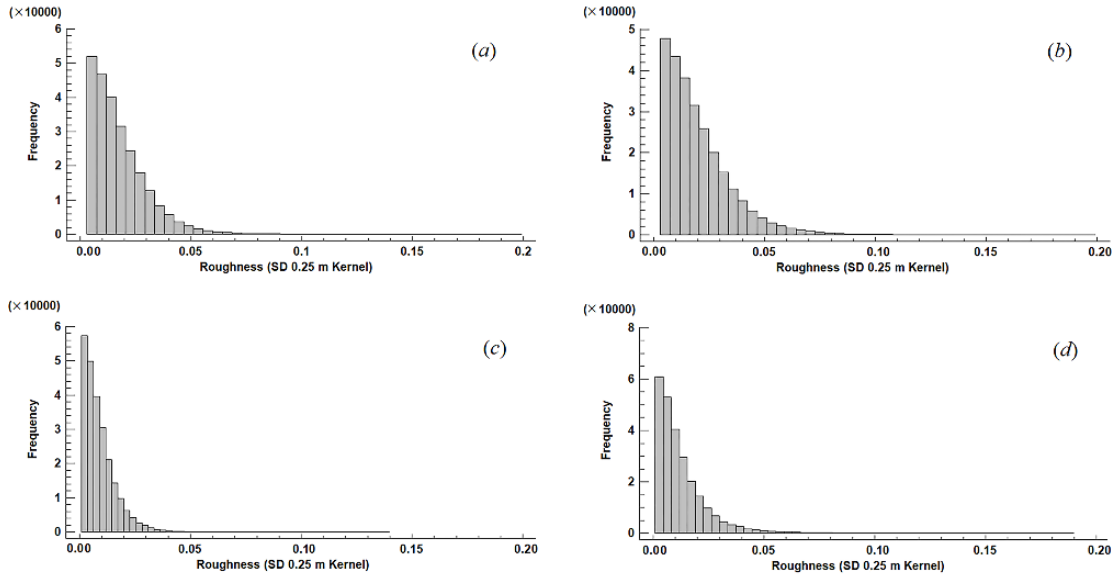


**Figure 4.11.** Frequency histograms of elevation errors for the proposed correction method with respect to the roughness model with standard deviation (SD) of 25 centimetres kernel (Top), (a) Proposed method (pool), (b) Proposed method (riffle). Frequency histograms of the elevation error based on the small angle refraction correction

method –SARC by Woodget (Woodget et al., 2015), with respect to the roughness model with standard deviation (SD) of 25 centimetres kernel (Bottom), (c) SARC method (pool), (d) SARC method (riffle).

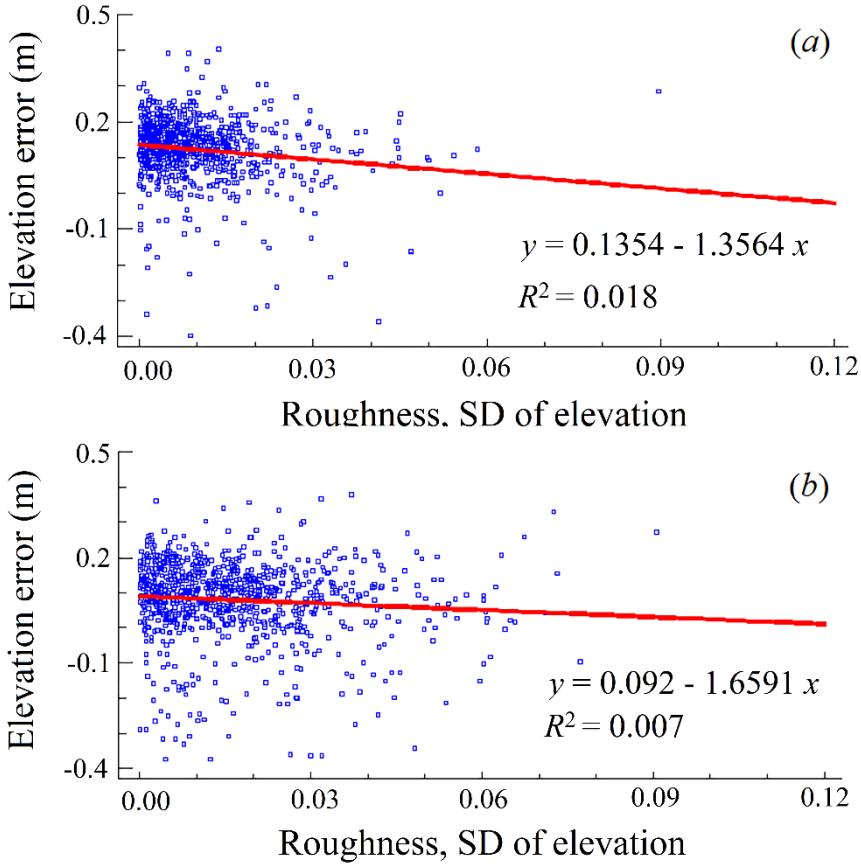


**Figure 4.12.** (a) Relationship between standard deviation (SD) of 25 centimetres kernel after small angle refraction correction method -SARC (Top). (b) Relationship between standard deviation (SD) of 25 centimetres kernel after our proposed correction method (Bottom).

## 4.4 Discussion

This investigation provides the first spatially-continuous, quantitative validation of a refraction based algorithm for correcting the location of submerged points extracted from SfM-based approach mapping stream bathymetry in complete mesohabitat units (or channel geomorphic units) at the pixel scale. The direct pixel-to-pixel validation of the SfM derived bathymetry is only possible by having both the stream model with water present and dry stream model, where water is absent. Using this method and the associated C++ code, we were able to reconstruct the submerged topography with lower mean errors with respect to the small angle refraction correction method (SARC) proposed by Woodget et al. (2015), when applied to our data. Furthermore, the continuous validation in situ by mesohabitat types fostered a more detailed assessment of the error distribution, both spatially and statistically.

Through a comprehensive comparison of our results against leading approaches, we could identify the key benefits and disadvantages of our method. Firstly, our approach permitted the generation of a high spatial resolution (15 millimetres per pixel) model, with sufficient quality to model the submerged topography of a stream reach. This small pixel size results from the very low flight altitude, facilitating the correction for refraction and data evaluation in much more detail than would be possible had we relied on coarser resolution remote sensing datasets – which are often the only datasets available openly. This is a highly relevant factor, because depending on the flight heights taken in projects of this type, the error rates and accuracies obtained can vary considerably (James and Robson, 2012). Several prior studies that used RPAS, such as Immerzeel et al. (2014) and Fugazza et al., (2015) relied on higher flight heights and fewer GCPs (250 metres maximum flight altitude; 20 GCPs), mainly due to the difficulties in accessing their study sites. Conversely, we decided a priori to acquire imagery at a much lower altitude because the flight platform would not provide sufficient stability at higher altitudes than 10 metres, and the winds in the area are occasionally quite strong.

Secondly, the use of many GCPs and CPs in this study strengthened our ability to georeference the model, thereby improving the DEM's accuracy and comparability of the datasets acquired on different dates (Table 4.2). However, and crucially, we anticipate that errors derived from the water surface are significant (e.g. elevations, waves, turbulent water and sun glint (Dietrich, 2017). Such inherent difficulties in accurately defining the position of a water body's surface would generate a chain of error within our proposed algorithm, since the construction and resolution of the mathematical equations that define the projection rays for each point in 3D space are reliant on knowing the exact, instantaneous position of the water surface. Recent work by Woodget, Dietrich, and Wilson (2019) provides a more robust method for estimating the water surface position. Although this work was not available for implementation in our model when it was built, it nonetheless warrants future consideration in refraction correction workflows.

Thirdly, subdividing the study site's stream reach into two sections with well-differentiated characteristics, as pool and riffle, strengthened our inference. Specifically, this let us verify how the proposed method of refraction correction generates less error in shallow areas with low water turbulence and greater errors in deeper areas with a more unstable water surface.

Relative to those reported by Dietrich (2017) and Woodget et al. (2019), albeit using different datasets, our results yielded higher mean error and standard deviation (Table 4.4). This discrepancy may be due to disparities in the density of the point cloud between the two methods; however, this is tentative, since there are studies showing similar accuracy when a larger cell size is used (Woodget, Dietrich, and Wilson 2019; Booth 2014; Schumann, Muhlhausen, and Andreadis 2019). Nevertheless, pixel size could be generally considered as a determining factor for the accuracy in areas where the geomorphological features are small and are marked by strong variability. In addition, the quality of the camera used will directly affect the products generated from the captured images; hence, the GoPro camera used in our method is also a potential factor contributing to the quality of results. Dietrich (2017) worked with a point cloud resampled at 300 millimetres spacing, whereas we worked with distances between points of just 12 millimetres. Our finer-scale point spacing may have increased the minimum irregularity in the generation of the rays that form the mathematical equations, thereby increasing the standard deviation of the error. This is further highlighted by the use of a smaller pixel

size in the resulting digital models, since they are subject to less smoothing or averaging of the error per cell. Further, our method was validated using a spatially continuous surface rather than discrete isolated points (in each of the two models), likely forcing it to be far more sensitive to minor errors in spatial positioning, and the effects of distorting parameters such as turbulence, sun glint, and vegetation. These effects, however, did not impact the Dietrich method so significantly, since the validation of that model is carried out at discrete sampling locations, via averages and ratios, rather than by a continuous dry model of the entire stream reach. Further quantitative comparison of these two approaches, on an identical dataset, is required to elucidate the reasons for the observed statistical differences.

Woodget, Dietrich, and Wilson (2019) have presented promising results in mapping submerged topography with a method to correct the effect of refraction with special attention in modelling the water surface. Their accuracy values are better than those of our proposed method which could be due to the enhanced representation of the water surface but also to the lower number of comparison points (Table 4.4).

**Table 4.4.** Statistical descriptors of the different campaigns of each correction method and the values obtained with our proposed method, in pool and riffle mesohabitat types.

| Statistical descriptor | Mean error (m) | Standard deviation (m) |
|---|---|---|
| Woodget's SARC method (2015) | 0.008 to 0.053 | 0.064 to 0.086 |
| Dietrich's method (2017) | -0.011 to 0.014 | 0.059 to 0.077 |
| (Woodget, Dietrich, Wilson 2019) | 0.006 to 0.041 | 0.061 to 0.101 |
| Proposed Method (Pool) | 0.119 | 0.125 |
| Proposed Method (Riffle) | 0.066 | 0.086 |

Comparing our results with those of the SARC method, *using the same dataset*, shows that our method provides a refraction-corrected model with smaller elevation errors than the SARC method (Table 4.3). Such a reduction is particularly notable in the riffle habitat, where the mean error obtained was 60% lower than that of the SARC method (i.e., 0.066 vs. the 0.114 for SARC). There was also an error reduction in the pool, but the magnitude of this was smaller (20% lower mean error). By contrast, the standard deviation of the errors was smaller when the SARC method was applied, and those of the proposed method exceeded those of other methods; this would seem justified, given our study site contains several points in critical areas that distorted the statistical results. Specifically, areas of the banks and areas close to the emerged elements produced larger variability in the correction, thus generating larger residuals from the sample mean. Again, the use of the refined water surface estimation method of Woodget, Dietrich and Wilson (2019) might help to eliminate these larger residuals.

In contrast to SARC, our analyses of the Palancia River results revealed larger mean errors than the original work by Woodget et al. (2015) based on a dataset from the United Kingdom (UK), and likewise differences in the observed standard deviations (Table 4.4). This may be because the SARC method uses a blanket application of refraction correction at the level of the DEM for the entire reach, without performing an individual correction for each and every point in the cloud. This is likely to produce an average and smoothed out version of possibly anomalous values. Moreover, the stretch of stream we investigated here featured abundant emergent elements that inevitably introduced many distortions, creating greater difficulties in accurately defining the

position of the water surface. Despite the use of a mask to remove these elements from the final model, we note that these features still produced some distortion in the estimated water surface position near those areas, and consequently an increase in elevation error (Figure 4.6). The presence of vegetation and shadows along the banks of the Palancia River also make it difficult to generate the model in a few areas. In some places, the velocity and morphology of the stream generate rapids and eddies, which caused significant irregularities in the point cloud, thus introducing additional errors. Further research is required to fully understand and ameliorate these complex issues. However, for this study site in Spain, we note that our proposed method provides a closer approximation of the true channel bed position than the SARC method, in two types of mesohabitats.

Concerning the potential relationship between elevation errors and roughness, several pertinent factors merit consideration. In the roughness calculation, those areas of emerged large sediment have been eliminated from the process, because the refraction correction operates only below the water surface. The contours of those large rocks, whose patterns are very irregular, are one predominant source of error in the calculations underpinning the refraction correction (see Figure 4.4). However, eliminating those emerged elements (high roughness) from the calculation leaves roughness not properly evaluated in the areas immediately surrounding these features, thereby limiting the potential relationship between the errors and roughness. A second factor is the size of the kernel used to calculate the roughness; it was a constant value for the entire stream, following previous studies (e.g., Vázquez-Tarrío et al., 2017). However, due to the sediment sizes in this stream and, furthermore, the different dominant substrates across river morphological types, differing kernel sizes could have been selected for each stream segment, to optimise the correct roughness calculation. Thirdly, the variability of sediment size is relatively low, in our study site dominated by medium-large substrate. This fact, coupled with the stream's dominant medium-low depths, seems to limit the range of errors, thereby contributing to the observed lack of relationship between elevation errors and roughness.

Other sources of error are likely to affect all refraction correction methods relying on imagery processed via SfM when they include areas of low radiometric resolution within the RPAS imagery. During the SfM process, errors are known to arise in those areas with a low chromatic spectrum, which makes point-matching a more difficult task (James and Robson, 2014; Carbonneau and Dietrich, 2017). Low roughness of the point cloud can also make it difficult to accurately discern the area of interest (Fonstad et al., 2013) but in our case this did not represent a significant problem.

Our independent analysis of the refraction-corrected models by mesohabitat type permitted an assessment of method performance in a manner not yet tried before. In the pool area, although the irregularities on the water surface are smaller and the flow velocity is lower, due to the greater water depth we observed higher error values than within the riffle section (likewise in the SARC method). Despite the emerging elements and the eddies formed in the riffle, the errors are lower in these shallower habitats. This indicates that water depth is a key factor limiting the success of our approach and suggests we did not fully eliminate the effects of refraction. Consequently, stratifying the survey by mesohabitat types, which account for both water depth and streambed roughness, may help better understand the elevation error distribution because error statistics based on the entire reach may be misleading. Thus, the presented approach may help other researchers

consider the potential errors for their specific applications in different morphological river types, with different proportions of mesohabitat units.

In terms of its practicality, the method we presented here is a computationally intensive approach, so its application to larger spatial scales is likely constrained at present. We also note that obtaining accurate results is more challenging in areas characterized by highly turbulent waters, whose shadows fall on the stream surface, and where external elements or glitters and flashes occur due to the sunlight's reflection on the water's surface. We anticipate better accuracy will be obtained in areas with smooth water surfaces, clear water, channel beds adequately illuminated to permit sufficient radiometric resolution for image matching, and limited shadows and reflections on the water surface. In these settings, our approach holds much promise for quantifying the topography of the channel bed and it could also be used to reliably estimate water volumes in future research.

In our proposed method, refraction correction is achieved through a more parsimonious algorithm, in terms of parameters and calculations, relative to the Dietrich's method (2017). Although both methods treat the data as clouds of independent points, for which the correction is calculated individually, our proposed method does not require additional parameters of camera configuration during the acquisition of images remotely. Therefore, an advantage of our method is its direct applicability to many types of image-capturing devices, whether fixed or mobile, such as mobile phones and cameras installed on airborne platforms or on raised poles above the water body surface, which can be processed. For instance, fixed poles with cameras are widely relied on in river geomorphology to monitor river-channel evolution and measure bank erosion rates (Fugazza et al., 2015; James and Robson, 2014, Visser et al., 2019), and to determine flow velocity and carry out bathymetric mapping (Tauro et al., 2016). Therefore, in similar cases, the use of several fixed cameras coupled to the application of our method may be especially valuable. As such, our method provides a simple and economical tool for general widespread use in the fields of river morphology and ecology.

In our opinion, the proposed approach deserves more ample testing in future research. Though our study site represents a natural space with notable morphological irregularities, testing in other more complex river sections, where the mesohabitat stratification is also implemented, is necessary. We expect to test this approach in a river section with a more diverse sediment arrangement, as well as in river habitats with more turbulence, to further establish its scope and application limits.

## 4.5 Conclusion

Quantifying river morphology is an essential part of monitoring and managing fluvial geomorphology, flow dynamics, and riparian habitats. Here, we presented an alternative methodology that explicitly accounts for the effects of refraction for the generation of digital elevation models (DEMs) of streambeds. The regulated nature of our study site provided an ideal opportunity to survey a section of the Palancia River during both its wet and dry period, and to use the dry-period topographic model to validate the outputs of our wet-period model computed using our refraction correction approach. To our knowledge, this is the first spatially continuous and high resolution validation of quantitative submerged river morphology models, which was performed on all the pixels

of the model within distinct mesohabitat types. Our novel refraction-correction processing algorithm computes the correction required for each point within a point cloud derived from an RPAS-SfM approach, by applying the principles of trigonometry and the rules of Snell's Law.

We show that our method produced smaller mean errors than those obtained using the small angle refraction correction method for the same dataset, especially in the mesohabitat of riffles. Yet the standard deviations of error are not significantly nor consistently better than those published by other studies (Woodget et al., 2015; Dietrich, 2017). We suggest that this may be related, in part, to our use of exceptionally high-resolution data, which has not been smoothed or filtered. Accuracy issues persist concerning areas of vegetation, shadowing, emergent features, and, perhaps most significantly, in areas where the water surface cannot be modelled adequately due to surface distortions, i.e., turbulence and reflections. Less accurate results are also obtained in areas of deeper water (i.e., pool mesohabitats) suggesting we have reduced rather than eliminated errors resulting from refraction. With future improvements of SfM mapping of submerged topography, we anticipate our method has promising potential in diverse applications within aquatic and riparian zones, including hydraulic modelling, habitat modelling, computing flow velocities, monitoring sediment evolution, and granulometry analysis.

## 4.6 References


Alcaraz-Hernández, J. D., Martínez-Capel, F., Peredo-Parada, M. and Hernández-Mascarell, A. B., 2011. "Mesohabitat Heterogeneity in Four Mediterranean Streams of the Jucar River Basin (Eastern Spain)." Limnetica 30 (2): 363–378.

Alfonso-Torreño, A., Gómez-Gutiérrez, A., Schnabel, S., Lavado Contador, J. F., de Sanjosé Blasco, J. J., and Sánchez Fernández, M., 2019. "SUAS, SfM-MVS Photogrammetry and a Topographic Algorithm Method to Quantify the Volume of Sediments Retained in Check-Dams." Science of the Total Environment 678. Elsevier B.V.: 369–382. doi:10.1016/j.scitotenv.2019.04.332.

Avtar, R., Anak Suab, S., Yunus, A. P., Kumar, P., Srivastava, P. K., Ramaiah, M. and Anak Juan, C., 2020. "Unmanned Aerial Vehicle: Applications in Agriculture and Environment." Unmanned Aerial Vehicle: Applications in Agriculture and Environment, 85–100. doi:10.1007/978-3-030-27157-2.

Bailly, J. S., le Coarer, Y., Languille, P., Stigermark, C. J., and Allouis, T., 2010. "Geostatistical Estimations of Bathymetric LiDAR Errors on Rivers." Earth Surface Processes and Landforms 35 (10): 1199–1210. doi:10.1002/esp.1991.

Belmar, O., Bruno, D., Martínez-Capel, F., Barquín, J. and Velasco, J., 2013. "Effects of Flow Regime Alteration on Fluvial Habitats and Riparian Quality in a Semiarid Mediterranean Basin." Ecological Indicators 30. Elsevier Ltd: 52–64. doi:10.1016/j.ecolind.2013.01.042.

Berni, J.A.J., Zarco-Tejada, P.J., Suárez, L., González-Dugo, V. and Fereres. E., 2009. "Remote Sensing of Vegetation from UAV Platforms Using Lightweight Multispectral and Thermal Imaging Sensors." Int. Arch. Photogramm. Remote Sens. Spatial Inform. Sci 38: 6 pp. doi: 10.1007/s11032-006-9022-5.

Biggs, H. J., Nikora, V. I., Gibbins, C. N., Fraser, S., Green, D. R., Papadopoulos, K. and Hicks, D. M., 2018. "Coupling Unmanned Aerial Vehicle (UAV) and Hydraulic Surveys to Study the Geometry and Spatial Distribution of Aquatic Macrophytes." Journal of Ecohydraulics 3 (1). Taylor & Francis: 45–58. doi:10.1080/24705357.2018.1466666.

Booth, D. T., 2014. "Modelling Wetland Microtopography Using Structure-from-Motion Photogrammetry," no. September 2014. https://www.researchgate.net/publication/275019151.

Brasington, J., Vericat, D. and Rychkov, I., 2012. "Modeling River Bed Morphology, Roughness, and Surface Sedimentology Using High Resolution Terrestrial Laser Scanning" 48 (April): 1–18. doi: 10.1029/2012WR012223.

Calle, M.l, Alho, P. and Benito, G., 2018. "Monitoring Ephemeral River Changes during Floods with SfM Photogrammetry." Journal of Iberian Geology 44 (3). Springer International Publishing: 355–373. doi: 10.1007/s41513-018-0078-y.

Carbonneau, P. E., and Dietrich, J. T., 2017. "Cost-Effective Non-Metric Photogrammetry from Consumer-Grade SUAS: Implications for Direct Georeferencing of Structure from Motion Photogrammetry." Earth Surface Processes and Landforms 42 (3): 473–486. doi:10.1002/esp.4012.

Carbonneau, P., Fonstad, M. A., Marcus, W. A. and Dugdale, S. J., 2012. "Making Riverscapes Real." Geomorphology 137 (1). Elsevier B.V.: 74–86. doi:10.1016/j.geomorph.2010.09.030.

Clapuyt, F., Vanacker, V. and Van Oost, K., 2016. "Reproducibility of UAV-Based Earth Topography Reconstructions Based on Structure-from-Motion Algorithms." Geomorphology 260. Elsevier B.V.: 4–15. doi:10.1016/j.geomorph.2015.05.011.

Coveney, S., and Roberts, K., 2017. "Lightweight UAV Digital Elevation Models and Orthoimagery for Environmental Applications: Data Accuracy Evaluation and Potential for River Flood Risk Modelling." International Journal of Remote Sensing 38 (8–10). Taylor & Francis: 3159–3180. doi:10.1080/01431161.2017.1292074.

Dietrich, J. T., 2017. "Bathymetric Structure-from-Motion: Extracting Shallow Stream Bathymetry from Multi-View Stereo Photogrammetry." Earth Surface Processes and Landforms 42 (2): 355–364. doi:10.1002/esp.4060.

Eisenbeiss, H., and Sauerbier, M., 2011. "Investigation of UAV Systems and Flight Modes for Photogrammetric Applications." Photogrammetric Record 26 (136): 400–421. doi:10.1111/j.1477-9730.2011.00657.x.

Eltner, A., Kaiser, A., Castillo, C., Rock, G., Neugirg, F. and Abellán, A., 2016. "Image-Based Surface Reconstruction in Geomorphometry-Merits, Limits and Developments." Earth Surface Dynamics 4 (2): 359–389. doi: 10.5194/esurf-4-359-2016.

Feurer, D., Bailly, J.S., Puech, C., Le Coarer, Y. and Viau, A. A., 2008. "Very-High-Resolution Mapping of River-Immersed Topography by Remote Sensing." Progress in Physical Geography 32 (4): 403–419. doi: 10.1177/0309133308096030.

Fonstad, M. A., Dietrich, J. T., Courville, B. C., Jensen, J. L. and Carbonneau, P. E., 2013. “Topographic Structure from Motion: A New Development in Photogrammetric Measurement.” Earth Surface Processes and Landforms 38 (4): 421–430. doi:10.1002/esp.3366.

Fugazza, D., Senese, A., Azzoni, R. S., Smiraglia, C., Cernuschi, M., Severi, D. and Adele Diolaiuti, G., 2015. “High-Resolution Mapping of Glacier Surface Features. the Uav Survey of the Forni Glacier (Stelvio National Park, Italy).” Geografia Fisica e Dinamica Quaternaria 38 (1): 25–33. doi:10.4461/GFDQ.2015.38.03.

Gallagher, K., and Lawrence, P., 2016. “Urban Sustainability: Policy and Praxis,” 217–232. doi: 10.1007/978-3-319-26218-5.

Govedarica, M., Jakovljevic, G. and Álvarez Taboada, F., 2018. “Flood Risk Assessment Based on LiDAR and UAV Points Clouds and DEM.” In Remote Sensing for Agriculture, Ecosystems, and Hydrology XX, edited by Christopher M. Neale and Antonino Maltese, 10783:102. SPIE. doi:10.1117/12.2513278.

Grabowski, R. C., Surian, N. and Gurnell, A. M., 2014. “Characterizing Geomorphological Change to Support Sustainable River Restoration and Management.” Wiley Interdisciplinary Reviews: Water 1 (5): 483–512. doi:10.1002/wat2.1037.

Haala, N., Cramer, M., Weimer, F. and Trittler, M., 2012. “Performance Test on Uav-Based Photogrammetric Data Collection.” ISPRS - International Archives of the Photogrammetry, Remote Sensing and Spatial Information Sciences XXXVIII-1/ (September 2012): 7–12. doi: 10.5194/isprsarchives-XXXVIII-1-C22-7-2011.

Immerzeel, W. W., Kraaijenbrink, P. D.A., Shea, J. M., Shrestha, A. B., Pellicciotti, F., Bierkens, M.F.P. and De Jong, S. M., 2014. “High-Resolution Monitoring of Himalayan Glacier Dynamics Using Unmanned Aerial Vehicles.” Remote Sensing of Environment 150. Elsevier Inc.: 93–103. doi:10.1016/j.rse.2014.04.025.

James, M. R., and Robson, S., 2012. “Straightforward Reconstruction of 3D Surfaces and Topography with a Camera: Accuracy and Geoscience Application.” Journal of Geophysical Research: Earth Surface 117 (3): 1–17. doi: 10.1029/2011JF002289.

James, M. R., and Robson, S., 2014. “Mitigating Systematic Error in Topographic Models Derived from UAV and Ground-Based Image Networks.” Earth Surface Processes and Landforms 39 (10): 1413–1420. doi:10.1002/esp.3609.

Kinzel, P. J., Legleiter, C. J. and Nelson, J. M., 2013. “Mapping River Bathymetry With a Small Footprint Green LiDAR: Applications and Challenges.” Journal of the American Water Resources Association 49 (1): 183–204. doi:10.1111/jawr.12008.

Koci, J., Jarihani, B., Leon, J. X., Sidle, R. C., Wilkinson, S. N. and Bartley, R., 2017. “Assessment of UAV and Ground-Based Structure from Motion with Multi-View Stereo Photogrammetry in a Gullied Savanna Catchment.” ISPRS International Journal of Geo-Information 6 (11): 8–10. doi: 10.3390/ijgi6110328.

Lane, S. N., Widdison, P. E., Thomas, R. E., Ashworth, P. J., Best, J. L., Lunt, I. A., Sambrook Smith, G. H. and Simpson, C. J., 2010. “Quantification of Braided River Channel Change Using Archival Digital Image Analysis.” Earth Surface Processes and Landforms 35 (8): 971–985. doi:10.1002/esp.2015.

Legleiter, C. J. and Harrison, L. R., 2019. "Remote sensing of river bathymetry: Evaluating a range of sensors, platforms, and algorithms on the upper Sacramento River, California, USA." Water Resources Research 55 (3): 2142–2169. doi: 10.1029/2018WR023586.

Mandlburger, G., Hauer, C., Wieser, M. and Pfeifer, N., 2015. "Topo-Bathymetric LiDAR for Monitoring River Morphodynamics and Instream Habitats-A Case Study at the Pielach River." Remote Sensing 7 (5): 6160–6195. doi: 10.3390/rs70506160.

Marcus, A. W., 2012. "Remote Sensing of the Hydraulic Environment in Gravel-Bed Rivers." In Gravel-Bed Rivers: Processes, Tools, Environments. doi:10.1002/9781119952497.ch21.

Martínez-Carricondo, P., Agüera-Vega, F., Carvajal-Ramírez, F., Mesas-Carrascosa, A. García-Ferrer, F. J. and Pérez-Porras, F. J., 2018. "Assessment of UAV-Photogrammetric Mapping Accuracy Based on Variation of Ground Control Points." International Journal of Applied Earth Observation and Geoinformation. doi:10.1016/j.jag.2018.05.015.

McKean, J., Nagel, D., Tonina, D., Bailey, P., Wayne Wright, C., Bohn, C. and Nayegandhi, A., 2009. "Remote Sensing of Channels and Riparian Zones with a Narrow-Beam Aquatic-Terrestrial LIDAR." Remote Sensing 1 (4): 1065–1096. doi: 10.3390/rs1041065.

Micheletti, N., Chandler, J. H. and Lane, S. N., 2015. "Structure from Motion (SfM) Photogrammetry." British Society for Geomorphology Geomorphological Techniques 2 (2): 1–12. doi: 10.5194/isprsarchives-XL-5-W4-37-2015.

Muñoz-Mas, R., Garófano-Gómez, V., Andrés-Doménech, I, Corenblit, D., Egger, G., Francés, F., Ferreira, M.T., García-Arias, A., Politti, E., Rivaes, R., Rodríguez-González, P.M., Steiger, J., Vallés-Morán, F.J. and Martinez-Capel. 2017, F., "Exploring the key drivers of riparian woodland successional pathways across three European river reaches." Ecohydrology, 10(8): e1888. doi: 10.1002/eco.1888.

Nouwakpo, S. K., Weltz, M. A. and McGwire, K., 2016. "Assessing the Performance of Structure-from-Motion Photogrammetry and Terrestrial LiDAR for Reconstructing Soil Surface Microtopography of Naturally Vegetated Plots." Earth Surface Processes and Landforms 41 (3): 308–322. doi:10.1002/esp.3787.

Pajares, G., 2015. "Overview and Current Status of Remote Sensing Applications Based on Unmanned Aerial Vehicles (UAVs)." Photogrammetric Engineering & Remote Sensing 81 (4): 281–330. doi:10.14358/PERS.81.4.281.

Pan, Z., Glennie, C., Hartzell, P., Fernandez-Diaz, J., Legleiter, C. and Overstreet, B., 2015. "Performance Assessment of High Resolution Airborne Full Waveform LiDAR for Shallow River Bathymetry." Remote Sensing 7 (5): 5133–5159. doi: 10.3390/rs70505133.

Polat, N., and Uysal, M., 2015. "Investigating Performance of Airborne LiDAR Data Filtering Algorithms for DTM Generation." Measurement: Journal of the International Measurement Confederation 63. Elsevier Ltd: 61–68. doi:10.1016/j.measurement.2014.12.017.

Remondino, F., Barazzetti, L., Nex, F., Scaioni, M. and Sarazzi, D., 2011. "Uav Photogrammetry for Mapping and 3D Modeling – Current Status and Future Perspectives –" XXXVIII (September): 14–16. doi: 10.5194/isprsarchives-XXXVIII-1-C22-25-2011.

Rivas Casado, M., Ballesteros González, R., Ortega, J. F., Leinster, P. and Wright, R., 2017. "Towards a Transferable UAV-Based Framework for River Hydromorphological Characterization." Sensors (Switzerland) 17 (10): 1–22. doi: 10.3390/s17102210.

Rusnák, M., Sládek, J., Kidová, A. and Lehotský, M., 2018. "Template for High-Resolution River Landscape Mapping Using UAV Technology." Measurement: Journal of the International Measurement Confederation 115: 139–151. doi:10.1016/j.measurement.2017.10.023.

Schumann, G. J.P., Muhlhausen, J. and Andreadis, K. M., 2019. "Rapid Mapping of Small-Scale River-Floodplain Environments Using UAV SfM Supports Classical Theory." Remote Sensing 11 (8). doi: 10.3390/rs11080901.

Shintani, C. and Fonstad, M. A., 2017. "Comparing Remote-Sensing Techniques Collecting Bathymetric Data from a Gravel-Bed River." International Journal of Remote Sensing 38 (8–10). Taylor & Francis: 2883–2902. doi:10.1080/01431161.2017.1280636.

Tauro, F., Olivieri, G., Petroselli, A., Porfiri, M. and Grimaldi, S., 2016. "Flow Monitoring with a Camera: A Case Study on a Flood Event in the Tiber River." Environmental Monitoring and Assessment 188 (2): 1–11. doi: 10.1007/s10661-015-5082-5.

Tonina, D., McKean, J. A, Benjankar, R. M., Wright, C. W., Goode, J. R., Chen, Q., Reeder, W. J., Carmichael, R. A. and Edmondson, M. R., 2019. "Mapping River Bathymetries: Evaluating Topobathymetric LiDAR Survey." Earth Surface Processes and Landforms 44 (2): 507–520. doi:10.1002/esp.4513.

Tonkin, T. N. and Midgley, N. G., 2016. "Ground-Control Networks for Image Based Surface Reconstruction: An Investigation of Optimum Survey Designs Using UAV Derived Imagery and Structure-from-Motion Photogrammetry." Remote Sensing 8 (9): 16–19. doi: 10.3390/rs8090786.

Van Iersel, W., Straatsma, M., Addink, E. and Middelkoop, H., 2018. "Monitoring Height and Greenness of Non-Woody Floodplain Vegetation with UAV Time Series." ISPRS Journal of Photogrammetry and Remote Sensing 141. The Authors: 112–123. doi:10.1016/j.isprsjprs.2018.04.011.

Vargas-Luna, A., Crosato, A. and Uijttewaal, W. S.J., 2015. "Effects of Vegetation on Flow and Sediment Transport: Comparative Analyses and Validation of Predicting Models." Earth Surface Processes and Landforms 40 (2): 157–176. doi:10.1002/esp.3633.

Vázquez-Tarrío, D., Borgniet, L., Liébault, F. and Recking, A., 2017. "Using UAS Optical Imagery and SfM Photogrammetry to Characterize the Surface Grain Size of Gravel Bars in a Braided River (Vénéon River, French Alps)." Geomorphology 285: 94–105. doi:10.1016/j.geomorph.2017.01.039.

Visser, F., Woodget, A., Skellern, A., Forsey, J., Warburton, J. and Johnson, R., 2019.

"An Evaluation of a Low-Cost Pole Aerial Photography (PAP) and Structure from Motion (SfM) Approach for Topographic Surveying of Small Rivers." International Journal of Remote Sensing 40 (24). Taylor & Francis: 9321–9351. doi:10.1080/01431161.2019.1630782.

Wackrow, R., Ferreira, E., Chandler, J. and Shiono, K., 2015. "Camera Calibration for Water-Biota Research: The Projected Area of Vegetation." Sensors (Switzerland) 15 (12): 30261–30269. doi: 10.3390/s151229798.

Westaway R. M., Lane, S. N. and Hicks, D. M., 2001. "Remote Sensing of Clear-Water, Shallow, Gravel-Bed Rivers Using Digital Photogrammetry". Photogrammetric Engineering and Remote Sensing 67 (11): 1271–1281. WoS: 000171928500007.

Westoby, M. J., Brasington, J., Glasser, N. F., Hambrey, M. J. and Reynolds, J. M., 2012. "'Structure-from-Motion' Photogrammetry: A Low-Cost, Effective Tool for Geoscience Applications." Geomorphology 179. Elsevier B.V.: 300–314. doi:10.1016/j.geomorph.2012.08.021.

Woodget, A. S., Carbonneau, P. E., Visser, F. and Maddock I. P., 2015. "Quantifying Submerged Fluvial Topography Using Hyperspatial Resolution UAS Imagery and Structure from Motion Photogrammetry." Earth Surface Processes and Landforms 40 (1): 47–64. doi:10.1002/esp.3613.

Woodget, A. S., Visser, F., Maddock, I. P. and Carbonneau, P. E., 2016. "The Accuracy and Reliability of Traditional Surface Flow Type Mapping: Is It Time for a New Method of Characterizing Physical River Habitat?" River Research and Applications 32 (9). John Wiley and Sons Ltd: 1902–1914. doi:10.1002/rra.3047.

Woodget, A. S., and Austrums, R., 2017. "Subaerial Gravel Size Measurement Using Topographic Data Derived from a UAV-SfM Approach." Earth Surface Processes and Landforms 42 (9): 1434–1443. doi:10.1002/esp.4139.

Woodget, A. S., Austrums, R., Maddock, I. P. and Habit, E., 2017. "Drones and Digital Photogrammetry: From Classifications to Continuums for Monitoring River Habitat and Hydromorphology." Wiley Interdisciplinary Reviews: Water 4 (4): e1222. doi:10.1002/wat2.1222.

Woodget, A. S., Dietrich, J. T. and Wilson, R. T., 2019. "Quantifying Below-Water Fluvial Geomorphic Change: The Implications of Refraction Correction, Water Surface Elevations, and Spatially Variable Error." Remote Sensing 11 (20): 1–33. doi: 10.3390/rs11202415.

Woodget, A., Visser, F., Maddock, I. and Carbonneau, P., 2015. "Quantifying Fluvial Substrate Size Using Hyperspatial Resolution UAS Imagery and SfM-Photogrammetry," no. December.

Zucchini, W., A. Berzel, and O. Nenadic. 2003. "Applied smoothing techniques. Part I: Kernel Density Estimation", vol. 15.

# 5. Classification of riparian vegetation types based on supervised classification algorithms. A case study in the Serpis River (Valencia)


## Abstract

The classification of riparian vegetation types is a key factor when modelling the behaviour of the river and its evolution over the years. The main objective of this work was to analyse and compare different algorithms for the automatic analysis and classification of succession phases of riparian vegetation, over a study area of the Serpis River (Valencia). For this, different methods of classification were applied to QuickBird© satellite images (2.4 m of spatial resolution), minimum distance, maximum likelihood, parallelepiped, Mahalanobis distance, and artificial neural networks in several cases (with different number of iterations to obtain stable results). In addition, all the classification methods were tested with a different number of vegetation classes (6, 5 and 4 classes). For each of the defined cases, a stretch of river was segmented into patches to obtain a calibration area and a validation area independent of each other. The best performing method was the maximum likelihood with 4 vegetation classes, according to the validation with vegetation patches surveyed in the field (Overall accuracy value 0.35). This classification model showed the best performance; although the accuracy was not high, the models of maximum likelihood and artificial neural networks provided a method to classify riparian succession phases that can be applied to the entire river length in a continuous manner, with the advantage of being faster and more operative than traditional methods of classification in the field. The different models showed different patterns in terms of omission and commission errors, which indicate future directions of research for modelling riparian vegetation dynamics when mature riparian trees, shrubs (young succession phases), pioneer plants or invasive species should be the target of applied studies for river conservation and management.



**Keywords:** Remote sensing, Riparian vegetation, Supervised classification, Fluvial restoration.

## 5.1 Introduction

Over the last few years, the use of remote sensing has become increasingly common and important, generating new applications in various areas of science that study the earth and its characteristics (Casagli et al., 2017; Rwanga and Ndambuki, 2017). This factor is also favoured by the great possibilities and advantages that this technology can generate, such as the location of geographical spaces, the observation and monitoring of multi-temporal phenomena and the integration of the results obtained in a Geographic Information System (GIS), which favours the reduction of work flow and therefore the investment and use of resources applied to these studies on the land surface (Blasch et al., 2015; Christopoulou et al., 2019; Ghamisi et al., 2018). The advantages that arise with the use of these data are, for instance; the total coverage one can obtain and the broad perspective that this type of data allows us to work with, detailed multiscale observation, specific information on non-visible spectral regions, temporal variability in the execution of the observations, transmission and reception of data in real time and its recording in digital databases (Cheng and Han, 2016; Chuvieco, 2008; Tewkesbury et al., 2015). The classification of elements of the land cover with remote sensing techniques allows us to develop inventories with quantitative aspects of their presence, constituting a key tool in management and conservation measures (Zeballos et al., 2020; Douda et al., 2016).

The presence of riparian vegetation has a direct implication on the processes that the riparian ecosystem can undergo. The flora and fauna in these spaces have a very marked relationship, so the events and changes that may be experienced can affect their natural development (López-Baucells et al., 2017; Kontsiotis et al., 2019). The riparian ecosystem accumulates a large proportion of terrestrial biodiversity (Blondel and Aronson, 1999; Naiman et al., 2008); its study and monitoring are therefore key for the ecosystems conservation and management. In addition, the hydro-geomorphological dynamics developed in the riparian ecosystem are also related to the presence, extension, and type of riparian vegetation (Corenblit et al., 2015; Politti et al., 2018; Garófano-Gómez et al., 2011).

Currently, the conservation of biodiversity and the normal functioning of ecosystems is a critical challenge, thus it is necessary to generate and develop new methodologies and algorithms to be able to know those elements better and subsequently to manage them in an optimal way (Cabello and Paruelo, 2008; Garófano-Gómez et al., 2011; Orimoloye et al., 2020; Vihervaara et al., 2017). In this line of action, remote sensing is a key tool, since it allows us to analyse the riparian habitats at different spatial and temporal scales, supporting deeper studies on the behaviour of their environmental elements. Traditionally, riparian vegetation areas have been studied using maps, photointerpretation, fieldwork and laboratory analysis, but satellite images offer additional information based on electromagnetic energy stored using several spectral bands. The methodology proposed by the supervised classification allows the delimitation of different vegetation succession phases, where the different vegetation classes obtained are the result of a subdivision of space based on objective characteristics and their response to the different wavelengths of the electromagnetic spectrum (Piramanayagam et al., 2018; Zanotta et al., 2018). Thus, it is possible to obtain valuable information on its characteristics, not perceptible in conventional aerial photographs (Houborg et al., 2015; Kaneko and Nohara, 2014) and its application over large areas by monitoring their main trends and characteristics (De Roeck et al., 2008; Feng et al., 2015).

The riparian ecosystem is threatened by the channelling of many river sections of the drainage network, the construction of hydraulic infrastructures and the replacement of these natural areas with agricultural and forestry crops. In addition, the appearance and proliferation of invasive species is a reality in these riparian habitats, so their monitoring and delimitation on a recurring basis can safeguard the integrity of the riparian forest and avoid imbalances and loss of native species (Zaimes, 2020; Nadal-Sala et al., 2017). In general, the diverse alterations of rivers and floodplains by human activity, including the presence of organic pollution, morphological alterations and modifications of the drainage network have caused a proliferation of invasive species in most riparian ecosystems in Europe (Schnitzler et al., 2007; González et al., 2017). The riparian forests in Mediterranean ecosystems comprise a wide variability of species in areas of land that are sometimes small; therefore, the proliferation of invasive species causes a direct harmful action on the natural development of the autochthonous ecosystem (Stella et al., 2013; Bruno et al., 2021). The possibility of developing classifications of plant species in these areas is a key tool in the river restoration of these spaces (Martínez-Fernández et al., 2018; Zema et al., 2018).

On the other hand, the study of riparian vegetation in Mediterranean areas by means of remote sensing techniques presents certain limitations due to the complexity of its distribution and the similarity in the spectral response that many of its species present (Huylenbroeck et al., 2020; Dufour et al., 2019). An additional difficulty for automatic classifications comes from the strong variability of its vegetative phases throughout the year and its different adaptation to the environment according to its location and environmental conditions (Rivaes et al., 2013; Camporeale and Ridolfi, 2006).

More specifically, in the Serpis river Basin (Júcar River Basin District) the ecological status (CHJ, 2019) is worse than good in the water bodies downstream of the Beniarrés dam, which constitutes the study area of this piece of research. Regarding the hydromorphological status, it presents some degree of hydrological alteration due to the dam operation, as well as morphological alteration or channelization, especially in the lower segments in the county of La Safor. Its biological status is good according to the macroinvertebrate biological indicator (IBMWP) and its chemical status is not good due to the chemical pollution associated with the presence of a surplus of nitrogen, derived from the intensive agricultural exploitation in the annexed areas. In the area of influence of the Serpis River, there is a notable extension of invasive plant species, such as the giant cane, which means specific threats to the correct development of the natural aquatic habitats, causing imbalances in their dynamics. The possibility of separating this invasive vegetation as an independent class from the rest will allow us to evaluate their distribution and colonization areas to carry out control and conservation tasks. The characteristic morphology and physiology of the giant cane (*Arundo donax*) in comparison with native riparian species allow it to dominate the riparian forest in most environmental conditions and therefore negatively affect the development of common native species (Coffman, 2007).

Considering the aforementioned threats and opportunities, this piece of research can contribute with a methodology for the classification of riparian vegetation, using remote sensing techniques on multispectral satellite images.

The main objective of this work was to propose a workflow and analyse the capability of remote sensing techniques and geographic information systems (GIS) in the classification of different succession phases of riparian vegetation, in a target section of the Serpis River. Due to restrictions in budget and image availability at the time of the study, this study is based on images of the QuickBird© platform. To carry out this general objective, the present work has been structured into various work phases:

• Analysis of the study area in the field to determine the phases of riparian vegetation succession to be classified in the riparian zone (Garófano-Gómez et al., 2013; García-Arias et al., 2013; Garófano-Gómez et al., 2010).

• Pre-treatment of radiometric and topographic correction of the multispectral QuickBird© images on which the supervised classification was performed.

• Application of different supervised classification methods on the multispectral image, in the calibration segment.

• Validation of the classification methods in the validation segment.

• Comparison of classification methods and discussion on the images quality and its suitability to classify vegetation in the riparian zone in Mediterranean regulated river systems.

## 5.2 Methods

### 5.2.1 Study area

The study area comprises the section of the Serpis River within the gorge named as "Estret del Infern" (translated as "Hell's gorge") below the Beniarrés dam, in the municipality of Villalonga (Figure 5.1).

The Beniarrés dam is the only one in the Serpis River from its source in the vicinity of the town of Alcoi to its mouth in the sea. The total length of the river is 74.5 km and its river basin has an area of 752.8 $km^2$. The predominant type of climate in the basin is the Mediterranean coast, with an average annual temperature of 16.3 ºC and an average annual rainfall of 630 mm (Garófano-Gómez et al., 2011). Its hydrological regime develops its maximum values of river flow in the month of January and its minimum in August, something very common in Mediterranean rivers. Along the river course we can find some areas with native riparian vegetation, related to the variable conditions in the channel morphology, the permanent water course and the abundant springs that it presents (Garófano-Gómez et al., 2011). However, there is an increasing presence of invasive species, especially the giant cane or elephant grass (*Arundo donax*), especially downstream of the gorge, which completely hinder the natural development of the riparian ecosystem.

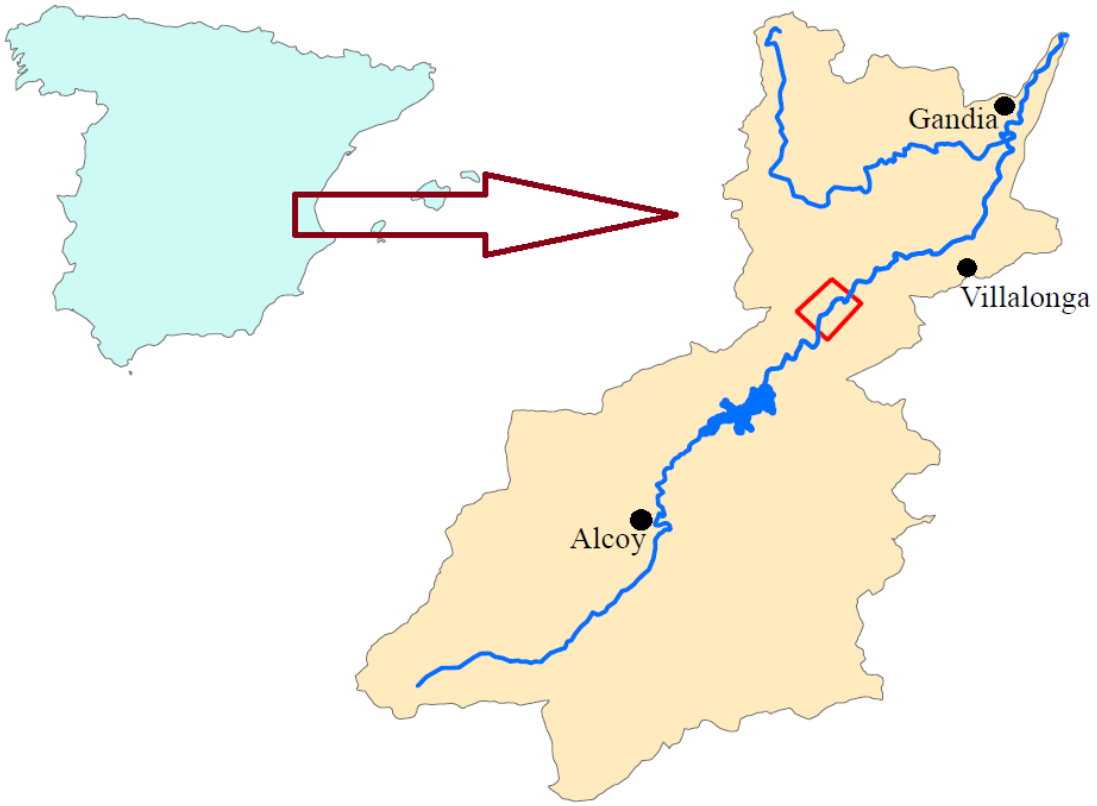


**Figure 5.1**. Location of the study area. The red square defines the Estret del Infern extension.

In the upper sections of the Serpis River, between Beniarrés dam and the Estret del Infern the variability of species is greater than in the lower sections, between the gorge and the Mediterranean Sea. In addition, along this low-lying area that circulates near the towns of Potries, Gandía, among others, the overpopulation of giant cane is very visible (Garófano-Gómez et al., 2011), which has a great impact on the natural course of the riparian ecosystem and the human activities in this territory, with a high cultural and environmental interests.

### 5.2.2 Classification of vegetation in succession phases

The succession phases were used to classify the habitats of riparian vegetation, based on the scientific report of the project "Riparian vegetation modelling for the assessment of environmental flow regimes and climate change impacts within the Water Framework Directive" (RIPFLOW). These phases allow us to observe and analyse how the riparian succession takes place, in relation with the hydrological conditions and the Mediterranean climate forest. The RIPLOW it is a distributed and dynamic model that, by establishing successions and retrogressions in response to physical parameters, is capable of simulating the distribution of riparian vegetation in time and space. It has an annual time step and is divided into five modules, corresponding to the five processes considered: recruitment, destructive effect of floods, duration of floods, plant transpiration and succession change (Garcia-Arias et al., 2011).

The classification of vegetation in phases of vegetation succession is key when entering the necessary data for the development of the model in its different modules. In

the first module of the RIPFLOW model (i.e., recruitment), the changes in morphology and elevations of the water table are considered to estimate the pioneer zones where the recruitment of the riparian woodland species can develop.

In the second module of the RIPFLOW model, it allows the evaluation of maps of shear stress in the river bed, in order to determine whether a given river flow in a given habitat could produce the removal and transport of the existing plants; this depends on the phase of succession in the habitat to be evaluated. In the module related to flood duration, the model contemplates the retrogression of the vegetation phases caused by physiological stress under inundation (related with lack of oxygen in the roots). Such stress or even the death of the plants relates with factors such as the succession phase, age of the plants and the severity of the impact (duration).

In the module of soil moisture, the availability of water in the soil is analysed by functional types of vegetation, in which the plants of the different succession phases would be clustered. Finally, the last module considers the results of the previous modules to evaluate whether the vegetation has reached sufficient age to evolve towards another phase or to another line of succession.

The succession phases, which represent the riparian habitats in the study area, were 6: Bare ground, herbs, giant cane, shrubs (young successional woodland), caducifolious trees, and perennial trees. Within herbs, the observations can gather species of different character, such as recruitment of woody riparian species (e.g., genus Salix and Populus), shrubs or herbs in the first stages of life. The trees usually cover the most mature stage of the vegetation; although some phases in the riparian succession only include riparian caducifolious trees, the most mature stage in the riparian woodland frequently include intolerant species and some terrestrial species combined with the strictly riparian ones. These phases reflect the range of vegetation that predominates in the Mediterranean riparian ecosystem (Garófano-Gómez et al., 2014; Rivaes et al., 2014).

The only class that exclusively represents an invasive vegetation type is the class of giant cane. This class has been introduced separately due to the interest of classifying these habitats that have spread widely throughout the region, and which needs urgent management and control measures (Maceda-Veiga et al., 2016; Coffman et al., 2010).

To obtain a classification of the study area, trying to avoid the complexity that the different vegetation phases present, we defined the succession phases of vegetation grouping the different types of riparian vegetation as defined in Figure 5.2. This responds to the need to use a series of classes that have a sufficient distance between them so that the interference that they could generate in the classified model is minimal.

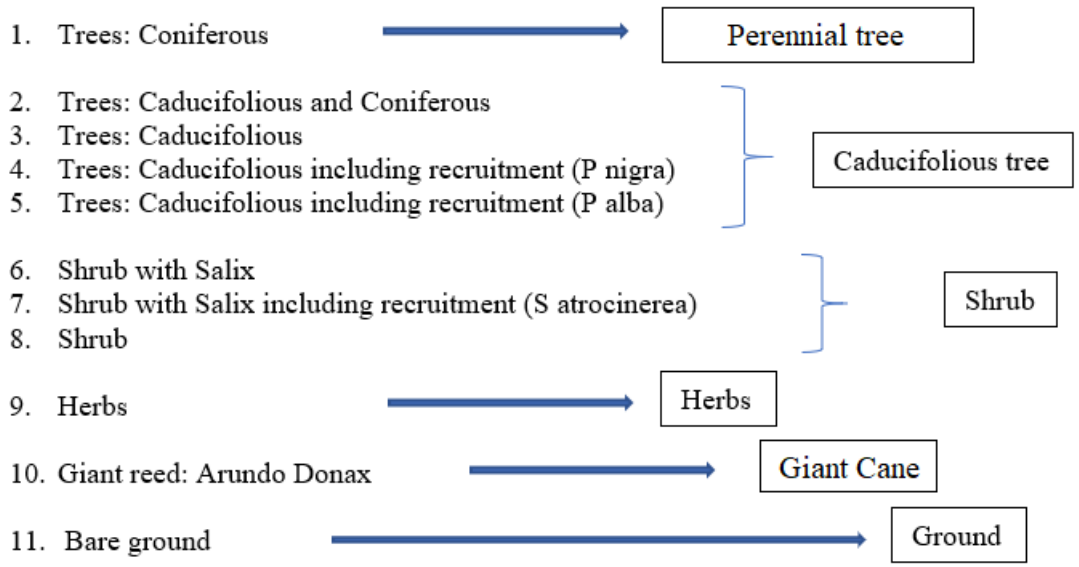


**Figure 5.2.** Simplification of plant categories. P represents Pinus, S refers to Salix.

The bare ground class was assigned to areas where there is no vegetation or exists with a low percentage. These phases correspond on the plant succession that are expected to be found in our study area, with the herbs class being the least evolved phase and perennial trees the most advanced.

The most common vegetation species of caducifolius trees in our study area (after Garófano et al., 2019) are *Populus nigra* and *Populus alba*. For its part, the perennial trees class presents types of coniferous vegetation such as *Pinus halepensis* and *Pinus pinaster*. The class of shrubs refer mainly to several species of Salix, *Salix eleagnos* subsp. angustifolia, *Salix atrocinerea*, *Salix purpurea*, and others like *Nerium oleander*, and perennial trees of small size and low height of the genus Pinus. The herbs phase comprises very diverse species in the area, where we can highlight some species such as *Scirpus holoschoenus*, *Sparganiun erectum*, *Thypha latifolia* and *Phragmites australis*. And finally, the giant cane class is constituted mostly by the invasive species Arundo donax (Garófano et al., 2019).

Considering the initial classification of the vegetation in succession phases, different cases were considered by reducing the number of classes. The second and third cases of analyses were intended to improve the results and reduce the errors associated with adjusting the classified values to reality. The second case consisted of 5 vegetation phases, bare ground, herbs, giant cane, deciduous trees, and non-deciduous trees. For this attempt the classes of perennial vegetation shrub and perennial trees were joined, justified by the fact that their vegetative state is very similar for the date of study. A third case considered 4 phases of vegetation, bare ground, herbs, caducifolious trees and perennial trees. For this, in addition to the previous fusion, herbs and giant canes classes were joined, due to the similarity and correspondence between the patterns that their spectral signature marks.

### 5.2.3 Data acquisition

A QuickBird© image registered in October 2008 was used in this study due to the possibility of coordinating the field data capture mission with this date. This satellite image has a multispectral sensor with four bands: blue (450 - 520 nm), green (520 - 600

nm), red (630-690 nm) and near infrared (760-900 nm) bands; its spatial resolution is 2.4 meters as a ground sample distance (GSD). A previous process of radiometric and topographic correction of the satellite image was applied. The Envi 5.0 © software were used, that provides the Fast Line-of-sight Atmospheric Analysis of Hypercubes (FLAASH©) tool to image radiometric calibration. This software has orthorectification tools to generate a geometric correction to the multispectral image based on the digital elevation model (DEM) and ground control points (GCPs) based on terrain real data.

The selection of the calibration segment was based on the criteria of sufficient presence of the different phases of vegetation succession aforementioned, and the possibility of access to the area for the field measurement. The absence of shadows in the multispectral satellite image to be classified in the calibration segment was also considered for the correct discrimination of the information (Song et al., 2015). The validation segment was delimited in an area totally independent from the calibration segment, but including the same vegetation succession phases. Its condition and characteristics were intended to be similar; therefore, this segment was also within the same gorge at a short distance from the calibration segment. Likewise the calibration segment, the segments presenting shadows or distortions in the radiometry of the satellite image were excluded from selection.

The field data for calibration were measured and recorded in a previous work (Garófano-Gómez et al., 2011). To capture this information, classical topography techniques were used in the 257 meters of length of this calibration segment. The complete field segmentation of the calibration zone was generated (Figure 5.3); for this task, each of the vegetation patches were identified with the dominant (> 80% of cover) vegetation succession phase. Other criteria for the patches delineation were an area equal or larger than 5 $m^2$, for greater clarity and representativeness of the samples (Garófano-Gómez et al., 2011). Table 5.1 indicates the distribution of vegetation succession phases in the calibration and validation river segment. In the validation segment, the polygons of vegetation were identified and delimited with the help of topographic references and aerial images. We attended the same classes aforementioned, and the same criteria concerning the dominant vegetation succession phase and the minimum polygon area. In the extraction process, we eliminated areas where due to the inclination of the sun and the orography and morphology, shadows invalidated the radiometric values of the land cover.

**Table 5.1.** Distribution of vegetation succession phases in the calibration and validation river segments.

| Class Value | Calibration area | | Validation area | |
|---|---|---|---|---|
| | Number of patches | Total area ($m^2$) | Number of patches | Total area ($m^2$) |
| caducifolious trees | 7 | 3420 | 9 | 2818 |
| perennial trees | 5 | 2832 | 14 | 4580 |
| shrubs | 14 | 2900 | 22 | 8560 |
| giant cane | 4 | 322 | 8 | 965 |
| herbs | 28 | 2400 | 19 | 5672 |
| Total | 58 | 11874 | 72 | 22595 |

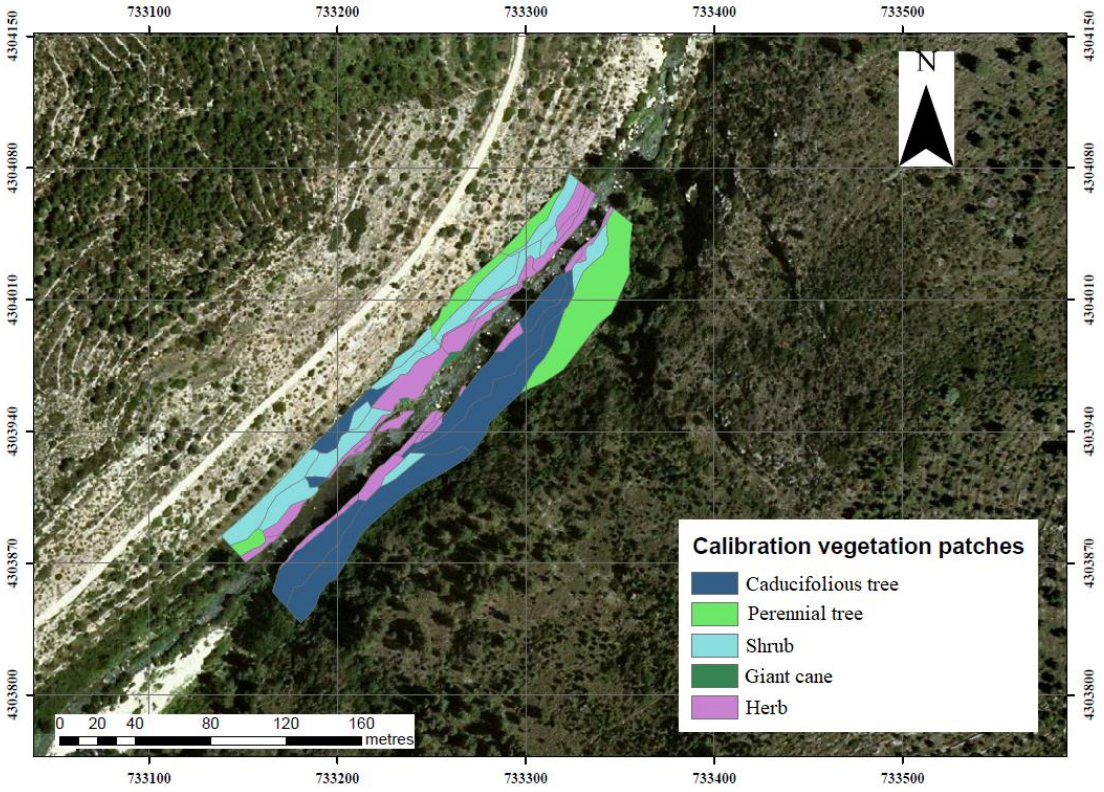


**Figure 5.3**. Map of the succession phases of riparian vegetation identified in the calibration segment of the Serpis River (WGS84 / UTM zone 30N).

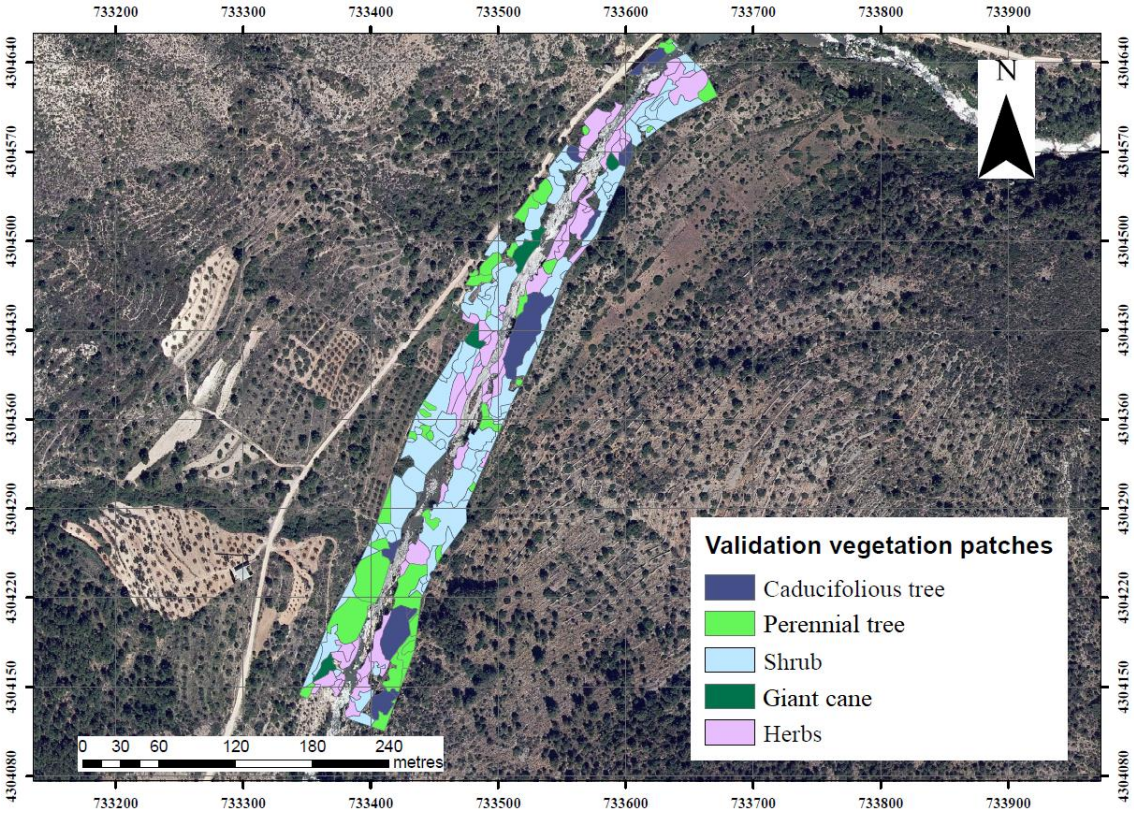


**Figure 5.4.** Segment of the Serpis River delimited as a validation zone and vegetation patches measured in the field (WGS84 / UTM zone 30N)

5.2.4 Calibration of supervised classification models

After delimiting the calibration segment in the field, square polygons of 2.4 meters side were defined in a vectorial file to represent the different succession phases. The distribution of these patches was performed to cover the entire calibration segment along the river stream, and that each polygon was separated from the others to avoid possible influence or overlaps (Figure 5.5). The number of regions was 20 for each class, the same number for all the succession phases. These patches were taken as calibration data to classify each of the vegetation phases.

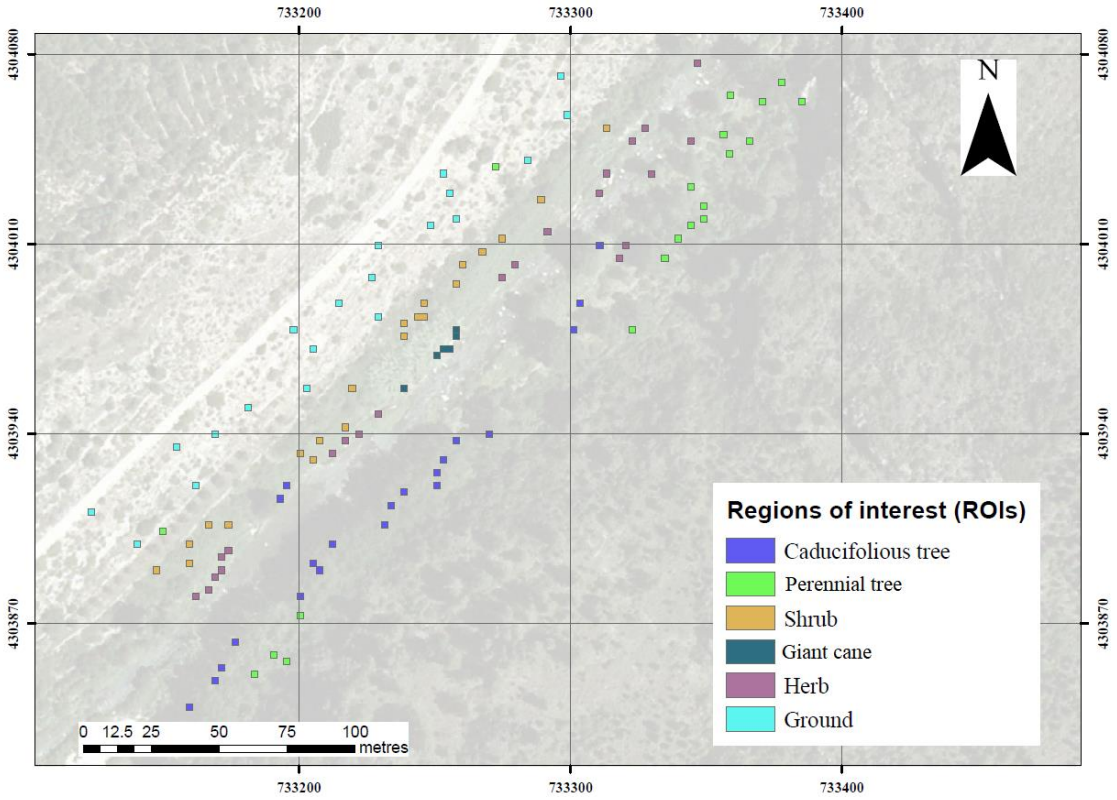


**Figure 5.5**. Regions of interest (ROIs) selected as training sample for supervised classification (WGS84 / UTM zone 30N), in the calibration zone.

Before applying the different supervised classification algorithms, a separability analysis was performed between the selected classes. For this task, the regions of interest defined in figure 5.5 were taken as patterns of the spectral response for each class. To analyse these values, we applied the Jeffries-Matusita distance analysis and the Transformed Divergence analysis, which indicate the separability between the ROI of the different classes, in values between 0.963 and 2.000 (Tables 5.2, 5.5 and 5.8). This analysis allowed us to verify the quality and spectral distance between the regions to be used as calibration areas in the supervised classification (Büttner et al., 1988; Metternicht and Zinck, 1998; Ustin et al., 2009). Furthermore, a study of the spectral signatures of the vegetation succession phases was carried out to analyse possible anomalous patterns.

The supervised classification methods used and compared in this study were minimum distance, maximum likelihood, parallelepiped, Mahalanobis distance and artificial neural networks (ANN).

These classification models were chosen because of their good results and applicability in the classification of land cover based on satellite multispectral images (Souza et al., 2013; Duarte et al., 2018). Previous studies compared and analysed the use of the classification methods maximum likelihood, minimum distance, Mahalanobis distance and parallelepiped methods in the vegetation classification and mapping from multispectral satellite images (Govender et al., 2008; Shen et al., 2010) providing good results with a good fit to the defined vegetation classes and high overall accuracy and kappa coefficient values. That is why we consider appropriate the use and analysis of these methods for our study area. In addition, other studies compared and evaluated the classification of vegetation utilizing maximum likelihood and ANN methods (Paola and Schowengerdt, 1995; Sunar et al. 2004) showing a trend in the results that improved those raised by simpler models based on distance calculation such as the minimum distance, Mahalanobis distance and parallelepiped methods. Diverse studies have used these vegetation classification methods on satellite multispectral images obtaining good results (Nivedita Priyadarshini et al., 2018; Sisodia et al., 2014), for this reason we decided to evaluate their application and behaviour obtained for our study area.

Maximum likelihood is a parametric method based on the normal statistical distribution of the values (Erdas, 1999). The probability density functions used in these methods are created for each of the classes based on the spectral values obtained from the training data (Hagner and Reese, 2007). In the classification process, all unclassified pixels are assigned a class membership, based on the results obtained in the relative probability function (Lillesand et al., 2004).

The ANN are based on a continuous learning of the values that are reached to better adjust the model values (Cromp, 1991; Short, 1991). The ANN are defined as a variable number of weighted and interconnected processing phases for each of the layers in the network. The phases acquire input data, analyse it and operate it, and then transfer it through predefined functions. The comparison of the resulting values with respect to the reference data is carried out and a readjustment of the weights between the realizations is carried out according to a specified learning rule. This process is repeated until the network has been trained with the continuous adjustment of the weights; it is possible to classify the training data obtaining results below a specified error threshold (Cairns, 2001).

Concerning the methods of minimum distance, parallelepiped, and Mahalanobis distance, they are based on the calculation of different kind of distances between the elements of the model (pixels) to determine the most probable class in each case. The calculation of the distance for each of the methods is based on different parameters. The minimum distance classifier is based on the minimum distance between the image data and each class value in a multi-feature space (Fisher, 1936; Wald, 1944). The Parallelepiped method generates decision boundaries attending on the values defined on the region of interest for each case and evaluating the distances between these and each pixel, its final value will be assigned (Pawlak, 1982; Komorowski, 1999). The dimensions of the parallelepiped boundaries are defined as a function of the mean of the standard deviation threshold for each class evaluated. If the pixel value is between the low and the high threshold for all n bands being classified, then the pixel is assigned to that class (Sun, 2016). The last method based on distances, Mahalanobis distance, refers the distance

calculation according to the statistical variation of each component using the covariance matrix of the observed sample (Mahalanobis, 1936).

In the case of ANN, the statistical values obtained in each iteration were analysed with the aim of analysing their trend and preventing the possible overfitting of the model. The model was trained with different number of iterations, in order to obtain the optimum number (100, 300, 500, 600, 700, 800, 900, 1000, 1100, 1200, 1500, 5000 and 8000 iterations). The overall accuracy value for each iteration was considered to evaluate the performance of the models.

After the application of each one of the supervised classification algorithms, the confusion matrix was generated for each of the obtained models, taking as reference (true values) the regions of interest (ROIs) of each class (vegetation succession phase). This matrix shows the number of cases correctly classified, the cases of false positives and the false negatives in the determination of each class. Based on this matrix, the performance of the model was evaluated with the overall accuracy and the kappa coefficient (Cohen, 1960; Congalton, 1991), and the omission and commission errors were considered for comparison.

Attending on the values of the confusion matrix for each classification method, we merged some phases of vegetation succession, thus generating different study cases. For each of the three cases, were created new ROIs to be the training areas for the model's calibration. For each of the classes defined, 20 ROIs were distributed throughout the calibration river segment.

### 5.2.5 Validation of supervised classification models

Once all the supervised classification algorithms had been applied to the calibration river segment, a statistical process of models validation was carried out. ArcGis© software allow us to generate the analysis and comparison process between the models results and the validation data.

To carry out the validation on the defined area, an extraction mask was applied to the entire QuickBird© satellite image already classified, to generate the process in an area with real field data independent of those used in the calibration phase. This validation segment has 580 metres of longitude along the river main axis (figure 5.4) and was divided in 95 patches (polygons) attending to the vegetation succession phases (Table 5.1).

The validation process using the ArcGis© software, was based on creating 20 control points per vegetation phase, randomly distributed throughout the validation polygons (vegetation patches). These points were assigned a real class value (data based on values taken on the images) and the estimated or modelled value obtained from each of the supervised classification models. With these points, a confusion matrix was generated, upon which we estimated the indicators of performance (quality of adjustment) aforementioned, for each of the supervised classification models, like in the calibration phase. In this validation phase, the performance indicators allow us to compare the models and discuss which works and best fit our data and the characteristics of our study area.

The use of the overall accuracy performance indicator is very common in characterization and classification studies of land cover and vegetation types. Through this indicator we can better understand the probability that an individual will be correctly classified by a model, this being the sum of the true positives together with the true negatives, all divided among the total samples analysed (Domaç and Süzen, 2006).

### 5.2.6 Stepwise procedure to select the optimal number of classes

After the initial classification in 6 classes of riparian vegetation succession phases, three consecutive cases of calibration and validation were performed, reducing the number of classes one by one. This process was carried out to find the best possible model (best performance) to fit to the vegetation classes present. In the second and third steps, the procedure consisted of merging two classes with similar radiometric and spectral behaviours, as well as similar plant status due to the time of year in which the study took place. The three cases of classification were the following:

- Case 1: 6 classes; Bare ground, herbs, giant cane, shrubs, caducifolious trees and perennial trees.
- Case 2: 5 classes; Bare ground, herbs, giant cane, caducifolious trees and perennial trees. For this case, the classes of perennial vegetation shrub and perennial trees were joined, justified by the fact that their vegetative state is very similar for the date of study.
- Case 3: 4 classes; Bare ground, herbs, caducifolious trees and perennial trees. For this, in addition to the previous fusion, herbs and giant cane classes were joined, due to the similarity and correspondence in the patterns of their spectral signatures.

For each of the cases, different ROIs were distributed in the two river segments, i.e. for calibration and validation. Such configurations were made to obtain the maximum separability between classes and in order to exclude or minimise possible correlations between their spectral signatures. Then the application of all the classification algorithms proposed was based on the ROIs values defined for each case. The validation was carried out based on those ROIs selected in the validation river segment, with the same number per class in the ArcGis© software (20 ROIs per class). The calibration and validation regions of interest were defined attending the best configuration and distribution of pixels at the study section. The main objective was to obtain the necessary values for each phase of the workflow obtaining the equal proportion and distribution of each of the vegetation succession phases.

### 5.3.7 Application of the selected model in an additional study area

Once the classification models had been calibrated and validated, the method that best suited our area and training classes was selected. We then proceeded to its application on another study area of the Serpis River, to produce a classification of the different phases of vegetation along 10 kilometres of the riparian zone. This area included the Serpis River downstream from the Beniarres dam; specifically from the river channel just

below the dam until a point below the town of Lorcha, about 3 km within the Estret de l' Infern.

On that image, an extraction mask of 25 meters was generated on each side of the river channel, without considering the strip of water. The resulting study area comprises all or most of the riparian forest, where the riparian management measures could be recommended. The selected best-performing model was applied to this new area; therefore, the percentage of pixels by class and the area that they occupy in the extension of the analysis area were calculated.

## 5.3 Results

In the three following sub-sections we present the results of the calibration in the three cases for classification of vegetation succession phases, in the five models. Due to the diverse cases raised and calculated for each classification, according to the number of classes to be modelled, in the fourth sub-section the results of validation are shown for the best-fitting model only.

### 5.3.1 Calibration

#### *5.3.1.1 Case 1: 6 classes*

In this case, 6 succession phases were separated; bare ground, herbs, giant cane, shrubs, caducifolious trees and perennial trees. The indicators of the separability, in Table 5.2, demonstrates the classes that present greater separability are caducifolious tree with respect to ground (1.997) and with respect to herbs (1.996). Meanwhile, the worst separability values are shown among herbs and giant cane (0.963).

**Table 5.2**. Maximum and minimum values of separability between classes for case 1. For brevity, the rest of combinations across classes were omitted in this table.

| Classes | Jeffries-Matusita | Transformed Divergence |
|---|---|---|
| shrubs-giant cane | 1.364 – 1.721 | 1.364 |
| shrubs-herbs | 1.343 – 1.542 | 1.343 |
| herbs-giant cane | 0.963 – 1.247 | 0.963 |
| caducifolious tree - herbs | 1.997 – 1.999 | 1.997 |
| caducifolious tree - ground | 1.996 – 2.000 | 1.996 |
| caducifolious tree - shrubs | 1.961 – 1.999 | 1.967 |

After the models calibration, the confusion matrix was generated for the five calibrated models, taking as reference marks the ROIs defined above (20 ROIs per class).

The best and worst values among the five models corresponded to the maximum likelihood with an overall accuracy of 88.33% and a kappa coefficient of 0.86, and the parallelepiped method with an overall accuracy of 54.17% and a kappa coefficient of 0.45, respectively. The following confusion matrices display the percentage of pixels that were correctly classified and those meaning model errors, that is, assigned to different class by the models (Tables 5.3 and 5.4). The reference class data (reference data, true class) is indicated in the heading of columns and the model result (classified data) in each of the classes are indicated in rows.

**Table 5.3.** Confusion matrix for calibration of the maximum likelihood method, in terms of percentage of pixels to the total. In bold, the cases correctly classified in each of the classes.

| | | Reference data | | | | | |
|---|---|---|---|---|---|---|---|
| | | CT | PT | S | GC | H | G |
| Classified data | CT | **95** | 0 | 0 | 0 | 0 | 0 |
| | PT | 0 | **90** | 5 | 0 | 5 | 0 |
| | S | 5 | 5 | **90** | 5 | 10 | 0 |
| | GC | 0 | 0 | 5 | **85** | 15 | 0 |
| | H | 0 | 5 | 0 | 10 | **70** | 0 |
| | G | 0 | 0 | 0 | 0 | 0 | **100** |
| | T | 100 | 100 | 100 | 100 | 100 | 100 |

CT= Caducifolious tree; PT= Perennial trees; S= Shrubs; GC=Giant cane; H=Herbs; G=Ground; T=Total

**Table 5.4.** Confusion matrix for calibration of the parallelepiped method, in terms of percentage of pixels to the total. In bold, the cases correctly classified in each of the classes.

| | | Reference data | | | | | |
|---|---|---|---|---|---|---|---|
| | | CT | PT | S | GC | H | G |
| Classified data | CT | **95** | 10 | 0 | 0 | 0 | 0 |
| | PT | 5 | **90** | 95 | 70 | 70 | 0 |
| | S | 0 | 0 | **5** | 5 | 5 | 0 |
| | GC | 0 | 0 | 0 | **25** | 15 | 0 |
| | H | 0 | 0 | 0 | 0 | **10** | 0 |
| | G | 0 | 0 | 0 | 0 | 0 | **100** |
| | T | 100 | 100 | 100 | 100 | 100 | 100 |

CT= Caducifolious tree; PT= Perennial trees; S= Shrubs; GC=Giant cane; H=Herbs; G=Ground; T=Total

The values of overall accuracy obtained for the series of iterations of the ANN are shown in Figure 5.6. A significant increase in the overall accuracy value with respect to the initial values was observed in the iteration 900.

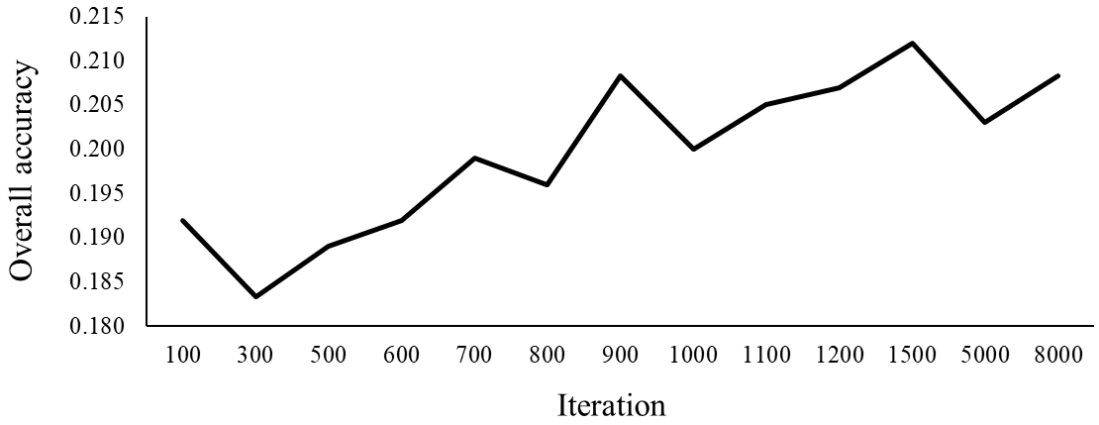


**Figure 5.6.** Overall accuracy values obtained for each ANN in the iteration, in the case 1 (6 classes).

*5.3.1.2 Case 2: 5 classes*

This second case was generated with 5 different classes; bare ground, herbs, giant cane, caducifolious trees and perennial trees (including shrubs).

The calculation of separability between classes using the Jeffries-Matusita distance analysis and the Transformed Divergence are shown in Table 5.5. Likewise the previous case, the classes that present greater separability are caducifolious tree with respect to ground (1.996) and with respect to herbs (1.998). And the worst separability corresponds to herbs and giant cane (0.916).

**Table 5.5.** Maximum and minimum values of separability between classes for case 2.

| Classes | Jeffries-Matusita | Transformed Divergence |
|---|---|---|
| caducifolious trees - perennial trees | 1.722 – 1.956 | 1.722 |
| perennial trees – herbs | 1.570 – 1.800 | 1.570 |
| herbs - giant cane | 0.916 – 1.109 | 0.916 |
| caducifolious trees – herbs | 1.998 – 1.999 | 1.998 |
| caducifolious trees - ground | 1.996 – 2.000 | 1.996 |
| caducifolious trees - giant cane | 1.982 – 1.999 | 1.982 |

Once the ROIs were re-classified into these 5 classes, each of the supervised classification algorithms were applied to obtain the corresponding models. Likewise, the confusion matrices were generated for each of the models, taking reference values from the ROIs defined in the classification process.

For this second case the best and worst values obtained from these matrices were for the maximum likelihood with an overall accuracy of 91% and a kappa coefficient of 0.89 and for the parallelepiped method with an overall accuracy of 65% and a kappa coefficient of 0.56, respectively. and for the maximum likelihood with an overall accuracy of 91% and a kappa coefficient of 0.89 and with the following confusion matrices (percentage values between the number of brands in each case with respect to the total) (Table 5.6 and 5.7). The confusion matrices display the percentage of pixels that were correctly classified and those meaning model errors. That is, assigned to different class by the models (Table 5.6 and 5.7). The reference class data (reference data) is indicated

in the heading of columns and the model result (classified data) in each of the classes are indicated in rows.

**Table 5.6.** Confusion matrix for the calibration of the maximum likelihood method, in terms of percentage of pixels to the total. In bold, the cases correctly classified in each of the classes.

| | | Reference data | | | | |
|---|---|---|---|---|---|---|
| | | CT | PT | GC | H | G |
| Classified data | CT | **95** | 0 | 0 | 0 | 0 |
| | PT | 5 | **95** | 0 | 5 | 0 |
| | GC | 0 | 0 | **90** | 20 | 0 |
| | H | 0 | 5 | 10 | **75** | 0 |
| | G | 0 | 0 | 0 | 0 | **100** |
| | T | 100 | 100 | 100 | 100 | 100 |

CT= Caducifolious trees; PT= Perennial trees; GC=Giant cane; H=Herbs; G=Ground; T=Total

**Table 5.7.** Confusion matrix for calibration of the parallelepiped method, in terms of percentage of pixels to the total. In bold, the cases correctly classified in each of the classes.

| | | Reference data | | | | |
|---|---|---|---|---|---|---|
| | | CT | PT | GC | H | G |
| Classified data | CT | **95** | 10 | 0 | 0 | 0 |
| | PT | 5 | **90** | 70 | 70 | 0 |
| | GC | 0 | 0 | **30** | 20 | 0 |
| | H | 0 | 0 | 0 | **10** | 0 |
| | G | 0 | 0 | 0 | 0 | **100** |
| | T | 100 | 100 | 100 | 100 | 100 |

CT= Caducifolious trees; PT= Perennial trees; GC=Giant cane; H=Herbs; G=Ground; T=Total.

Also for this case 2, the overall accuracy values obtained for the different iterations of the ANN were calculated and shown in Figure 5.7. For this second case, we found an improvement in the overall accuracy with respect to the initial values, and the trend shows that around the iteration 900 it presents a better value.

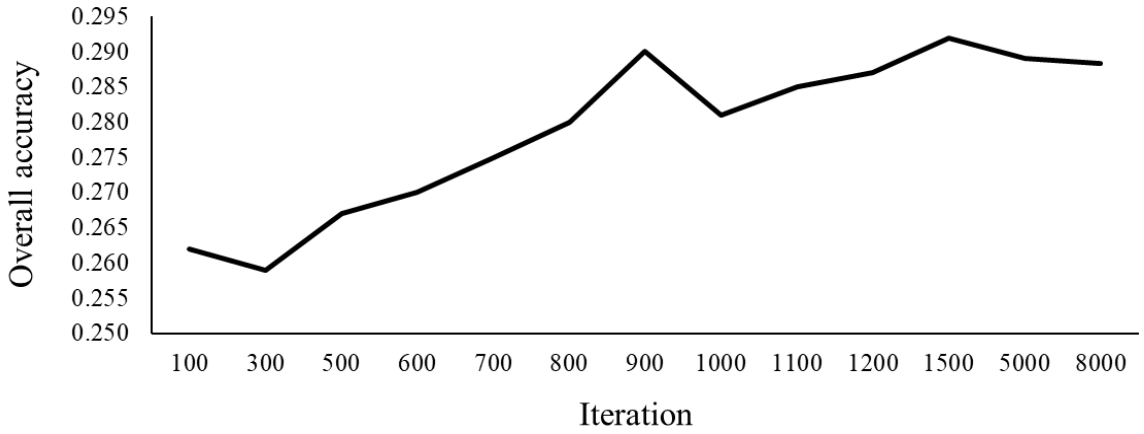


**Figure 5.7.** Overall accuracy values obtained for each ANN iteration at case 2.

*5.3.1.3 Case 3: 4 classes*

The last case had 4 classes; bare ground, herbs (including giant cane), caducifolious trees and perennial trees. This case offered the separability values shown in the Table 5.8. For this last case the classes that present greater separability are caducifolious tree with respect to the ground (1.998) and with respect to herbs (1.997). The worst separability corresponded to perennial trees *versus* herbs (1.570).

**Table 5.8.** Maximum and minimum values of separability between classes for case 3.

| Classes | Jeffries-Matusita | Transformed Divergence |
|---|---|---|
| caducifolious trees - perennial trees | 1.722 – 1.956 | 1.722 |
| perennial trees – herbs | 1.570 – 1.800 | 1.570 |
| herbs - ground | 1.802 – 2.000 | 1.802 |
| perennial trees - ground | 1.912 – 1.999 | 1.912 |
| caducifolious trees - herbs | 1.997 – 2.000 | 1.997 |
| caducifolious trees - ground | 1.998 – 2.000 | 1.998 |

For this third case the best and worst values of performance were for the maximum likelihood, with an overall accuracy of 96.25% and a kappa coefficient of 0.95, and for the parallelepiped method with an overall accuracy of 78.75% and a kappa coefficient of 0.72, respectively. The confusion matrices, in percentage of pixels, corresponded to the Tables 5.9 and 5.10. The reference class data (reference data) is indicated in the heading of columns and the model result (classified data) in each of the classes are indicated in rows.

**Table 5.9.** Confusion matrix for maximum likelihood method calibration, in terms of percentage of pixels to the total. In bold, the cases correctly classified in each of the classes.

| | | Reference data | | | |
|---|---|---|---|---|---|
| | | CT | PT | H | G |
| Classified data | CT | **95** | 0 | 0 | 0 |
| | PT | 5 | **95** | 5 | 0 |
| | H | 0 | 5 | **95** | 0 |
| | G | 0 | 0 | 0 | **100** |
| | T | 100 | 100 | 100 | 100 |

CT= Caducifolious tree; PT= Perennial trees; H=Herbs; G=Ground; T=Total

**Table 5.10.** Confusion matrix for calibration of the parallelepiped method, in terms of percentage of pixels to the total, in terms of percentage of pixels to the total. In bold, the cases correctly classified in each of the classes.

| | | Reference data | | | |
|---|---|---|---|---|---|
| | | CT | PT | H | G |
| Classified data | CT | **95** | 10 | 0 | 0 |
| | PT | 5 | **90** | 70 | 0 |
| | H | 0 | 0 | **30** | 0 |
| | G | 0 | 0 | 0 | **100** |
| | T | 100 | 100 | 100 | 100 |

CT= Caducifolious trees; PT= Perennial trees; H=Herbs; G=Ground; T=Total

In this case, the overall accuracy for the iterations of the ANN were calculated and shown in Figure 5.8. Finally, in the last case, we find also an improvement in the overall accuracy value with respect to the previous case, and presents the best values at the iteration 900.

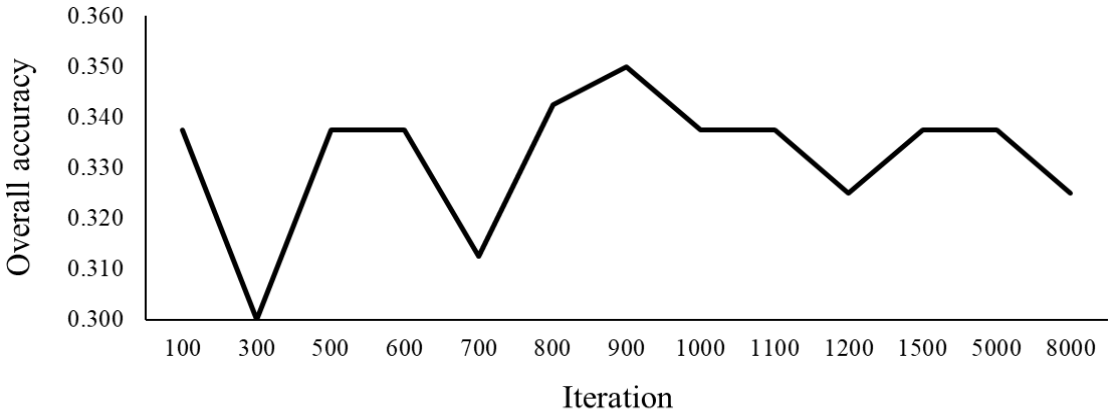


**Figure 5.8.** Overall accuracy values obtained for each ANN iteration at case 3.

5.3.2 Validation

The following Table 5.11 presents a summary of the overall accuracy obtained in the validation process for each of the applied methods, in the three cases. For the artificial

neural network (ANN), the overall accuracy corresponds to the same model indicated in the calibration phase.

**Table 5.11.** Values of overall accuracy for each classification method in the three cases. In bold, the best value in each of the cases.

| Supervised classification method | 6 classes | 5 classes | 4 Classes |
|---|---|---|---|
| Minimum distance | 0.167 | 0.280 | 0.320 |
| Maximum likelihood | **0.258** | **0.330** | **0.350** |
| Parallelepiped | 0.194 | 0.231 | 0.338 |
| Mahalanobis distance | 0.233 | 0.270 | 0.313 |
| Artif. neural network (900 iterations) | 0.208 | 0.290 | 0.340 |

*5.3.2.1 Validation - case 1*

In the first case, the maximum likelihood presented the best performance among the five models (0.258), followed by the Mahalanobis distance method with a very similar value (0.233). For the second case (5 classes), the performance was only slightly higher; the best model evaluated with the overall accuracy was maximum likelihood (0.330) again, and the second was the ANN with 900 iterations (0.290). For the third case (4 classes), there was another slight increase of performance; the highest overall accuracy corresponded to the model of maximum likelihood (0.350), although the ANN (with 900 iterations) obtained a practically equal fit (0.340).

Considering the general view of the validation in the 3 study cases, it is generally the model of maximum likelihood the one offering the best performance in the river segment of validation. Nevertheless, the overall accuracy for this model tends to reduce the differences with the rest of the models, as the number of vegetation classes is reduced.

Table 5.12 is the confusion matrix for the model of maximum likelihood (case 1), where the reference class data (true class) is indicated in the heading of columns and the model result (classified data, or modelled data) in each of the classes are indicated in rows. For brevity, the confusion matrices of other models are not presented here, for the case 1.

In this first case, with 6 classes, considering the value of the user accuracy, the classes that shows lowest number of false positives is giant cane and caducifolious tree thus they have fewer commission errors (Table 5.12). On the other hand, the class with the best producer accuracy is herbs, thus there are fewer false negatives (omission errors). Going for details about this model's errors, the caducifolious tree presented 4 errors per commission and 15 by omission. The perennial trees had 15 errors per commission and 15 by omission. The shrubs class had 25 errors by commission and 15 by omission. The herbs class had 32 commission errors and 9 omission errors; some pixels of all the other types were classified as herbs by mistake. The giant cane had 3 commission errors and 16 by omission, and the ground class has 10 commission errors and 19 by omission.

Considering the user and producer accuracy values, in this first case we can see important differences between the two for most of the classes. The omission errors for the caducifolious tree, giant cane and ground are high, thus the model tend to

underestimate their extension; herbs and shrubs suffer from more commission errors, i.e., the model overestimate their presence.

**Table 5.12.** Confusion matrix for the validation of the maximum likelihood method (case 1). The values in each cell of the matrix represent the number of ROIs related to each case (N = 20 per class). In bold, the cases correctly classified by class.

| | | Reference data | | | | | | | |
|---|---|---|---|---|---|---|---|---|---|
| | | CT | PT | S | GC | H | G | T | UA |
| Classified data | CT | **5** | 2 | 2 | 0 | 0 | 0 | 9 | 0.556 |
| | PT | 5 | **5** | 0 | 3 | 2 | 5 | 20 | 0.25 |
| | S | 6 | 4 | **5** | 4 | 4 | 7 | 30 | 0.167 |
| | GC | 0 | 0 | 1 | **4** | 2 | 0 | 7 | 0.571 |
| | H | 3 | 5 | 9 | 8 | **11** | 7 | 43 | 0.256 |
| | G | 1 | 4 | 3 | 1 | 1 | **1** | 11 | 0.091 |
| | T | 20 | 20 | 20 | 20 | 20 | 20 | 120 | |
| | PA | 0.25 | 0.25 | 0.25 | 0.2 | 0.55 | 0.05 | | |

CT= Caducifolious trees; PT= Perennial trees; S= Shrubs; GC=Giant cane; H=Herbs; G=Ground; T=Total; UA=User accuracy; PA=Producer accuracy

Table 5.13 shows the confusion matrix for the model of Mahalanobis distance, where the class with the lowest number of false positives (commission errors) is giant cane. On the other hand, the class with the best producer accuracy is shrubs, having fewer false negatives (omission). The user accuracy for herbs, ground and caducifolious trees were low, thus they tend to overestimate these classes. Considering the confusion matrix, the user and producer accuracy by class, the comparison with maximum likelihood was made in more detail (Table 5.12 and 5.13). For this method, the caducifolious trees presented 16 errors per commission and 16 by omission (very well balanced). The perennial trees had 11 errors per commission and 16 by omission. The shrubs had 33 errors by commission and 10 by omission. The herbs class had 12 commission errors and 17 omission errors. The giant cane had 4 commission errors and 17 by omission, and the ground class had 16 commission errors and 16 by omission.

The omission errors for the perennial trees, herbs and giant cane classes are high, thus they tend to underestimate the spatial extension of the class, whereas shrubs suffered more commission errors and tend to be overestimated.

**Table 5.13.** Confusion matrix for the validation of the model with Mahalanobis distance. The values in each cell of the matrix represent the number of ROIs related to each case (N = 20 per class). In bold, the cases correctly classified by class.

| | | Reference data | | | | | | | |
|---|---|---|---|---|---|---|---|---|---|
| | | CT | PT | S | GC | H | G | T | UA |
| Classified data | CT | **4** | 5 | 4 | 3 | 1 | 3 | 20 | 0.20 |
| | PT | 1 | **4** | 2 | 2 | 3 | 3 | 15 | 0.27 |
| | S | 8 | 5 | **10** | 6 | 5 | 9 | 43 | 0.23 |
| | GC | 2 | 0 | 0 | **3** | 1 | 1 | 7 | 0.43 |
| | H | 4 | 4 | 1 | 3 | **3** | 0 | 15 | 0.20 |
| | G | 1 | 2 | 3 | 3 | 7 | **4** | 20 | 0.20 |
| | T | 20 | 20 | 20 | 20 | 20 | 20 | 120 | |
| | PA | 0.20 | 0.20 | 0.50 | 0.15 | 0.15 | 0.20 | | |

CT= Caducifolious trees; PT= Perennial trees; S= Shrubs; GC=Giant cane; H=Herbs; G=Ground; T=Total; UA=User accuracy; PA=Producer accuracy

In this first case, we observe how the two best methods tend to underestimate the class of giant cane and overestimate the class of shrubs.

*5.3.2.2 Validation - case 2*

For the case 2, where 5 classes were considered, the validation indicated maximum likelihood as the best classification method. The confusion matrix for this model, in Table 5.14, shows the reference class data was defined at each column and the classified class data was presented for each row.

**Table 5.14.** Confusion matrix for the validation of the maximum likelihood method. The values in each cell of the matrix represent the number of ROIs related to each case (N = 20 per class). In bold, the cases correctly classified by class.

| | | Reference data | | | | | | |
|---|---|---|---|---|---|---|---|---|
| | | CT | PT | GC | H | G | T | UA |
| Classified data | CT | **4** | 1 | 1 | 0 | 2 | 8 | 0.5 |
| | PT | 5 | **4** | 1 | 1 | 6 | 17 | 0.24 |
| | GC | 1 | 4 | **7** | 3 | 2 | 17 | 0.41 |
| | H | 8 | 8 | 7 | **14** | 6 | 43 | 0.33 |
| | G | 2 | 3 | 4 | 2 | **4** | 15 | 0.27 |
| | T | 20 | 20 | 20 | 20 | 20 | 100 | |
| | PA | 0.2 | 0.2 | 0.35 | 0.7 | 0.2 | | |

CT= Caducifolious trees; PT= Perennial trees; GC=Giant cane; H=Herbs; G=Ground; T=Total; UA=User accuracy; PA=Producer accuracy

In this case, the value of the user accuracy shows that the class with the lowest number of false positives is also giant cane and caducifolious trees, so they have fewer commission errors (Table 5.14). On the other hand, the class with the best producer accuracy is herbs, so there are fewer false negatives, and therefore contains minor errors of omission.

Concerning the maximum likelihood method, the caducifolious trees presented 4 errors per commission and 16 by omission. The perennial trees class had 13 errors per commission and 16 by omission. The herbs class had 29 commission errors and 6 omission errors. The giant cane class had 10 commission errors and 13 by omission, and the ground class had 11 commission errors and 16 by omission.

The omission errors for the caducifolious trees, perennial trees, giant cane and ground classes are high, thus they tend to present an underestimated area distribution; the herbs class generate more commission errors, thus it tends to be overestimated.

The Table 5.15 shows the confusion matrix for the ANN (900 iterations) where the user accuracy indicated the lowest number of false positives corresponds to caducifolious trees (therefore, fewer commission errors). On the other hand, the class with the best producer accuracy is perennial trees.

**Table 5.15.** Confusion matrix for the validation of the ANN method with 900 iterations. The values in each cell of the matrix represent the number of ROIs related to each case (N = 20 per class). In bold, the cases correctly classified by class.

| | | Reference data | | | | | | |
|---|---|---|---|---|---|---|---|---|
| | | CT | PT | GC | H | G | T | UA |
| Classified data | CT | **6** | 2 | 2 | 1 | 4 | 15 | 0.40 |
| | PT | 3 | **9** | 5 | 2 | 8 | 27 | 0.33 |
| | GC | 5 | 1 | **5** | 9 | 1 | 21 | 0.24 |
| | H | 2 | 3 | 1 | **2** | 0 | 8 | 0.25 |
| | G | 4 | 5 | 7 | 6 | **7** | 29 | 0.24 |
| | T | 20 | 20 | 20 | 20 | 20 | 100 | |
| | PA | 0.30 | 0.45 | 0.25 | 0.10 | 0.35 | | |

CT= Caducifolious trees; PT= Perennial trees; GC=Giant cane; H=Herbs; G=Ground; T=Total; UA=User accuracy; PA=Producer accuracy

Concerning the balance of errors by class in the ANN, the caducifolious trees presented 9 errors per commission and 14 by omission. The perennial trees had 18 errors per commission and 11 by omission. The herbs had 6 commission errors and 18 omission errors. The giant cane class had 16 commission errors and 15 by omission (good balance), and ground had 22 commission errors and 13 by omission. Therefore, the omission errors for caducifolious trees and herbs are high, then they tend to be underestimated. On the other way, ground and perennial trees suffer more commission errors and tend to be overestimated, whereas giant cane had a good balance in the two types of errors.

Therefore, the second case in general shows the two best methods tend to underestimate the spatial extension of caducifolious trees and to overestimate the ground class. In this case again, the values of user and producer accuracy shows that maximum likelihood offers better results than the ANN with 900 iterations.

*5.3.3.3 Validation - case 3*

Finally, in the last case with 4 classes, the confusion matrix is shown in Table 5.16 for the best method, maximum likelihood. The user accuracy shows the lowest number

of false positives for caducifolious trees, whereas the best producer accuracy was for herbs once more; that is, fewer errors of omission.

Finally, the omission and commission errors by class were the following. Caducifolious trees presented 2 errors per commission and 17 by omission. The perennial trees class had 14 errors per commission and 13 by omission (good balance). Herbs had 29 commission errors and 6 omission errors, and the ground class had 7 commission errors and 16 by omission. The omission errors for the caducifolious trees and ground classes are high, i.e., the model tend to underestimate these classes in a great manner. On the other hand, perennial trees and herbs had more commission errors.

**Table 5.16.** Confusion matrix for the validation of the maximum likelihood method. The values for each of the classes in each cell of the matrix represent the number of ROIs related to each case (N = 20 per class). In bold, the cases correctly classified by class.

| | | Reference data | | | | | |
|---|---|---|---|---|---|---|---|
| | | CT | PT | H | G | T | UA |
| Classified data | CT | **3** | 1 | 0 | 1 | 5 | 0.6 |
| | PT | 6 | **7** | 3 | 5 | 21 | 0.33 |
| | H | 9 | 10 | **14** | 10 | 43 | 0.33 |
| | G | 2 | 2 | 3 | **4** | 11 | 0.36 |
| | T | 20 | 20 | 20 | 20 | 80 | |
| | PA | 0.15 | 0.35 | 0.7 | 0.2 | | |

CT= Caducifolious trees; PT= Perennial trees; H=Herbs; G=Ground; T=Total; UA=User accuracy; PA=Producer accuracy

The values of the confusion matrix for the ANN (Table 5.17) shows that, amongst the vegetation classes, the lowest number of false positives for caducifolious trees, i.e., fewer commission error. On the other hand, the best producer accuracy was for herbs and perennial trees, i.e., fewer false negatives or omission errors.

These two classes were clearly under-predicted, the caducifolious trees (5 commission error, 16 omission error) and ground (7 commission errors, 16 omission errors). On the contrary, the other two classes suffered an important over-prediction, perennial trees (19 commission errors, 10 omission errors) and herbs class (21 commission errors, 10 omission errors).

Once more, the details of results in the confusion matrices demonstrated that the accuracy of the maximum likelihood method superseded the ANN with 900 iterations. Nevertheless, in this last case with four classes we have verified the differences between models in terms of accuracy are smaller than in the previous cases.

**Table 5.17.** Confusion matrix for the validation of the ANN method with 900 iterations. The values in each cell of the matrix represent the number of ROIs related to each case (N = 20 per class). In bold, the cases correctly classified by class.

| | | Reference data | | | | | |
|---|---|---|---|---|---|---|---|
| | | CT | PT | H | G | T | UA |
| Classified data | CT | **4** | 2 | 1 | 2 | 9 | 0.44 |
| | PT | 8 | **10** | 4 | 7 | 29 | 0.34 |
| | H | 7 | 7 | **10** | 7 | 31 | 0.32 |
| | G | 1 | 1 | 5 | **4** | 11 | 0.36 |
| | T | 20 | 20 | 20 | 20 | 80 | |
| | PA | 0.20 | 0.50 | 0.50 | 0.20 | | |

CT= Caducifolious trees; PT= Perennial trees; H=Herbs; G=Ground; T=Total; UA=User accuracy; PA=Producer accuracy

5.3.3 Application of the selected model in an additional study area

Considering the three cases and the results of the different supervised classification methods, the algorithm that best adjusted to our study area and the vegetation classes was applied (Figure 5.9). Therefore, the maximum likelihood method was applied with 4 classes of vegetation. The Table 5.15 shows the summary of results in the riparian zone within the additional study area of the Serpis River.

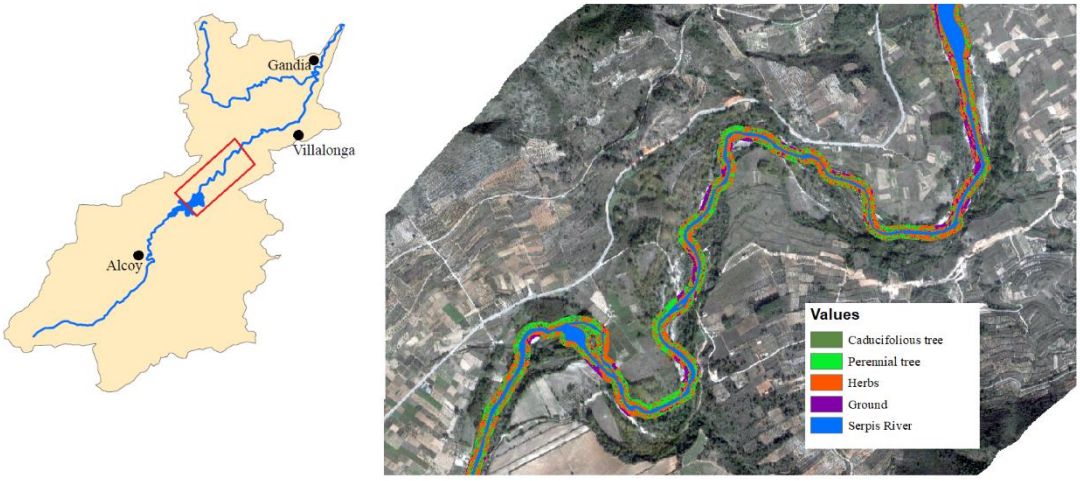


**Figure 5.9.** Additional study area where the best model, based on maximum likelihood, was applied to classify the vegetation succession phases in the riparian zone. The red rectangle means the contour of the Quickbird satellite image classified.

The application of this model to the additional study area of 10 km length, estimated that more than 80% of the analysed riparian area on both sides of the river is occupied by different phases of succession of the vegetation, while the rest belongs to bare ground. Within this dominant vegetation cover, one half (40.19%) is occupied by the youngest succession phase, herbs. The rest of the vegetation corresponds to perennial trees (27.30 %) and caducifolious trees (13.42%).

**Table 5.15.** Proportion of the number of pixels with respect to the total per class and area of vegetation in the riparian forest in the additional study area

| Class | Presence (%) | Occupation area ($m^2$) |
|---|---|---|
| Caducifolious trees | 13.42 | 32464.8 |
| Perennial trees | 27.30 | 66045.6 |
| Herbs | 40.19 | 97214.4 |
| Ground | 19.09 | 46176 |

## 5.4 Discussion

The proposed methodology was focused on the supervised classification of riparian habitats, for the monitoring of the plant succession in the riparian forest. This piece of research provides with an evaluation of the quality of different classification models based on remote sensing, in a study area dominated by riparian Mediterranean vegetation. These models, focused on phases of vegetation succession, mean a positive step in the generalised automatic characterisation of the starting condition of dynamic succession models for the riparian vegetation, such as RIPFLOW, and CASiMiR – vegetation. And likewise, for the automatic generation of different maps of succession phases that such dynamic models need to be calibrated and validated, in extensive segments of Mediterranean rivers, beyond the relatively short stretches used in pilot studies in Europe.

Different studies related to the characterization of the land cover and the classification of vegetation have been developed recurrently over time (Xie et al., 2008). Most of them present much better performance indicators and statistical validations than those presented herein; nevertheless in most of those studies the classes were much more generalist in terms of the types of land cover (Yang, 2007; Huylenbroeck et al., 2020). Unlike them, our study tries to define the classes associated with the different phases of succession of the vegetation (RIPFLOW), with very relevant ecological meaning for the dynamics and the evolution of the riparian ecosystem.

On the other hand, many of those works based on the application of supervised classification models were developed on data with a higher spatial resolution and in areas where the gradient of class variability is smaller (more gradual in space) than in the Mediterranean riparian ecosystem (Congalton et al., 2003; Akasheh et al., 2008). That is, the mean size of the vegetation patches, or the length where the habitats changed was around 15 to 60 metres, in contrast with this study, where the patches of relatively uniform vegetation had between 5 and 10 metres.

One crucial process in this work was the choice of regions within these calibration patches for the training of supervised classification algorithms (ROIs); this process was focused on defining the ROIs without distortions in the reference spectral signature for each class. However, the main difficulties were; the overlapped and mixed presence of diverse types of vegetation in a small (relatively narrow) riparian area; the difficult extraction of vegetation patches for a single dominant class; and the pixel size (2.4 meters) of the multispectral image to be classified, in comparison with the size of some of the groups of shrubs or trees in the field. For each case, a configuration and distribution of

ROI was defined that would guarantee sufficient separability between types of vegetation, and therefore mitigating the overlap and distortion between classes, intended to improve the supervised classification process.

One of the limiting factors in this piece of research has been the spatial resolution of our image to be classified, due to the extension of the study area and its variability of classes, as a fundamental characteristic of the Mediterranean riparian forest. In our case, considering the extension of the study area, the use of UAVs or aircraft with sensors of smaller pixel size could have helped to discriminate and precisely delimit the different features (Huylenbroeck et al., 2020; Michez et al., 2016). Other works on vegetation showed the high variability and overlap among the types of vegetation in the riparian forest, which make their delimitation and classification complex with the use of sensors mounted on satellite platforms, justifying the use of airborne sensors at a lower height to alleviate this drawback (Congalton et al., 2003; Dunford et al., 2009).

The calibration of the five models presented favourable results in the three cases. The separability analysis allowed us to verify the sufficient difference between the ROIs of each class, thus we were able to define our reference data precisely. In addition, the calculation of the confusion matrix and the overall accuracy for each of the models defined the behaviour and adjustment by vegetation classes. Considering the performance estimators such as the overall accuracy and kappa coefficient, the methods analysed in this study showed good calibration results in the three cases. Considering these positive results, we expected that the values obtained in the validation phase would be also good. The fact of losing quality in the validation results with respect to the results obtained in calibration is due to the characteristics of both zones. The calibration segment was defined by larger patches and with less mix of different classes of vegetation, while on the contrary, the validation segment presented a more confused distribution and with a smaller surface delimitation of patches. The general trend for the three cases suggested the best calibrated classes were ground and caducifolious tree, being the worst herbs and giant cane.

The validation of our classification models based on the confusion matrix, as well as the producer and user accuracy, have allowed us to evaluate the correspondence and correlation between the real values and those classified in the different regions defined for this purpose (Akay et al., 2013; Bhaskaran et al., 2010). In general, the two indicators of performance were very low in the three cases presented. The possibility of counting errors by omission and commission allowed us to understand the distribution of errors concerning the prediction of each of the vegetation succession phases. The low values of user and producer precision, in the three cases, showed an erratic trend. The errors behaviour is also an indicator of how the similarity between classes makes the classification complex and the confusion between classes (evolving errors by omission and commission) is general for all the classes, in the three cases. Furthermore these commission and omission errors did not follow a consistent trend across the three cases; thus the trends of overestimation or underestimation for a class depended on the classification method and the case (number of classes). A higher presence of commission errors with respect to omission errors will cause that the model behave according to that proportion of errors, the final consequence will be the prediction of more area of a class than there is in reality. In an analogous way it happened with the presence of the errors

by commission. These results show us the non-existence of a clear pattern in the definition and classification of the classes.

Regardless the best general behaviour of the maximum likelihood method, it is interesting to evaluate the possibility of having a good balance of errors or a slightly over-predictive model for the invasive giant cane. The ANN model in case 2 indicated a good balance of omission and commission errors for the giant cane. This model could be proposed as a good alternative for calculating and estimating the presence of this invasive species, that produces serious alterations in the natural cycles of the riparian ecosystem. Given a certain number of errors, the possibility of over-estimating this class can have positive implications, instead of the under-prediction. Because it would facilitate the natural resources managers and the water managers to make plans of conservation and control measures for said species in riverbank areas, with potential maps of distribution that overestimate the area. This is preferable to the underestimation of the serious problem of the biological invasions, and the reduction of budget with a consequent impossibility to carry out the planned management actions.

The general trend of results, in the three cases, does not present a model that allows overestimating the presence of caducifolious trees (typical terrestrial plants) whose proliferation in Mediterranean riparian ecosystems means the progressive alteration and colonization of non-riparian species, as may be the case of the pine, closer and closer to the main river channel. The tendency of the models to the underestimation could mean a consequent problem of neglecting the problem of anthropogenic disturbances like for eutrophication or terrestrialization process. (Papastergiadou et al., 2008; Zhang et al., 2016). Therefore, it may lead to insufficient management for the control and monitoring of this process in the riparian zones, and the consequent reduction of vegetation biodiversity.

Considering the low values presented by the performance indicators in the validation, another limitant factor of the study can be the season of the work. Working during the autumn period cause the spectral response of the vegetation not to show its most intense values. The lower possibility of discriminating the digital levels manifested by their spectral signatures causes a distortion factor in the application of the supervised classification processes applied, depending on the season of the year (Fernandes et al., 2013; Bertoldi et al., 2011).

Despite the different attempts to improve class selection, the results reflected the difficulty of differentiating among similar classes in terms of spectral response, especially between herbs, giant cane and shrubs. The results obtained with the application of the classification methods, and the respective confusion matrix, showed this defect of similarity between classes added to the variability of the vegetation cover present in the study area, conditioned to the low spatial heterogeneity at our spatial scale of work (2.4 m). Furthermore, the pixel size of the Quickbird© image causes a generalization and smoothing of reality in many areas of the riparian forest. It must be considered that our riparian study area covers an average width of about 27 meters on each side, with respect to the riverbank. This implies that on each bank of the river and measured on the transverse profile we have an average of 10 pixels where all the information on the series of riparian vegetation is condensed.

For the ***first case*** with 6 classes, the methods that best fit our vegetation classes and the proposed work scenario are the maximum likelihood method and the ANN method.

It is important to understand the operation of the supervised classification methods to be used and their behaviour according to the characteristics of the study area. (Abburu and Babu Golla, 2015). The maximum likelihood method is a parametric method, which considers the statistical distribution of the pixel values for each vegetation class. The probabilistic model used by this algorithm is based on the normal distribution using the mean and the covariance matrix of the training areas as the base parameters of the model (Jha et al., 2019; Lyons et al., 2018). These characteristics allow the method not to be so affected by the characteristics of the study area in terms of class separability and the generalization of information due to the spatial resolution of the work.

The ANN, applied with different iterations to identify the best approximation of the result, generates results like the maximum likelihood for the conditions of this work. This method based on the continuous learning of the sample values and the environment to be modelled allows an iterative adjustment when classifying the image (Pande-Chhetri et al., 2017; Pelletier et al., 2019). In our study, several attempts with a different number of iterations were proposed to analyse the trends and adjustment of this method and how the error was stabilizing as the number of iterations increased. In addition, when selecting the number of iterations in the model validation, it was considered the importance of reducing or avoiding the model overfitting.

On the other hand, considering the results, the methods that adjusted the worst and whose validation had low statistical values were the method of the minimum distance, the parallelepiped and the Mahalanobis distance.

The method of minimum distance is based on assigning to each pixel of unknown identity of the original image that class whose Euclidean distance to the centroid of this is smaller. This fact causes the low sensitivity of the algorithm to the variance values in the spectral responses of the study classes; therefore, it is not very appropriate in our case study where the classes have a reduced spectral separability (Patil et al., 2012). Furthermore, this method tends to over-classify the image since it will assign each pixel a class value despite having some uncertainty in the process.

For its part, the parallelepiped classification method is based on defining the working space in hyper-rectangles for each of the classes and defining their limits from the maximum and minimum values of the training regions (ROIs). This adjustment allows us to give this method greater sensitivity with respect to the variances of our work classes, but still generates discrepancies when classifying them due to their low separability (Perumal and Bhaskaran, 2010). This implies that overlaps between parallelepipeds may occur in the classification of each pixel, generating uncertainty or, on the contrary, that it does not fall into any one and its value remains unassigned.

The Mahalanobis distance method gave better values than the previous ones in the first case, with similar quality to the maximum likelihood and better than the ANN. Again, it must be considered that this method, also based on the distance between pixels in a multivariate space, suffers from defects due to the low separability of the classes (García-

Santillán and Pajares, 2018). Despite this condition, this method considers the weighting of the classification distance, considering the covariance matrix of the set of values and therefore its results tend to better than the other distance based methods in our study area, because it mitigates the problem of separability between classes.

For the ***second case***, with 5 classes, the shrubs class was merged with the perennial trees due to their similar spectral response at the time of the image. After carefully analysing each stage of the process, it was resolved that once again the strong variability of the riparian forest vegetation together with the spatial resolution of the multispectral images caused a distortion in the separability between classes, affecting the application of the classification methods. The validation for the different methods continued showing low values. This fusion of classes shows a slight improvement in the models (in terms of overall accuracy) but without producing significant changes in the results.

For this reason, this work raised a third case in which the number of classes were 4, merging the classes of herbs and giant cane, due to its similar spectral signature for the multispectral bands. The calibration data improved with respect to case 2 as well as the validation values. Due to the simplification of classes, the variability and separability between them decreased. In this last case, the new fusion of classes shows again a low improvement in terms of overall accuracy in all the models, but the improvements do not exceed a 5%. The union of the herbs and giant cane classes (case 3) caused very over-predictive results on the herbs class, possibly due to the existence of a lot of data in those classes in the calibration phase, which determines the construction of the model. This trend did not occur in the previous case when the giant cane and herbs class were separated.

Considering the three cases and analysing the variations of the performance indicator, the maximum likelihood model with 4 vegetation classes has been considered as the one that best adapts to the riparian area under study.

The results obtained after the application of this most favourable classification model on the additional area of application showed a high percentage of herbs. This result may indicate the development of young habitats or perhaps it may be due to the presence and colonization of these spaces by giant cane. It would be very useful, in future research, to to refine the models proposed in this study, in order to improve the distinction between herbs and giant cane, and therefore to correctly evaluate the invasion of the cane in an extensive and automatic manner.

The class with second place in extension was the perennial trees, which implies that species such as Pinus, characteristics of the terrestrial ecosystem and not the riparian, occupy a relevant proportion of these habitats. A possible reason for this behaviour may be that these habitats are becoming drier, and that is why these species can better compete in these areas with respect to the riparian ones. Attending to the results obtained, we observe the abundance of natural species in drier areas such as Pinus and Mediterranean shrubs, increasingly tend to occupy areas closer to the channel, and therefore to colonize a greater proportion of the floodplain. The regulation of the flow due to the presence of dams together with scarce and spaced rain processes causes a lower frequency of flooding in these riparian spaces, which is why the trend of contraction of the development of the riparian forest has been more pressing day by day. This phenomenon is related to the

*terrestrialization*, a process by which the dry areas of the riparian habitat are colonized by plant species (Caskey et al., 2015).

## 5.5 Conclusions

The methodology presented in this work develops the results of the application of different supervised classification models on different plant succession phases distributed in the study area and that have previously been established as learning samples.

The use of this type of tools based on multispectral images is important to understand the state and distribution of the vegetation and how its succession phases evolve and colonize the riparian ecosystem. As a general recommendation, depending on the conditions of another study area, it will be necessary to use data according to the spatial distribution and the degree of heterogeneity of the species in order to optimize their degree of characterization and discrimination.

In this work, it has been possible to model the vegetation occupation area that the riparian succession phases have on a segment of the Serpis River. This will make possible to define the magnitude of the situation and have one more tool to evaluate and make decisions for the conservation and rehabilitation of the riparian zones. The continuous expansion of invasive species in these riparian ecosystems means an adverse impact on the autochthonous species that must be controlled continuously over time.

The results showed limitations in the classification using QuickBird© satellite images as a reference. For the date of the study, this multispectral cartographic source was presented as the best in terms of spatial resolution in the years of this study, but it has demonstrated deficient in the characterization of the riparian vegetation phases in the Mediterranean riparian forest. Although the calibration offered very good results, the validation indicated an opposite trend; this may indicate the need of improving the definition of validation areas. In addition, considering the general approach of this study, future research lines may cover the specific modelling of each one of vegetation classes considered, focusing on more specific objectives (e.g., invasive species). However, it will be necessary to incorporate sensors with higher spatial and spectral resolution which allows the better characterization of the species and series of vegetation. The ample application of UAV technology can allow data collection to house these improvements and the results obtained can improve considerably.

Through this discipline we will be able to generate classified 3D point clouds derived from images taken from a photogrammetric flight with a drone. In addition, the incorporation of airborne multispectral sensors in this type of vehicle will allow us to record precise information with high temporal and spatial resolutions, facilitating the validity of these products in work areas of reduced dimensions such as the study area of this work.

## 5.6 References


Abburu, S. and Babu Golla, S., 2015. Satellite Image Classification Methods and Techniques: A Review. International Journal of Computer Applications, 119(8), 20–25. https://doi.org/10.5120/21088-3779

Akasheh, O. Z., Neale, C. M.U. and Jayanthi, H., 2008. "Detailed Mapping of Riparian Vegetation in the Middle Rio Grande River Using High Resolution Multi-Spectral Airborne Remote Sensing." Journal of Arid Environments 72 (9): 1734–1744. doi:10.1016/j.jaridenv.2008.03.014.

Akay, A. E, Sivrikaya, F. and Gulci, S., 2013. "Analyzing Riparian Forest Cover Changes along the Firniz River in the Mediterranean City of Kahramanmaras in Turkey." doi:10.1007/s10661-013-3575-7.

Bertoldi, W., Drake, N. A. and Gurnell, A. M., 2011. "Interactions between River Flows and Colonizing Vegetation on a Braided River: Exploring Spatial and Temporal Dynamics in Riparian Vegetation Cover Using Satellite Data." Earth Surface Processes and Landforms 36 (11): 1474–1486. doi:10.1002/esp.2166.

Bhaskaran, S., Paramananda, S. and Ramnarayan, M., 2010. "Per-Pixel and Object-Oriented Classification Methods for Mapping Urban Features Using Ikonos Satellite Data." Applied Geography 30 (4). Elsevier Ltd: 650–665. doi:10.1016/j.apgeog.2010.01.009.

Blasch, G., Spengler, D., Hohmann, C., Neumann, C., Itzerott, S. and Kaufmann, H. 2015. Multitemporal soil pattern analysis with multispectral remote sensing data at the field-scale. Computers and Electronics in Agriculture, 113, 1–13. https://doi.org/10.1016/j.compag.2015.01.012

Blondel, J. and Aronson, J., 1999. Biology and wildlife of the Mediterranean region. Oxford University Press, Oxford. 328 pp.

Bruno, D., Zapata, V., Guareschi, S., Picazo, F., Dettori, E., Carbonell, J. A., Millán, A., Velasco, J. and Robledano, F., 2021. "Short-Term Responses of Aquatic and Terrestrial Biodiversity to Riparian Restoration Measures Designed to Control the Invasive Arundo Donax L." Accessed April 21. doi:10.3390/w11122551.

Büttner, Gy., Csillag, F. and Mather, P. M., 1988. Spectral And Spatial Information Content Of Spot Data. In: Geoscience and Remote Sensing Symposium, 1988. IGARSS '88. Remote Sensing: Moving Toward the 21st Century. International; 10/1988 DOI: 10.1109/IGARSS.1988.570172

Cabello, J. and Paruelo, J. M., 2008. La teledetección en estudios ecológicos, 17(3), 1–3.

Cairns, D. M., 2001. "A Comparison of Methods for Predicting Vegetation Type." Plant Ecology 156 (1): 3–18. doi:10.1023/A:1011975321668.

Camporeale, C. and Ridolfi, L., 2006. "Riparian Vegetation Distribution Induced by River Flow Variability: A Stochastic Approach." Water Resources Research 42 (10). doi:10.1029/2006WR004933.

Casagli, N., Frodella, W., Morelli, S., Tofani, V., Ciampalini, A., Intrieri, E. and Lu, P., 2017. Spaceborne, UAV and ground-based remote sensing techniques for landslide mapping, monitoring and early warning. Geoenvironmental Disasters, 4(1), 1–23.

https://doi.org/10.1186/s40677-017-0073-1

Caskey, S.T., Tyanna S. B., Wohl, E., Schnackenberg, E., Merritt, D. M. and Dwire, K.A., 2015. “Downstream Effects of Stream Flow Diversion on Channel Characteristics and Riparian Vegetation in the Colorado Rocky Mountains, USA.” Earth Surface Processes and Landforms 40 (5): 586–598. doi:10.1002/esp.3651.

Cheng, G. and Han, J., 2016. A survey on object detection in optical remote sensing images. ISPRS Journal of Photogrammetry and Remote Sensing, 117, 11–28. https://doi.org/10.1016/j.isprsjprs.2016.03.014

Christopoulou, A., Mallinis, G., Vassilakis, E., Farangitakis, G. P., Fyllas, N. M., Kokkoris, G. D. and Arianoutsou, M., 2019. Assessing the impact of different landscape features on post-fire forest recovery with multitemporal remote sensing data: The case of Mount Taygetos (southern Greece). International Journal of Wildland Fire, 28(7), 521–532. https://doi.org/10.1071/WF18153

Chuvieco, E., 2008. Teledeteccion ambiental.

Coffman, G. C., Ambrose, R.F. AND Rundel, P.W., 2010. “Wildfire Promotes Dominance of Invasive Giant Reed (Arundo Donax) in Riparian Ecosystems.” Biological Invasions 12 (8): 2723–2734. doi:10.1007/s10530-009-9677-z.

Coffman, Gretchen Christina. 2007. “Factors Influencing Invasion of Giant Reed (Arundo Donax) in Riparian Ecosystems of Mediterranean-Type Climate Regions.” Dissertation, 1–282.

Cohen, J., 1960. A coefficient of agreement for nominal scale, Educational and Psychological Measurement, 2O:37-46

Confederación Hidrográfica del Júcar (CHJ), 2019. Seguimiento del Plan Hidrológico del Júcar. Ciclo de planificación hidrológica 2015-2021. Año 2018

Congalton, R. G., Birch, K., Jones, R. and Schriever, J., 2003. “Evaluating Remotely Sensed Techniques for Mapping Riparian Vegetation.” Computers and Electronics in Agriculture 37 (1–3). Elsevier: 113–126. doi:10.1016/S0168-1699(02)00108-4.

Congalton, R. G., 1991. A review of assessing the accuracy of classification of remotely sensed daIa, Remote Sensing of Environment, 37 :35-46

Corenblit, D., Davies, N. S., Steiger, J., Gibling, M.R. and Bornette, G., 2015. “Considering River Structure and Stability in the Light of Evolution: Feedbacks between Riparian Vegetation and Hydrogeomorphology.” Earth Surface Processes and Landforms 40 (2): 189–207. doi:10.1002/esp.3643.

Cromp, R. F., 1991. Automated extraction of metadata from remotely sensed satellite imagery, in Proc. ACSM-ASPRS (American Congress of Survey Mapping/American Society of Photogrammetry and Remote Sensing), v. 3, Bethesda, Maryland, p. 111-120.

De Roeck, E. R., Verhoest, N. E. C., Miya, M. H., Lievens, H., Batelaan, O., Thomas, A. and Brendonck, L., 2008. Remote sensing and wetland ecology: A South African case study. Sensors, 8(5), 3542–3556. https://doi.org/10.3390/s8053542

Domaç, A. and Süzen, M. L., 2006. “Integration of Environmental Variables with Satellite Images in Regional Scale Vegetation Classification.” International

Journal of Remote Sensing 27 (7): 1329–1350. doi:10.1080/01431160500444806.

Douda, J., Boublík, K., Slezák, M., Biurrun, I., Nociar, J., Havrdová, A., Doudová, J., 2016. "Vegetation Classification and Biogeography of European Floodplain Forests and Alder Carrs." Applied Vegetation Science 19 (1): 147–163. doi:10.1111/avsc.12201.

Duarte, D. C., Zanetti, J., Gripp Junior, J. and Medeiros N., 2018. "Comparison of Supervised Classification Methods of Maximum Likelihood, Minimum Distance, Parallelepiped and Neural Network in Images of Unmanned Air Vehicle (UAV) in Viçosa - MG." Revista Brasileira de Cartografia 70 (2): 437–452. doi:10.14393/rbcv70n2-45377.

Dufour, S., Rodríguez-González, P.M. and Laslier, M., 2019. "Tracing the Scientific Trajectory of Riparian Vegetation Studies: Main Topics, Approaches and Needs in a Globally Changing World." Science of the Total Environment. Elsevier B.V. doi:10.1016/j.scitotenv.2018.10.383.

Dunford, R., Michel, K., Gagnage, M., Piégay, H. and Trémelo, M.L., 2009. "Potential and Constraints of Unmanned Aerial Vehicle Technology for the Characterization of Mediterranean Riparian Forest." International Journal of Remote Sensing 30 (19): 4915–4935. doi:10.1080/01431160903023025.

Erdas Inc., 1999. Erdas Field Guide. Erdas Inc., Atlanta, Georgia.

Feng, Q., Liu, J. and Gong, J., 2015. UAV Remote sensing for urban vegetation mapping using random forest and texture analysis. Remote Sensing, 7(1), 1074–1094. https://doi.org/10.3390/rs70101074

Fernandes, M. R., Constança Aguiar, F., Ferreira, M.T. and Cardoso Pereira, J.M., 2013. "Spectral Separability of Riparian Forests from Small and Medium-Sized Rivers across a Latitudinal Gradient Using Multispectral Imagery." International Journal of Remote Sensing 34 (7): 2375–2401. doi:10.1080/01431161.2012.744491.

Fisher, R.A., 1936. The use of multiple measurements in taxonomic problems, Ann. Eugenics 7. 179–188

Garcia-Arias, A., Frances, F.,Andrés-Domenech, I., Vallés, F., Garófano-Gómez, V. and Martinez-Capel, F., 2011. "Modelación Dinámica de La Vegetación de Ribera. Calibración Del Modelo RIPFLOW y Su Aplicación En Escenarios de Regulación de Caudales." II Jornadas de Ingeniería del Agua. Barcelona (España), 5-6 Octubre 2011.

García-Arias, A, Francés, F. Ferreira, T., Egger, G., Martínez-Capel, F., Garófano-Gómez, V., Andrés-Doménech, I., Politti, E., Rivaes, R. and Rodríguez-González. P.M., 2013. "Implementing a Dynamic Riparian Vegetation Model in Three European River Systems." Ecohydrology 6 (4). Affiliation: Research Institute of Water and Environmental Engineering, Universitat Politècnica de València, Valencia, Spain; Affiliation: Forest Research Center, Instituto Superior de Agronomia, Technical University of Lisbon, Lisbon, Portugal; Affiliati: 635–651. doi:10.1002/eco.1331.

García-Santillán, I. D. and Pajares, G., 2018. On-line crop/weed discrimination through the Mahalanobis distance from images in maize fields. Biosystems Engineering, 166, 28–43. https://doi.org/10.1016/j.biosystemseng.2017.11.003

Garófano-Gómez, V., Martínez-Capel, F., Peredo-Parada, M., Marín, E. J. O., Mas, R. M., Costa, R. M. S. and Pinar-Arenas, J. L., 2011. Assessing hydromorphological and floristic patterns along a regulated Mediterranean river: The Serpis River (Spain). Limnetica, 30(2), 307–328.

Garófano-Gómez, V., Martínez-Capel, F., Bertoldi, W.,Gurnell, A., Estornell, J. and Segura-Beltrán, F., 2013. "Six Decades of Changes in the Riparian Corridor of a Mediterranean River: A Synthetic Analysis Based on Historical Data Sources." Ecohydrology 6 (4): 536–553. doi:10.1002/eco.1330.

Garófano-Gómez, V, Martínez-Capel, F., Muñoz-Mas, R., Costa, R.M.S., Villanueva-García, J.F. and Francés, F.F., 2010. "Response Curves of Hydrological Variables for Riparian Woody Species, Oriented to Water Management of Mediterranean Rivers in Spain." 8th International Symposium on Ecohydraulics, 1679–1686.

Garófano Gómez, V., Vezza, P., Di Torino, P., Martinez-Capel, F. and Francés F., 2014. Key Drivers of Riparian Vegetation Successional Pathways in a Mediterranean River System SUDOE-CERES View Project Soil and Water Conservation in West Africa View Project. https://www.researchgate.net/publication/263661795.

Garófano Gómez, V., Martínez Capel, F., Delgado Artes, R., 2019. Les riberes del Serpis. Gestió de l'aigua per a la seua conservació. CEIC Alfons El Vell. http://hdl.handle.net/10251/129317

Ghamisi, P., Rasti, B., Yokoya, N., Gloaguen, R., Wang, Q., Höfle, B. and Benediktsson, J. A., 2018. Multisource and Multitemporal Data Fusion in Remote Sensing. ArXiv, (march).

González, E., Felipe-Lucia, M.R., Bourgeois, B., Boz, B., Nilsson, C., Palmer, G.and Sher, A.A., 2017. "Integrative Conservation of Riparian Zones." Biological Conservation 211 (July). Elsevier Ltd: 20–29. doi:10.1016/j.biocon.2016.10.035.

Govender, M., Chetty, K., Naiken, V. and Bulcock, H., 2008. "A Comparison of Satellite Hyperspectral and Multispectral Remote Sensing Imagery for Improved Classification and Mapping of Vegetation." Water SA 34 (2): 147–154. doi:10.4314/wsa.v34i2.183634.

Hagner, O. and Reese, H., 2007. "A Method for Calibrated Maximum Likelihood Classification of Forest Types." Remote Sensing of Environment 110 (4): 438–444. doi:10.1016/j.rse.2006.08.017.

Houborg, R., Fisher, J. B. and Skidmore, A. K., 2015. Advances in remote sensing of vegetation function and traits. International Journal of Applied Earth Observation and Geoinformation, 43, 1–6. https://doi.org/10.1016/j.jag.2015.06.001

Huylenbroeck, L., Laslier, M.. Dufour, S., Georges, B., Lejeune, P. and Michez, A., 2020. "Using Remote Sensing to Characterize Riparian Vegetation: A Review of Available Tools and Perspectives for Managers." Journal of Environmental Management 267 (March). Elsevier Ltd: 110652. doi:10.1016/j.jenvman.2020.110652.

Jha, S., Das, J., Sharma, A., Hazra, B. and Goyal, M. K., 2019. Probabilistic evaluation of vegetation drought likelihood and its implications to resilience across India. Global and Planetary Change, 176(January), 23–35. https://doi.org/10.1016/j.gloplacha.2019.01.014

Kaneko, K. and Nohara, S., 2014. Review of Effective Vegetation Mapping Using the UAV (Unmanned Aerial Vehicle) Method. Journal of Geographic Information System, 06(06), 733–742. https://doi.org/10.4236/jgis.2014.66060

Komorowski, J., Pawlak, Z., Polowski, L. and Skowron, A., 1999. Rough Sets: A Tutorial. In S. K. Pal, A. Skowron editors, Rough Fuzzy Hybridization, Springer, p 3-98

Kontsiotis, V., Zaimes, G.N., Tsiftsis, S., Kiourtziadis, P. and Bakaloudis, D., 2019. "Assessing the Influence of Riparian Vegetation Structure on Bird Communities in Agricultural Mediterranean Landscapes." Agroforestry Systems. doi:10.1007/s10457-017-0162-x.

Lillesand, T., Kiefer, R. and Chipman, J., 2004. Remote Sensing and Image Interpretation (5th ed.). John Wiley and Sons. 763 p.

López-Baucells, A., Casanova, L., Puig-Montserrat, X., Espinal, A., Páramo, F. and Flaquer, C., 2017. "Evaluating the Use of Myotis Daubentonii as an Ecological Indicator in Mediterranean Riparian Habitats." Ecological Indicators. doi:10.1016/j.ecolind.2016.11.012.

Lyons, M. B., Keith, D. A., Phinn, S. R., Mason, T. J. and Elith, J., 2018. A comparison of resampling methods for remote sensing classification and accuracy assessment. Remote Sensing of Environment, 208(February), 145–153. https://doi.org/10.1016/j.rse.2018.02.026

Maceda-Veiga, A., Basas, H., Lanzaco, G., Sala, M., de Sostoa, A. and Serra, A., 2016. "Impacts of the Invader Giant Reed (Arundo Donax) on Riparian Habitats and Ground Arthropod Communities." Biological Invasions 18 (3). Springer International Publishing: 731–749. doi:10.1007/s10530-015-1044-7.

Mahalanobis, P.C., 1936. On the generalised distance in statistics, Proceedings of the National Institute of Science of India 12. 49–55.

Martínez-Fernández, V., Van Oorschot, M., De Smit, J., González del Tánago, M. and Buijse, A.D., 2018. "Modelling Feedbacks between Geomorphological and Riparian Vegetation Responses under Climate Change in a Mediterranean Context." Earth Surface Processes and Landforms 43 (9): 1825–1835. doi:10.1002/esp.4356.

Metternicht, G. I. and Zinck, J. A., 1998. Evaluating the information content of JERS-1 SAR and Landsat TM data for discrimination of soil erosion features. ISPRS Journal of Photogrammetry & Remote Sensing, 53, 143–153. DOI: 10.1016/s0924-2716(98)00004-5

Michez, A., Piégay, H., Jonathan, L., Claessens, H. and Lejeune, P., 2016. "Mapping of Riparian Invasive Species with Supervised Classification of Unmanned Aerial System (UAS) Imagery." International Journal of Applied Earth Observation and Geoinformation 44. Elsevier B.V.: 88–94. doi:10.1016/j.jag.2015.06.014.

Nadal-Sala, D., Sabaté, S., Sánchez-Costa, E., Poblador, S., Sabater, F. and Gracia, C., 2017. "Growth and Water Use Performance of Four Co-Occurring Riparian Tree Species in a Mediterranean Riparian Forest." Forest Ecology and Management 396. Elsevier B.V.: 132–142. doi:10.1016/j.foreco.2017.04.021.

Naiman, R. J., Latterrell, J.J., Pettit, N.E. and Olden, J.D., 2008. Flow variability and the biophysical vitality of river systems. C. R. Geosciences, 340: 629–643.

Nivedita Priyadarshini, K., Kumar, M., Rahaman, S.A. and Nitheshnirmal, S., 2018. "A Comparative Study of Advanced Land Use/Land Cover Classification Algorithms Using Sentinel-2 Data." ISPRS - International Archives of the Photogrammetry, Remote Sensing and Spatial Information Sciences XLII–5 (November): 665–670. doi:10.5194/isprs-archives-xlii-5-665-2018.

Orimoloye, I. R., Kalumba, A. M., Mazinyo, S. P. ans Nel, W., 2020. Geospatial analysis of wetland dynamics: Wetland depletion and biodiversity conservation of Isimangaliso Wetland, South Africa. Journal of King Saud University - Science, 32(1), 90–96. https://doi.org/10.1016/j.jksus.2018.03.004

Pande-Chhetri, R., Abd-Elrahman, A., Liu, T., Morton, J. and Wilhelm, V. L., 2017. Object-based classification of wetland vegetation using very high-resolution unmanned air system imagery. European Journal of Remote Sensing. https://doi.org/10.1080/22797254.2017.1373602

Paola, J. D., and Schowengerdt, R.A., 1995. "A Detailed Comparison of Backpropagation Neural Network and Maximum-Likelihood Classifiers for Urban Land Use Classification." IEEE Transactions on Geoscience and Remote Sensing 33 (4): 981–996. doi:10.1109/36.406684.

Papastergiadou, E. S., Retalis, A.,Apostolakis, A. and Georgiadis TH., 2008. "Environmental Monitoring of Spatio-Temporal Changes Using Remote Sensing and GIS in a Mediterranean Wetland of Northern Greece." Water Resources Management 22 (5): 579–594. doi:10.1007/s11269-007-9179-7.

Patil, M. B., Desai, C. G. and Umrikar, B. N., 2012. Image Classification Tool for Land Use / Land Cover Analysis : A Comparative Study of Maximum Likelihood. International Journal of Geology, Earth, and Environmental Sciences, 2(3), 189–196.

Pawlak, Z., 1982. "Rough Set," Int. J. Inform. Comput. Sci. 11, pp, 341-356

Pelletier, C., Webb, G. I. and Petitjean, F., 2019. Temporal convolutional neural network for the classification of satellite image time series. Remote Sensing, 11(5), 1–25. https://doi.org/10.3390/rs11050523

Perumal, K. and Bhaskaran, R., 2010. Supervised Classification Performance of Multispectral Images, 2(2), 124–129. Retrieved from http://arxiv.org/abs/1002.4046

Piramanayagam, S., Saber, E., Schwartzkopf, W. and Koehler, F. W., 2018. Supervised classification of multisensor remotely sensed images using a deep learning framework. Remote Sensing, 10(9), 1–25. https://doi.org/10.3390/rs10091429

Politti, E., Bertoldi, W., Gurnell, A. and Henshaw, A., 2018. "Feedbacks between the Riparian Salicaceae and Hydrogeomorphic Processes: A Quantitative Review." Earth-Science Reviews 176 (July 2017). Elsevier: 147–165. doi:10.1016/j.earscirev.2017.07.018.

Rivaes, Rui, Rodríguez-González, P.M., Albuquerque, A., Pinheiro, A.N., Egger, G. and Ferreira, M.T., 2013. "Riparian Vegetation Responses to Altered Flow Regimes

Driven by Climate Change in Mediterranean Rivers." Ecohydrology 6 (3): 413–424. doi:10.1002/eco.1287.

Rivaes, R. P., Rodríguez-González, P.M., Ferreira, M.T., Pinheiro, A.N., Politti, E., Egger, G., García-Arias, A. and Francés, F., 2014. "Modeling the Evolution of Riparian Woodlands Facing Climate Change in Three European Rivers with Contrasting Flow Regimes." PLoS ONE 9 (10). Public Library of Science. doi:10.1371/journal.pone.0110200.

Rwanga, S. S. and Ndambuki, J. M., 2017. Accuracy Assessment of Land Use/Land Cover Classification Using Remote Sensing and GIS. International Journal of Geosciences, 08(04), 611–622. https://doi.org/10.4236/ijg.2017.84033

Schnitzler, A., Hale, B.W. and Alsum, E.M., 2007. "Examining Native and Exotic Species Diversity in European Riparian Forests." Biological Conservation 138 (1–2). Elsevier: 146–156. doi:10.1016/j.biocon.2007.04.010.

Shen, G., Sakai, K. and Hoshino, Y., 2010. "High Spatial Resolution Hyperspectral Mapping for Forest Ecosystem at Tree Species Level." Agricultural Information Research 19 (3): 71–78. doi:10.3173/air.19.71.

Short, J. N., 1991, A real-time expert system and neural network for the classification of remotely sensed data, in Proc. ACSM-ASPRS (American Congress of Survey Mapping/American Society of Photogrammetry and Re- mote Sensing), v. 3, Bethesda, Maryland, p. 406-418

Sisodia, P. S., Tiwari, V. and Kumar, A., 2014. "A Comparative Analysis of Remote Sensing Image Classification Techniques." Proceedings of the 2014 International Conference on Advances in Computing, Communications and Informatics, ICACCI 2014. IEEE, 1418–1421. doi:10.1109/ICACCI.2014.6968245.

Song, W., Mu, X., Yan, G. and Huang, S., 2015. "Extracting the Green Fractional Vegetation Cover from Digital Images Using a Shadow-Resistant Algorithm (SHAR-LABFVC)." Remote Sensing 7 (8): 10425–10443. doi:10.3390/rs70810425.

Souza, C. H. W., Mercante, E., Prudente, V.H.R. and Justina, D.D.D., 2013. "Methods of Performance Evaluation for the Supervised Classification of Satellite Imagery in Determining Land Cover Classes." Ciencia e Investigación Agraria 40 (2): 419–428. doi:10.4067/s0718-16202013000200016.

Stella, J. C, Rodríguez-González, P.M., Dufour, S. and Bendix, J., 2013. "Riparian Vegetation Research in Mediterranean-Climate Regions: Common Patterns, Ecological Processes, and Considerations for Management." doi:10.1007/s10750-012-1304-9.

Sun, D.W., 2016. Computer Vision Technology for Food Quality Evaluation: Second Edition. Computer Vision Technology for Food Quality Evaluation: Second Edition. Elsevier Inc. doi:10.1016/C2014-0-01718-2.

Sunar Erbek, F., Özkan, C. and Taberner, M., 2004. "Comparison of Maximum Likelihood Classification Method with Supervised Artificial Neural Network Algorithms for Land Use Activities." International Journal of Remote Sensing 25 (9). Taylor and Francis Ltd.: 1733–1748. doi:10.1080/0143116031000150077.

Tewkesbury, A. P., Comber, A. J., Tate, N. J., Lamb, A. and Fisher, P. F., 2015. A critical synthesis of remotely sensed optical image change detection techniques. Remote Sensing of Environment, 160, 1–14. https://doi.org/10.1016/j.rse.2015.01.006

Ustin, L. S., Valko, P. G., Kefauver, S. C., Santos, M. J., Zimpfer, J. F. and Smith, S. D., 2009. Remote sensing of biological soil crust under simulated climate change manipulations in the Mojave Desert. Remote Sensing of Environment 113, 317–328. DOI: 10.1016/j.rse.2008.09.013

Vihervaara, P., Auvinen, A. P., Mononen, L., Törmä, M., Ahlroth, P., Anttila, S. and Virkkala, R., 2017. How Essential Biodiversity Variables and remote sensing can help national biodiversity monitoring. Global Ecology and Conservation, 10, 43–59. https://doi.org/10.1016/j.gecco.2017.01.007

Wald, A., 1944. On the statistical problem arising in the classification of an individual into one of two groups, Ann. Math.Statist. 15.145–162

Xie, Y., Sha, Z. and Yu. M., 2008. "Remote Sensing Imagery in Vegetation Mapping: A Review." Journal of Plant Ecology 1 (1): 9–23. doi:10.1093/jpe/rtm005.

Yang, X., 2007. "Integrated Use of Remote Sensing and Geographic Information Systems in Riparian Vegetation Delineation and Mapping." International Journal of Remote Sensing 28 (2): 353–370. doi:10.1080/01431160600726763.

Zaimes, G. N., 2020. "Mediterranean Riparian Areas-Climate Change Implications and Recommendations." Journal of Environmental Biology 41 (5): 957–965. doi:10.22438/JEB//41/5/MRN-1454.

Zanotta, D. C., Zortea, M. and Ferreira, M. P., 2018. A supervised approach for simultaneous segmentation and classification of remote sensing images. ISPRS Journal of Photogrammetry and Remote Sensing, 142(April), 162–173. https://doi.org/10.1016/j.isprsjprs.2018.05.021

Zeballos, S. R., Giorgis, M.A., Cabido, M.R., Acosta, A.T.R., Iglesias, M. R. and Cantero, J.J., 2020. "The Lowland Seasonally Dry Subtropical Forests in Central Argentina: Vegetation Types and a Call for Conservation." Vegetation Classification and Survey 1 (1): 87–102. doi:10.3897/vcs/2020/38013.

Zema, D. A., Bombino, G., Denisi, P., Lucas-Borja, M.E. and Zimbone, S.M., 2018. "Evaluating the Effects of Check Dams on Channel Geometry, Bed Sediment Size and Riparian Vegetation in Mediterranean Mountain Torrents." Science of the Total Environment. doi:10.1016/j.scitotenv.2018.06.035.

Zhang, X., Huili Wang, A.W., Jian Yin, L.Z., Liu, Z. and Yu, D., 2016. "The Overgrowth of Zizania Latifolia in a Subtropical Floodplain Lake: Changes in Its Distribution and Possible Water Level Control Measures." Ecological Engineering 89. Elsevier B.V.: 114–120. doi:10.1016/j.ecoleng.2016.01.069.

# 6. Conclusions

Throughout the different chapters, the processes and dynamics in different riparian ecosystems have been analysed and discussed, considering different perspectives, and applying different methodologies. With all this, the morphological behaviour of the riverbed has been characterized and considering the hydraulic characteristics of the study area on ephemeral channels. Thus we were able to verify the severe changes in the characteristics and disposition of sediments that took place after relevant hydrologic events, thanks to the techniques used. In addition, in a permanent river we performed the classification of the riparian forest, in a way that the changes in the riparian dynamics could be analysed and modelled, including the invasive species.

Therefore, this thesis is presented as a compilation of interesting and highly applicable methodologies in the management and study of the riparian environment, both for a field of geomorphological analysis and for the study of the succession phases of riparian vegetation.

Hereafter, the conclusions of this thesis are detailed, divided into blocks, according to the organization of the document already explained.

Combining SfM Photogrammetry and Terrestrial Laser Scanning to Assess Event-Scale Sediment Budgets along a Gravel-Bed Ephemeral Stream.

- The characterization of the channel morphology was presented, applying massive high-resolution data capture techniques, and implementing a theoretical and practical methodology for its potential application in the monitoring of ephemeral and semi temporary channels.

- Considering the magnitude of the events in relation to the geomorphological process and the morphological adjustments, we found that large floods tend to produce vertical sedimentary accretion, after having mobilized a large amount of bed load upstream the study site, due to high power gradients and excess energy. On the contrary, other moderate high flows were only capable of exerting a superficial washing, selective transport, and local scrubbing, mainly affecting the active low bars.

- Event scale implied short-term changes in the bed elevation depending on the peak flow. Such changes were satisfactorily evaluated through the combined use of SfM-MVS and TLS, according to the spatial scale and geomorphic scenario.

Changes in stream power and morphological adjustments at the event-scale and high spatial resolution along an ephemeral gravel-bed channel

- The morphological dynamics and adjustments are responding to complex flow dynamics at each event scale, the approach proposed, based on the integration and combination of UAV-SfM and TLS, has allowed this assessment to be satisfactorily and correctly solved.

- The largest discharge events showed the highest values of stream power and important spatial variability. These peak flows produced a large quantity of bedload, inducing to a large transitory erosion and leading to overall vertical accretion. By contrast, lower stream power values were associated with the removal of bank-failure deposits and moderate changes in active low bars.

- The continuous increase in the frequency of flash floods due to climate change was indicated by previous studies. Our results indicate that bed aggradation during the major flood is based on a relationship with mean stream power gradient at peak flood discharges, with consequent changes in bed elevation. Otherwise, during other moderate events bed scour took place at bankfull and sub-bankfull stages. In this way, the increase in the contribution of coarse sediments from the slopes was promoted, thus causing lateral erosion and widening the channel.

Spatial validation of submerged fluvial topographic models by mesohabitat units.

- A refraction correction algorithm for submerged topography has been presented to determine the morphology of the submerged river bed, and thus to analyse the hydraulic variables associated.

- The spatially continuous and high resolution validation of quantitative submerged river morphology models, which was performed on all the pixels of the model within distinct mesohabitat types, demonstrates greater robustness and allows it to be considered for its application in different scenarios.

- Pool mesohabitat presents less irregularity on the water surface and the flow velocity was lower than in the riffle mesohabitat, but the effect caused by the greater water depth in the pools produced higher errors than in the riffle. Despite the emerging elements and the eddies formed in the riffle, the errors were lower in these shallower habitats.

Classification of riparian vegetation types based on supervised classification algorithms. A case study in a Serpis River segment (Valencia).

- We developed a methodology for the study and classification of the succession phases of riparian vegetation in a Mediterranean river, with the future goal of automatically defining the distribution and the processes of vegetation succession and the colonization by invasive species.

- The use of multispectral satellite images of high spatial resolution (2.4 m pixel) presented limitations in the characterization of the riparian vegetation phases in the Mediterranean riparian forest.

- The expansion of the invasive species, such as the giant cane or elephant grass, in the riparian forest and its spectral similarity with autochthonous species of the Mediterranean riparian ecosystem constitutes a difficulty when it comes to its unequivocal classification.

# 7. Future lines of research

Based on the results obtained in this doctoral thesis, the following future lines of research have been proposed:

- Analyses of the behaviour of successive rainfall and sediment transport events in the study areas of Rambla de la Azohía (Murcia). Obtaining a greater range of information and trends in the riverbed forms and the changes in the sedimentary budget. This work will allow us to improve the prediction of trajectories of morphological change and future scenarios in ephemeral rivers facing the global change.

- Integration of remote sensing techniques such as the terrestrial laser scanner (TLS) and UAVs, for instance using airborne Laser Imaging Detection and Ranging (LiDAR) mounted in UAVs of different types. These techniques allow the collection of precise and massive information, in large extensions, using shorter times in fieldwork campaigns. We will be able to carry out high resolution characterizations, improving the temporary resolution of the works and with total autonomy.

- Further development and application of the correction of the refraction in submerged topography. This technique can be further developed, to obtain detailed morphology of the river bed in a wide variety of river streams with different types of mesohabitats and the evaluation of its precision and reliability. This fact will allow the adjustment of the proposed method to be calibrated and evaluated in different environments, improving its robustness and applicability.

- Evaluation of classification models with remote sensors of higher spatial and radiometric resolution, for riparian vegetation. This will allow the improvement of the calibration and validation of supervised classification models for the succession phases of Mediterranean riparian vegetation. The modelling itself, and further detailed study of the trends of the models, for the different classes of vegetation, will allow further improvements in the classification and definition of actual and past scenarios in riparian environments, with subsequent positive results in riparian modelling.